Durham E-Theses

Optical Deformation of Microdroplets at Ultralow Interfacial Tension

ALEXANDER LEIGHTON HARGREAVES

Optical Deformation
of Microdroplets at
Ultralow Interfacial Tension

Alexander L. Hargreaves

A Thesis presented for the degree of
Doctor of Philosophy

Supervisor: Prof. Colin D. Bain
Department of Chemistry
University of Durham
United Kingdom

2016

I dedicate this work
to my earnest friends
of many years and of few.

Optical Deformation of Microdroplets at Ultralow Interfacial Tension

Hargreaves, A. L.

Submitted for the degree of Doctor of Philosophy

April 2016

Abstract

What is the shape of a droplet? Its interfacial tension dictates that it is very close to a perfect sphere. Herein, the interfacial tension is reduced to ultralow values ($0.1 - 100$ μNm^{-1}) by careful formulation of surfactant additives, such as for mixtures that form microemulsions. The droplet need not be spherical but can accommodate external forces of a similar magnitude. The control and precision of forces afforded simply by light - in the form of highly focused Nd:YAG laser beams - are exploited in this work to deform hydrocarbon oil-in-water emulsion droplets of 1-10 μm diameter. To this end, a novel, integrated platform for microfluidic generation, optical deformation and 3D fluorescent imaging of droplets is presented.

Previous attempts to characterise optically-controlled microdroplet shapes have been limited to 2D projections. Here, that ambiguity is resolved using 3D confocal laser scanning- and structured illumination microscopy. 2D and 3D arrays of up to four Gaussian point traps are generated by holograms and acousto-optics. A variety of regular, prolate, oblate and asymmetric shapes are produced and correlated with parameters such as optocapillary number, trap separation and capillary length. Exotic shapes exhibiting zero or negative mean and Gaussian curvatures are presented alongside their brightfield counterparts.

The complex phase behaviour of emulsion droplets and their parent phases is observed to couple strongly to thermal absorption of the beams. The rich interfacial chemistry, its relation to the forces determining droplet shape and the surprising ability to create nanofluidic networks between droplets are investigated.

Declaration

The work in this thesis is based on research carried out under the supervision of Prof. Colin D. Bain, Department of Chemistry, University of Durham, United Kingdom. No part of this thesis has been submitted elsewhere for any other degree or qualification. All parts consist solely of my own work, unless referenced to the contrary within.

Acknowledgements

I would like to thank my family and friends for their rather saintly levels of patience and immeasurable support. First abuse, then bemuse, that's my M.O.

I am lastingly grateful to Prof. Colin D. Bain and my wonderful colleagues under him - particularly Andy K. Kirby and Oliver W. J. Burnham, plus the groups of Sharon Cooper in Durham and of Makoto Aratono in Kyushu University, Japan, for every action of encouragement down to the last cup of tea!

As for those who prefer strong coffee, I am strongly indebted to Guido Bolognesi and Oscar Ces of Imperial College London and Andy Ward of STFC. Our trips have been fun.

Always enlivening the Optonanofluidics project were: David Tapp, Jonny Taylor, Buddho Chakrabarti, Lian Hutchings, Gordon Love, Mark Neil, Xize Niu, Alex Lubansky and in an honorary capacity, Andrew Howe and David Woods. The project students Will Taylor, Danni Hainsworth and Flo Gregson made an outstanding difference to my first experiences of collaborative research and mentoring.

Thanks also to Chris Saunter, Andy and Jonny for a headstart with the behemoth of code!

Contents

Contents

vii

List of Figures

List of Tables

Introduction

Rationale

Since Ashkin's pioneering work [1], optical tools have been employed in the manipulation of microscopic matter across the sciences. Optical tweezers are routinely used to study soft matter, microbiological and related model systems [2–4]. This follows wider recognition of their capability for highly sensitive, non-invasive and responsive measurement and manipulation. Optical tweezers are highly focused lasers, typically of moderately high power (10 mW - 1 W), which exert forces on the piconewton scale. They rely on the momentum transfer that occurs on refraction through a microscopic particle, in order to confine that particle's position near the focus of the beam. The laser focus is provided by a microscope objective of high numerical aperture, which also facilitates imaging of the particle. As such, the micron scale of the experiments is dictated by considering the largest object that can be trapped stably, in comparison with the smallest that can be interrogated by optical microscopy.

As microparticles diversify, a wide range of technological solutions opens up. Photonic and meta-materials require a large number of reproducible 3D features on the near- or sub-wavelength scale. Properties of electronic microcomponents also rely on precise morphology. Tissue templating and drug delivery responses emerge from topographical and chemical stimuli for biological cells, for which anisotropic microparticles could pose a feasible model. From a scientific perspective, these microparticles are relatively simple systems, with which the interactions between light and matter can be probed.

Whilst solid microparticles have been created for many purposes, *complex liquids* represent a reservoir of unexplored science. Immediately, solution chemistry, flow physics and deformable shapes become imaginable. The latter is the central rationale for this thesis.

The chief impediment to this vision is that for liquid microdroplets, surface (or interfacial) tension minimises surface area, thereby imposing a spherical interface. However, authors within this collaboration have demonstrated previously [5] that systems of conventional optical traps are able to deform oil-in-water emulsion drops displaying ultralow interfacial tension (ULIFT). At ULIFT conditions, forces other than the interfacial tension influence the statics and dynamics of the droplet shapes significantly. Alongside the contrast in refractive index across the interface, ULIFT is therefore an important requirement for optical deformation [6]. Following these authors, the present work finds that these conditions are fulfilled by certain amphiphile/alkane/aqueous systems - those capable of forming efficient microemulsions.

Previous studies have been limited in scope; until now, the optical trap locations have been confined to a 2D plane. Moreover, prior attempts to quantify optical deformation relied only on conventional 2D imaging; for example, brightfield microscopy allows a straightforward - if ambiguous - assessment of the 3D surface *in situ*. True 3D techniques are used to overcome this ambiguity. Modern emulsion chemistry admits a vast range of materials, organic and inorganic, that can be optically manipulated on the submicron scale. A microfluidic approach provides a precise, flexible, high-throughput production method. In addition to the optical forces, effects relevant to deformable droplets are explored herein, including thermally-excited fluctuations, viscous flows, thermocapillarity and buoyancy.

The summarised aims of the project collaboration are to optically deform emulsion droplets for the following purposes:

1. to explore possible shapes with 'conventional' Gaussian optical tweezers,

2. to relate the liquid morphology to the droplet characteristics and trapping conditions;

3. to produce nanothread networks and explore their stability and dynamics.

The presented thesis covers a subset of these aims, namely:

- to pursue reproducible methods for generating droplets that can be deformed with optical tweezers,

- to implement a suitable hierarchy of optical tweezing capabilities for multiple independent trapping positions,

- to formulate emulsions that are optimised for the deformation experiment, primarily those displaying an ultralow interfacial tension,

- to develop the experimental capability for and theory underlying nonlinear deformations and nanothread networks in 3D, and

- to exploit 3D fluorescence imaging for the interrogation of droplet shapes at equilibrium, focusing on polygonal prisms (2D arrays) and polyhedra (3D arrays).

Chapter guide

Chapter 1 reviews current understanding of **ultralow interfacial tension** phenomena and the parent microemulsion systems. It describes the author's practical **formulation** and assessment of microemulsions, in some cases novel, to obtain reliable ULIFT with different oils and tunable dependence on temperature,

Chapter 2 introduces the concepts of **optical tweezers**, and describes the author's practical implementation of multiple optical tweezers in three different set-ups: split-polarisation, acoustic-optical deflection and holography-based, with a view to a novel, comprehensive optonanofluidic platform,

Chapter 3 describes the **manual** and **microfluidic** methods used herein for controlled **droplet production**. The author presents the design, development and performance of a novel platform for automated microfluidics of ultralow interfacial formulations. The novel phase behaviour of oily microemulsion droplets with changes in temperature and salinity are explored and categorised,

Chapter 4 presents a wide range of novel experimental results and a cohesive theory regarding the dynamic **phase behaviour** of oily microemulsion droplets when **exposed to focused lasers**, particularly the effect of laser heating; the traps are generated using the split-polarisation technique,

Chapter 5 is a short aside that summarises the author's contribution to the understanding of droplet bifurcation into **nanothreads**, under the action of optical tweezers. Novel theoretical insights into the interfacial physics are used to qualify experimental deformation results in 2D imaging, both original and literary,

Chapter 6 presents the **static 3D images** of optically-deformed oil droplets and networks, as obtained by position-calibrated confocal and structured illumination microscopy; the traps are generated using the acousto-optic deflection and adaptive holographic methods;

Conclusions build on the Chapter discussions to summarise the work and explore its implications in the fields of microfluidics, optical tweezing and emulsion technology.

Technical acknowledgements

Although an individual thesis, this project is associated with and forms part of a group effort. It is therefore fitting that the author acknowledges the technical contributions of others to each section, as follows.

Chapter 1 - GB first defined the deformability scales for droplets (1-4) and provided PIT calibration curves for literature spinning drop tensiometry. DH performed SAXS runs on middle phases. The author thanks MCP for valuable use of the sessile drop apparatus. FG helped to produce the temperature insensitive emulsions used in Chapter 4.

Chapter 2 - The author designed and constructed the first platform (Setup A) without assistance. FG, AKK and the author rebuilt this setup with refinements at a later date as used in Chapter 4 by FG and the author. For the second platform (Setup B) the *LabView* control software for the AODs was authored by AW and his former student MP. For the third platform (Setup C), AKK and the author worked together on the electrical construction, optical alignment and programming. AKK designed and built the structured illumination microscopy (SIM) arm (§ 6.1.2) and authored server code that coordinated the camera, stages and SIM refocusing optics (§ 2.4.3). OWJB constructed the Raman spectrometer arm referred to in the author's presented design.

Chapter 3 - GB was responsible for designing and prototyping the microfluidic observation chambers (ObC) and establishing suitable flow rate regimes for droplet generation (§ 3.4.1). AKK championed the electrical construction and microprocessor debugging associated with the automated microfluidic valves (§ 3.4.3).

Chapter 4 - Microscopy and optical tweezing shown in this chapter were planned and performed in conjunction with FG and uses stills from her video datasets. The discussion and interpretation of these shared, published results is solely the author's own. The finite element model calculation for laser heating was written in COMSOL by GB.

Chapters 5 & 6 - The confocal microscope scan head was arranged by AW and SB on Setup B. GB and the author performed the deformation experiments jointly, in which the brightfield and confocal images of thread networks and droplets were obtained. On Setup C, MN and AKK provided the holograms and SIM stacks respectively for the tetrahedral arrays.

Legend

AKK Andrew K. Kirby, Univ. Durham,

AW Andrew D. Ward, STFC Central Laser Facility,

DH Danielle Hainsworth, Univ. Durham,

FG Florence Gregson, Univ. Durham,

GB Guido Bolognesi, Imperial College London,

MCP Marie-Capucine Pope, Univ. Durham,

MN Mark Neil, Imperial College London,

MP Mark Pollard, Univ. Oxford,

OWJB Oliver W. J. Burnham, Univ. Durham,

SB Stan Botchway, STFC Central Laser Facility.

Chapter 1

Microemulsion Formulation and Optimisation

1.1 The origin of ULIFT

Thermodynamically stable mixtures of oil, water and surfactant, known as microemulsions, are of great practical importance for their solubilisation capacity [7], in enhanced oil recovery [8], and as media for enzymatic catalysis [9, 10]. Microemulsions exhibit ultralow interfacial tensions (ULIFT) between co-existing aqueous, oleic and 'middle' phases (the latter having a bicontinuous structure composed of interconnected aqueous and oleic phases). ULIFT results in interesting effects including complete wetting or non-wetting of surfaces, stability of jets and threads, and extreme deformability under body or surface forces [11, 12].

1.1.1 The defining properties of an interface

In general, molecules at an interface will be subject to an imbalance in intermolecular forces. If the bulk densities are to be adopted on either side, the surface molecules would be subject to a net force, pointing normally into the respective bulk. Each set of surface molecules are necessarily more tightly packed and have a higher potential energy (Figure 1.1). One may imagine a dividing surface of tension, along which an

interfacial tension, a cohesive *force per unit length*, acts.
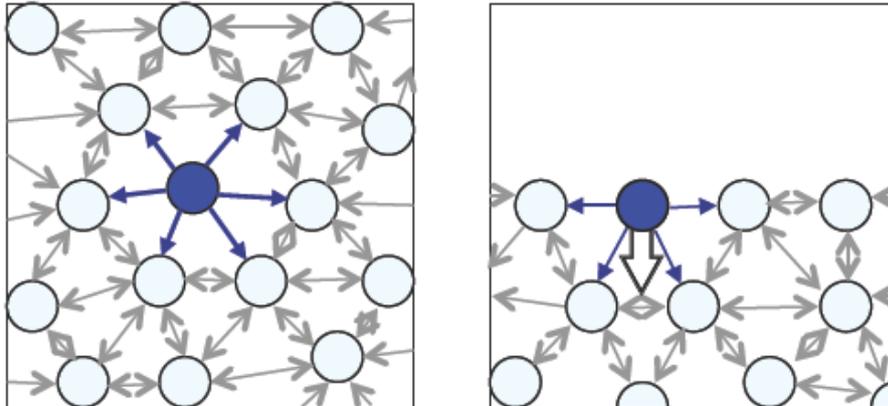
Figure 1.1: The net forces on uniformly-distributed molecules are zero in bulk fluid (*left*), but non-zero at the surface (*right*, against vacuum) causing them to compress and have higher potential energy.

Equivalently, interfacial tension (IFT, or σ) can be defined as the minimum differential work required to create new surface area, A. As such, it can also be expressed as a differential *energy per unit area*:

$$\sigma \equiv \frac{\partial G}{\partial A}_{N,p,T} \tag{1.1.1a}$$

at constant molar number N, pressure p and temperature T. The change in Gibbs free energy, G, describes the spontaneity of a process at constant pressure and temperature. This is therefore the *equilibrium* interfacial tension, which for a stable interface is always positive and finite.

The surface energy of solids is related, but not equivalent to the IFT, since some solid surfaces may relax from a cleaved state whereas fluids cannot. Nevertheless, fluid surfaces which include adsorbed components behave differently, as they have an IFT which is necessarily reduced from the bare value. These fluids will immediately exhibit temporarily higher *dynamic* IFT (closer to the bare value) when the surface is created. This effect is only perceptible when the surface is expanded much faster than adsorption kinetics allow the components to react; however, most *surfactants* adsorb on a millisecond timescale or faster, except at trace concentrations

[13]. Where IFT varies across a surface (e.g. differential evaporation of a mixture), spontaneous flow will occur from regions of low- to high-IFT. This phenomenon is called the *Marangoni* effect [14].

Any fluid interface, whether dynamic or in equilibrium, has a characteristic length l e.g. channel diameter, density contrast $\Delta\rho$ and viscosity η, flowing at an average speed v whilst subject to gravitational acceleration g. Description of the expected kind of fluid mechanics is greatly simplified by the use of dimensionless numbers [15]. These are ratios (thus indicating the relative importance) of the forces on fluids arising from different effects. The Bond number Bo compares buoyancy and interfacial forces, whereas the capillary number Ca compares viscous and interfacial forces. A third, the Reynolds number Re, compares inertial and viscous forces; it does not directly relate to IFT, but is an important metric for distinguishing laminar and turbulent flow regimes. All work in this thesis concerns systems near equilibrium IFT in strictly laminar flow ($Re \ll 10^3$).

$$Bo = \frac{\Delta\rho g l^2}{\sigma} \quad Ca = \frac{\eta v}{\sigma} \quad Re = \frac{\Delta\rho v l}{\eta} \tag{1.1.1b}$$

For a given volume of substance with no geometric constraints, the minimisation of surface area yields a spherical interface; hence fluid bubbles and droplets adopt this form. A general law in this regard is the Young-Laplace theorem [15], which shows how the local (Laplace) pressure difference across an interface, p_L, increases with the local mean curvature, H:

$$p_L = \sigma\nabla \cdot \hat{\mathbf{A}} = 2\sigma H \tag{1.1.1c}$$

$$H = \frac{c_1 + c_2}{2} \tag{1.1.1d}$$

where $\hat{\mathbf{A}}$ is the interfacial normal vector and H is defined as the mean of the local principal (extremum) curvatures c_1, c_2.

As a result of the IFT acting across the surface, a smaller droplet (which is more strongly curved) has a greater internal pressure than a larger one. Even in isolation,

it is less thermodynamically stable. This pressure difference manifests itself widely: in the nucleation of a new phase at a critical point, for example. The Laplace pressure provides an instrument by which the IFT contributes to the stability, or otherwise, of a particular droplet shape and size.

The reason ULIFT ($\sigma < 10^{-4}$ Nm^{-1}) is not typically encountered is that it requires particular conditions, in which the net interactions of the two bulk phases with the interface are almost identical. This is very different to the common situation where some, but not all, of the interactions are insignificant; for example, at the free surface of a liquid.

The surface tension of simple molecular interfaces scales as $\sigma \approx U/a$ where a is a molecular surface area and U is the depth of the interaction potential [16]. For larger molecules, U increases. so IFT remains the same order, $\sigma \sim k_B T/\text{nm}^2 \sim 10^{-2}$ Nm^{-1}. When near a critical thermodynamic point at which binary phases converge in density and become miscible, the interactions become similar on either side of the interface and so the effective IFT disappears. However, all other distinguishing factors also necessarily recede, including the refractive index contrast required for optical trapping.

1.1.2 Surface-active agents

The largest category of colloids are lyophobic (solvent-hating) and are formed with insoluble components. Very specific formulations in this class, such as demixed polymer and nanosilica fluids, display the lowest stable ULIFT known, (of order $\sigma_{LL'} \sim 0.01$ μN m^{-1}) since the length scale is much larger for a similar thermal energy well. This effect has been used to probe fluid mechanics at ULIFT [17]. Yet the fact that these are not true solutions limits the generality of their application. Again, the refractive index contrast is extremely low.

By contrast, lyophilic colloids are true solutions of amphiphilic substances. Emulsions (immiscible mixtures of molecular liquids) are a manifestation of the hydropho-

bic effect. This process is partly enthalpic; polar-polar interactions are stronger than similar polar-nonpolar interactions, which are consequently minimised by exclusion to form an interface. However, the exclusion is mostly driven by an entropy difference; polar molecules become strongly-oriented around non-polar solutes in an unfavourably small number of configurations. Many amphiphilic substances which have both polar and non-polar moieties (such as alcohols) are surface-active, i.e. show a tendency to adsorb to interfaces; in doing so they reduce the IFT (thus the process is spontaneous). The most important subset of these molecules are 'surface-active agents' or surfactants.

A distinctive feature of surfactants is that they are able to form oriented aggregates or monolayers, both at interfaces and in bulk solution. In most cases an emulsion interface lies between aqueous and hydrocarbon phases, so the surfactants must have a hydrophobic 'tail' (hydrocarbon chain, though occasionally aromatic, fluorocarbon or siloxane) and a hydrophilic 'head' (polar or charged structure). The simplest and most common categorisation is by head group type.

In stabilising large surfaces, surfactants merit an array of purposes. Anionic and nonionic surfactants are principally used in emulsion as soaps/detergents, foaming or wetting agents. Cationics are most often used in surface modification of solids giving rise to anticorrosion or lubrication properties [18]. Surface activity is often compared using various definitions of 'efficiency' or 'effectiveness' parameters, which denote the extent of surface tension reduction as a function of concentration. Underlying this is the general thermodynamic concept of a *surface excess* concentration, Γ, as illustrated by the Gibbs adsorption isotherm [19],

$$\Gamma = \frac{-1}{n_S RT}\left(\frac{\partial \sigma}{\partial \ln(\gamma)}\right)_{\gamma \leq cmc} \tag{1.1.1e}$$

where n_S is the dissociation number of the surfactant. The surface excess is so named as it represents the concentration of a substance at the surface surplus to that in the bulk, γ; since a real surface is gradual on the molecular scale, the dividing Gibbs surface is chosen so that the excess of the solvent is zero.

Type	Examples
Nonionic	pentaethylene glycol dodecyl ether, $C_{12}E_5$ *Triton X-100*
Anionic	sodium dodecyl sulphate, SDS sodium bis(2-ethylhexyl) sulfosuccinate, AOT
Cationic	n-cetyltrimethylammonium bromide, CTAB n-didodecyldimethylammonium bromide, DDAB
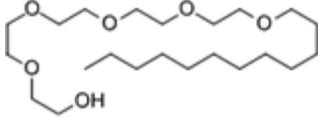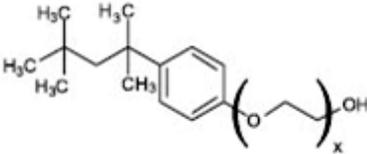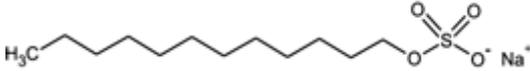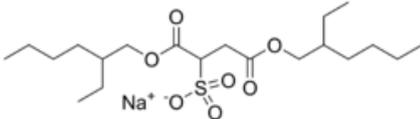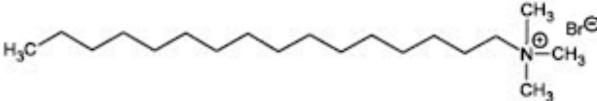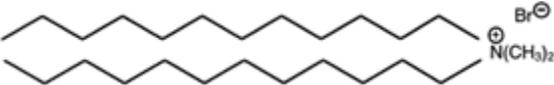
Table 1.1: Commercial surfactants depicting the three major head group types. Illustrated with *ChemDraw*®. In the work covered by this thesis, the nonionics, $C_{12}E_4$ and $C_{12}E_5$, and the anionics AOT and SDS are studied.

The exceptional ability of surfactants to self-aggregate is only observed above a critical micellar concentration or *cmc* characteristic of the surfactant-solvent pair. Typically, the *cmc* is below 0.01 M. As the *cmc* is approached, the surface excess reaches a characteristic packing fraction. Most subsequently introduced surfactant

tails then become cooperatively excluded (into groups of 50-200 molecules) via the hydrophobic effect. This produces oily nanodomains or micelles in aqueous solution and *vice versa* for solutions in oil [20]. However, above the *cmc*, the surfactant's chemical potential no longer changes and § 1.1.2 is no longer applicable. Past this point the IFT does not decrease appreciably with higher surfactant concentration. This is typically $\sigma \sim 10^{-3}$ N m^{-1}, which suffices for familiar applications but does not constitute ULIFT.

The Krafft point for ionic surfactants, T_K, is the temperature at which the *cmc* is equal to the molecular solubility of the surfactant in a particular solvent (almost always referring to aqueous solution). Below this temperature, no equilibrated aggregates can form as they become less stable than the bulk surfactant phase. Additional surfactant precipitates such that only monomeric surfactant remains in solution (Figure 1.2).
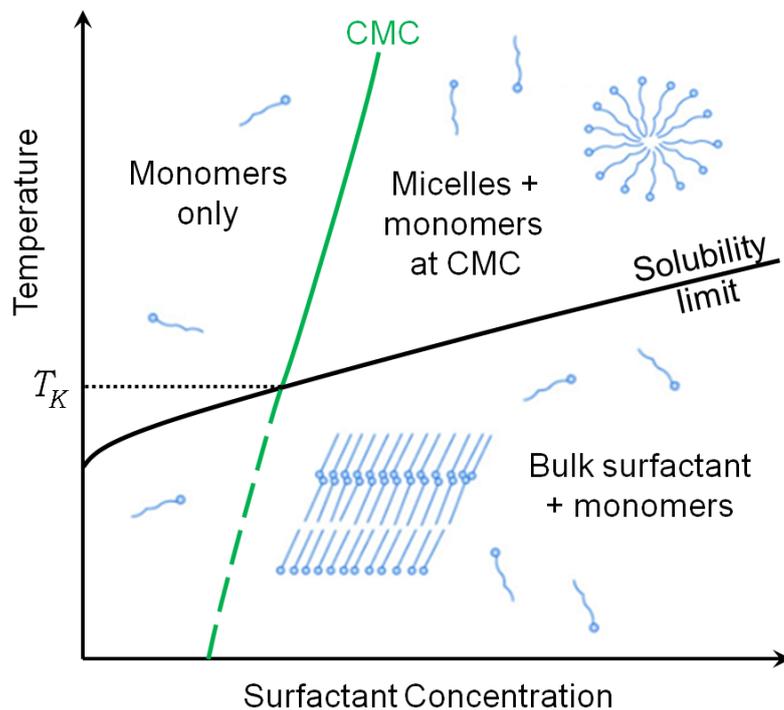
Figure 1.2: Schematic of solubility and *cmc* dependence on temperature for a typical ionic surfactant in a single solvent. The Krafft point occurs at their intersection.

The Krafft point is therefore a lower limit to the range of their general use. For a given molecular weight, T_K is depressed for larger head groups and branched surfactants, since the steric repulsion frustrates any crystalline order. It follows that T_K can also be reduced by decreasing the *cmc*, e.g. by increasing ionic strength of the solution.

For many non-ionic surfactants, there is a cloud point temperature, T_C, above which the aqueous solution phase separates. This yields surfactant-rich and surfactant-poor regions; both dehydration of the surfactant and greater colloidal interactions between the micelles cause them to flocculate above T_C [21].

Of the immiscible media in an emulsion, the more hydrophilic is usually water-based. Thus formulators speak of oil-in-water (o/w) or water-in-oil (w/o) emulsions when specifying the internal and external phases of a droplet emulsion. Bancroft's rule states that the preferred continuous phase is that in which the amphiphiles (in all forms) are most soluble. Although commonly verified, it has been superseded by Binks et al., who state that the preferred continuous phase is the *microemulsion* phase (see § 1.2), i.e. the phase in which stable aggregates are most soluble. Bancroft's rule implies correctly that for a given surfactant, the predominant emulsion type is strongly dependent on the surfactant structure. There are several semi-quantitative descriptions based on this correlation of performance and structure.

The hydrophilic-lipophilic balance (HLB) is an empirical scale of increasing net hydrophilicity (Figure 1.3), for which the references are oleic acid (HLB ≡ 1) and potassium oleate (HLB ≡ 20). Griffin's method [22] relates the fraction of 'hydrophilic' chemical groups in a surfactant to the applications for which it is expected to be suitable.

The preferred aggregate type is observed with *decreasing* HLB to follow the sequence: spherical, cylindrical, bilayer, laminar to inverse structures. Mitchell [23] provides a physical explanation for this sequence by correlating it with the critical

packing parameter, CPP $= V_\gamma/a_\gamma l_\gamma$ with a_γ being the head area, l_γ the hydropho-
bic tail length and V_γ the tail volume. This comparison of head and tail area is
quantitatively correct for a micellar or microemulsion aggregate. However, the in-
terfacial curvature of an emulsion droplet is typically orders of magnitude smaller
than any inverse molecular dimension. That the preferred emulsion type still follows
the preferred microemulsion type suggests that some equipartition of curvature en-
ergy occurs between thermally-equilibrated droplets and aggregates, even when the
droplet size is itself not yet equilibrated under surface tension.
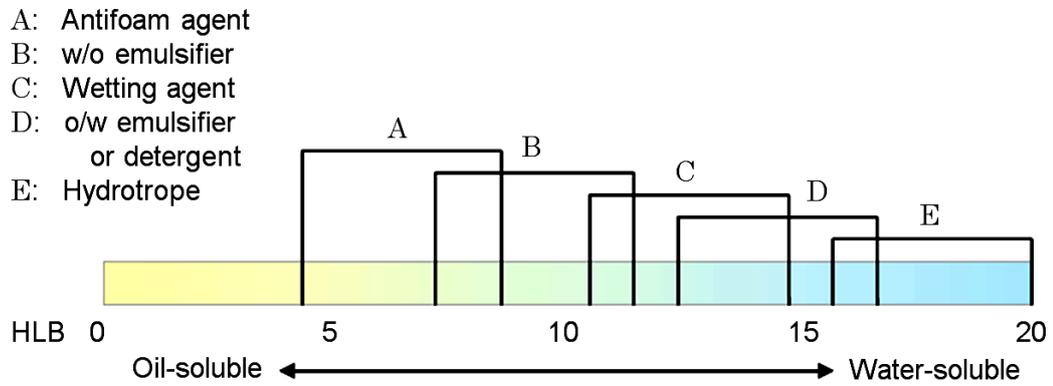
Figure 1.3: The HLB spectrum of surfactant hydrophilicity, including ranges iden-
tified with particular uses [22]. Surfactants used without additives for ULIFT are
typically found in the central region HLB $= 10 - 12$.

Alternatively, Winsor's R-ratio directly addresses the balance of interaction en-
thalpies A (between heads H, tails T, water W and oil O). Where the R-ratio
is greater than unity, the monolayer is hydrophilic and *vice versa*. Although this
is an exact physical interpretation, the individual constants cannot be quantified
easily; some approximations use Hildebrand solubility parameters or enthalpies of
vaporisation.

$$R\text{-ratio} = \frac{A_{HW} - A_{WW} - A_{HH}}{A_{TO} - A_{OO} - A_{TT}} \approx \frac{A_{HW}}{A_{TO}} \qquad (1.1.1\text{f})$$

The Winsor theory [24] confirms that the balance is essentially a result of match-
ing the oil-tail and water-head interactions. Notwithstanding restrictions in tem-

perature, T_K, T_C, most low-molecular weight oils can be emulsified with a given aqueous surfactant solution above the *cmc*. However, unless the terminal IFT is very low, the Laplace pressure will prohibitively destabilise smaller droplets, so that emulsions will coarsen and separate over time, either through coalescence or Ostwald ripening. Although this can be slowed, it cannot be stopped, *i.e.* emulsions can only be kinetically stabilised. However, highly dividing the bulk also gives rise to an entropic gain from the new configurations of the numerous, small, resultant structures. If the IFT is depressed below a threshold value, emulsification becomes favourable; these compositions are called microemulsions.

1.2   Microemulsions

Given that optical deformation is proposed for oil droplets in water, it may not seem obvious why understanding microemulsions is important. Yet the fact that microemulsions exist at all is a result of ULIFT. For any lyophilic colloid, an ability to produce ULIFT is therefore intimately related to the type and behaviour of the microemulsion formed at moderate surfactant concentrations.

The term 'microemulsion' is actually a historical misnomer, since the feature size is typically much smaller than a micron (for droplets, much less than 50 nm diameter). Insight into why microemulsions form is gained by considering the required Gibbs free energy. The system in question is a surfactant film between the immiscible phases, in equilibrium with a reservoir of surfactant in solution. The larger the total film area, the more divisions or conformations it can adopt and so the configurational entropy of the system increases. This favourable entropy change is counterbalanced by the finite surface tension of the film. For isothermal division of the bulk at constant IFT,

$$\Delta G = \sigma \Delta A - T \Delta S. \tag{1.2.1g}$$

When the surface tension is sufficiently low such that $\Delta G \leq 0$, enlarging the area of the film by $\Delta A = T \Delta S / \sigma$ (into a highly divided emulsion at fixed internal volume)

becomes a spontaneous process. Although metastable emulsions (nanoemulsions) with similar properties can be produced with similar materials, microemulsions are fundamentally different; they are thermodynamically (rather than kinetically) stable. As such, they have an indefinite shelf life and will never phase-separate under the conditions which formed them.

Historically, definitions of what constitutes a microemulsion invoke an arbitrary length cutoff based on the scattering of light, or feature size, for the convenience of practical identification [25]. It is important to define microemulsions solely by their thermodynamically stable, mutual solubilisation of otherwise immiscible solvents. This state is a direct result of the ULIFT provided by the amphiphilic monolayer.

Winsor described that if a particular mixture allows a microemulsion to form, there are four types of phase equilibria which can occur, denoted WI-WIV. A microemulsion phase cannot in general be diluted; the external and internal phases are intimately balanced and have both preferred (average) structure and volumetric ratio. Thus excesses of oil or water may appear. According to the relative phase densities, they form layers.
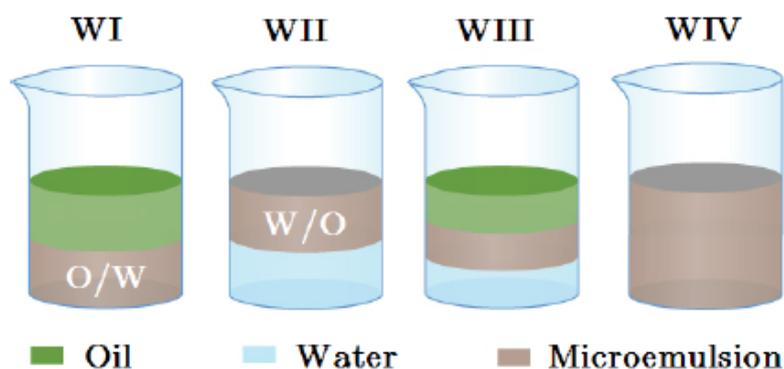
Figure 1.4: The phase variations of systems giving rise to a microemulsion: WIII (bicontinuous phase) lies intermediate between the extremes WI (oil in water) and WII (water in oil); WIV encompasses any of these which fills the entire volume.

The WI (lower) and WII (upper) phase microemulsions are analogues of conventional o/w or w/o emulsions respectively, with nanoscopic particle size (swollen micelles). The WIII middle phase microemulsion represents an intermediate situation where the layers have very little mean curvature; surfactant interactions between oil and water are similar. The WIV, found at high surfactant concentration is distinguished only by its lack of excess phases. In practice, it may be variously w/o, o/w or a neutral structure depending on the proximity to the other three regions. In accordance with Bancroft's rule, the surfactant migrates to the continuous phase (which holds the microemulsion) either side of the phase inversion point from WI–WIII–WII.

The stability of the various microemulsions can be identified using the Gibbs phase rule: $F = C - P + 2$ [26]. It shows the number of degrees of freedom F remaining when a number of phases P coexist, for a given number of components C. For a ternary ($C = 3$) phase diagram at constant temperature and pressure, there are two independent degrees of freedom: the oil and water chemical potentials (which constrain that of the surfactant). Thus a single phase (WIV) occupies at most a bidimensional region, the two phase equilibrium (WI or WII) a binodal curve and the three phase equilibrium (WIII) an isolated point.

The miscibility gap spanned by three phases implies the equivalence of three chemical potentials near three free energy minima and thus a triangular WIII region on the ternary (Figure 1.5). The tie lines in the WIII area point toward the vertices of the triangle, whilst the phase inversion zone in which ULIFT is observed lies approximately along its vertical bisection. Microemulsions are formed above the critical microemulsion concentrations ($c\mu c$s) in each solvent [27] (related to, but not to be confused with the cmcs) which form the lower oil- and water-rich corners of the WIII triangle. The specific formulation where the microemulsion phase becomes the entire mixture is the X- or 'fish-tail' point (Figure 1.6). The amount of surfactant required at this point represents its efficiency in creating enough area to solubilise the two bulk substances; as a result it can be used as a positively-correlated marker

for ULIFT.

However, this ideal phase diagram only holds under a unique set of conditions (temperature and pressure) which allow phase inversion. Either side of the balance, the diagram becomes skewed towards either WI or WII and the WIII region disappears. This is why WIII (and the corresponding ULIFT) are more difficult to formulate than other microemulsions.
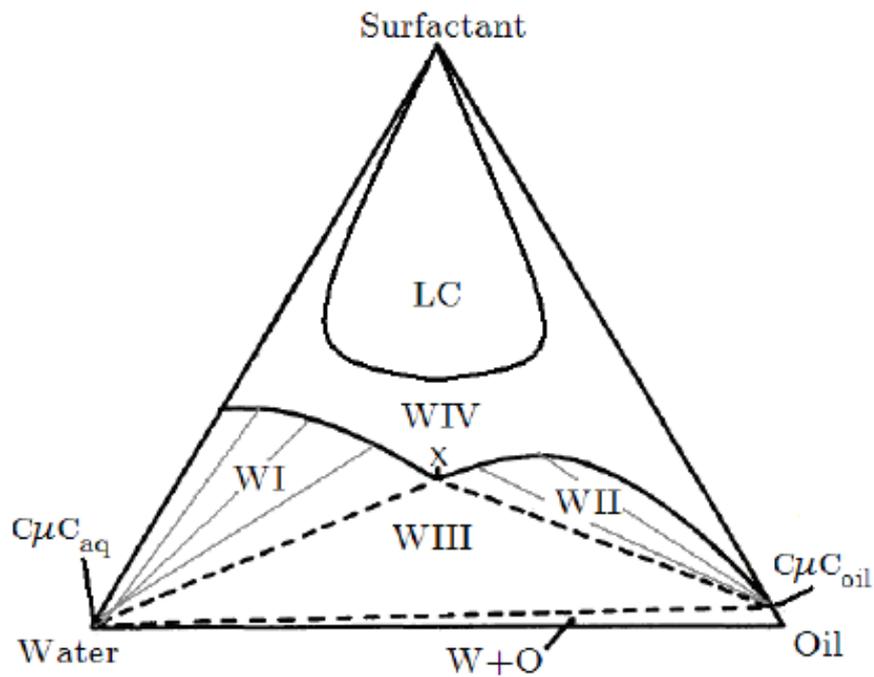
Figure 1.5: A simple ternary phase diagram of oil, water and surfactant near the phase inversion point where the microemulsion is bicontinuous. It shows the liquid crystal region (LC) and the 'X' point, representing the smallest amount of surfactant required for WIV miscibility of oil and water.

Where WIII middle phases do exist, proton NMR self-diffusion measurements, cryo-electron microscopy, small-angle neutron or X-ray scattering (SANS/SAXS) [28], conductivity and electrochemical [29] measurements all confirm a random, monodisperse, self-similar and bicontinuous structure. As the WIII region is approached, oil or water droplets overlap and unbend into an interconnected geometry

in which the locally immiscible environments of oil and water are interchangeable and equivalent. Since confined w/o drops collapse to form water-connected chains, this is related to the phenomenon of *percolation* in which electrical conductivity sharply increases [30].

The WIV is unique from a interfacial tension perspective. Since there are no excess phases, the internal volume is fixed. The only means of creating more surface area (from reducing the surface tension) is by subdividing the existing volume. This makes the feature size smaller and so less light is scattered. However, when an excess phase is present, it can instead be depleted to swell the existing microemulsion structures, yielding a *larger* feature size as IFT is reduced. This explains the common misconception that all microemulsions must become more transparent as they become more efficient; this only applies to single-phase formulations. However, it also poses the question as to why, given the freedom to do so, a larger feature size (i.e. a lower preferred curvature), would be associated with a lower tension.

1.3   Interfacial curvature in the middle phase

Curvature is a necessary aspect of microemulsion behaviour. The simple entropic argument given above fails to impose any significant preference for the geometry of the new interfacial area. Models such as the critical packing parameter allude to the role of changes in membrane interactions in favouring certain shapes over others, as evidenced by the variety of known microemulsion structures. In effect, this bias redefines the IFT as a curvature-dependent quantity, distinct from that of a planar surface [23]. The uniform curvature of the spherical systems (WI/WII) is both intuitive and accessible both experimentally and theoretically. A range of methods are commonly used to measure droplet radii and estimate ULIFT. In the last three decades, however, predictive methods for WIII phase transitions [31] have been developed from models of curvature energy. The curvature elastic energy per

unit area is commonly expressed using the Helfrich equation [32]:

$$\left(\frac{\partial G}{\partial A}\right)_{NPT} = \sigma_{pl} + 2\kappa(H - H_0)^2 + \bar{\kappa}K + \mathcal{O}(c^4) \qquad (1.3.1\text{h})$$

$$H = \frac{c_1 + c_2}{2} \quad K = c_1 c_2 \qquad (1.3.1\text{i})$$

This represents a quadratic expansion of the surface free energy per unit area in terms of the local principal curvatures c_1, c_2. The parameters which dictate the energy penalty for local increases in either curvature are the bending moduli: for mean curvature (H) this is splay constant or bending modulus (κ); for Gaussian curvature (K) this is the saddle-splay constant ($\bar{\kappa}$). Their values are typically reported in units of thermal energy $k_B T$.

The spontaneous curvature (H_0) is the preferred curvature of the surfactant monolayer. Chiefly, it is necessary to explain stability of non-minimal ($\langle H \rangle \neq 0$) surfaces such as spherical aggregates; for this reason it is important in understanding the phase inversion behaviour. The surface tension σ_{pl} in this expression is that of the planar reference state at absolute-zero, for which $H = K = 0$. However, when the thermodynamically preferred surface has non-uniform curvature from point to point, the *surface of tension* no longer corresponds to the interface itself. Even though the surface is packed, the Laplace pressure is homogeneous, and there is no Marangoni flow, the concept of a tension which acts mechanically loses its definition [33]. For the WIII microemulsion, theory relies instead on the definition of a free energy per unit area, which includes any bending energy effects in the reproduction of the surface.

Local minima of measured oil-water IFT occur in parameter space where the surface excess entropy of the aggregates is equal to that of a planar monolayer [34]. As such, the preferred mean curvature of the oil-water interface, H_0, becomes zero at these points.

For fixed amphiphile concentrations and a fixed ratio of solvents, the phase behaviour is also determined by H_0. When H_0 changes sign under influences such as

temperature or ionic strength, emulsions tend to undergo phase inversion [35]. Thus $1/H_0$ is a useful length scale for predicting *which* kind of microemulsions are possible. As ULIFT is strongly correlated with phase inversion, this poses the question: can the Helfrich free energy provide a theoretical basis for the measured ULIFT?

The system Helfrich considered is thermodynamically open such that the area is extrinsic (i.e. constant area per adsorbed surfactant molecule). It is valid for packed surfactant layers for which the curvatures are much smaller than the inverse layer thickness. Minimising this expression gives the preferred average curvatures. Certain stability constraints on any membrane are straightforward to derive, such as $2\kappa + \bar{\kappa} > 0$, below which aggregates become unstable with respect to a planar surface and thus emulsification fails. The bending moduli are not easily interpreted from experiment, so it is easier to first assume an idealised geometry.

In the de Gennes and Talmon-Prager (GTP-type) models, an infinite lattice of oil or water domains, of width d, is permuted subject to thermal Helfrich fluctuations [36, 37]. Correlations between the fluctuations occur on a scale denoted the persistence length, ξ:

$$\xi = l_\gamma \exp\left(\frac{4\pi\kappa}{3k_BT}\right) \tag{1.3.1j}$$

where l_γ is the layer thickness. According to this model the minimum IFT is:

$$\sigma_{OW} \approx 0.44\frac{k_BT}{\xi^2} \tag{1.3.1k}$$

The prefactor stems from the modelled cubic symmetry, i.e. lattice coordination number $n_L = 6$. In the model, ξ can be estimated geometrically:

$$\xi \approx \frac{n_L\phi_O\phi_W l_\gamma}{\phi_\gamma} \tag{1.3.1l}$$

Fixing all other parameters, the minimum tension is predicted to occur when the solubilised oil and water volume fractions (ϕ_O, ϕ_W, respectively) are equal. This prediction is loosely related to Winsor's argument that the net molecular interactions per area between the oil/water and the surfactant must be equal at the optimal point, thus $H_0 = 0$. Unlike spherical or cylindrical aggregates, a bicontinuous sur-

face is minimal and so to exist at equilibrium, $H_0 \approx 0$ is a necessary condition.

The GTP-type, Gitzberg-Landau functional and Gaussian random-field models [38] describe how the bending moduli, and thus the surface free energy are renormalised by thermal fluctuations at ultralow surface tension. Since thermal modes of longer wavelength have greater amplitude, a major outcome is that the moduli become scale-dependent [39].

$$\kappa(x) = \kappa - \frac{3k_B T}{4\pi} \ln(x/l_\gamma) \tag{1.3.1m}$$

$$\bar{\kappa}(x) = \bar{\kappa} + \frac{5k_B T}{6\pi} \ln(x/l_\gamma) \tag{1.3.1n}$$

In other words, the constants κ, $\bar{\kappa}$ in the Helfrich expression only represent bending at the molecular scale, l_γ. This is in keeping with the definition of ξ, in that folding a film of this size incurs no energy penalty. The scaling shows that a larger membrane is both more flexible (material is easier to bend with larger aspect ratio) and less topologically complex [40].

The relevant scale for the microemulsion curvature behaviour is the domain size $x = d$. The Exxon model balances the curvature free energy per unit volume, based on $\kappa(d)$, against an entropic free energy per unit volume of a simple binary mixture. This successfully reproduces the complex phase behaviours in the fish diagram as a result of changing H_0 and ϕ_γ. Highly negative $\bar{\kappa}(d)$, such that $2\kappa + \bar{\kappa} < 0$, destabilises spherical aggregates in favour of a bicontinuous microemulsion [41].

The Exxon model is consistent with the GTP-type models in the case where $\phi_O = \phi_W \gg \phi_\gamma$:

$$\sigma \approx 0.41 \frac{k_B T}{\xi} + 2\kappa H_0^2 + \mathcal{O}(\bar{\kappa}) \tag{1.3.1o}$$

The neglect of *configurational* entropy is surprising, as the true number of permutations must be counted at a molecular scale of mixing [42]. However, Strey and other authors have indicated [43] that all reversible phase inversions around critical points follow a principle of corresponding states. In this theory, microemulsions belong to a specific universality class of the Ising model, which associates the in-

teractions at various surfactant orientations with the geometry of the surface. This simplification allowed them to characterise $\sigma(T)$ over a range of 19 nonionic WIII formulations with only $\kappa(d)$ and $\bar{\kappa}(d)$ as fitting parameters, together with measurements of the WIII temperature range. The authors experimentally identified a self-similar ratio of $d/\xi \approx 2$ for their C_IE_J surfactant systems (C and E denoting methylene and ethyleneglycol moieties respectively), and additionally that:

$$\langle \sigma \xi^2 \rangle = 0.44 \pm 0.10 \ k_B T \approx \langle -\bar{\kappa}(d) \rangle \tag{1.3.1p}$$

For sufficiently short-tailed surfactants compared to the oil, the minimum IFT becomes higher so that the microemulsion actually wets the interface [44]. Decreasing the surface tension in practice would imply increasing κ, which is related to the conformational entropy afforded by a long, flexible tail [45]. Indeed, κ increases with at least the square of the tail length l_γ. Theoretical work [31] also points to the strategy $\bar{\kappa} \to -0$ where asymmetrically curved configurations $|c_1| \neq |c_2|$ become accessible. In agreement with the Helfrich model, it is observed that the lowest IFT minima have the narrowest WIII regions, the strongest dependence on spontaneous curvature and the highest κ [46].

However, formation of a disordered, highly divided system precludes $d/\xi \geq 2$ and thus limits κ and l_γ. Highly-ordered lamellar phases are observed with long chain systems such as lipids which have more extreme bending moduli ($\kappa \gg 0$, $\bar{\kappa} \ll 0$) [47]. This suggests using very large heads and tails is preferable for ULIFT, but again, the solid or liquid crystal forms become favoured.

A moderate value of $\kappa \approx k_B T$, as observed for most ternary-component WIIIs [48], is necessary in practice to prevent excessive surfactant self-association which induces the formation of lamellar LCs or precipitation. Since liquid crystals are found at high surfactant concentrations, it appears the changes in preferred geometry are dependent on monolayer interactions in addition to composition. Any strategy for formulating lower IFT must account for the fine line between long-scale disorder and self-associated order.

1.4   Theory of formulation

In general, making a desired microemulsion may present far too many degrees of freedom to consider a systematic search of the large formulation space. In the simplest case of microemulsifying a chosen oil in water at room temperature, there are 4: surfactant concentration and water-oil ratio from Gibbs' phase rule (§ 1.2) at $C, P = 3$, plus choices of surfactant head and tail sizes. To progress, it is crucial that a subset space is considered which reflects roughly equivalent effects of the important parameters on ULIFT. This is a central tenet of the methodology known as *statistical design of experiments*.

The foremost of these variable sets is the type of surfactant, for which the HLB is relevant. The model is crude, in that it reduces the head and tail properties to a single number assigned to each surfactant. It is a yardstick for matching surfactant chemical structure to commonly desired properties such as detergency.

The hydrophilic-lipophilic difference (HLD) model has been developed primarily by formulating scientists [49], in order to produce specific Winsor microemulsions quickly. It introduces the other environmental and composition variables ignored by HLB, prominently, the nature of the emulsified oil. Like HLB, it is almost entirely empirical and does not give a direct account of the spontaneous curvature H_0. However, it is roughly proportional to H_0 and succeeds in quantifying the effects of the actual formulation and conditions on the thermodynamic balance. Much like a simplified Winsor theory, it is defined here as the free energy difference associated with moving surfactant aggregates from bulk water to bulk oil:

$$\text{HLD} \equiv \frac{\mu_O^o - \mu_W^o}{RT} \propto H_0 \tag{1.4.1q}$$

For ionic surfactants:

$$\text{HLD} = c_{\text{EACN}}\text{EACN} + c_\gamma + c_T(T - T^\circ) - \ln\left(\frac{S}{S^\circ}\right) + f(\phi_A) \tag{1.4.1r}$$

For nonionic polyethoxylated surfactants:

$$\text{HLD} = c_{\text{EACN}}\text{EACN} + c_\gamma + c_T(T - T^\circ) - c_S S + f'(\phi_A) \tag{1.4.1s}$$

where the parameters are defined in Table 1.2. When the surfactant interactions are equal, HLD, $H_0 = 0$ and the IFT is minimised with respect to at least one variable. For these variables, the values resulting in $H_0 = 0$ are referred to as 'optimal', for example *optimal salinity*. An optimal temperature is commonly known as a *phase inversion temperature* (PIT).

If HLD, $H_0 > 0$, the surfactant has a hydrophilic preference, so any microemulsion is expected to lie on the WI side of the minimum IFT. Conversely, for HLD, $H_0 < 0$, the surfactant is hydrophobic and forms a WII equilibrium.

Variable	Term	Ionic HLD	PEO nonionic HLD
Effective alkane carbon N°	EACN	↑	↑
Characteristic surfactant curvature	c_γ	↓	↓
Ethylene oxide N°, J	c_γ	-	↑
Temperature	T	↑	↓
Aqueous salinity	S	↓	↓
Alcohol cosurfactant	ϕ_A	↓	↓

Table 1.2: A summary of influences on the spontaneous curvature as encountered in the empirical HLD model.

The major assumption made by HLD theory is of linearity in the formulation-ULIFT space; there are no coupling terms. In practice, a statistical design approach verifies that the variables are not confounded. The variables are only very weakly dependent on one another, since the free energy contributions are additive. This rule-of-thumb holds especially well for homologous series of surfactants such as $C_I E_J$, so that for each the coefficients are constant. Exceptions do exist, such as the non-ideal partitioning of cosurfactant.

In principle, the one-dimensional optimum condition $H_0 = 0$ can be obtained by tuning any one variable. What is more, corresponding and opposing changes of

two variables retains the condition $H_0 = 0$. This method allows monotonic, step-wise minimisation of IFT in formulation space. The model is not only employed for comparing optimal and nonoptimal formulations (different H_0) in the same microemulsion system, but also for comparing different systems at the same H_0 even if they have no common parameters.

One of the most surprising results of the work on HLD has been the association of complex hydrocarbons with an equivalent alkane carbon number (EACN) [50]. This value represents the lipophilicity of a given oil compared to the normal alkanes in the context of microemulsification. A linear mixing rule can be applied to predict the EACN of a mixture that does not partition into the aqueous phase [51]. All else constant, each surfactant has an EACN for which the water-oil IFT is minimum. At 1M salinity and ambient temperature with no other additives, this coincides with $-c_\gamma/c_{\mathrm{EACN}}$, yielding the surfactant characteristic 'curvature' c_γ [52]. Similarly dimensionless, this is the contribution most readily correlated with the traditional HLB. For $C_I E_J$ surfactants, this parameter decreases linearly with the headgroup length J. The IFT-salinity curves of aqueous AOT solutions with alkanes increase and broaden with carbon number from heptane [53].

Since the coefficients are quite small, $c_{\mathrm{EACN}} \approx 0.16$, a single surfactant is useful for microemulsifying oils in a modest range of EACN. With conventional surfactants where this minimum falls at a low EACN, very hydrophobic oils such as hexadecane do not readily produce ULIFT and are difficult to emulsify [54].

The temperature shift is measured relative to an ambient reference, $T^\circ \equiv 25$ °C. For ionic surfactants, entropy favours the release of counterions, increasing the charge density at higher temperature. However these ions are solvated by water and so the shift with increasing temperature is hydrophilic and small ($c_T \approx 0.01$ K^{-1}). For polyethoxylated nonionics, increase in temperature causes a fairly strong hydrophobic shift due to entropic dehydration of the head group ($c_T \approx 0.06$ K^{-1}, weakly coupled to J) [43].

The salinity provides precise and stable control of the behaviour of ionic surfactants towards a hydrophobic state. In general, the repulsive Coulombic forces between alike surfactant head groups will cause aggregates to be smaller. However, this is screened by added salt which decreases interaction with water [55]. For nonionics, there is also a screening of dipolar interactions, with a weaker linear effect, $c_S \approx 0.13$ L g^{-1}. However, the coefficient describing HLD dependence on salinity differs with counter-ion type, even at the same ionic strength [56, 57]. As a result, common salt (NaCl) is used almost exclusively. At very high surfactant concentration, the ionic surfactants interact, which causes the 'tail' of the fish diagram to tilt upwards. Monolayer charge density significantly increases the magnitude of both bending moduli; consequently, lower ULIFT minima are usually observed when the optimum corresponds to a *low salt concentration*.
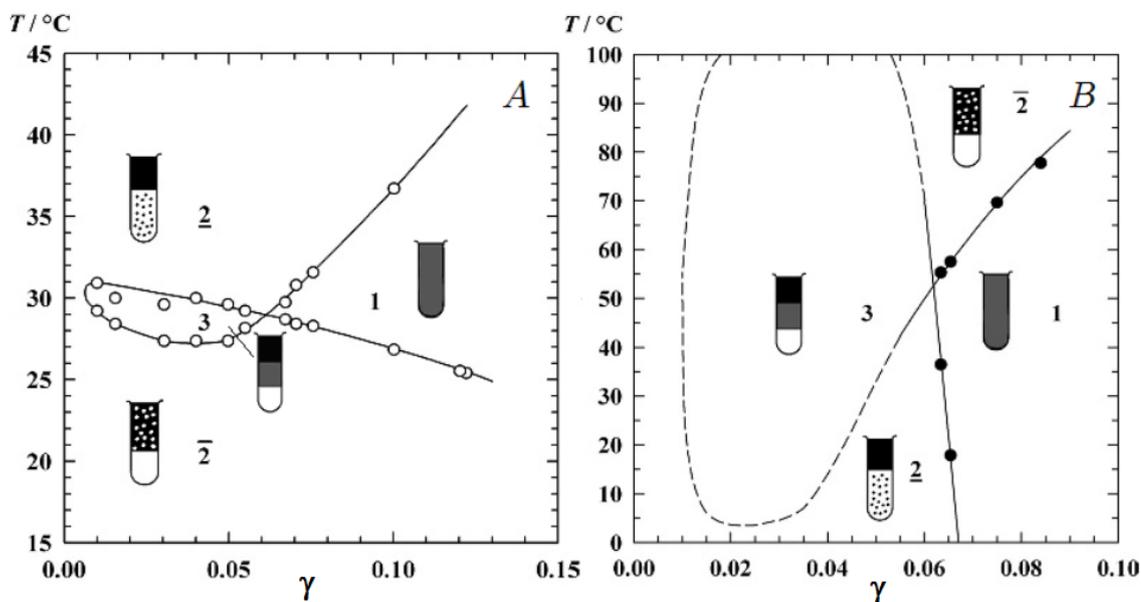
Figure 1.6: 'Fish' phase diagrams showing n-decane/brine/surfactant systems at [NaCl] = 100 mM and equal brine and oil volumes: (*a*) AOT surfactant only ($\chi = 1$); (*b*) less temperature-sensitive AOT + C$_{12}$E$_4$ mixed system; AOT constitutes $\chi = 0.60$ of total surfactant by weight. Figures reproduced from [10], ©Wiley.

Addition of medium-chain alkanols (C$_4$E$_0$-C$_{10}$E$_0$) as cosurfactants also causes a

decrease in H_0. The heavier/more linear the alcohol chain, the greater the molar efficiency of reduction [58]. The alcohol for which $f(\phi_A) = 0$ is usually sec-butanol; shorter, more hydrophilic alcohols largely dilute the surfactant at the interface. The alcohol additive becomes less effective when its length exceeds the surfactant tail [41]. The tendency of medium-chain alcohols to inhibit lyotropic order between surfactant chains, is well-documented [59]. This also reduces the Krafft temperature. In curvature terms, this disordering effect is due to a decrease in the ratio $-\bar{\kappa}/\kappa$ such that saddle bending is favoured. It is experimentally observed that IFT is minimised when cosurfactant length is the difference of the oil and surfactant tail lengths. These longer chain alcohols are interpreted as being lipophilic 'linkers' rather than simple cosurfactants [60]. Whilst being amphiphilic, they fail to adsorb strongly enough to displace surfactant in the monolayer. They increase order in the vicinity of the packed interface and increase its effective l_γ, such that solubilisation improves at the optimum point. This accounts for the common observation that dodecanol impurities increase the apparent surface activity of SDS.

The addition of small amounts of amphiphilic diblock copolymers to nonionic microemulsions improves the solubilisation without strong viscosity increase [61]. These copolymers are ultra-long chain analogues of the $C_I E_J$ surfactants, thus increasing effective l_γ without inducing crystallisation through self-interaction. Conversely, addition of surface-inactive homopolymers is reported to decrease both the efficiency of the surfactant and κ with increasing molecular weight and concentration [62], whilst greatly increasing the viscosity of the phases to which they partition.

1.4.1 Surfactant concentration

The surfactant concentration does not formally change the IFT (although the ionic strength may vary weakly for ionic surfactants). Its primary effect is to extend the WIII microemulsion phase to a larger volume at fixed composition. If $H_0 = 0$ is maintained as the concentration increases, the X-point is reached ($\gamma = \gamma_X$) and a bicontinuous WIV is created so that no macroscopic oil-water interface remains. This unique volume fraction can be identified with the ULIFTs not only of the excess

phases with the middle phase, $\sigma_{OM,WM}$, but also that between the excess phases σ_{OW}.

Huh proposed an empirical relation governing the IFT between an excess phase and microemulsion phase. It states that the IFT depends on the amount of excess phase that is solubilised into the microemulsion per amount of surfactant. As such, it can be expressed in terms of volume fractions in the microemulsion phase:

$$\sigma_{OM,WM} \propto \left(\frac{\phi_\gamma}{\phi_{O,W}}\right)^2 \tag{1.4.1t}$$

This volumetric ratio ϕ_O/ϕ_γ is known as the *solubilisation parameter*, in this case for the oil phase. Huh found the proportionality constant to be 300 μN m^{-1} [63]. This is consistent with the form given in the Exxon model:

$$\sigma_{OW} \propto \frac{\phi_\gamma^2}{\phi_O \phi_W} \tag{1.4.1u}$$

As the σ_{OM} or σ_{WM} is reduced for a given amount of surfactant, the microemulsion will swell to incorporate more oil and/or water respectively. Interactions between dissimilar excess phases are more repulsive than those with the microemulsion and so $\sigma_{OW} > \sigma_{OM,WM}$ in all cases. In order for the oil-water interface to exist, the WIII microemulsion of intermediate density must fail to wet it fully. Lensing of microemulsion droplets is indeed observed in the majority of cases, and Neumann's triangle proves that $\sigma_{OW} \leq \sigma_{OM} + \sigma_{WM}$. Hence, knowledge of the tensions of the excess phases with the microemulsion phase confines an estimate of the oil-water IFT. Furthermore, σ_{WM}, σ_{OM} are proportional to the counterpart works of adhesion A_{HW}, A_{TO}; thus, Winsor's R-theory indicates a balanced monolayer when the two microemulsion-excess phase IFTs are equal.

Commonly, nonionic microemulsions require 10-30% wt. surfactant to produce a single phase (WIV), but in accordance with the Huh relation $\sigma(\phi_\gamma)$, these do not produce good ULIFT. The value of γ_X reduces to less than 5% wt. for the most efficient surfactant systems.

The cutoff at low surfactant concentration is the $c\mu c$, where the middle phase is depleted and only a single interface appears to remain at conventionally low IFT. Other than the implied microemulsion formation, little is known about how this transition occurs or whether a microemulsion is stabilised at the surface by disjoining pressure, given its intermediate dielectric permittivity. Below this $c\mu c$ point (found to be roughly $5 \times cmc$ [64]), Winsor transitional phase inversion is not observed. Certainly, any metastable emulsion formed below the cmc will not transitionally invert even if H_0 is changed; only a catastrophic inversion [65] can take place.

Notably for all cosurfactant additives, the phase diagram can become skewed due to their unequal partitioning between oil and water. The development of linkers (and the explosion in associated formulation variables) means that they are increasingly being incorporated into the surfactant structure themselves. Namely, this is a new class of *extended* surfactants. Groups of intermediate hydrophilicity/ hydrophobicity such as propylene-oxide are placed along the centre of the chain allowing for a more gradual change in polarity across the interface [66]. Even longer oils such as triglycerides can be microemulsified [67]. This reduces the attainable ULIFT to the order of 0.1 μN m^{-1} - certainly suitable for optical deformation, but bending rigidity is high ($\kappa \approx 1.4\ k_B T$) so that the timescale for equilibration increases to several weeks [68, 69].

1.5 Phase-volume methods for optimisation

A handful of recipes for WIII equilibria and high-solubilisation WI and WII equilibria are reported in the literature, but present a number of issues. Fundamentally, very few have sufficiently low ULIFT minima accessible for optical deformation, around 1 μN m^{-1} or lower. Nonetheless, techniques exist to adapt those formulations for global ULIFT minima, with the following caveats. On the practical side, they often consist of an excessive number of components, each associated with additional degrees of freedom. Thus the formulation space becomes untenably large compared to the region in which desirable ULIFT occurs. Also, prediction of

ULIFT is complicated by components that partition significantly between both oil and water phases. This partitioning couples the ULIFT to the water-to-oil ratio $\Omega \equiv \phi_W/\phi_O$, which is weighted strongly towards the water phase in the intended experiment, $\Omega > 200$. The process of formulation is simplified significantly by using equal volume fractions of oil and water $\Omega = 1$, so partitioning should be avoided where possible.

It is prudent to use a near-minimal formulation space within which ULIFT is known to exist. The simplest possible system is a ternary composition of two pure molecular solvents microemulsified with one surfactant. However, this becomes too restrictive. With the exception of temperature, the remaining degrees of freedom at ambient pressure are the discrete choices of the chemicals. Use of temperature as a formulation variable is less practical than other continuous parameters such as concentration, which do not depend on external influences. Moreover, ULIFT is particularly narrow in its temperature range and widely varying in its central temperature, so far more difficult to find. A superior alternative is to attempt to fix the working temperature and to use the concentration of a single solute as the formulating parameter. In this work at least a quaternary system is used, where the principal formulating variable is the aqueous salinity, S.

Optimisation does not require measurement of H_0 or even IFT directly in a quantitative sense. Instead, observations of macroscopic phase behaviour at $\Omega = 1$ can be relied upon to find Winsor III microemulsions, $\gamma > c\mu c$, of high and equal solubilisation of oil and water, where they exist. The solubilised volumes are easily measured in thin cylindrical vials. The excess volumes only contain a relatively small amount of surfactant (compared to the microemulsion) and can be neglected when the middle phase fraction is larger than the ratio $c\mu c/\gamma_X \approx 0.1$.

1.5.1   Materials and methods

The materials Brij-L4 and $C_{12}E_{4/5}$ (dodecyl tetra/pentaethyleneglycol ethers, 98%, *Aldrich*), toluene,*n*-butanol, NaCl (all AR grade, *Fisher*) and deuterium oxide, D_2O (*Cambridge Isotope Labs.*) were all used as received. Ultra-pure H_2O was obtained from a *MilliPore* unit (*MilliQ*, 18.2 M Ω cm^{-1}). The oils *n*-heptane, *n*-decane and *n*-dodecane (>99%, *Fisher*) were purified through silica under N_2. To remove inhibitor, styrene, lauryl methacrylate and isobornyl acrylate monomers (*Aldrich*) were either washed with two parts 2M potassium hydroxide, then three parts water, or vacuum distilled and desiccated. No difference in formulation behaviour was found between the two variants, which were kept foiled at 5 °C. Piranha solution, a strong oxidising agent used to clean glass coverslips and slides, was mixed freshly from 1 part hydrogen peroxide (30% in H_2O, Fisher) and 2 parts sulphuric acid (98%, Fisher). Sodium dodecyl sulfate (SDS, *Aldrich*) was twice recrystallised from ethanol before use. Aerosol OT (sodium bis(2-ethylhexyl) sulfosuccinate) was analysed by NMR, Karl-Fischer titration and dynamic pendant-drop tensiometry at 100 mM NaCl to check for hydrolytic impurity; the *cmc* was in agreement with literature value of 0.5 mM at 20 °C [57]. The IFT of equilibrated water with air also enabled estimation of the AOT partition coefficient between the water and heptane in the presence of 100 mM NaCl, which at $1 : 1.8 \pm 0.2$ was consistent with the ratio of the respective *cμc*s. At 1 mM AOT concentration, the characteristic adsorption time from Ward-Tordai pendant tensiometry [70] was around 10 ms. The chosen supply of AOT (96%, *Acros Organics*) was invariant under Soxhlet extraction and each batch was used as received within 3 weeks to avoid hydrolysis. AOT is known to form vesicles on dissolution [71], particularly in conditions of moderate salinity > 100 mM and AOT > 10 mM; this was avoided where possible. The Krafft point of AOT is normally below 0 °C but increases sharply with sodium ion concentration.

	AOT	$C_{12}E_4$	$C_{12}E_5$
H_2O + NaCl	0.4, 0.5^a (0.5^b)	0.016	0.025, $< 0.046^b$ (0.060^b)
Heptane	(0.4^a)	(30^c)	(10^b)
Decane	(0.6^d)	(20^c)	-
$c\mu c(\Omega = 1)$		6	2
γ_X		53	64

Table 1.3: Critical micellar concentrations (cmc) determined here by partition pendant drop tensiometry are listed alongside critical microemulsion concentrations ($c\mu c_{I,N}$, in parentheses) for relevant combinations of surfactant and solvent at a representative temperature and aqueous salinity (20 °C, 100 mM NaCl). For the temperature insensitive AOT/nonionic mixtures at (χ^*, S^{**}, see Chapter 4), the estimated total critical microemulsion concentration ($c\mu c$) and the middle-phase surfactant concentration (γ_X) measured using the Huh theory are given for $\Omega = 1$. All quantities in mM. Literature values are marked as follows: [a][53] [b][72] [c][73] [d][10].

Each 15 mL composition was enriched in surfactant until bluish, typically $\gamma = 1\%$ wt., agitated manually to mix, then allowed to resolve into layers. Separation took place for 1 week at 18 ± 2 °C, after which no change in phase volumes was detected. Incomplete creaming/sedimentation resulted in volumetric errors that were notably independent of temperature cycles, and were mitigated by centrifugation at 2000 g.

1.5.2   Temperature-sensitive formulations

Polymerisable formulations

A preliminary step towards the concept of fixing the deformed droplets[1] was the formulation for ULIFT emulsions with the monomer styrene, based on modification of a literature toluene recipe. The styrene example puts the formulation theory above into practice, as applied to all recipes used in this thesis.

A salinity scan across the phase inversion point [75] of the toluene WIII was performed (Figure 1.7). With this information the local minima in ULIFT were identified using the Huh theory as shown in Figure 1.8. The results provided a starting point for substitution with the aromatic monomer, styrene; repeating the procedure with the new oil gave ULIFT of the same magnitude (Figure 1.9).

The presence of excess phases means that a ternary microemulsion remains unaffected by the change in the water-oil ratio Ω within the WIII region. The exception is unequal bulk partitioning of the butanol between the oil and water. A smaller Ω reduces the concentration of butanol in oil and thus its availability to reduce H_0 of the interface. The total mass of the surfactant added is known; its effective density within the monolayer is given by $\rho_\gamma = \bar{M}_\gamma/N_A a_\gamma L_\gamma \approx 1$ kg L^{-1}, where $\bar{M}_\gamma$ is the molecular weight. In any case, the Huh theory appears to neglect the volume frac-

---

[1]In the ONF project, the initial collaboration considered the possibility of manufacturing polymer beads of bespoke shape, for which Ward et al. showed proof-of-concept [74] based on a photointiated monomer oil. The latter collaboration proposed following the polymerisation by ratiometric Raman spectroscopy - a capability built into the design presented in Setup C (see § 2.4.3), though realised separately by fellow doctoral student OWJB. It was postulated that addition of polymer chains to the oil could aid the shape retention of a polymerising droplet by two mechanisms. First, the increased viscosity is expected to reduce any recoiling flow caused by the sharp rise in surface tension. Second, the shrinkage due to bond condensation would be reduced proportionately. A sensible starting choice of polymer is one formed from the same monomer as the solvent, but even so, the chain length and concentration introduce additional formulation variables. Which are best for both the process and the quality of the end product? These avenues of research remain to be explored.

tion of cosurfactant (here this constitutes no more than 4%), but this is partially accounted for by the reduction of a_γ from a Langmuir-Blodgett monolayer value.

These WIII systems have surfactant concentrations of $\gamma \approx 150$ mM SDS, far exceeding the aqueous cmc. They equilibrate noticeably faster (a matter of a few minutes) near the optimum point where emulsion coalescence is promoted by deformation under ULIFT [76]. The phase volumes follow the expected trend from large excess of oil at low salt (near WI) to excess of water at high salt (near WII). The lowest bounds for the oil-water surface tension is found at the intersection of the two middle-phase interfacial tensions, $S = (1.11 \pm 0.03)$ M, $\sigma_{OM,WM} = 3.5$ μN m^{-1}. SLS, SANS and SAXS on this same composition give almost identical IFT curves based on Doppler tensiometric or Teubner-Strey/Huh models [77–79]. The value of $\sigma_{OW} \approx 5$ μN m^{-1} is therefore known within a factor of $\sqrt{2}$. The optimum microemulsion volume fractions, $\phi_O = 0.45$ and $\phi_W = 0.49$ are almost equal. This observation reaffirms the concept of interchangeability between the bicontinuous water and oil volumes [80].

The dipole moment of styrene is threefold weaker than that of toluene. When changing oil to styrene a small increase in the lipophilicity of the oil is expected and thus also a relative hydrophilic shift in H_0 for the surfactant [81]. Roughly extrapolated figures [82] suggest the replacement of toluene with styrene involves a change of EACN = 1 → 3. The changes in HLD compensate such that $H_0 \to 0$. Adding BuOH instead of NaCl prevents 'salting out' of the surfactant [83, 84]. Styrene, being larger and more polarisable, has a greater dispersion interaction with butanol than the toluene it replaces. Thus the butanol has a lower relative affinity to SDS in styrene solution. This reduces the solubility of the SDS, such that the salinity scans form the expected sequence only when heated to 65 °C.

This styrene formulation clearly shows ULIFT comparable with the toluene analogue, notably at a higher salinity. By cutting the salt content further and instead replacing its hydrophobic contribution to H_0 with dropwise additional butanol, the
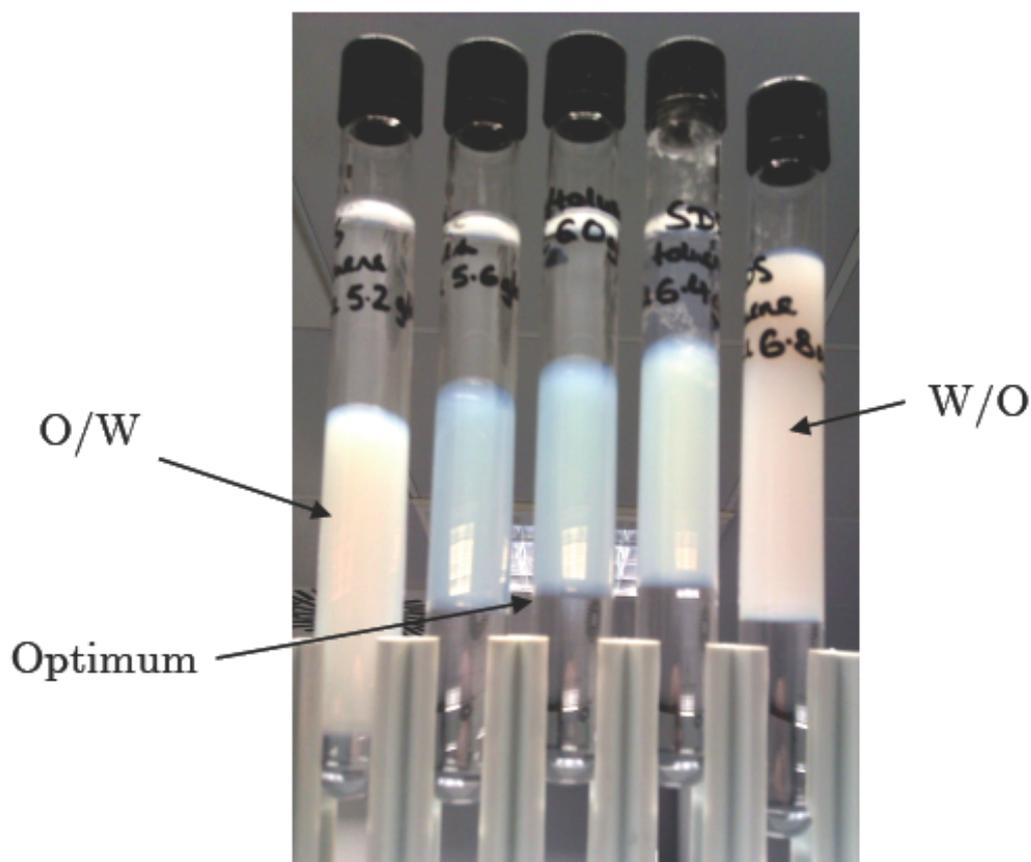
Figure 1.7: Salinity scan at 19 °C for the toluene/SDS/butanol/brine system showing the opalescent middle phases in transition from WI through WIII to WII. Note labels correspond to wt%. NaCl in brine: 5.2, 5.6, 6.0, 6.4, 6.8 from left to right. Samples are shown one hour after agitation.

Krafft point drops below room temperature whilst maintaining $H_0 = 0$. Phase volume measurements were taken 20 min after each addition and agitation cycle. Measuring the phase volumes gives a rough estimate of the solubility parameter at the optimum point, such that the minimum $\sigma_{OW} = 15$ μN m^{-1}. A phase-inverting microemulsion with a useful level of ULIFT was formed at room temperature with styrene monomer.
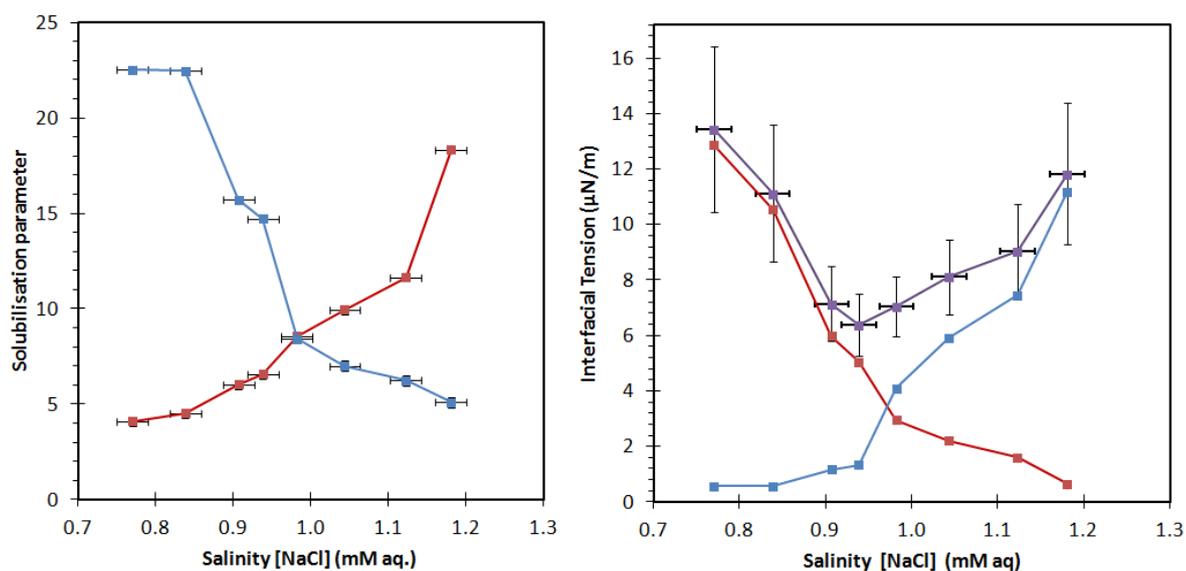
Figure 1.8: Phase volume tensiometry along a salinity scan in the toluene/SDS/butanol/brine system at 19 °C: (*left*) solubilisation parameters for oleic (*red*) and aqueous (*blue*) phases; (*right*) interfacial tensions with the microemulsion (*purple*) are extracted using the Huh equation and added, to bound the IFT value between oil and water.
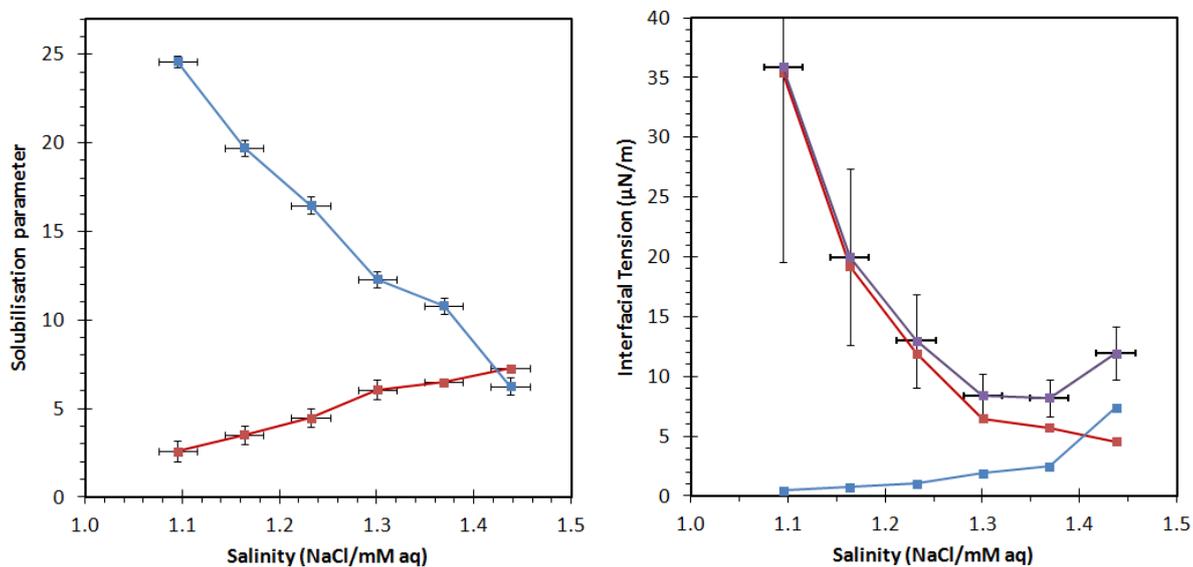
Figure 1.9: Phase volume tensiometry along a salinity scan in the styrene/SDS/butanol/brine system containing 4% wt. BuOH and heated to 65 °C. Legend as for Figure 1.8.
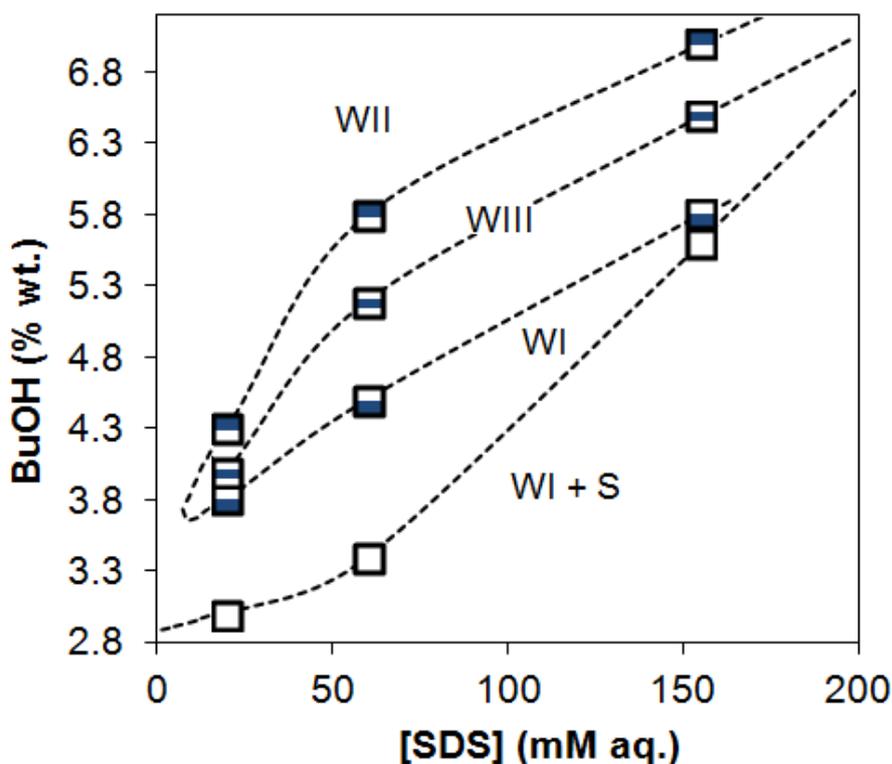
Figure 1.10: A Winsor phase diagram of the styrene/SDS/butanol/brine system with cosurfactant and amphiphile content at fixed salinity $S = 1.08$ M, temperature $T = 19$ °C and water-oil ratio $\Omega = 0.9$ is presented; this is analogous to a fish diagram with cosurfactant influencing H_0 instead of temperature. Note the SDS becomes more soluble in the presence of butanol. The slope of the ULIFT locus equals the ratio of BuOH to SDS in the monolayer, which approaches unity.

Alkane-based quaternary systems

The AOT/alkane/brine quaternary systems [53] are notable among those bearing ULIFT, for they do not require a cosurfactant. They invert in the sequence WII-WIII-WI with increasing temperature, as typical for ionic monolayers. Previous work gave ULIFT well suited to optical deformation [6, 85]. Heptane, decane and dodecane were formulated for minimum IFT. Although refractive contrast with water, Δn, increases with EACN, σ_0 increases more rapidly (Tables 1.4 and 4.1). Thus, heptane was found to give an optimal deformability ratio k/σ.

1.5.3 Temperature-insensitive quinary formulations

The nonionic quaternary systems formed using the $C_I E_J$ family of surfactants follow the opposite sequence WI-WIII-WII in accordance with the hydrophobic cloud-point effect [43, 86]. The surfactants express preferred curvatures of opposite temperature dependence, so their respective quaternary systems show contrary sequences of phase inversion [87, 88]. By mixing the two, the temperature coefficient c_T is negated. This forms the efficient and markedly less temperature-dependent quinary systems: AOT/$C_{12}E_5$/n-heptane/NaCl-brine and AOT/Brij-L4($C_{12}E_4$)/n-decane/NaCl-brine as used previously for optical tweezing [85]. The salinity and amphiphilic ratio can then be fine-tuned to give the desired H_0 and its temperature-sensitivity, as shown in Chapter 4.

1.5.4 Deuterated solvent

In much of the collaboration's later work, D_2O was substituted into the heptane quaternary - and heptane and decane quinary - systems, to lessen laser heating. For heptane/AOT/D_2O/NaCl (*i.e.* $\chi = 1$), the optimal salinity at the ambient temperature, 21 °C, was located around 30 mM. The corresponding PIT for the H_2O system is 42 mM; that's a similar ratio of salinities to that associated with changing the oil from heptane to octane. While the hydrophobic effect is largely entropic, the contribution is almost identical in water and in D_2O. A lower ionic strength permits AOT aggregates to leave the aqueous phase, which suggests an increase in the cohesive energy of that phase (which outweighs any increase in its interaction with AOT). The hydrogen bonding in D_2O is about 3% stronger than in water and so the relative change on deuteration is enthalpic [89]. The sequence of deformability summarised in Figure 1.11 is consistent with a PIT of 21.0 ± 0.3 °C at 30.0 ± 0.2 mM NaCl. The slope of PIT with salinity is roughly the same as the H_2O system, with a coefficient of +0.6 ± 0.1 K mM^{-1}.
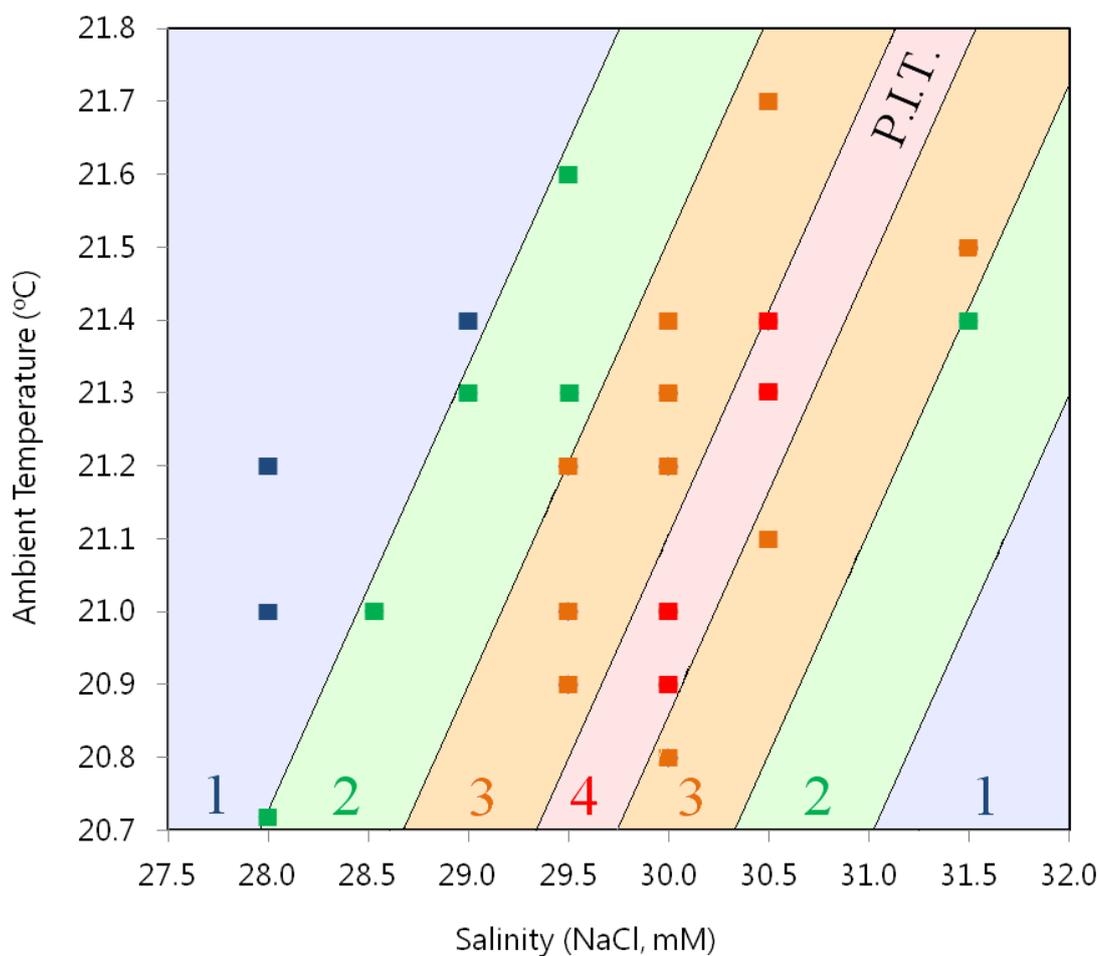
Figure 1.11: Deformability map revealing the PIT-salinity curve for droplets encountered in heptane/AOT/D$_2$O/NaCl experiments in Chapter 6. Assignment is based on a qualitative deformability scale, where #1-4 correspond to the extrema of droplet categories A-C in Table 3.2. Solid lines are estimated contours of deformability and therefore of IFT also.

1.6 Alternative macroscopic methods for optimisation

1.6.1 Small angle X-ray scattering (SAXS)

The Huh equation gives an indirect estimate of the IFT from the correlation length of the microemulsion ξ. In turn this can be measured by small-angle scattering of matter waves (neutrons) or light (X-rays) with a comparable wavelength. The latter technique is SAXS. The isolated, pre-equilibrated phases were interrogated with a *Bruker Nanostar* instrument using Cu Kα radiation. For each, a capillary of 1 mm diameter was run at 25 °C for 1 h with a sample-to-detector distance of 1.5 m. The exposures corresponding to excess water and excess oil were averaged and normalised in order to provide a background subtraction for the exposure corresponding to the middle phase. As shown in Figure 1.12, the scattering intensity was fitted with the structure-independent Teubner-Strey model [90, 91] to yield the average membrane dimensions and thus the minimum oil-water interfacial tension.

	$C_{12}E_5$/AOT/ heptane/120 mM NaCl	$C_{12}E_4$/AOT/ decane/170 mM NaCl
Periodicity, d (nm)	66 ± 7	60 ± 4
Correlation length, ξ (nm)	44 ± 1	37.4 ± 0.7
Domain size, $d/2$ (nm)	33 ± 3	30 ± 2
Lifshitz ratio, d/ξ	1.5 ± 0.1	1.6 ± 0.1
Interfacial tension, $0.44\,k_BT/\xi^2$	0.9 ± 0.1	1.3 ± 0.1
Surfactant fraction γ_X	0.028 ± 0.002 (53 mM)	0.033 ± 0.002 (64 mM)
Thread tension, $2\pi\sqrt{2\kappa\sigma}$ (pN)	0.54 ± 0.04	0.58 ± 0.05
Bending modulus, κ/k_BT	1.1 ± 0.1	1.0 ± 0.1

Table 1.4: Middle-phase domain and interfacial properties derived from SAXS at 25 °C, together with bending moduli derived from Stokes recoil of threads; see § 5.4.1. IFT quoted in μN m^{-1}.
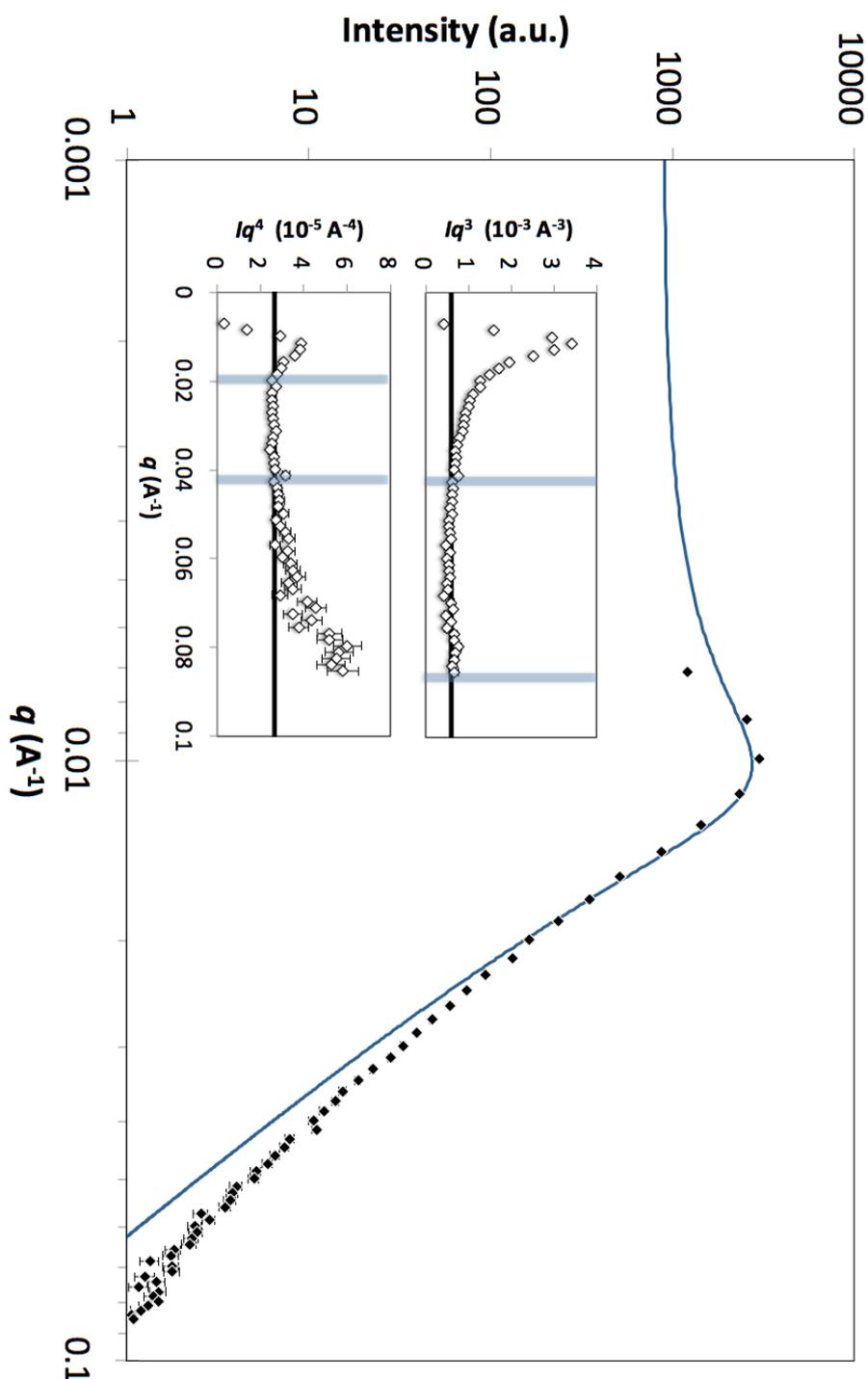
Figure 1.12: Small-angle scattering curve for the middle microemulsion phase of decane/AOT/$C_{12}E_4$/NaCl$_{(aq)}$, $S = 170$ mM, extracted and interrogated at 25 °C. The data is fitted with the Teubner-Strey model (solid line) to extract the average dimensions of the microemulsion domains. Inset: third and fourth moments of scattering signal to show regions that scale with scattering vector to the (*top*) third power, i.e. fractal monolayer structure, and (*bottom*) fourth power, i.e. Porod's Law for the specific interfacial area of the scattering domains.

1.6.2   Gravitational and centrifugal gauges of ULIFT

For emulsions that have adequately resolved, there is a variety of accessible methods for measuring the liquid-liquid IFT directly. However, these are less effective for measuring ULIFT. Gauges such as the Wilhelmy plate or pendant-drop methods become imprecise since the force or volume measured is proportional to the surface tension. Compensating for this effect in pendant drop tensiometry by miniaturisation [92] proves difficult, as drop profiles are not easily resolved and other effects such as evaporation and Brownian motion may become important.

Alternative methods exist whereby the measured phenomenon and/or the related approximations become stronger as the surface tension weakens. Spinning drop tensiometry is perhaps the most direct tool to measure ULIFT between liquids [93]. It relies on a centrifugal distortion of a droplet in a thin tube, surrounded by the denser phase. The acceleration due to gravity is typically much smaller than that due to rotation of a droplet less than a millimetre in size, and can be neglected. As the angular frequency ω increases, the spherical droplet is deformed to have a smaller radius $R_\omega < R_D$ perpendicular to the axis of rotation. The sphere thins asymptotically to a cylinder thinner than the capillary length [94] such that $\sigma = \Delta\rho\omega^2 R_\omega^3/4$. The spinning drop method becomes difficult to interpret for three phase systems, since the microemulsion may envelop the oil droplet. Another drawback of this method is the high rotational speed ($\omega > 100$ s^{-1}) required to measure thinning as droplets become smaller or as the IFT increases, but at this point, conventional methods become reliable as complementary techniques. Aveyard et al. used this technique to characterise the water-oil IFT of the heptane/AOT/brine system as a function of salinity and temperature. Their range of temperature data includes the shoulders either side of the PIT, but omits much of the present experimental window of ~ 2 K.

In sessile drop methods, gravity assumes a role analogous to the centrifugal force. In general, the measurement involves an additional interaction with a solid surface and so depends on a three-phase contact angle [95]. However, near-perfect wetting or dewetting is expected at ULIFT from Young's equation. Contact angles can be
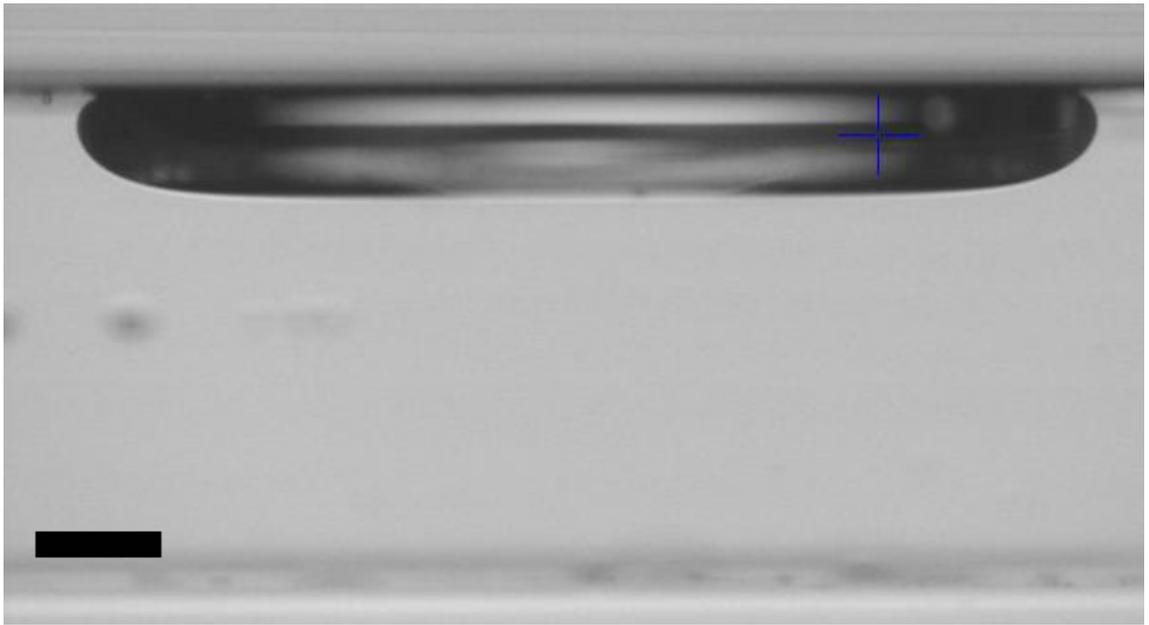
Figure 1.13: Side view in brightfield of a 2 mm-diameter decane droplet in water, sessile upon the upper internal surface of a prone quartz cuvette. The droplet is flattened under its own buoyancy to a thickness characteristic of the oil-water ULIFT. The oil and water correspond to the isolated excess phases of the WIII in the decane/AOT/$C_{12}E_5$/H_2O/NaCl system at $\gamma = c\mu c$, $S = 120$ mM, $T = 20$ °C. Scale bar 0.25 mm.

assumed 180 ° for a sufficiently hydrophilic surface such as clean quartz. Moreover, this method is distinctive in that larger droplets provide more precise measurements. A sessile oil drop larger than the capillary length, $R_D > L_C$, flattens into an oblate shape. In the limit $R_D \gg L_C$, its central thickness, h, depends only on the capillary length such that $\sigma = \Delta\rho g h^2 / 2$. Figure 1.13 shows such a decane droplet deforming on a horizontal surface at an IFT of about 100 μN m^{-1}.

1.6.3   Strata resolution rates

When microemulsion formulations are agitated to facilitate mixing, turbid kinetic emulsions are produced. Subsequently, the phase layers of the true equilibrium resolve under density gradients. Resolution is hindered, to the extent that metastable states can occur, by frustrated packing of droplets and the reduced density contrast associated with a microemulsion phase. Obtaining homogeneous, isolated phases from the WIII equilibria with adequate reproducibility is tedious and difficult even with centrifugation. A more convenient, if uncalibrated, method focuses on the kinetics of relaxation rather than the equilibrium state.

The rate of resolution is dependent on the IFT between phases. Lower ULIFT reduces the driving force for coalescence, but increases attraction between droplets, encouraging them to flocculate [69, 76]. Potential coalescence events become more frequent. Low IFT also facilitates the rearrangement of concentrated droplets into a denser packing accelerating exclusion of the continuous phase. Thus, the overall resolution rate *increases* sharply at the PIT [96]. This remarkable behaviour contradicts that of standard emulsions below the $c\mu c$, where conventionally low IFT is associated with increased surfactant concentrations, stabilised foam films and frustrated resolution [73].

A useful outcome is that a formulation of minimum IFT in a microemulsion series can be identified readily as that which *requires the minimum time to resolve* into clarified layers. When the oil-water volume ratio is unity, $\Omega = 1$, the resolution rate reaches a maximum at the optimal salinity and temperature (Figure 1.14). As a result, the resolution dynamics give a straightforward, empirical route to minimum IFT. This technique is verified by comparison with the interpolated PIT-salinity curve obtained by the spinning drop method [53].
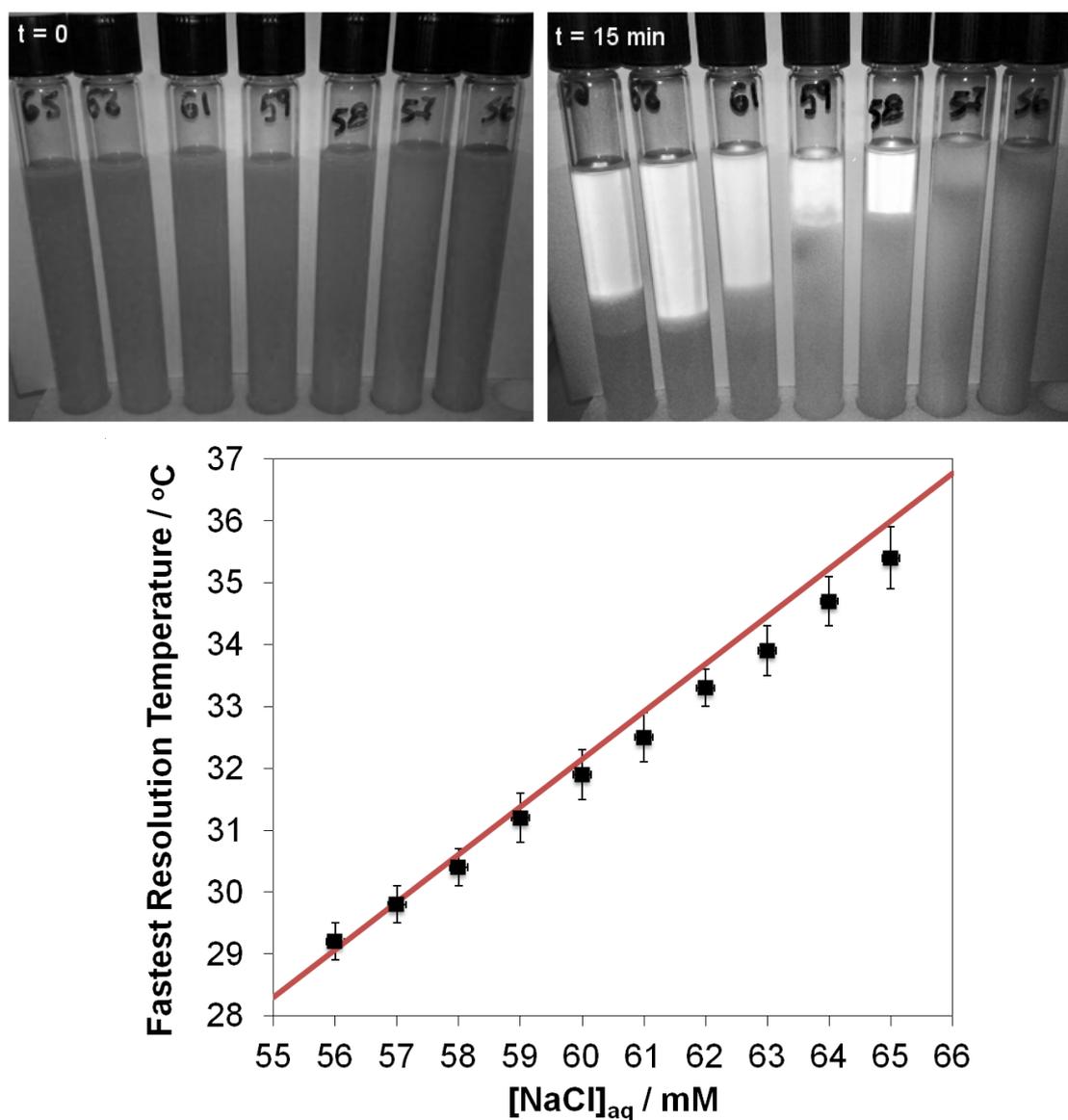
Figure 1.14: Photographs of heptane/AOT/H_2O/NaCl formulations at a range of salt concentrations, *(top, left)* immediately after shaking; *(top,right)* after 15 min. *(bottom)* The temperature at which the layers resolve in the shortest time for each sample (squares) corresponds to the PIT as a function of salinity (solid line interpolated from [53]).

1.6.4   Summary

The range of formulations obtained in this work is summarised in Table 1.5. Only the IFT minima in the heptane/AOT and decane/AOT systems proved sufficiently

low to pursue nonlinear optical deformation. The temperature-insensitive recipes with added nonionic surfactant are used in Chapter 4, whilst all other chapters refer exclusively to the temperature-sensitive (AOT only, $\chi = 1$) recipes, with heptane as oil unless otherwise stated.

Oil	Amphiphile	γ (mM aq.)	[NaCl] (mM aq.)
Temperature-sensitive			
Heptane	AOT	2 - 20	35–65
Decane	AOT	2 - 15	100–130
Dodecane	AOT	15	165–175
Toluene	SDS	10	95–120
	BuOH	1	
Styrene	SDS	10	96–106
	BuOH	1	
Temperature-insensitive			
Heptane	AOT	8–20	100–120
	$C_{12}E_5$	4–16	
Decane	AOT	8–20	100–120
	$C_{12}E_4$	4–16	

Table 1.5: Refined formulation recipes for WIII microemulsions with hydrocarbon oils, at ULIFT suitable for deformation under optical tweezing near room temperatures 18-27 °C.

Glossary

Symbol	Definition	Unit
A	Interfacial area	m^2
A_{AB}	Enthalpy of adhesion between phases A and B	$J\ m^{-2}$
AOT	Aerosol OT, ionic surfactant	
a	Molecular area	m^2
Bo	Bond number	-
BuOH	n-butanol	
Ca	Capillary number	-
C	Number of chemical components	-
$C_I E_J$	J-oxyethylene glycol I-ether nonionic surfactant	-
cmc	Critical micellar concentration	M
$c\mu c$	Critical microemulsion concentration	M
c_1, c_2	Principal curvatures	m^{-1}
CPP	Critical packing parameter	-
d	Microemulsion domain size	m
EACN	Equivalent alkane carbon number	-
F	Degrees of freedom	-
G	Gibbs free energy	J
g	Acceleration due to gravity	$m\ s^{-2}$
H	Mean curvature	m^{-1}
H_0	Spontaneous curvature	m^{-1}
HLB	Hydrophilic-lipophilic balance	-
HLD	Hydrophilic-lipophilic difference	-
IFT	Interfacial tension	$N\ m^{-1}$
J	Ethylene oxide number, nonionic surfactant	-
K	Gaussian curvature	m^{-1}
k	Optical trap strength	$N\ m^{-1}$
k_B	Boltzmann's constant	$J\ K^{-1}$
l	Length (characteristic)	m
l_γ	Surfactant tail length	m
L_C	Capillary length	m

LC	Liquid crystal	
$\bar{M}_\gamma$	Molar mass	kg mol^{-1}
N	Molar number, amount of material	mol
N_A	Avogadro's constant	mol^{-1}
$n, \Delta n$	Refractive index, contrast	-
n_L	Lattice coordination number	-
n_s	Dissociation number	-
o/w	Oil-in-water emulsion	
P	Number of phases	-
p	Pressure (ambient)	N m^{-2}
p_L	Pressure (Laplace)	N m^{-2}
PIT	Phase inversion temperature	°C
R	Gas constant	J K^{-1} mol^{-1}
R_D, ω	Droplet radius (spherical, centrifuged)	m
R-ratio	Winsor ratio	-
Re	Reynolds number	
S	Salinity, aqueous NaCl concentration	M
ΔS	Entropy change	J K^{-1}
SANS/SAXS	Small angle neutron/X-ray scattering	-
SDS	Sodium dodecyl sulfate, ionic surfactant	
T	Temperature (ambient)	K
T_C	Cloud-point temperature	K
T_K	Krafft temperature	K
U	Interaction energy	J
ULIFT	Ultralow interfacial tension, < 0.1 mN m^{-1}	N m^{-1}
V	Volume	m^3
v	Velocity (characteristic)	m s^{-1}
WI/WII/WIII/WIV	Winsor phase equilibria	
w/o	Water-in-oil emulsion	
γ	Surfactant bulk concentration	M or % wt.
γ_X	Surfactant concentration, Winsor X-point	M or % wt.
Γ	Surface excess concentration	mol m^{-2}
χ	Fraction of ionic surfactant in total surfactant	-

$\rho, \Delta\rho$	Density or specific gravity, difference in.	kg m^{-3}
σ_{AB}	Interfacial tension between phases A and B	
η	Dynamic viscosity	N s m^{-2}
ϕ_A	Volume fraction of phase A	-
$\kappa, \bar{\kappa}$	Bending modulus, saddle-splay modulus	J
μ°	Chemical potential	J mol^{-1}
ξ	Persistence or correlation length	m
Ω	Volumetric water-to-oil ratio	-
ω	Angular velocity	s^{-1}

References

[1] A. Ashkin, "Acceleration and trapping of particles by radiation pressure", *Phys. Rev. Lett.* Vol. 24, no. 4, p. 156, 1970.

[2] K. Dholakia and T. Cizmar, "Shaping the future of manipulation", *Nature Photonics*, vol. 5, no. 6, pp. 335–342, 2011.

[3] K. C. Neuman and S. M. Block, "Optical trapping", *Rev. Sci. Instrum.* Vol. 75, no. 9, pp. 2787–2809, 2004.

[4] Y. Kimura, "Microrheology of soft matter", *J. Phys. Soc. Jpn.* Vol. 78, no. 4, p. 041 005, 2009.

[5] A. Ward, C. Bain, and C. Mellor, *Droplet deformation.* 2012, US Patent 8,183,540.

[6] D. A. Woods, C. D. Mellor, J. M. Taylor, C. D. Bain, and A. D. Ward, "Nanofluidic networks created and controlled by light", *Soft Matter*, vol. 7, pp. 2517–2520, 6 2011.

[7] J. L. Salager, *Emulsion Properties and Related Know-how to Attain Them.* CRC Press, 2000.

[8] J. L. Salager, M. Bourrel, R. S. Schechter, and W. H. Wade, "Mixing rules for optimum phase-behavior formulations of surfactant/oil/water systems", *Soc. Pet. Eng.* Vol. 19, no. 05, 1979.

[9] K. Holmberg, "Organic reactions in microemulsions", *Eur. J. Org. Chem.* Vol. 5, 731–742, 2007.

[10] T. Sottmann and C. Stubenrauch, "Phase behaviour, interfacial tension and microstructure of microemulsions", *Microemulsions: Background, New Concepts, Applications, Perspectives, ed. C. Stubenrauch, John Wiley & Sons, Oxford*, 2009.

[11] S. L. Anna, N. Bontoux, and H. A. Stone, "Formation of dispersions using flow focusing in microchannels", *Appl. Phys. Lett.* Vol. 82, no. 3, pp. 364–366, 2003.

[12]   G. Bolognesi, A. Hargreaves, A. D. Ward, A. K. Kirby, C. D. Bain, and O. Ces, "Microfluidic generation of monodisperse ultra-low interfacial tension oil droplets in water", *RSC Adv.* Vol. 5, pp. 8114–8121, 11 2015.

[13]   S. Banerjee, *Functional materials preparation, processing and applications.* London: Elsevier, 2012, ISBN: 9780123851420.

[14]   M. Velarde, *Interfacial phenomena and the Marangoni effect.* Wien New York: Springer, 2002, ISBN: 9783211836965.

[15]   S. Mitra and S. Chakraborty, *Microfluidics and Nanofluidics Handbook*, ser. Chemistry, Physics, and Life Science Principles. CRC Press, 2011, pp. 621–650, ISBN: 9781439816776.

[16]   S. Zeppieri, J. Rodríguez, and A. L. López de Ramos, "Interfacial tension of alkane + water systems", *J. Chem. Eng. Data*, vol. 46, no. 5, pp. 1086–1088, 2001.

[17]   H. Lekkerkerker, V. de Villeneuve, J. de Folter, M. Schmidt, Y. Hennequin, D. Bonn, J. Indekeu, and D. Aarts, "Life at ultralow interfacial tension: wetting, waves and droplets in demixed colloid-polymer mixtures", *Eur. Phys. J. B*, vol. 64, no. 3-4, pp. 341–347, 2008, ISSN: 1434-6028.

[18]   M. Beauvais, L. Serreau, C. Heitz, and E. Barthel, "How do silanes affect the lubricating properties of cationic double chain surfactant on silica surfaces?", *J. Colloid Interface Sci.* Vol. 331, no. 1, pp. 178–184, 2009, ISSN: 0021-9797.

[19]   R. P. Borwankar and D. T. Wasan, "Equilibrium and dynamics of adsorption of surfactants at fluid-fluid interfaces", *Chem. Eng. Sci.* Vol. 43, no. 6, pp. 1323–1337, 1988, ISSN: 0009-2509.

[20]   M. Fukuda, "The importance of lipophobicity in surfactants: methods for measuring lipophobicity and its effect on the properties of two types of nonionic surfactant", *J. Colloid Interface Sci.* Vol. 289, no. 2, pp. 512–520, 2005, ISSN: 0021-9797.

[21]   K.-Y. Lai, *Liquid Detergents.* Boca Raton: Taylor & Francis, 2006, ISBN: 9781420027907.

[22]   R. C. Pasquali, N. Sacco, and C. Bregni, "The studies on hydrophilic–lipophilic balance (HLB): sixty years after William C. Griffin's pioneer work (1949–2009)", *Lat. Am. J. Pharm.* Vol. 28, no. 2, pp. 313–317, 2009.

[23]   D. J. Mitchell and B. W. Ninham, "Micelles, vesicles and microemulsions", *J. Chem. Soc., Faraday Trans. 2*, vol. 77, pp. 601–629, 4 1981.

[24]   J. Stauff, "Solvent properties of amphiphilic compounds by P. A. Winsor, 1954.", *Angewandte Chemie*, vol. 68, no. 15, pp. 504–504, 1956, ISSN: 1521-3757.

[25]   D. J. McClements, "Nanoemulsions versus microemulsions: terminology, differences, and similarities", *Soft Matter*, vol. 8, pp. 1719–1729, 6 2012.

[26] M. Hillert, *Phase Equilibria, Phase Diagrams and Phase Transformations: Their Thermodynamic Basis*. Cambridge University Press, 2007, ISBN: 9781139465861.

[27] S. Burauer, T. Sachert, T. Sottmann, and R. Strey, "On microemulsion phase behaviour and the monomeric solubility of surfactant", *Phys. Chem. Chem. Phys.* Vol. 1, pp. 4299–4306, 18 1999.

[28] O. Regev, S. Ezrahi, A. Aserin, N. Garti, E. Wachtel, E. W. Kaler, A. Khan, and Y. Talmon, "A study of the microstructure of a four-component nonionic microemulsion by cryo-TEM, NMR, SAXS, and SANS", *Langmuir*, vol. 12, no. 3, pp. 668–674, 1996.

[29] S. Yoshitake, A. Ohira, M. Tominaga, T. Nishimi, M. Sakata, C. Hirayama, and M. Kunitake, "Electrochemistry in middle phase microemulsion composed of saline and toluene with sodium dodecylsulfate and n-butanol", *Chem. Lett.* Vol. 31, no. 3, pp. 360–361, 2002.

[30] L. Mukhopadhyay, P. Bhattacharya, and S. Moulik, "Additive effects on the percolation of water/AOT/decane microemulsion with reference to the mechanism of conduction", *Colloids Surf. A*, vol. 50, pp. 295–308, 1990, ISSN: 0166-6622.

[31] O. Lade and A. Krawietz, "A bending elasticity approach to the three-phase coexistence of microemulsions", *J. Chem. Phys.* Vol. 115, no. 23, pp. 10 986–10 997, 2001.

[32] S. Ljunggren and J. Eriksson, "Minimal surfaces and Winsor III microemulsions", *Langmuir*, vol. 8, no. 5, pp. 1300–1306, 1992.

[33] S. Ljunggren, J. Eriksson, and P. Kralchevsky, "Minimization of the free energy of arbitrarily curved interfaces", *J. Colloid Interface Sci.* Vol. 191, no. 2, pp. 424–441, 1997.

[34] B. P. Binks, "Emulsion type below and above the CMC in AOT microemulsion systems", *Colloids Surf., A*, vol. 71, no. 2, pp. 167–172, 1993, ISSN: 0927-7757.

[35] K. Shinoda, "The correlation between the dissolution state of nonionic surfactant and the type of dispersion stabilized with the surfactant", *J. Colloid Interface Sci.* Vol. 24, no. 1, pp. 4–9, 1967, ISSN: 0021-9797.

[36] P. G. De Gennes and C. Taupin, "Microemulsions and the flexibility of oil/water interfaces", *J. Phys. Chem.* Vol. 86, no. 13, pp. 2294–2304, 1982.

[37] C. Taupin, "New ideas for microemulsion structure: the Talmon-Prager and de Gennes models", in *Progress in Microemulsions*, ser. Ettore Majorana International Science Series, S. Martellucci and A. Chester, Eds., vol. 41, Springer US, 1989, pp. 113–123, ISBN: 978-1-4899-0811-7.

[38] M. Peltomäki, G. Gompper, and D. Kroll, "Scattering intensity of bicontinuous microemulsions and sponge phases", *J. Chem. Phys.* Vol. 136, no. 13, p. 134 708, 2012.

[39] L. Peliti and S. Leibler, "Effects of thermal fluctuations on systems with small surface tension", *Phys. Rev. Lett.* Vol. 54, pp. 1690–1693, 15 1985.

[40] S. Komura, "Mesoscale structures in microemulsions", *J. Phys.: Condens. Matter*, vol. 19, no. 46, p. 463 101, 2007.

[41] W. K. Kegel and H. Lekkerkerker, "Competition between a lamellar and a microemulsion phase in an ionic surfactant system", *J. Phys. Chem.* Vol. 97, no. 42, pp. 11 124–11 133, 1993.

[42] H. Reiss, H. M. Ellerby, and J. Manzanares, "Configurational entropy of microemulsions: the fundamental length scale", *J. Chem. Phys.* Vol. 99, no. 12, pp. 9930–9937, 1993.

[43] T. Sottmann and R. Strey, "Ultralow interfacial tensions in water-n-alkane-surfactant systems", *J. Chem. Phys.* Vol. 106, no. 20, pp. 8606–8615, 1997.

[44] J. L. Lebowitz and C. Domb, *Phase transitions and critical phenomena*. Academic Press, 2001, vol. 20, pp. 7–40.

[45] L. M. Bergström, "Bending elasticity of charged surfactant layers: the effect of layer thickness", *Langmuir*, vol. 22, no. 8, pp. 3678–3691, 2006.

[46] H. Kellay, B. Binks, Y. Hendrikx, L. Lee, and J. Meunier, "Properties of surfactant monolayers in relation to microemulsion phase behaviour", *Adv. Colloid Interface Sci.* Vol. 49, pp. 85–112, 1994.

[47] M. Gradzielski, "Bending constants of surfactant layers", *Curr. Opin. Colloid Interface Sci.* Vol. 3, no. 5, pp. 478–484, 1998, ISSN: 1359-0294.

[48] B. P. Binks, J. Meunier, O. Abillon, and D. Langevin, "Measurement of film rigidity and interfacial tensions in several ionic surfactant-oil-water microemulsion systems", *Langmuir*, vol. 5, no. 2, pp. 415–421, 1989.

[49] V. Nardello, N. Chailloux, J. Poprawski, J.-L. Salager, and J.-M. Aubry, "HLD concept as a tool for the characterization of cosmetic hydrocarbon oils", *Polymer International*, vol. 52, no. 4, pp. 602–609, 2003.

[50] S. Queste, J.-L. Salager, R. Strey, and J. Aubry, "The EACN scale for oil classification revisited thanks to fish diagrams", *J. Colloid Interface Sci.* Vol. 312, no. 1, pp. 98–107, 2007.

[51] L. Cash, J. L. Cayias, G. Fournier, D. Macallister, T. Schares, R. Schechter, and W. Wade, "The application of low interfacial tension scaling rules to binary hydrocarbon mixtures", *J. Colloid Interface Sci.* Vol. 59, no. 1, pp. 39–44, 1977.

[52] J.-L. Salager and R. Antón, "Physico-chemical characterization of a surfactant: a quick and precise method", *J. Dispersion Sci. Technol.* Vol. 4, no. 3, pp. 253–273, 1983.

[53] R. Aveyard, B. P. Binks, S. Clark, and J. Mead, "Interfacial tension minima in oil-water-surfactant systems: behaviour of alkane-aqueous NaCl systems containing Aerosol-OT", *J. Chem. Soc., Faraday Trans. 1*, vol. 82, pp. 125–142, 1 1986.

[54]   F. Ysambertt, R. E. Antón, and J.-L. Salager, "Retrograde transition in the phase behaviour of surfactant-oil-water systems produced by an oil equivalent alkane carbon number scan", *Colloids Surf. A*, vol. 125, no. 2, pp. 131–136, 1997.

[55]   G. Førland, J. Samseth, H. Høiland, and K. Mortensen, "The effect of medium chain length alcohols on the micellar properties of sodium dodecyl sulfate in sodium chloride solutions", *J. Colloid Interface Sci.* Vol. 164, no. 1, pp. 163–167, 1994.

[56]   M. Aarra, H. Høiland, and A. Skauge, "Phase behavior and salt partitioning in two-and three-phase anionic surfactant microemulsion systems: Part I, phase behavior as a function of temperature", *J. Colloid Interface Sci.* Vol. 215, no. 2, pp. 201–215, 1999.

[57]   I. Umlong and K. Ismail, "Micellization of AOT in aqueous sodium chloride, sodium acetate, sodium propionate, and sodium butyrate media: a case of two different concentration regions of counterion binding", *J. Colloid Interface Sci.* Vol. 291, no. 2, pp. 529–536, 2005.

[58]   J. Velásquez, C. Scorzza, F. Vejar, A. M. Forgiarini, R. Antón, and J.-L. Salager, "Effect of temperature and other variables on the optimum formulation of anionic extended surfactant–alkane–brine systems", *J. Surfactants Deterg.* Vol. 13, no. 1, pp. 69–73, 2010.

[59]   D. Langevin, "Recent advances in the physics of microemulsions", *Physica Scripta*, vol. 1986, no. T13, p. 252, 1986.

[60]   A. Graciaa, J. Lachaise, C. Cucuphat, M. Bourrel, and J.-L. Salager, "Improving solubilization in microemulsions with additives: 1. The lipophilic linker role", *Langmuir*, vol. 9, no. 3, pp. 669–672, 1993.

[61]   F. Marchal, P. Guenoun, J. Daillant, D. W. Holley, and J. Mays, "Unprecedented microemulsion boosting effect induced by a charged diblock copolymer: bending modulus and curvature frustration of the surfactant film", *Soft Matter*, vol. 5, no. 20, pp. 4006–4014, 2009.

[62]   D. Siano and J. Bock, "A polymer-microemulsion interaction: the coacervation model", *J. Colloid Interface Sci.* Vol. 90, no. 2, pp. 359–372, 1982, ISSN: 0021-9797.

[63]   C. Huh, "Formation of a middle-phase from a lower or upper-phase microemulsion", *J. Colloid Interface Sci.* Vol. 97, no. 1, pp. 201–219, 1984, ISSN: 0021-9797.

[64]   B. P. Binks, "Relationship between microemulsion phase behavior and macroemulsion type in systems containing nonionic surfactant", *Langmuir*, vol. 9, no. 1, pp. 25–28, 1993.

[65]   G. E. J. Vaessen and H. N. Stein, "The applicability of catastrophe theory to emulsion phase inversion", *J. Colloid Interface Sci.* Vol. 176, no. 2, pp. 378–387, 1995.

[66]   M. Miñana-Perez, A. Graciaa, J. Lachaise, and J.-L. Salager, "Solubilization of polar oils with extended surfactants", *Colloids Surf. A*, vol. 100, pp. 217–224, 1995.

[67] E. Van Hecke, M. Catte, J. Poprawski, J.-M. Aubry, and J.-L. Salager, "A novel criterion for studying the phase equilibria of non-ionic surfactant–triglyceride oil–water systems", *Polymer International*, vol. 52, no. 4, pp. 559–562, 2003.

[68] T. Phan, C. Attaphong, and D. Sabatini, "Effect of extended surfactant structure on interfacial tension and microemulsion formation with triglycerides", *J. Am. Oil Chem. Soc.* Vol. 88, no. 8, pp. 1223–1228, 2011.

[69] P. D. I. Fletcher and D. I. Horsup, "Droplet dynamics in water-in-oil microemulsions and macroemulsions stabilised by non-ionic surfactants. correlation of measured rates with monolayer bending elasticity", *J. Chem. Soc., Faraday Trans.* Vol. 88, pp. 855–864, 6 1992.

[70] A. B. Pedrosa, J. I. Briz, and M. M. Velazquez, "Effect of additives on the adsorption of sodium bis(2-ethyl hexyl sulfosuccinate) at the air-water interface studied by equilibrium and dynamic surface tension measurements", *J. Surfact. Deterg.* Vol. 5, no. 4, pp. 397–402, 2002, ISSN: 1558-9293.

[71] E. A. Kubatta and H. Rehage, "AOT-vesicles produced at the oil-water interface", *Tenside Surfactants Deterg.* Vol. 48, no. 3, pp. 221–227, 2011.

[72] R. Aveyard, B. P. Binks, S. Clark, and P. D. I. Fletcher, "Effects of temperature on the partitioning and adsorption of $C_{12}E_5$ in heptane-water mixtures", *J. Chem. Soc., Faraday Trans.* Vol. 86, pp. 3111–3115, 18 1990.

[73] B. Binks, P. Fletcher, and D. Horsup, "Effect of microemulsified surfactant in destabilising water-in-oil emulsions containing $C_{12}E_4$", *Colloids and Surfaces*, vol. 61, pp. 291–315, 1991, ISSN: 0166-6622.

[74] A. D. Ward, M. Berry, P. Ash, D. Woods, and C. D. Bain, "The polymerisation of emulsion droplets deformed using laser tweezers to create microscopic polymer particles", *Central Laser Facility Ann. Rep*, vol. 2007, pp. 199–201, 2006.

[75] P. Guering and B. Bjoern Lindman, "Droplet and bicontinuous structures in microemulsions from multicomponent self-diffusion measurements", *Langmuir*, vol. 1, no. 4, pp. 464–468, 1985.

[76] B. P. Binks, W.-G. Cho, P. D. I. Fletcher, and D. N. Petsev, "Stability of oil-in-water emulsions in a low interfacial tension system", *Langmuir*, vol. 16, no. 3, pp. 1025–1034, 2000.

[77] Pouchelon, A., Meunier, J., Langevin, D., and Cazabat, A.M., "Light scattering from oil-water interfaces : measurements of low interfacial tensions", *J. Physique Lett.* Vol. 41, no. 10, pp. 239–242, 1980.

[78]   H. Rosano, D. Jon, and J. Whittam, "Considerations on formation and stability of oil/water dispersed systems", *Journal of the American Oil Chemists' Society*, vol. 59, no. 8, pp. 360–363, 1982, ISSN: 1558-9331.

[79]   Guest, D., Auvray, L., and Langevin, D., "Persistence length measurements in middle phase microemulsions", *J. Physique Lett.* Vol. 46, no. 22, pp. 1055–1063, 1985.

[80]   Meunier, J., "Measurement of the rigidity coefficient of a surfactant layer and structure of the oil or water microemulsion interface", *J. Physique Lett.* Vol. 46, no. 21, pp. 1005–1014, 1985.

[81]   S. Kawano, S. Nishi, R. Umeza, and M. Kunitake, "Propagation of polymer nanosheets from silica opal membrane gaps by thermal polymerization of bicontinuous microemulsions", *Chemical Communications*, no. 13, pp. 1688–1690, Mar. 2009, ISSN: 1359-7345.

[82]   S. Kiran, E. Acosta, and K. Moran, "Evaluating the hydrophilic-lipophilic nature of asphaltenic oils and naphthenic amphiphiles using microemulsion models", *J. Colloid Interface Sci.* Vol. 336, no. 1, pp. 304–313, 2009, ISSN: 0021-9797.

[83]   H. Nakayama, K. Shinoda, and E. Hutchinson, "The effect of added alcohols on the solubility and the Krafft point of sodium dodecyl sulfate", *J. Phys. Chem.* Vol. 70, no. 11, pp. 3502–3504, 1966.

[84]   X. Zhou and J. Hao, "Solubility of NaBr, NaCl, and KBr in surfactant aqueous solutions", *J. Chem. Eng. Data*, vol. 56, no. 4, pp. 951–955, 2011.

[85]   H. M. Bunyan, "Optical deformation of emulsion droplets", Master's thesis, University of Durham, University of Durham, UK, 2010.

[86]   R. Aveyard, B. P. Binks, T. A. Lawless, and J. Mead, "Interfacial tension minima in oil + water + surfactant systems: effects of salt and temperature in systems containing non-ionic surfactants", *J. Chem. Soc., Faraday Trans. 1*, vol. 81, pp. 2155–2168, 9 1985.

[87]   B. P. Binks, P. D. I. Fletcher, and D. J. F. Taylor, "Temperature insensitive microemulsions", *Langmuir*, vol. 13, no. 26, pp. 7030–7038, 1997.

[88]   M. Kahlweit and R. Strey, "Phase behavior of quinary mixtures of the type water-oil-nonionic amphiphile-ionic amphiphile-salt", *J. Phys. Chem.* Vol. 92, no. 6, pp. 1557–1563, 1988.

[89]   C.-H. Chen, "Interactions of lipid vesicles with solvent in heavy and light water", *J. Phys. Chem.* Vol. 86, no. 18, pp. 3559–3562, 1982.

[90]   M. Teubner and R. Strey, "Origin of the scattering peak in microemulsions", *J. Chem. Phys.* Vol. 87, no. 5, pp. 3195–3200, 1987.

[91]   S. Chen, S. Chang, and R. Strey, "Structural evolution within the one phase region of a three component microemulsion system: water-n-decane-sodium-bis-ethylhexylsulfosuccinate (AOT)", *J. Chem. Phys.* Vol. 93, no. 3, pp. 1907–1918, 1990.

[92]   J. Holgado-Terriza, J. Gomez-Lopera, P. Luque-Escamilla, C. Atae-Allah, and M. Cabrerizo-Vilchez, "Measurement of ultralow interfacial tension with ADSA using an entropic edge-detector", *Colloid Surf. A*, vol. 156, no. 1-3, pp. 579–586, 1999, ISSN: 0927-7757.

[93]   B. Vonnegut, "Rotating bubble method for the determination of surface and interfacial tensions", *Rev. Sci. Instrum.* Vol. 13, no. 1, pp. 6–9, 1942.

[94]   J. Viades-Trejo and J. Gracia-Fadrique, "Spinning drop method: from Young-Laplace to Vonnegut", *Colloid Surf. A*, vol. 302, no. 1-3, pp. 549–552, 2007, ISSN: 0927-7757.

[95]   L. Schramm, D. B. Fisher, S. Schurch, and A. Cameron, "A captive drop instrument for surface or interfacial tension measurements at elevated temperatures and pressures", *Colloid Surf. A*, vol. 94, no. 2-3, pp. 145–159, 1995, ISSN: 0927-7757.

[96]   R. Aveyard, B. P. Binks, P. D. I. Fletcher, and X. Ye, "Coalescence lifetimes of oil and water drops at the planar oil-water interface and their relation to emulsion phase inversion", in *Trends in Colloid and Interface Science VI*, ser. Progress in Colloid & Polymer Science, C. Helm, M. Loesche, and H. Moehwald, Eds., vol. 89, Steinkopff, 1992, pp. 114–117, ISBN: 978-3-7985-0913-9.

Chapter 2

Optical Rigs for Tweezing and Imaging Microdroplets

2.1 Premise and theory of optical tweezers

Optical tweezing is the ability to manipulate the position or orientation of microscopic particles, simply with focused light. Developed from seminal experiments by Ashkin [1] in the 1970s-80s, as a contactless procedure it has become a mainstay of biological [2] and microforce measurements.

2.1.1 Radiation pressure

On refraction or reflection, conservation of momentum implies that each photon imparts momentum to the medium of higher refractive index n, in its initial direction of propagation. This is called *radiation pressure*. There are two complementary theoretical frameworks in which the effect of radiation pressure on a dielectric interface may be considered [3]. The Abraham momentum associated with the kinetic energy of a photon is $|\boldsymbol{p}_A| = 2\pi\hbar/n\lambda$, where $\hbar$ is the reduced Planck's constant and λ is the photon's wavelength in vacuum. The Minkowski momentum describes the canonical wave momentum, $|\boldsymbol{p}_M| = 2\pi n\hbar/\lambda$. The Minkowski momentum flux carried by a beam of N photons is therefore:

$$|\boldsymbol{F}_{beam}| = \frac{d}{dt}(N|\boldsymbol{p}_M|) = \frac{nP}{c},\qquad(2.1.1a)$$

60

where c is the speed of light and P is the optical power. The interface is a closed body of characteristic radial size R_D. In the limit that the object is smaller than the photon wavelength, the interaction resembles a point dipole induced by the local, modulated electric field. This is the *Rayleigh* approximation $R_D \ll \lambda$.

Alternatively, if the object is significantly larger than the photon wavelength, the interaction is better described by an emergent, continuum model based on refraction. This is the ray-tracing or *geometric* limit, $R_D \gg \lambda$. Light becomes refracted upon crossing a dielectric interface, according to the ratio of propagation speeds in the media on either side. These speeds are given by the real parts of the refractive indices, n_1, n_2; a higher index indicates that the electromagnetic wave travels more slowly. Snell's law shows that refraction involves a change of direction from $\theta_1 \rightarrow \theta_2$ when the ratio $m = n_2/n_1 \neq 1$:

$$\sin(\theta_2) = \sin(\theta_1)/m$$

2.1.2 Gradient and scattering components

For a non-zero angle of incidence, a component of this momentum will be transferred in the opposite direction to that in which the wavefronts are refracted. For a plane wave, there is only a net force away from the light source; this is the *scattering force* $\boldsymbol{F}_{scat}$. If a convergent beam with a unimodal intensity profile is used, however, there is a focus of high, smoothly varying intensity; this is the case when a Gaussian laser beam is focused through a high numerical-aperture (NA) objective lens.

A convex object of index n_2 will refract convergent/divergent rays in such a way as to produce a restoring force towards the focus regardless of its location; this is the gradient force $\boldsymbol{F}_{grad}$. Tweezing studies are primarily concerned with this force component, as it constrains the object to lie near the focus.

A general Maxwellian equation for force exists, based on conservation of electro-
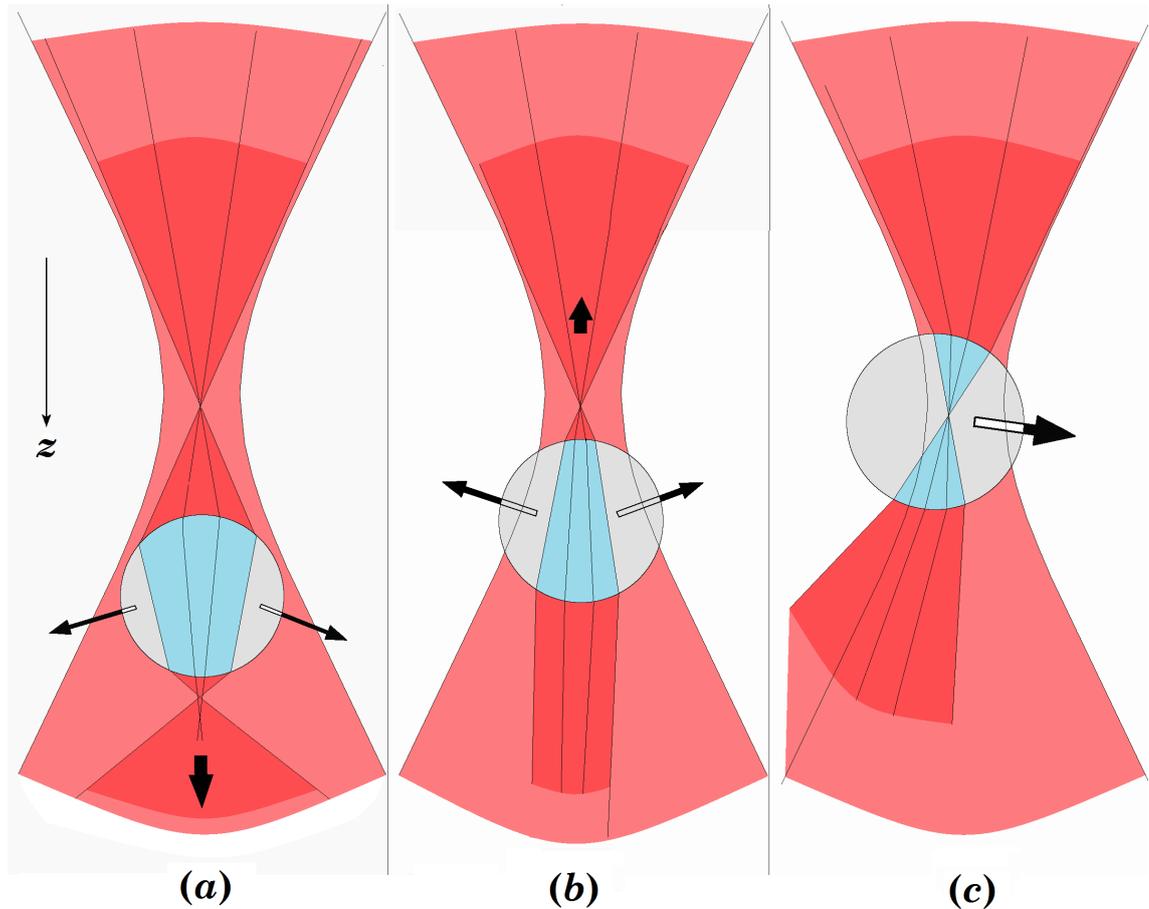
Figure 2.1: Convex particles of higher refractive index than the surrounding medium are attracted along an intensity gradient. Optical forces appear due to refraction and are *(a)* weakly scattering, particularly downstream of the trap at the low NA shown for clarity, but restore the object's position within the trap volume (or at higher NA) at both *(b)* axial and *(c)* radial displacements.

magnetic and mechanical momentum as follows:

$$\boldsymbol{F} = \int_V \left(\nabla \cdot \overleftrightarrow{\boldsymbol{T}} - \frac{n^2}{c^2} \frac{d\boldsymbol{S}}{dt} \right) dV \qquad\qquad = \Delta \int_A \overleftrightarrow{\boldsymbol{T}} \cdot d\boldsymbol{A} \qquad (2.1.1b)$$

where $\overleftrightarrow{\boldsymbol{T}}$ is the Maxwell stress tensor [4], $\boldsymbol{S}$ is the Poynting vector and $d\boldsymbol{A}$ (dV) are the surface area (volume) elements of the object. However, in applying this $\overleftrightarrow{\boldsymbol{T}}$-matrix theory, the physics are obscured by arduous numerical integration on both sides of the interface. The main obstacle for an exact analytical calculation of $\boldsymbol{F}_{grad}$ is that, in general, it must account for the pathlength-dependent phase shift in the

scattered light [5]. Notably, Mie theory does so, but is applicable only to perfect spheres. However, this phase shift vanishes approximately in the two limits $R_D \neq \lambda$. In the Rayleigh limit, the forces scale as [6]:

$$|\boldsymbol{F}_{scat}| \propto \frac{R_D^6}{\lambda^4} \Big(\frac{m^2 - 1}{m^2 + 2}\Big)^2 \times I \tag{2.1.1c}$$

$$|\boldsymbol{F}_{grad}| \propto R_D^3 \Big(\frac{m^2 - 1}{m^2 + 2}\Big) \times |\boldsymbol{\nabla} I| \tag{2.1.1d}$$

Here the intensity of the beam is I and its total power illuminating the object is P. Note that both components of radiation pressure rely on the refractive index contrast $m \neq 1$. In the geometric limit, the contribution of each ray to $|\boldsymbol{F}_{scat}|$ and $|\boldsymbol{F}_{grad}|$ also depends on the angle of incidence[7]. Oblique rays at the periphery of the focused beam are more strongly refracted and contribute lateral momentum, so a higher NA tends to increase $|\boldsymbol{F}_{grad}|$.

Trapping of *any size* R_D can only occur if the gradient force holding the particle near the focus dominates the forward scattering force; i.e. for microscopic, optically dense particles in a strongly focused beam. If the refractive indices are reversed, $m < 1$, then the particles seek low-field; only unconventional beams with intensity minima at the focus can trap them. Such exotic modes as Bessel or Laguerre-Gaussian beams are also known to exert axial stress and rotational torque on irradiated particles [8]. In this work, Gaussian beams are used exclusively.

The spatial intensity distribution of a Gaussian laser beam is well described by:

$$I(r, z) = \frac{2P}{\pi \omega(z)^2} \exp \Big(- 2\frac{r^2}{\omega(z)^2}\Big) \tag{2.1.1e}$$

$$\omega(z) = \omega_0 \sqrt{1 + \frac{z^2}{z_R^2}} \quad \text{where} \quad z_R = \frac{\pi \omega_0^2}{\lambda} \tag{2.1.1f}$$

This form is derived in the paraxial limit $NA \ll n$, which neglects terms of field curvature along the axial direction in the Helmholtz equation [9]. This approximation breaks down in the region within $\lambda/2$ of the beam focus. Nonetheless, it remains a good estimate of the profile if the beam waist is taken as $\omega_0 \approx \lambda n/\pi NA$ (see § 4.7).

Shorter wavelengths of light provide tighter foci, though use of ultraviolet radiation is prevented by strong absorption; visible and near IR wavelengths are often used for trapping. In this work, $\lambda = 1064$ nm is provided by Nd:YAG diode lasers.

2.2 Trap characterisation

2.2.1 Trap strength and escape force

In absence of all other forces, the equilibrium position of a trapped particle lies along the axis of the beam where the scattering and gradient forces cancel. For a Gaussian beam, the trap's potential well is approximately harmonic (Hooke's law) for small displacements and so characterised by its stiffness or *trap strength* $\boldsymbol{k}$ at the equilibrium point.

$$\boldsymbol{k} \equiv \boldsymbol{\nabla} \boldsymbol{F}_{grad} \quad (\boldsymbol{r} = \boldsymbol{r}_{eq}) \tag{2.2.1g}$$

On the other hand, $\boldsymbol{F}_{esc}$ is the maximum in the force-displacement curve - the maximum force that the trap can exert on the surface of a spherical object of that size and refractive index in that direction. In a truncated Hookean approximation, the escape force is roughly proportional to the harmonic trap strength $\boldsymbol{k}$. In general these are anisotropic and require a tensor description, but since the beam intensity changes more rapidly in the focal plane than along the axial direction, the escape force and trap strength have approximate prolate-spheroidal symmetry around the focal point. It is sufficient to describe the values in axial and equatorial directions: $F_{esc,r} \sim k_r$ and $F_{esc,z} \sim k_z$. The latter is the downstream value, as the scattering force makes this the weakest point of the trap.

Although experimental measurements are typically performed with spheres, the concepts of escape force and trap strength are extensible to nonspherical objects. They represent derivatives of a trapping potential as a function of position of the centre of mass. In the Rayleigh theory, the contribution of the optical gradient interaction to this spatially-varying potential will resemble a convolution between the polarisability field (i.e. the shape of the object) and the optical intensity (the

shape of the beam). Thus the potential well has a width that is the sum of the beam width and the particle diameter. Similarly, ray tracing predicts that the particle remains in the trap up to $r \approx R_D$ in the transverse direction [10]. The additional angular degrees of freedom introduced by anisotropy are constrained by the axisymmetry of the beam in a similar fashion; for example a trapped thin rod will align along the beam.

2.2.2 Efficiency factor representation

The sum of optical gradient and scattering forces at each point in space may be described as an empirical fraction of the beam's total momentum flux $n_1 P/c$ by a dimensionless efficiency factor $\boldsymbol{Q}$ [11]. The motivation for this approach is that the escape force and trap strength scale proportionally with optical power, whilst the ratios $\boldsymbol{F}_{grad}/|\boldsymbol{F}_{beam}|$ and $\boldsymbol{F}_{scat}/|\boldsymbol{F}_{beam}|$ are invariant with applied power. Normalising the trapping efficiency with respect to power allows it to be compared between different cases with less ambiguity. If a beam cannot trap an object at moderate powers (~ 10 mW, where buoyancy is typically overcome), for example appearing to push the object away, then simply increasing the laser power will not provide an improvement, since $\boldsymbol{Q}$ does not change.

Where stable trapping exists, the escape force in a given direction, F_{esc}, is proportional to the efficiency factor's maximum value along a line from the equilibrium trapping point in that direction, Q_{max}.

$$\boldsymbol{Q}(R_D, m, NA, \lambda) \equiv \frac{\boldsymbol{F}_{grad} + \boldsymbol{F}_{scat}}{|\boldsymbol{F}_{beam}|} \tag{2.2.1h}$$

$$\boldsymbol{F}_{esc} = \frac{n_1 P \boldsymbol{Q}_{max}}{c} \tag{2.2.1i}$$

For diffraction-limited traps at high NA, the scattering force on low m particles is small relative to the gradient component, such that the scaling of Q_{max} approximately follows that of the gradient force. In the geometric limit, considering a summation over internally refracted rays allows $Q_{max} \approx 2(m-1)$ to be derived from the Fresnel coefficients [12]. Unlike the Rayleigh prediction of $Q_{max} \propto R_D^3$, the

geometric scaling is closer to $Q_{max} \propto 1/R_D$ [13].

Comparing these trends, one might expect that a maximum efficiency factor lies near $R_D \approx \lambda$, which is usually the case. At high m, the approximation breaks down; interference occurs between waves scattered from the front and rear interfaces of the object, causing modulations in trapping efficiency with particle size (see Figure 2.2). In water ($n_1 \approx 1.33$), trapping is most effective for particles in the colloidal to microscopic scales (between $R_D \sim 50$ nm - 50 μm) of index $n_2 = 1.4 - 1.7$.
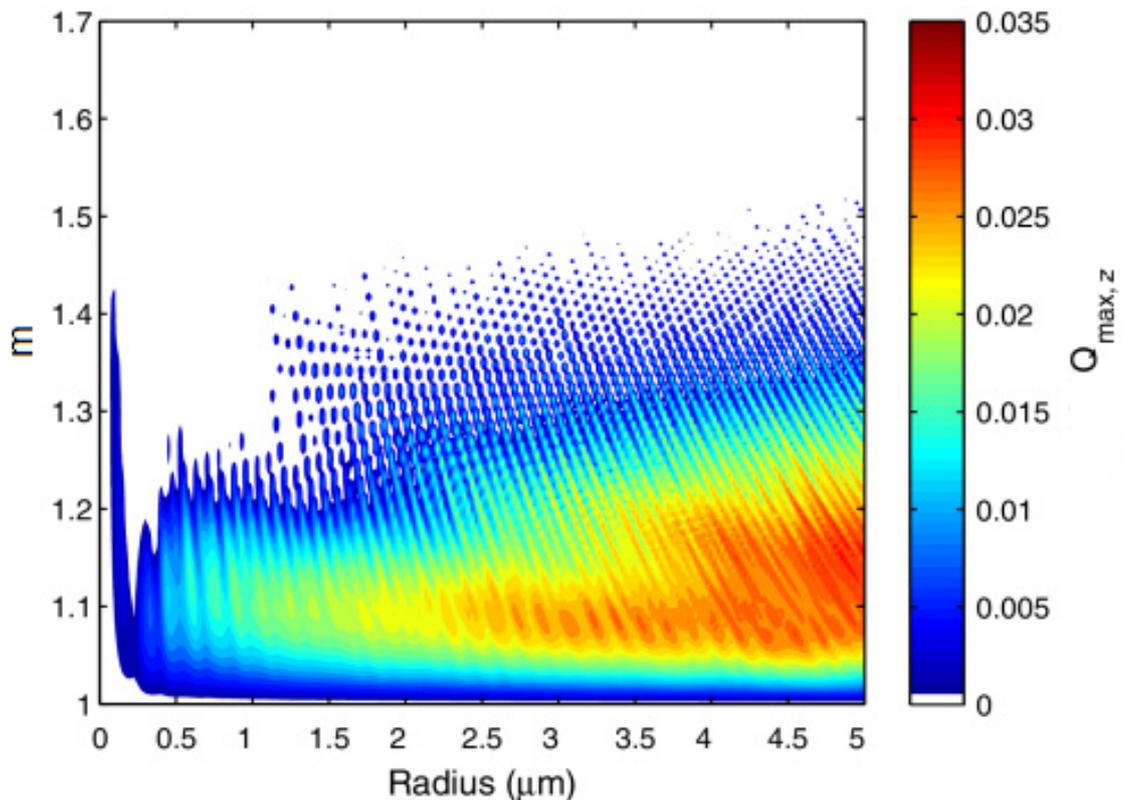
Figure 2.2: A relief map of axial trapping efficiency $Q_{max,z}$ as calculated by T-matrix theory against particle radius R_D and relative refractive index m, for the case of spherical particles in water $n_1 = 1.33$, with $\lambda = 532$ nm at $NA = 1.2$. At higher m, resonances appear and scattering dominates. Note that practical trapping will be impaired at high particle radius due to weight ($\propto R_D^3$) increasing more quickly than efficiency. Figure reproduced from [14], ©OSA.

For the relevant example of a heptane droplet ($n_2 \approx 1.38$) in water, the approximations given above yield an ideal trapping efficiency of $Q_{max,r} = 8\%$ or $F_{esc,r}/P$ = 0.3 pN/mW, which are comparable to experimentally obtained values; Woods et al. quote an estimate of 0.69 pN/mW [15].

Numerical schemes allow exact calculation of optical forces and thus $\boldsymbol{Q}$. These are rigorous for *arbitrary* input fields and particle shapes across all three size regimes, but require significant computational investment [16]. The quantities $F_{esc,r}$, $F_{esc,z}$ and k_r are more readily obtained by experiment and then normalised by an estimate of the power at the sample. Three approaches are detailed for calibrating the strength of an effective trap.

Escape force

The most intuitive method of calibration is to balance the force exerted on the trapped object against an external reference force. By moving the laser relative to the surrounding fluid using the microscope stage, the object is subject to a drag force which competes with the optical gradient force. For small displacements relative to the particle diameter, the trap is approximately harmonic and the trap strength can be estimated from the displacement:

$$k_x = \frac{\beta v_x}{\Delta x} \tag{2.2.1j}$$

However, the displacements are difficult to measure precisely as a result of optical resolution and Brownian motion. With increasing speed, the drag force dominates, such that above a critical speed the particle can no longer be trapped. Equating the drag and gradient forces at this critical escape speed v_{esc}, yields:

$$\mathbf{F_{esc}} = \beta\mathbf{v_{esc}} \tag{2.2.1k}$$

where β is the drag coefficient. If the trapped object passes within about $20R_D$ of a solid wall, it will be subject to additional drag not accounted for by Stokes' Law (see Equation (3.2.1b)). If this cannot be avoided, but the distance is a known constant (i.e. the surface normal is perpendicular to the direction of motion), then Faxen's

corrections can be used. The method can be used in the equatorial - and even the axial - directions, if the stage speed can be controlled and the observation cell is sufficiently large. Thus $F_{esc,r}$ and $F_{esc,z}$ can be found. The ratio $F_{esc,z}/F_{esc,r} \approx k_z/k_r$ is a valuable measure of the anisotropy of the trap; ideally, it has the diffraction-limited value NA/n, although typically it is much lower due to optical aberrations.

Equipartition and displacement variance

With the harmonic Hookean approximation $V = \frac{1}{2}k_r x^2$ and the equipartition theorem $E = \frac{1}{2}k_B T$ the trap strength can be expressed in terms of the variance in particle position along a chosen equatorial direction:

$$k_r = \frac{k_B T}{\langle x^2 \rangle} \tag{2.2.1l}$$

Thus the trap strength can be determined directly from traces of the particle centroid. The sampling interval must be of the order (and the trace duration must be far in excess) of the characteristic relaxation time $\tau_r = \beta/2k_r \approx 1$ ms. This is the shortest timespan over which the particle motion can be distinguished from that under free diffusion. As the integration time increases, a histogram of displacements tends to a normal distribution whose variance yields $\langle x^2 \rangle$, as shown in Figure 2.3. A related method uses the normally-distributed blur of the particle image over a known exposure time in excess of τ_r [17]. For weaker traps, the variance becomes large; the accuracy scales as $1/k_r$.

Power spectral analysis

Alternatively, a similar treatment can be performed but in frequency space. The Brownian noise spectrum of the particle is analysed, either from Köhler illumination or backscattered laser light [18]. The trap establishes a *corner frequency*:

$$\nu_r = \frac{1}{4\pi\tau_r} = \frac{k_r}{2\pi\beta} \approx 1 \text{ kHz}, \tag{2.2.1m}$$

below which the thermal fluctuations are suppressed and the power spectral density is flat instead of the usual diffusive $1/\nu^2$ dependence. Identifying this cutoff, analogous to the characteristic time, yields the trap strength as shown in Figure 2.4.
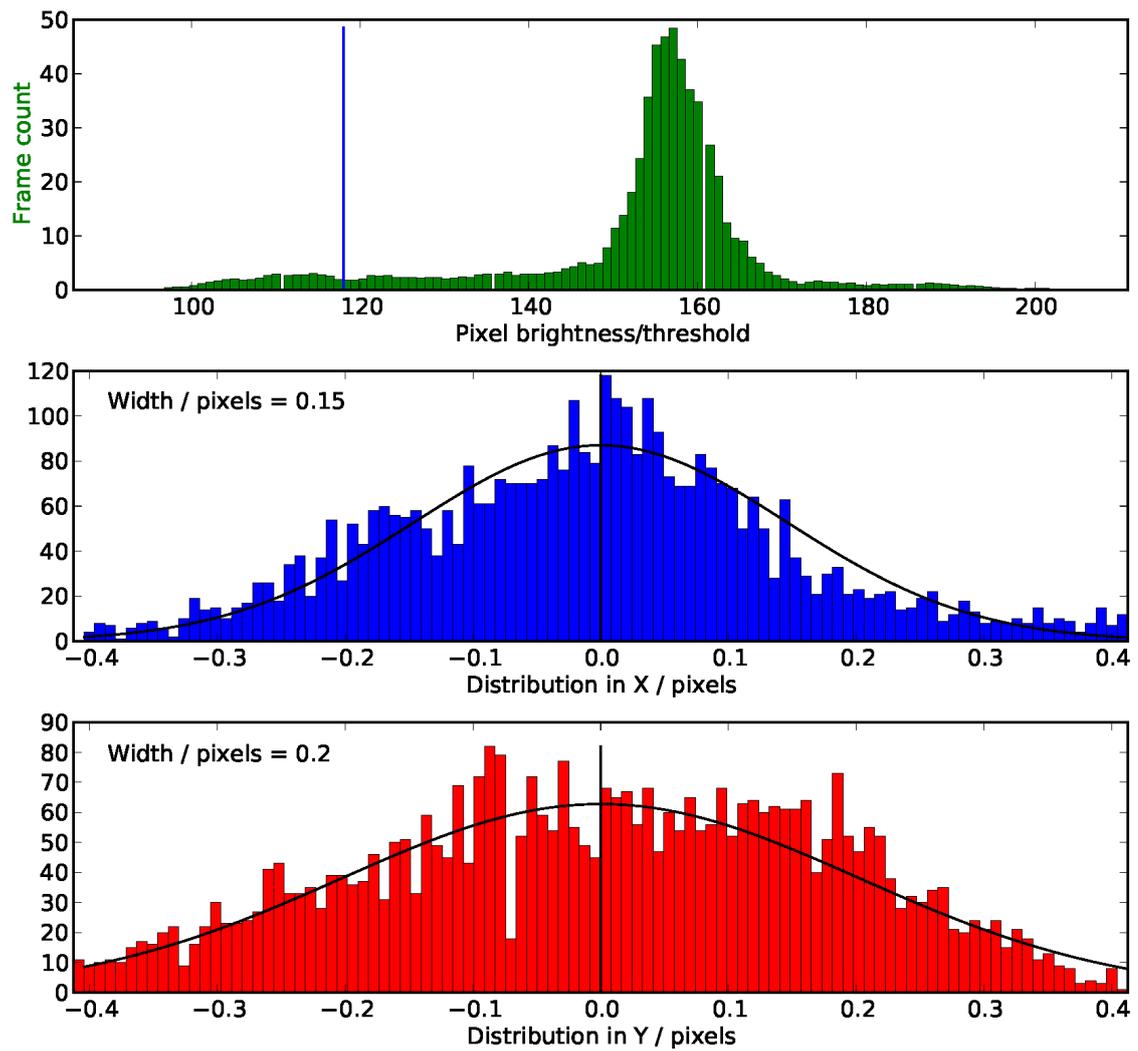
Figure 2.3: (*middle, bottom*) a pair of histograms recording orthogonal displacements of a polystyrene bead, $R_D = 2$ μm, in a single trap at 3 W source power in Setup C (see § 2.4.3). Similarity of the two indicates cylindrical symmetry of the trap; (*top*) a pixel brightness histogram for the video frames used to calculate the displacements, indicating an optimal binary threshold of 118/255 separating object and background pixels.
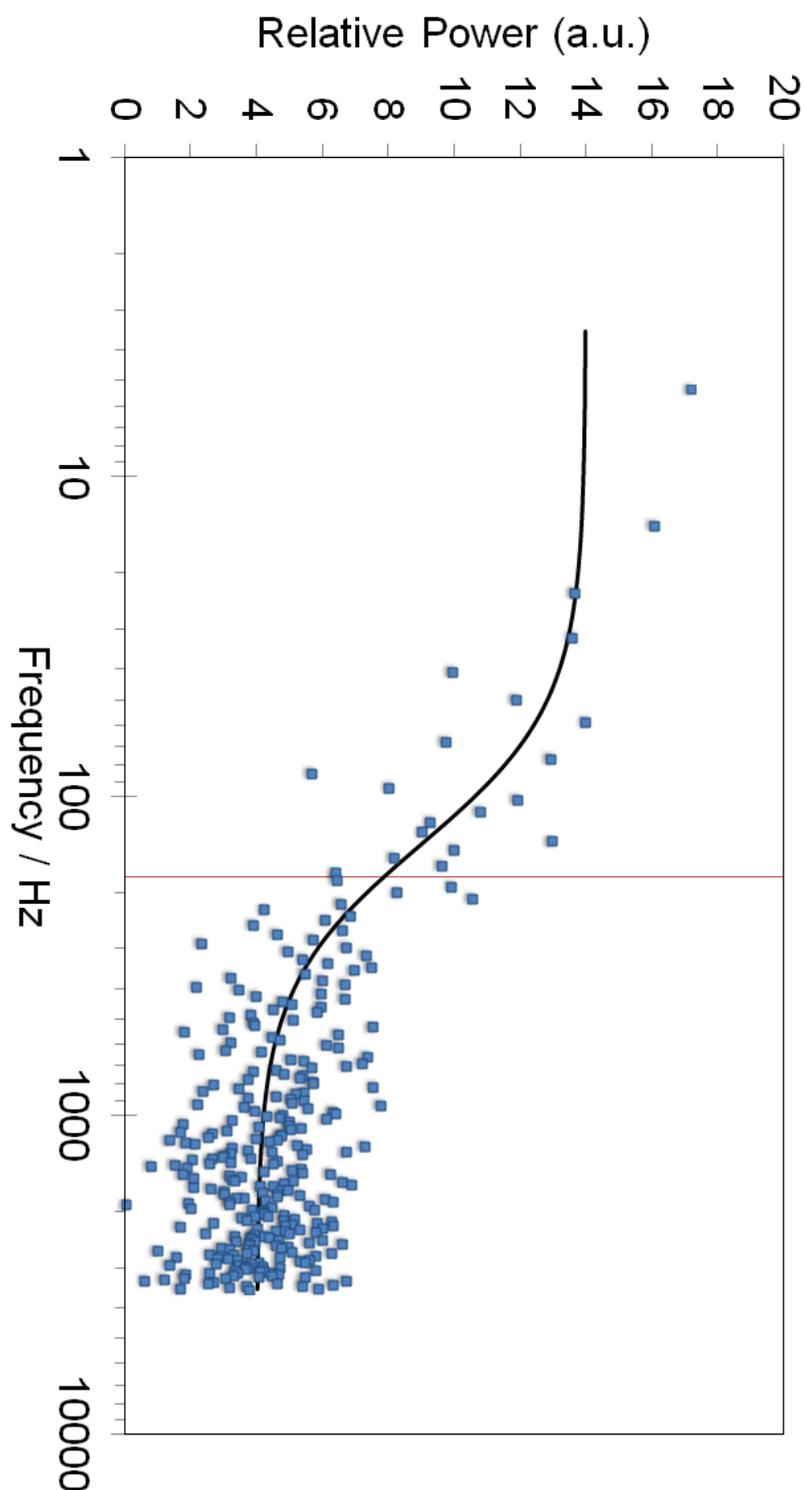
Figure 2.4: The power spectrum for displacements of a polystyrene bead, $R_D = 2$ μm, in a single trap at 3 W source power in Setup C (see § 2.4.3). A Lorentzian curve is fitted (black line), whose maximum slope yields the corner frequency (red line).
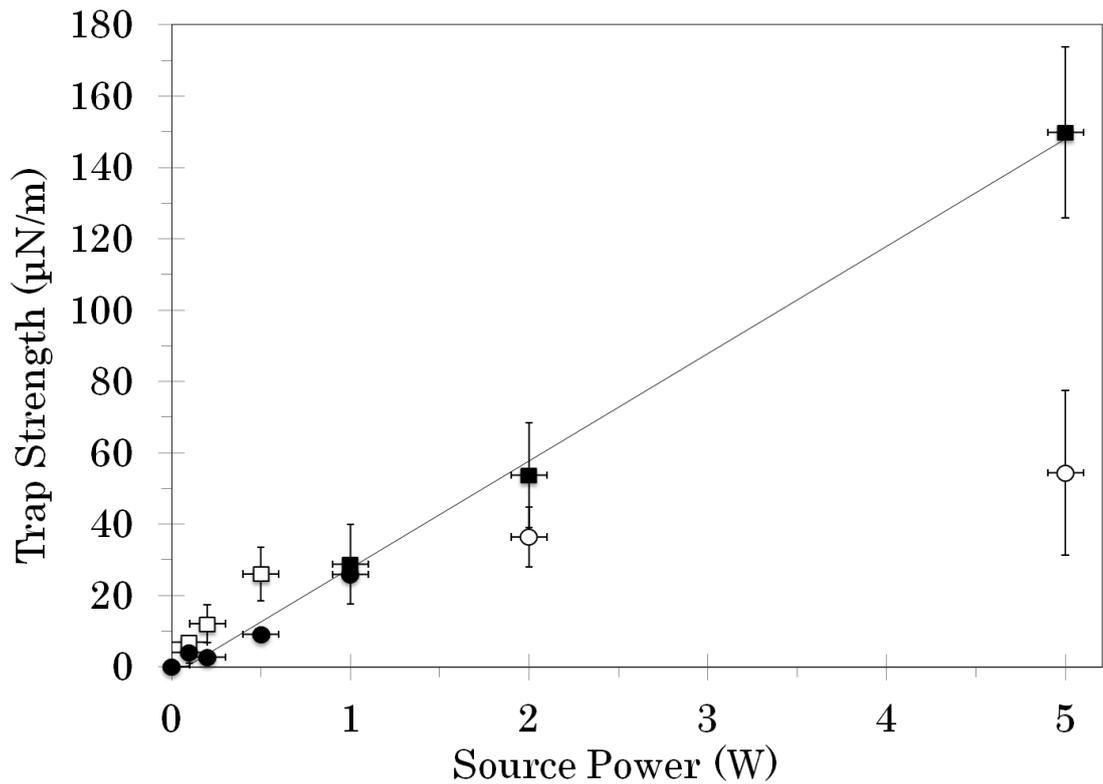
Figure 2.5: Trap strength measured as a function of laser power at source in Setup C (see § 2.4.3). Above a trap strength of 30 μN m^{-1}, power spectral method (squares) are accurate to the proportional relationship expected at constant Q_{max} (solid line, least-squares fit to all filled points, $R^2 = 0.997$), whilst below this trap strength, the equipartition method (circles) is preferred.

A detector of considerable frequency bandwidth is needed, such as a high-speed camera or quadrant photodiode. As data of fixed-time intervals congregate in the limit of high frequency, the accuracy of this method improves as k_r. Thus for stronger traps, the technique complements the variance method. In practice, each estimate is limited by motion blur or point-spread function, depending on the trap stiffness and the particular imaging technique. This complementarity is demonstrated in Figure 2.5, where the gradient is proportional to Q_{max} for polystyrene beads of $R_D = 2$ μm. Accounting for the source-to-object transmission coefficient of around 12%, the modified gradient of $k_r/P = 0.24$ μNm^{-1}mW^{-1} is of the expected order for this trap; for a Hookean trap approximation, this corresponds to

$F_{esc,r}/P = 0.5$ pN mW^{-1} which compares well with literature (§ 2.2.2).

2.3 Application of optical tweezers to fluid interfaces

The scenario in which a rigid, spherical particle is trapped in liquid continuum permits calibration of the imaging quality, trap aberrations and the magnitude of these trap forces [19]. However, this work is ultimately concerned with a 'soft' liquid droplet in place of a rigid particle, and thus a deformable liquid-liquid interface. For deformable fluids, the localised response is governed by a more general principle. The majority of the optical force acts along intensity gradients, such that material of high refractive index (oil) tends to displace that of lower index (water) from the regions of highest intensity.

During the last two decades, optical deformations of liquid-liquid interfaces have been explored in bulk [20–22] and in emulsion microdroplets [15, 23].

2.3.1 Prior deformations of planar liquid surfaces

The most systematic studies of optical deformation at ULIFT have been pursued with planar interfaces at low numerical aperture where the scattering forces are significant fraction of the total. For the free liquid surface, a comprehensive, quantitatively validated solution is known, [24] while for the liquid-liquid interface, an analytic solution is available for small deformations. The radiation pressure of a focused Gaussian beam, normally incident from a low-to-high refractive index (upwards from water to oil), produces a bell-shaped depression into the low index medium, whose width is similar to the beam waist [20].

If a downwards beam is used, the depression still occurs into the low-index medium; this is proof that the relevant momentum flux of the beam is the Minkowski,

rather than the Abraham, form [25]. At radiation pressures roughly four times the Laplace pressure, the concavity acts to totally-internally reflect and concentrate the beam. This bends the interface into a light-guiding jet of very high aspect ratio > 100, stabilised against the Rayleigh-Plateau breakup, which supports optically induced flow along the beam path.

In the bell-curve regime, the phenomenon can be used to measure the IFT between bulk phases. Trapped liquids benefit from fast thermal equilibration, but this effect decreases with larger length scales. Since vibrations and thermal lensing are problematic, efforts have been made to implement measurements of the surface gradient from its action as a tilted mirror [26]. Even for pure liquid tensions where the peak displacements are as small as 10 nm (gradient $\approx$ 1 mrad), this is a sensitive technique, with a large dynamic range. The interrogated interfacial spot, over which the signal is averaged, is of millimetre order in diameter.

2.3.2 Prior deformations of emulsion droplets

Woods *et al.* show how optical tweezing techniques can be used to deform individual emulsion droplets [15]. Optical tweezing is still an ideal tool in this case, since objects of similar dimensions to the wavelength of the light used (0.2-20 μm) can be subjected to trapping or distorting forces. For multiple point traps, the number of configurations is only limited by the minimum trapping power at each site, typically around 10 mW, and the spatial freedom of movement. This technique produces polygonal shapes and networks connected by nanometric threads. These threads are qualitatively different to the waveguided jets of Delville *et al.*; they do not require intrinsic support by optical forces, but result solely from interfacial properties. These experiments largely form the motivation and context for the practical work in this thesis, but will also be discussed alongside the theoretical results presented in Chapter 5.

2.4 Original constructions for trap generation and imaging

To extend particle deformation to non-axisymmetric shapes, more than one trap is required. Multiple traps with similar characteristics may be produced from splitting a single beam, but interference effects can cause adjacent traps to weaken one another. There are three strategies for avoiding interference, each with its own merits:

1. orthogonal polarisation of trap pairs,

2. timesharing so that the traps do not coincide, or

3. holographic modulation of the optical phase to allow the traps' coexistence in the object-plane intensity distribution.

Each option was implemented in turn. The former are simpler and more readily constructed, while the latter enable more precise control over a greater number of degrees of freedom.

2.4.1 Setup A: Dual polarisation tweezers

The *orthogonal polarisation* technique is limited to a maximum of two overlapping beams, but can be achieved using relatively simple optics [27]. The lack of lossy diffractive optic elements allows the sample to be exposed to very high trapping powers > 100 mW and therefore significant laser heating; this section is relevant to results in Chapter 4.

The optical set-up, shown in Figure 2.6, is based around a conventional upright microscope (*Leica* DM-LM), in conjunction with a 1064 nm TEM_{00} CW Nd:YAG laser, with 600 mW maximum power (*Forté, LaserQuantum*). The objective lens is an oil immersion model with NA=1.25, 100× (*Leica* 506072).
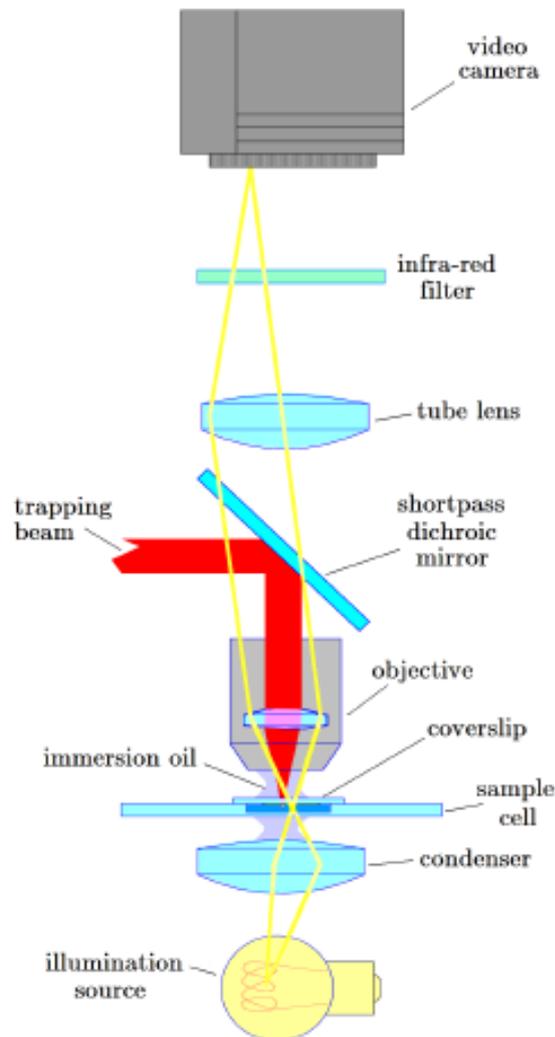
Figure 2.6: Schematic of the conjugated polarising beamsplitter array in Setup A, for the separation and recombination of the fixed and scanning coplanar traps. The latter is moved relative to the other trap by rotating the gimballed mirror.

All refractive trapping optics (except the objective and coverslips) are anti-reflection-coated for $\lambda = 1064$ nm. Optimal trapping results from slightly 'overfilling' the exit pupil D_{EP} at the back aperture of the objective; the beam is expanded using a simple Keplerian telescope, magnification f_2/f_1, such that $2w \sim 1.1 D_{EP}$. The planoconvex telescope lenses are placed with flat sides together to minimise field curvature aberrations.

Oil immersion lenses are designed such that spherical aberration at high NA is

compensated for. However, in aqueous media the indices do not match and this holds only at a very short distance ~ 20 μm from the coverslip, so traps become weak with depth [28]. This spreading of the focus can be mitigated by adding a controlled amount of spherical aberration of the opposite sense. The simplest way to do this is by readjustment of the beam expander length to change the angle of convergence (i.e. the effective tube length) at the objective back aperture. This also provides a compromise for chromatic aberration in the objective such that the imaging (visible) and trapping (NIR) focal planes coincide correctly.

An orthogonal polarisation split is achieved as follows (Figure 2.7). Firstly, the slightly elliptical polarisation output of the cavity is corrected to a vertical linear polarisation using a waveplate of thickness $\lambda/4$. The dual beams are created by passing the expanded beam through the first polarising beamsplitter and recombined with an identical second beamsplitter. This configuration bears some resemblance to the Mach-Zehnder interferometer [29]. However, one scanning beam is steered independently of the other, fixed beam using a 2" gimbal-mounted mirror.

A waveplate of thickness $\lambda/2$, placed before the splitting array, is used to rotate the linear polarisation direction to select the power ratio of the two resultant beams without significant loss. The extinction ratio is estimated as 1:20, which suffices for basic experiments where only one beam is desired; the remaining weak beam can be removed by blocking its unique path.
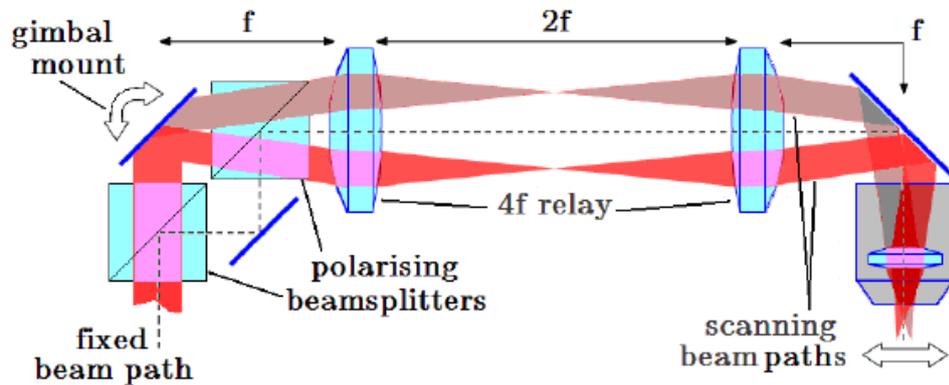
Figure 2.7: Profile diagram of the conjugated polarising beamsplitter array for the separation and recombination of the fixed and scanning beams in Setup A.

Without additional optics, the inter-trap displacement would be quickly limited by the scanning beam walking off the back of the objective. To ensure both beams enter the objective (albeit at different angles), a 4f lens relay was assembled so that the back of the objective and the centre of the gimbal were made conjugate. When the traps were positioned centrally, the beam quality could be refined by placing a spatial filter at the focus of the 4f relay. In order to reach the microscope, a periscope was required; for safety reasons this was capped by a beam block and the long sections of the beam path were enclosed by beam-tubes.

Brightfield illumination was used for all experiments, from a Xe white light source focused by an oil-immersion condenser lens, $NA = 1.1$ (*Leica*). The dichroic mirror (shortpass <900 nm) allowed the trapping laser to enter the sample but not the camera CCD (*Ximea*, `xiQ/MQ013MG-E2`) at 60 fps which is also screened by an IR filter.

Rudimentary temperature control was achieved by a objective collar coil (*Warner Instruments*), as calibrated with the melting points of waxy alkanes.

2.4.2 Setup B: AODs, z-refocusing tweezers and confocal imaging

This setup is relevant to Chapters 5 and 6.

The *timesharing* technique involves deflection of the beam across several locations much faster than the trapped objects can escape. Each trap location is disabled for a time no longer than the diffusion timescale. This timescale can be estimated based on the Stokes-Einstein equation [30]:

$$\tau < \frac{3\pi\eta R_D \Delta^2}{k_B T} \approx 0.5 \text{ ms}, \tag{2.4.1n}$$

where $\Delta \sim 0.2$ μm is the lateral microscope resolution. This technique also splits the available power between the trapping locations, whilst preventing interference between them.

The optical trapping on this kit was based on a 1064 nm laser (*Laser Quantum, Ventus*), steered by acousto-optical deflectors into a *Nikon* `EZ-C1` confocal microscope. The acousto-optical deflector (AOD) control software (*LabView*) enabled the timeshared production of triangular or rectangular groups of traps at 50 kHz, or > 10 kHz per cycle. The traps were confined to the same focal xy plane, but their separation was tuned in real-time. After focusing by the $NA = 1.2$, $63\times$ water-immersion objective (*Leica* `506279`), the maximum total power delivered to the sample was 40 mW. The brightfield CCD camera (*Sony* `XC-ST51CE`) gave a field-of-view of roughly 75 μm.

Scanning a 532 nm laser in epi-illumination at a power of 2 mW (source power 6 mW), with focus insufficient to affect trapping, across a field of view of 10 - 25 μm, fluorescence is excited in the oil-soluble dye, pyrromethene-597 (PM597), with peak emission at 580 nm. This emission was filtered and detected by photomultiplier tube with 120 - 160 dB gain.

Focal length (mm)		Spacing (mm)	
2:	100	1-2:	100
3:	100	2-3:	200
5:	Water NA 1.2	3-4:	90
6:	100	3-5:	90
7:	300	6-7:	400
8:	Water NA 1.2	7-8:	300
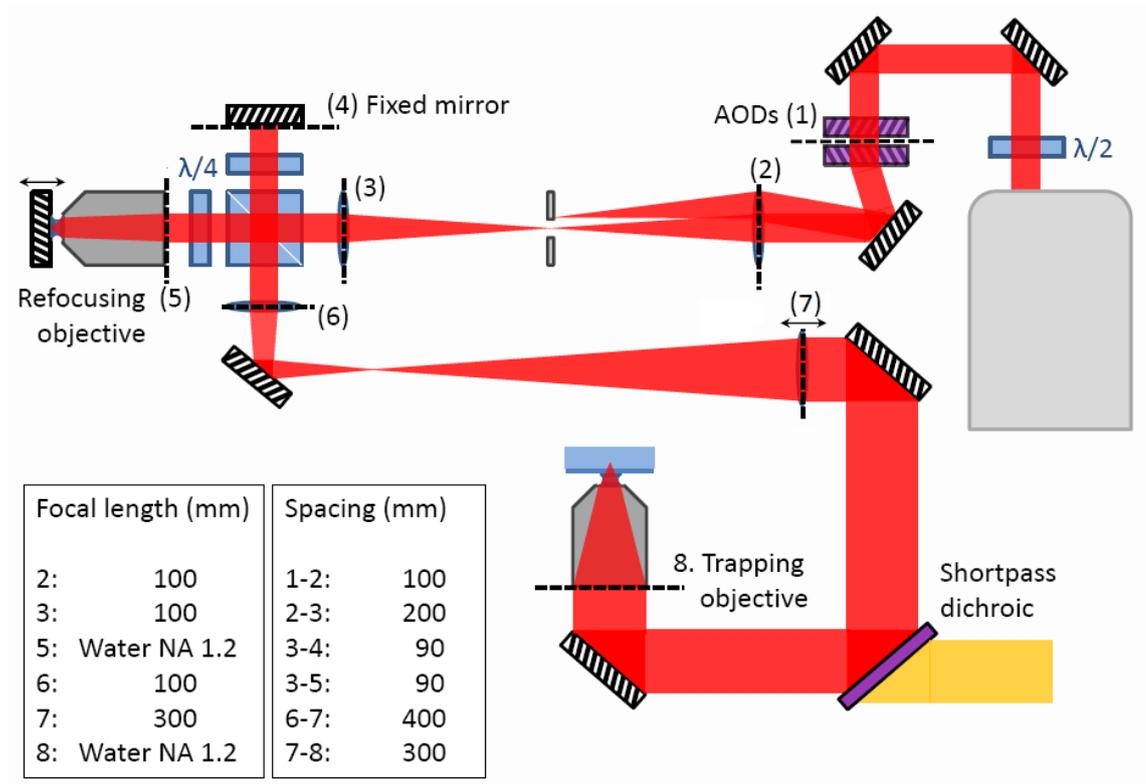
Figure 2.8: Schematic for optical generation of time-shared multiple traps with AODs. The traps are always coplanar at a depth fixed by the positions of the *Zaber*-translated telescope lens #7 and/or refocusing mirrors, but the x, y positions are controlled interactively.

In order to measure the droplet's 3D shape with the scan head of the inverted confocal microscope, the z-stack was built up from independent x, y frames at a rate of ~ 1 Hz between axial steps. The average of a small number of frames (10 unless otherwise specified) was recorded at each position to reduce the effects of noise and transient debris. The data, Cartesian volume arrays of fluorescent return, were saved as 16-bit, green-channel `.ids, .ics` pairs and animated cross-section `.avi` files. The post-processing of these involved volume-rendering and careful thresholding to yield each object's surface.

For a sample fixed relative to the stage (e.g. attached to a coverglass), each z-stepping sequence was automated using the *Nikon* control software. The objective

moved by a specified interval on the order of -0.2 μm/step (downwards from the top of the object). For trapped samples, the objective and therefore the confocal scan plane were kept fixed; instead the trapping plane was refocused to a different depth by translating a telescope lens (#7 in Figure 2.8) or the retropropagation mirror with a linear micrometer (*Zaber*). A typical object of 10 μm diameter required a scan time of $\leq$10 min. For full details see § 6.6.

2.4.3 Setup C: Holographic tweezers and structured illumination imaging

The third setup used holographic control to fully determine a 3D trapping array, with independent control of position and strength of each trap.

A custom-built inverted microscope was built with standard bench optomechanics (*ThorLabs*) with xy motorised stage (*Prior* `Proscan III`) and z-micrometer (*Zaber*). A high-performance water-immersion objective (*Zeiss*, `C-Apochromat x63 NA 1.2`) was chosen for its high numerical aperture, good transmission and aberration corrections over a wide wavelength range. Microfluidic observation chambers of 100 μm depth were used (§ 3.4.1), to which either the handshaken emulsions or microfluidic output could be introduced. The setup accommodated UV illumination (405 nm LED) for fluorescence imaging with the oil-soluble polyaromatic hydrocarbon dye, perylene (470 nm excitation maximum in heptane). Brightfield illumination was provided by a pseudo-collimated 450 nm LED. A 532 nm, 5 W, TEM$_{00}$ CW laser (*Laser Quantum* `Opus`) is used, interchangeably with a 1070 nm, 10 W, Yb-fibre laser (*IPG* `YLM-10-LP-SC`). This laser was collimated and expanded by telescope, linearly polarised and delivered to the reflective spatial light modulator (SLM). The diffractive output was demagnified $\times$ 1/2.2 to overfill the 5 mm rear aperture of the microscope objective via an edge dichroic beamsplitter (*RazorEdge, Semrock*). The 8-bit nematic liquid crystal SLM (model `X10468 LCOS-SLM`, *Hamamatsu*; see below) had a resolution of 800 $\times$ 600 with a pixel size of 20 μm, equivalent to (0.1 mrad) 0.3 μm (angular) resolution and maximum (angular) tilt of (30 mrad) 90 μm.
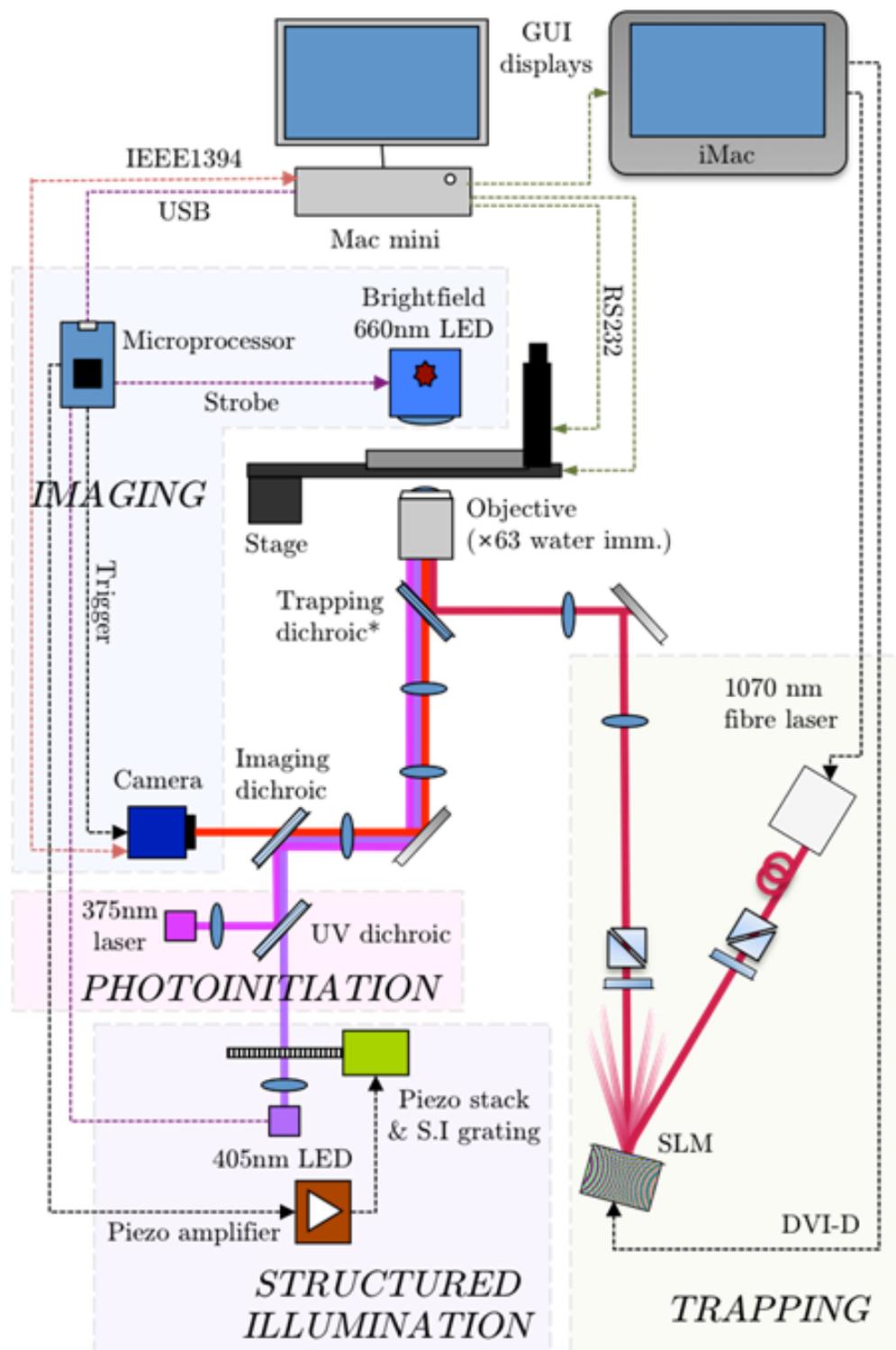
Figure 2.9: The platform referred to as Setup C, used for optical deformation of emulsion droplets at infrared wavelengths and fluorescent shape analysis with structured illumination sectioning. *The longpass dichroic mirror is redrawn here as shortpass for brevity.

Spatial light modulators

The most flexible procedure of creating optical traps uses interference to its advantage by generating a trap array holographically. This is done with an array of liquid crystal pixels called an SLM. Depending on the applied voltage, each pixel is able to induce a phase shift, ideally of at least 2π, in the locally reflected wave and/or reduce its amplitude. As the light reaches the focal plane, it interferes with other rays from the SLM in a well-defined way to create the desired intensity field. The modifications are encoded in the 2D phase pattern or *kinoform* displayed on the SLM. Only the intensity distribution in the focal plane is relevant to the trapping. The redundancy of the phase distribution at the traps allows phase-only control at the SLM, which is preferred here since the total power is conserved.

Fourier holograms

Since the SLM operates in a doubly-conjugate position to the focal plane, the 'far field' Fourier approximation applies. The intensity pattern is essentially a convolution of the input beam intensity profile on the SLM and the Fourier transform of the hologram. The Fourier transform can be related to the *classical aberrations* added to the beam phase distribution by the diffractive optic element.

- **Piston**: A constant phase shift across the array has no interference effect within a particular beam, but different beams from the same kinoform can be made to interfere constructively or destructively when overlaid in position.

- **Tilt**: A sawtooth wave kinoform gives a constant phase gradient, which causes the affected beam to be displaced by an amount proportional to the wave's frequency. The SLM acts as a diffraction grating and as such generates a series of diffraction orders. The 1st order beam is used for trapping, so a fixed minimum tilt has to be added to displace this from the brighter 0th order beam that is unaffected by the hologram.

- **Defocus**: A parabolic phase profile causes the beam focus to be displaced in the same way as a thin Fresnel lens.

Holographic phase terms corresponding to aberrations of higher order such as astigmatism, coma and spherical aberration can also be imposed in an adaptive optics sense, using the orthonormal basis of Zernike polynomials.

Diffraction efficiency

The advantage of using a ferroelectric liquid crystal (FLC) SLM is that switching is exceptionally fast; frame rates of 25 kHz are achievable [31]. This speed enables timesharing of traps by cycling the display between holograms dedicated to each individual trap. This rotation occurs on a timescale far shorter than any detectable diffusion of the object (as for the AODs in § 2.4.2). However, the FLC SLM is restricted to switching between binary $\{0,\pi\}$ states in each pixel. The 1-bit kinoform is composed of discrete π phase steps, so the diffraction grating has an added triangular wave component relative to the ideal slope. The triangular Fourier series includes higher order odd harmonics, decaying as $1/n^2$. The grating is also symmetric and thus there is ambiguity between positive and negative diffractive orders. The diffractive power efficiency of the 1st order beam is therefore severely reduced; the theoretical maximum is $(2/\pi)^4 \approx 16\%$ of the incoming beam.

Timesharing was attempted using an FLC SLM (`SXGA-R3`, *Forth Dimension*). The diffraction efficiency was less than 6% in practice, partly due to the unit's optimisation for visible wavelengths rather than the NIR.

For a nematic liquid crystal (NLC), the switching is arbitrary, and so an 8-bit SLM is able to produce smooth phase gradients in a blazed grating. As a result, the theoretical diffraction efficiency approaches $1/2$. In practice, this is around 30%. The number of array pixels sets the maximum tilt that can be obtained; in this limit the blazing reduces to a square wave and thus the diffraction efficiency falls off steeply at the edges of travel. The main limitation of the NLC SLM is that refreshing the display is slow, at only video rates of 60 Hz. Though tweezing for a single, continuous trap locus is maintained, interrupting the trap is not feasible for deformation as it is slower than the viscous relaxation time $\tau = \eta R_D/\sigma \approx 1$ ms.

Algorithms

While the NLC SLM cannot support deformation under discontinuous positioning for one trap, it is possible to display holograms that simultaneously generate multiple traps. The Fourier hologram enables the 3D position and phase of a given trap to be specified. However, neither simple linear addition (phase retardation), nor complex addition (superposition) of these phase holograms results in a direct combination of the intensity distributions. Despite the linearity of the subsequent Fourier convolution, linearity of the hologram itself is not preserved since the optical phase is a 2π-modular function. Instead, superposition is an underdetermined problem where the total intensity is poorly controlled. In trap configurations of high symmetry it can give rise to undesirable 'ghost' traps.

An alternative method is to produce each trap independently with different areas of the SLM. The random mixing algorithm displays an independent Fourier hologram for each of the desired traps over a randomly distributed subset of SLM pixels. This is a straightforward, fast calculation scaling only as the number of traps, M. Ghost traps are avoided, since the optical amplitude is coupled independently from each pixel to the corresponding trap location (Figure 2.10). Conversely, the optical *power* in each trap is proportional to the *square* of the area fraction dedicated to it, and is controlled as such. Unlike timesharing, the total power shared between the traps is not conserved. The algorithm quickly becomes inefficient as the total decreases as $1/M$. The remainder of the optical power $(1 - 1/M)$ is scattered uniformly into the volume of all possible traps by the random mask pattern. The device pixellation acts as a soft low pass filter for the hologram, which exacerbates how traps degrade towards the edges of view.

Furthermore, the traps are generated simultaneously and are subject to optical interference when they overlap one another. If the traps cannot act independently, positioning them to stretch the interface is no longer intuitive. Randomising the relative phases of traps was not observed to improve the trapping stability of closely spaced trap pairs. Fortunately, the droplets are much larger than the traps' focal

volumes and deformation is essentially unaffected.

Given its ease of implementation and well-defined intensity distribution, and despite its poor scaling of trap power, the random-mixing algorithm is used herein for a large majority of the SLM work. In practice, the scope of this project is largely fulfilled with four simultaneous traps. A sophisticated graphical user interface (GUI) was written in `wxpython` from which traps overlaid on the droplet images could be controlled in real-time with click-and-drag commands.

Arbitrary kinoforms

Thus far, the 2D intensity pattern has been selected in a chosen z-plane whose normal lies in the direction of propagation. The degrees of freedom afforded by an SLM allow an arbitrary 2D pattern limited only by array size, pixel size and microscope resolution. However, finding such a hologram is an underdetermined problem and is not necessarily a unique solution for the chosen slice. There may be a range of 3D intensity distributions that satisfy the Maxwell-Helmholtz equations while including the constrained plane.

The identity properties of the Gaussian beam under Fourier transformation make it especially suitable for generating diffraction-limited point traps. In turn, these behave well in 3D, as a diffraction limited spot can only be produced by rays focused at high NA, giving a suitably steep axial intensity gradient.

For more diffuse 2D distributions, it is likely that a majority of 3D solutions will not be conducive to axial trapping at the intended sites. Iterative algorithms including the adaptive-additive and direct search schemes allow numerical convergence to a specified 3D distribution. In the Gerchberg-Saxton algorithm, this distribution can be specified *a priori* without measurement feedback, though requires substantial computational investment and is susceptible to divergence. Deformation in real-time requires moving the traps and therefore updating the hologram displayed at a similar rate.
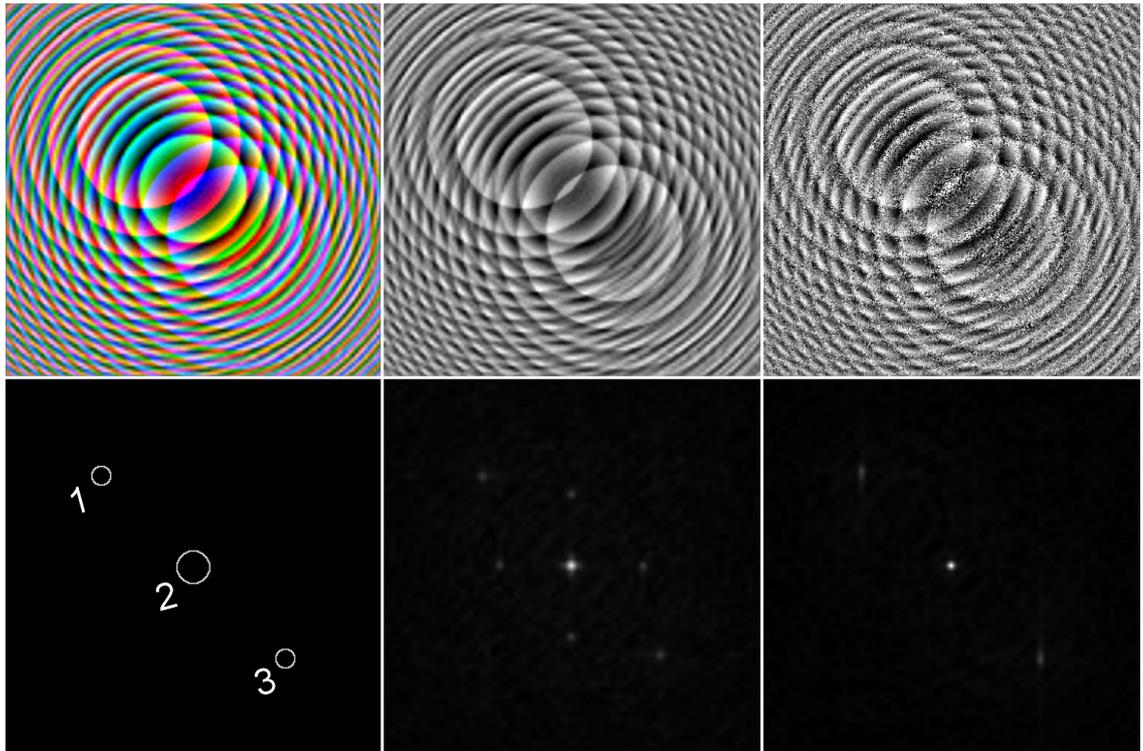
Figure 2.10: Holograms corresponding to three traps displaced in 3D. (*left*) Three-colour RGB image with each colour channel representing the Fourier hologram for each trap separately (R, top left; G, centre; B, bottom right). The concentric rings correspond to the Fresnel zones; (*left, below*) The intended position of the three beams tilted and defocused to different depths; (*centre*) complex superposition of the three component traps; (*centre, below*) the corresponding simulated focal intensity pattern, in which off-diagonal ghost traps are visible; (*right*) random mixing, with an equal SLM partition for each of the three component traps; (*right, below*) the random mixing intensity pattern is 1/3 weaker, but the unwanted traps are absent.

Non-iterative, open-loop techniques exist to generate specific families of 3D intensity distributions; of particular future interest are the wireframe traps of Rodrigo et al. [32]. Thus, interactive HOTs in real-time remains an active area of research [33–35] for which Padgett provides a useful review [36, 37]. In some cases, the parallel architecture of graphic processing units (GPUs) has accelerated HOT calculations [38]. The use of pre-calculated hologram videos was also considered for

specific deformation functions. In this work (§ 6.1.2), Gerchberg-Saxton algorithm-based holograms are used to produce regular tetrahedral arrays of point traps.

Adaptive optics and image processing for calibration

The SLM is 'flattened' in diffractive terms by applying a calibrated phase image as a background for the useful kinoform. A phase calibration was obtained by a Monte Carlo direct-search algorithm as follows. A bead was trapped using a known single Fourier hologram, and its rms displacement was minimised pixel-by-pixel starting from the factory-tested SLM image. The Fourier hologram was then subtracted. Fitting a Gaussian histogram to the same displacement data also calibrated the trap strength by the equipartition theorem. Brightfield imaging with a small region of interest (10 μm) was found to be adequate. The centroiding method was preferred to the power spectral method, as the upper frequency was limited by the camera frame rate of 400 Hz.

For speedy hologram calculation, the optimised calibration image was compressed using a truncated rectangular Legendre basis to match the SLM dimensions. Using Zernike polynomials modified for a rectangular aperture[1] would reveal the aberrations introduced by the laser delivery optics. However, this step is unnecessary as the calibration cancels them implicitly.

Structured illumination imaging

The output of a 405 nm, 1 W LED (ThorLabs) is collimated and immediately passes through the structured illumination mask, joins the imaging train via a dichroic and is relayed into the object plane via matched achromats ($f = 35$ mm) and the objective. The masking is implemented with a high-opacity Ronchi transmission grating

---

[1]This basis is used in unpublished work regarding how aberrations propagate through optical systems with varying aperture.

(chrome on glass, Applied Image) at 50 μm/lp. This corresponds to a spatial frequency in the focal plane of $f = 1.3$ μm^{-1}, chosen such that (for 3 frames per slice, introduced at $> 4f$) artefacts fall above the modulation transfer function (MTF) cutoff of 5.1 μm^{-1} and lose all contrast. In practice, the MTF of the system is confirmed as diffraction-limited by Fourier transforming the spatial derivative of a brightfield-imaged grating edge. This particular choice of grating allows the contrast to remain relatively high, ~ 0.6, whilst yielding a theoretical sectioning response near the optimal FWHM of ~ 0.4 μm. Using a second piezoactuator (*Zaber*) one of the achromats is moved relative to the other to obtain images at axial step sizes of > 0.2 μm and automate a SIM acquisition sequence over a 10 μm range. The CCD camera (*AVT Pike*) is used with a typical frame rate of 120 Hz, leading to sequence duration $\sim$2 s. Coding in Python allows RS232, IEEE1394, FireWire, USB and video control of each function to be de-centralised across an arbitrary computer network.

Trapping must allow objects to be held strongly enough so that they are effectively static over the course of a structured imaging routine. If detectable motion were periodic for some reason, such as vibrational or rotational motion, then strobing the illumination would be an acceptable solution. However, weakly held or untrapped objects will instead blur images under stochastic diffusive motion. This leads to the appearance of random transverse discontinuities and significant uncertainty in the sampled interval. By equipartition, the minimum trap strength to preserve diffraction limited imaging at 4σ performance (i.e. discontinuity-free over 100 routines of 50 sections each) is:

$$k > \frac{16k_B T}{(\lambda/2NA)^2} \sim 10^{-6} \text{ Nm}^{-1} \tag{2.4.1o}$$

which is easily achieved. This can be an underestimate in practical microfluidics (Chapter 3) where external influences such as hydrodynamic fluctuations increase the probability of the maximum displacement becoming detectably large. Notably, a shorter SIM duration t_{SIM} truncates sampling of the displacement distribution. If such a drift in continuous fluid velocity averaged over this time is represented as $\dot{\nu}$,

a more realistic requirement is:

$$k > \frac{\beta \dot{\nu} t_{SIM}}{\lambda/2NA} \sim 10^{-5} \text{ Nm}^{-1} \tag{2.4.1p}$$

This is largely limited by the camera frame rate and the ability to avoid pressure gradients, particularly from syringe motion and elasticity in walls and piping.

2.4.4 Setup C+: An integrated design for photo-polymerisation of deformed droplets

In this section, an integrated, optimised platform for future apparatus is proposed, as first presented in Figure 2.11, [39]. A trapping wavelength of 532 nm would allow timesharing with an FLC SLM, or optical landscaping with a nematic SLM. The optical photothermal absorption of both H_2O and D_2O are negligible at this wavelength (spectroscopists refer to the 'water window'), thus easing the problem of incidental heating across the PIT as strongly determined the results in this project. For non-fluorescent objects, the high power, high NA focal volume would be useful for Raman spectroscopy at speeds of 1-100 Hz. For example, one might follow a photopolymerisation reaction in a deformed droplet. The combination of *Raman tweezers* at 532 nm is a proven technique for organic microparticles [40].

The high numerical aperture optics required for the former enhance the signal from the latter, whilst Raman detection has little impact on the optics or methodology of tweezing. Using Raman tweezers removes the need for a separate laser and its unwanted additional radiation pressure. Also, a single longitudinal mode laser is unnecessary, since a suitable laser bandwidth is an order less than the typical spectral linewidth, typically ~ 100 GHz. In this scheme, the Raman signal and gradient forces are coupled through the input intensity distribution, such that a minimum trapping power is required for sufficient spectral output. Much like the stability issue with SIM, as long as this minimum power falls below that required to trap the object of interest, then Raman spectroscopy can be performed without hindrance. By the same token, structuring the Raman probe is clearly not an option when trapping, so instead a more subtle confocality is established with the spectrometer's

spatial filter.

Waveband (nm)	Function	Major components
375	Photoinitiation of monomer oil	UV laser
405	Fl. excitation with SIM masking	UV LED; grating; achromats
440-490	Fluorescent emission	Perylene fluorophore
470	Brightfield illumination	Blue LED
532 (or 1070)	Trapping beam	Green (NIR) laser; SLM
>532	Backscattered Raman signal	Spectrograph; pinhole; CCD

Table 2.1: Spectral divisions for Setup C+, an integrated Raman tweezing apparatus for polymerisable droplets.

In this framework (Table 2.1), it is possible to perform brightfield imaging and Raman spectroscopy simultaneously on trapped, deformed and polymerised microdroplets. On the other hand, fluorescence is often described as anathema to Raman microscopy due to the higher fluorescent scattering cross-sections. In samples doped with fluorophore it is likely that it will overwhelm the Raman signal even at wavelengths distant from peak emission.
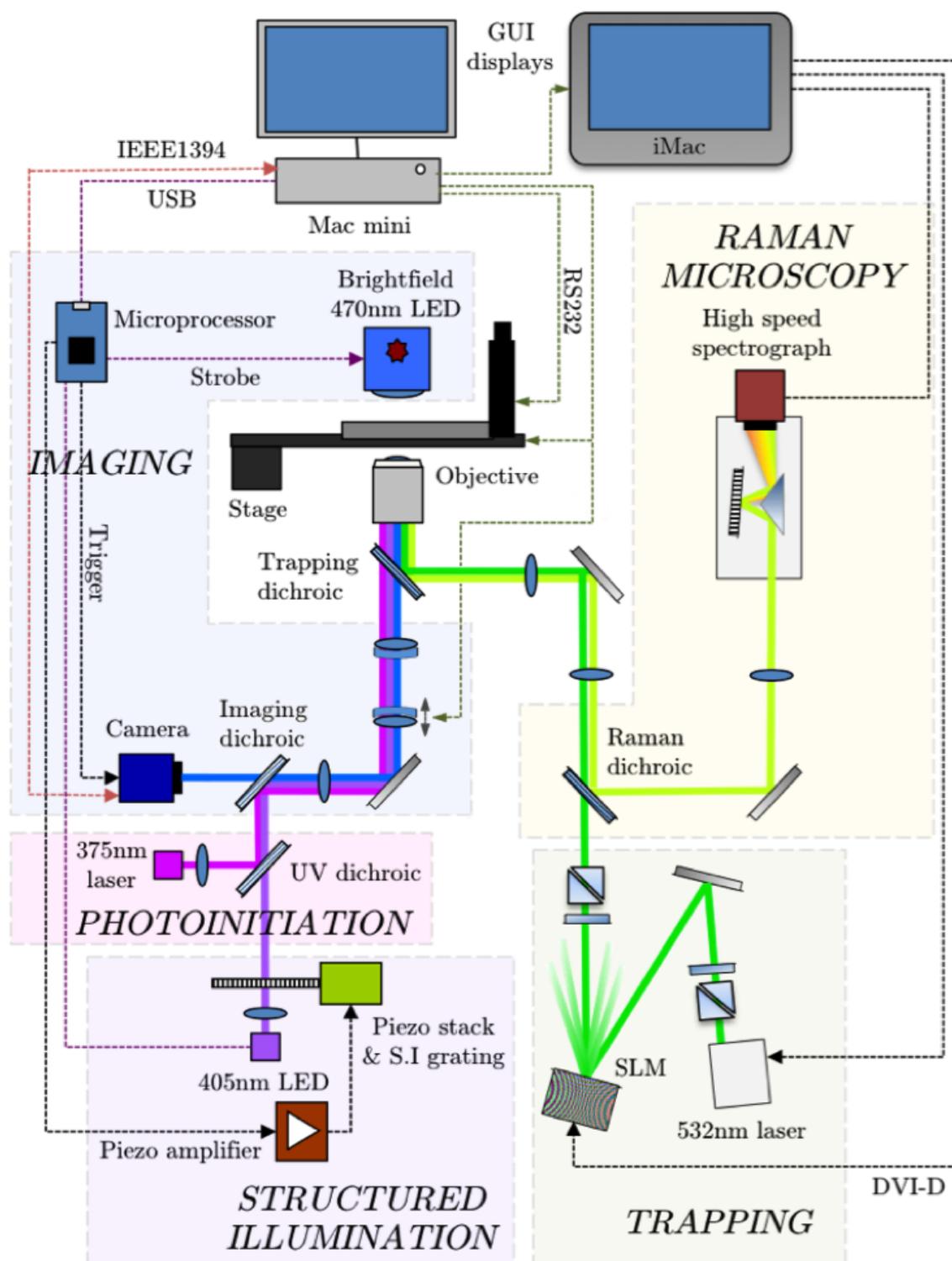
Figure 2.11: A modified Setup C+ proposed for optical deformation of emulsion droplets and for Raman photopolymerisation or fluorescent shape analysis.

Glossary

Symbol	Definition	Unit
AOD	Acousto-optical deflector	
c	Speed of light in vacuum	m s^{-1}
CCD	Charge-coupled device, camera	
CW	Continuous wave (laser)	
D_{EP}	Exit pupil diameter	m
f_1, f_2	Lens focal length	m
F_{esc}	Escape force from trap	N
$\mathbf{F}_{grad}$	Optical gradient force	N
$\mathbf{F}_{scat}$	Optical scattering force	N
FLC/NLC	Ferroelectric/nematic liquid crystal	
FWHM	Full-width-half-maximum of distribution	
GPU	Graphics processing unit	
GUI	Graphical user interface	
$\hbar$	Reduced Planck's constant	N s m^{-1}
HOTs	Holographic optical tweezers	
I	Optical intensity	W m^{-2}
$\mathbf{k}, k_{r,z}$	Optical trapping strength	N m^{-1}
LED	Light-emitting diode	
MTF	Modulation transfer function	
N	Number of photons	-
NA	Numerical aperture	-
NIR	Near-infrared	
$n, \Delta n$	Refractive index, contrast	-
m	Refractive index ratio, object/medium	-
P	Optical power	W
$\mathbf{p}_{A,M}$	Linear momentum (Abraham, Minkowski)	N s
r	Coordinate perpendicular to beam axis	m
R_D	Droplet radius (spherical)	m
RGB	Red-green-blue image	
SIM	Structured illumination microscopy	

SLM	Spatial light modulator	
Q	Trapping efficiency factor	-
UV	Ultraviolet	
v_{esc}	Escape velocity from trap	m s^{-1}
Δx	Displacement	m
z	Coordinate along beam axis	m
z_R	Rayleigh range of Gaussian beam	m
t	Time	s
β	Drag coefficient	N s m^{-1}
2D/3D	Two/three-dimensional	
λ	Optical wavelength	m
τ	Viscous relaxation time	s
θ	Angle of propagation	rad
ω_0	Beam waist	m

References

[1] A. Ashkin, "Acceleration and trapping of particles by radiation pressure", *Phys. Rev. Lett.* Vol. 24, no. 4, p. 156, 1970.

[2] A. Ashkin, J. M. Dziedzic, and T. Yamane, "Optical trapping and manipulation of single cells using infrared laser beams", *Nature*, vol. 330, no. 6150, 769–771, 1987.

[3] S. M. Barnett, "Resolution of the Abraham-Minkowski dilemma", *Phys. Rev. Lett.* Vol. 104, p. 070 401, 7 2010.

[4] J. M. Taylor, *Optical Binding Phenomena: Observations and Mechanisms*. University of Durham, UK: Springer Theses, 2011, ISBN: 9783642211942.

[5] A. Callegari, M. Mijalkov, A. G. Burak, and G. Volpe, "Computational toolbox for optical tweezers in geometrical optics", *J. Opt. Soc. Am. B*, vol. 32, no. 5, B11–B19, 2015.

[6] S. Chu, J. E. Bjorkholm, A. Ashkin, and A. Cable, "Experimental observation of optically trapped atoms", *Phys. Rev. Lett.* Vol. 57, pp. 314–317, 3 1986.

[7] A. Ashkin, "Forces of a single-beam gradient laser trap on a dielectric sphere in the ray optics regime", *Biophys. J.* Vol. 61, no. 2, 569–582, 1992.

[8] M. P. MacDonald, L. Paterson, K. Volke-Sepulveda, J. Arlt, W. Sibbett, and K. Dholakia, "Creation and manipulation of three-dimensional optically trapped structures", *Science*, vol. 296, no. 5570, pp. 1101–1103, 2002.

[9] W. S. C. Chang, *Principles of Lasers and Optics.* Cambridge University Press, 2005, Cambridge Books Online, ISBN: 9780511755712.

[10] N. Malagnino, G. Pesce, A. Sasso, and E. Arimondo, "Measurements of trapping efficiency and stiffness in optical tweezers", *Opt. Commun.* Vol. 214, no. 1-6, pp. 15–24, 2002, ISSN: 0030-4018.

[11] A. Rohrbach and E. H. K. Stelzer, "Trapping forces, force constants, and potential depths for dielectric spheres in the presence of spherical aberrations", *Appl. Opt.* Vol. 41, no. 13, pp. 2494–2507, 2002.

[12] D. J. Stevenson, F. Gunn-Moore, and K. Dholakia, "Light forces the pace: optical manipulation for biophotonics", *J. Biomed. Opt.* Vol. 15, no. 4, pp. 041 503–041 503, 2010.

[13] T. Nieminen, V. Loke, A. Stilgoe, G. Knoener, A. Branczyk, N. Heckenberg, and H. Rubinsztein-Dunlop, "Optical tweezers computational toolbox", *J. Opt. A: Pure Appl. Opt.* Vol. 9, no. 8, S196, 2007.

[14] D. Burnham and D. McGloin, "Modeling of optical traps for aerosols", *J. Opt. Soc. Am. B*, vol. 28, no. 12, pp. 2856–2864, 2011.

[15] D. A. Woods, C. D. Mellor, J. M. Taylor, C. D. Bain, and A. D. Ward, "Nanofluidic networks created and controlled by light", *Soft Matter*, vol. 7, pp. 2517–2520, 6 2011.

[16] D. Bonessi, K. Bonin, and T. Walker, "Optical forces on particles of arbitrary shape and size", *J. Opt. A: Pure and Applied Optics*, vol. 9, no. 8, S228, 2007.

[17] T. Lindballe, M. Kristensen, A. Kylling, D. Palima, J. Glueckstad, S. Keiding, and H. Stapelfeldt, "Three-dimensional imaging and force characterization of multiple trapped particles in low NA counterpropagating optical traps", *J. Eur. Opt. Soc.* Vol. 6, 2011, ISSN: 1990-2573.

[18] J. Huisstede, K. van der Werf, M. Bennink, and V. Subramaniam, "Force detection in optical tweezers using backscattered light", *Opt. Express*, vol. 13, no. 4, pp. 1113–1123, 2005.

[19] K. Berg-Sørensen and H. Flyvbjerg, "Power spectrum analysis for optical tweezers", *Rev. Sci. Instrum.* Vol. 75, no. 3, pp. 594–612, 2004.

[20] A. Casner and J.-P. Delville, "Giant deformations of a liquid-liquid interface induced by the optical radiation pressure", *Phys. Rev. Lett.* Vol. 87, p. 054 503, 5 2001.

[21] J. Delville, M. R. de Saint Vincent, R. Schroll, H. Chraibi, B. Issenmann, R. Wunenburger, D. Lasseux, W. W. Zhang, and E. Brasselet, "Laser microfluidics: fluid actuation by light", *J. Opt. A: Pure Appl. Opt.* Vol. 11, no. 3, p. 034 015, 2009.

[22] A. A. Verhoeff, F. A. Lavergne, D. Bartolo, D. G. A. L. Aarts, and R. P. A. Dullens, "Optical trapping of interfaces at ultra-low interfacial tension", *Soft Matter*, vol. 11, pp. 3100–3104, 16 2015.

[23] A. D. Ward, M. G. Berry, C. D. Mellor, and C. D. Bain, "Optical sculpture: controlled deformation of emulsion droplets with ultralow interfacial tensions using optical tweezers", *Chem. Commun.* Pp. 4515–4517, 43 2006.

[24] R. Wunenburger, B. Issenmann, E. Brasselet, C. Loussert, V. Hourtane, and J.-P. Delville, "Fluid flows driven by light scattering", *J. Fluid Mech.* Vol. 666, pp. 273–307, 2011, ISSN: 1469-7645.

[25] L. Zhang, W. She, N. Peng, and U. Leonhardt, "Experimental evidence for Abraham pressure of light", *New J. Phys.* Vol. 17, no. 5, p. 053 035, 2015.

[26] K. Sakai, D. Mizuno, and K. Takagi, "Measurement of liquid surface properties by laser-induced surface deformation spectroscopy", *Phys. Rev. E*, vol. 63, no. 4, 2, pages, 2001.

[27] K. Visscher, S. Gross, and S. M. Block, "Construction of multiple-beam optical traps with nanometer-resolution position sensing", *IEEE J. Sel. Top. Quantum Electron.* Vol. 2, no. 4, pp. 1066–1076, 1996.

[28] S. N. S. Reihani, M. A. Charsooghi, H. R. Khalesifard, and R. Golestanian, "Efficient in-depth trapping with an oil-immersion objective lens", *Opt. Lett.* Vol. 31, no. 6, 766–768, 2006.

[29] E. Fällman and O. Axner, "Design for fully steerable dual-trap optical tweezers", *Appl. Opt.* Vol. 36, no. 10, pp. 2107–2113, 1997.

[30] C. C. Miller, "The Stokes-Einstein law for diffusion in solution", *Proc. Royal Soc. A*, vol. 106, no. 740, pp. 724–749, 1924.

[31] G. Love and R. Bhandari, "Optical properties of a QHQ ferroelectric liquid crystal phase modulator", *Opt. Commun.* Vol. 110, no. 5-6, pp. 475–478, 1994, ISSN: 0030-4018.

[32] J. Rodrigo, T. Alieva, E. Abramochkin, and I. Castro, "Shaping of light beams along curves in three dimensions", *Opt. Express*, vol. 21, no. 18, pp. 20 544–20 555, 2013.

[33] G. C. Spalding, J. Courtial, and R. Di Leonardo, "Chapter 6 - Holographic Optical Tweezers", in *Structured Light and Its Applications*, D. Andrews, Ed., Burlington: Academic Press, 2008, pp. 139–168, ISBN: 978-0-12-374027-4.

[34] D. McGloin, "Optical tweezers: 20 years on", *Philos. Trans. R. Soc. London, Ser. A*, vol. 364, no. 1849, pp. 3521–3537, 2006, ISSN: 1364-503X.

[35] D. Grier and Y. Roichman, "Holographic optical trapping", *Appl. Opt.* Vol. 45, no. 5, pp. 880–887, 2006.

[36] M. Lee and M. Padgett, "Optical tweezers: a light touch", *J. Microsc.* Vol. 248, no. 3, pp. 219–222, 2012, ISSN: 1365-2818.

[37] M. Persson, D. Engstrom, and M. Goksor, "Real-time generation of fully optimized holograms for optical trapping applications", *Proc. SPIE*, vol. 8097, pages, 2011.

[38] R. Bowman, G. Gibson, A. Linnenberger, D. Phillips, J. Grieve, D. Carberry, S. Serati, M. Miles, and M. Padgett, "'Red Tweezers': fast, customisable hologram generation for optical tweezers", *Comput. Phys. Commun.* Vol. 185, no. 1, pp. 268–273, 2014, ISSN: 0010-4655.

[39] A. L. Hargreaves, A. K. Kirby, C. D. Bain, G. D. Love, G. Bolognesi, O. Ces, M. Neil, and A. D. Ward, "An optical platform for the production, trapping, manipulation and visualization of ultra-low interfacial tension emulsion droplets", *Proc. SPIE*, vol. 8810, 88101W–13, 2013.

[40] K. Ajito and K. Torimitsu, "Near-infrared Raman spectroscopy of single particles", *TrAC, Trends Anal. Chem.* Vol. 20, no. 5, pp. 255–262, 2001, ISSN: 0165-9936.

Chapter 3

Generation and Phenomenology of Emulsion Droplets

3.1 Premise

The thesis statement prompts many questions: which droplets? How small, how many? What kind of vessel does one hold a microdroplet in to deform it? How long do they 'last' for? What's different in making a ULIFT droplet?

In this chapter, oil-in-water droplets between 2 and 12 μm diameter are made so that they can be manipulated optically in isolation for periods of order 10 min, within a thin, transparent chamber. The droplets need not be identical, but the less polydisperse the emulsion, the more reproducible the initial conditions are for subsequent trapping experiments. A particular strength of microfluidic methods is that they generate emulsions of low polydispersity; yet the size distribution must be preserved in spite of the mechanical fragility of ULIFT droplets.

Whilst a protocol was developed for microfluidic production, a much simpler method was used to create droplets in different ULIFT systems.

3.2   Hand-shaken emulsions

3.2.1   Droplet size and stability

Under ULIFT conditions, the energy input required to mix oil and water is lowered by many orders of magnitude. Simply adding a small amount of oil to the required aqueous phase and agitating by hand causes the oil to atomise into a dilute, highly polydisperse emulsion. These are 'hand-shaken' emulsions.

Shearing an emulsion in a turbulent manner produces a droplet size distribution that is approximately log-normal [1]. This rule-of-thumb arises since for a fixed dispersed volume, larger droplets are far fewer in number and thus collide less frequently, such that the rate ratio of coalescence to splitting events scales inversely with droplet size. The deformation experiment benefits, since there are relatively few droplets smaller than the most common size. Smaller droplets are undesirable as they diffuse quickly and adhere to the trapped droplet, obscuring its shape and perturbing its behaviour in the trap.

Considering the critical capillary number (§ 1.1.1) in turbulent Newtonian shear flow, dimensional analysis gives a scaling expression for the modal droplet radius $\langle R_D \rangle$ [2],

$$\langle R_D \rangle \approx \frac{\sigma_{OW}}{\sqrt{(\rho_W + \rho_O)\eta_W f^3 L}} \approx 1 - 100 \ \mu\text{m}, \qquad (3.2.1\text{a})$$

depending on the amplitude L and frequency f of agitation, the interfacial tension, σ_{OW}, and the specific density ρ_W and viscosity η_W of the continuous water phase [3]. The dependence on the bulk properties of the dispersed phase, ρ_O, η_O, is weak since they are of the same order as the continuous phase, whose volume fraction is significant.

After agitation ceases, the droplets experience a low Reynolds number (§ 1.1.1). The oil droplets will cream at a rate dictated by their buoyancy and dispersion size. This rate can be estimated under the assumptions that the droplets are spherical,

separated widely relative to their size and have uniform surface tension under shear. Equating Stokes expression for the drag with Basset's slip correction [4] to the buoyancy force yields an upper limit for the terminal velocity:

$$F_{drag} = F_{buoy} \tag{3.2.1b}$$

$$\beta v_{cream} = \frac{4\pi R_D^3}{3}(\rho_W - \rho_O)g, \text{ where } \beta = \left(\frac{1 + 2\eta_O/\eta_W}{1 + 3\eta_O/\eta_W}\right) 6\pi\eta_W R_D \tag{3.2.1c}$$

$$v_{cream} \approx \frac{2(\rho_W - \rho_O)gR_D^2}{9\eta_W} \approx 1 \ \mu\text{m s}^{-1} \tag{3.2.1d}$$

where g is the acceleration due to gravity. The drag coefficient β depends on the viscosities $\eta_{O,M}$ of object and medium due to tangential shear at the interface, so is effectively the familiar $\beta = 6\pi\eta_W R_D$ for a solid bead but reduces to around 70% of this value for spherical droplets of heptane or decane in water. Such a micron-sized drop in a typical Gaussian trap (with 10 mW optical power) is subject to piconewton trapping forces (see Chapter 2). It therefore has an escape velocity of:

$$F_{drag} = F_{trap} \tag{3.2.1e}$$

$$v_{escape} = \frac{F_{trap}}{\beta} > \frac{50 \ \mu\text{m s}^{-1}}{R_D(\mu\text{m})} \tag{3.2.1f}$$

Comparing the two, conventional optical tweezers are easily able to capture micron-sized droplets, as found at the smaller end of the range produced by manual agitation.

Next, the droplets have the potential to change in size whilst they are handled. Ostwald ripening is a diffusive net motion of monomer oil to larger droplets driven by IFT and facilitated by the aqueous solubility of the oil (molar fraction $x_\infty \sim 10^{-8}$). The rate of disproportionation in droplet size can be expressed as [5]:

$$\frac{d\langle R_D \rangle}{dt} = \frac{8\sigma x_\infty V_O^2 D_O}{27k_B T V_W \langle R_D \rangle^2} \sim 0.01 - 1 \ \mu\text{m h}^{-1} \times \sigma(\text{mN m}^{-1}) \tag{3.2.1g}$$

where D_O is the diffusion rate of oil monomers in water, V_i are molecular volumes,

and $k_B T$ is the Boltzmann thermal energy. This rate is negligibly low for any microscopic oil droplet in a ULIFT scenario. It would take months for Ostwald ripening to alter the size distribution noticeably.

However, coalescence of droplets is strongly favoured at the extremes of ULIFT (§ 1.6.3). It can be mitigated by immobilising droplets onto a surface, or for droplets intended for optical trapping, simply by dilution.[1]

3.2.2 Chamber geometry and wettability

A 2 mm-deep manipulation chamber allows an experimental window of up to an hour before the emulsion decays through creaming. Freely dispersed droplets can be captured using optical tweezers. In this case, coalescence is postponed by dilution.

On the other hand, in a thin coverslip-spaced cell of 200 μm depth, coalescence is avoided by allowing droplets to settle on the coverslip within minutes. Provided that a higher dilution is used to account for the depth of the cell, the droplets form an incomplete monolayer. They are then pinned and unlikely to coalesce. However, for deformation experiments, they must be pulled from the coverslip using optical tweezers. This strategy is feasible only if the glass is sufficiently hydrophilic such that it is not wet by the oil.

Glass coverslips and slides - used to construct passive observation chambers - were cleaned and hydrophilised using piranha solution (§ 1.5.1). Even following this treatment, the mean contact angle of sessile droplets of aqueous AOT solution in air on glass remained at $\theta_{AWG} = 25 \pm 5°$, though compared well with literature [6, 7]. Use of Young's equation [8] allows these values to be related the contact angle of a oil droplet on glass submerged in this solution, θ_{WOG}:

---

[1]Some unexpected effects of dilution on the compositional stability of the oil droplet are discussed in § 3.6.

$$\cos\left(\theta_{WOG}\right) = \frac{\sigma_{AO}(1 + S_{AOG}) - \sigma_{AW}\cos\left(\theta_{AWG}\right)}{\sigma_{OW}} \tag{3.2.1h}$$

where $S_{AOG} \approx +0.1$ is the spreading coefficient of oil on glass in air. At ULIFT (i.e. $\sigma_{OW} \ll \sigma_{AO}, \sigma_{AW}$), the denominator is small and the contact angle diverges such that the submerged oil droplet either wets or non-wets completely, depending on the aqueous affinity for the glass. A sufficient condition for droplet non-wetting is therefore:

$$\theta_{AWG} < \arccos\left(\frac{\sigma_{AO}}{\sigma_{AW}(1 + S_{AOG})}\right) \approx 30°, \tag{3.2.1i}$$

which is marginally satisfied. In practice, dynamic wetting on the glass surface is observed as a function of emulsion age and temperature. Whilst new samples are almost exclusively non-wetting, older emulsion samples are more likely to wet irreversibly. This effect is poorly reproducible and is most likely due to cumulative adsorption of hydrophobic contaminants on the glass surface; the incidence reduces after NaOH treatment. In isolation, neither temperature nor salinity appear to affect the disposition of droplets to wet the coverslip, though passing through a phase inversion temperature (PIT) can induce wetting.

3.3 Microfluidics

3.3.1 Concepts and design

Manual shaking cannot produce a monodisperse emulsion; neither the distribution - nor the environment - of the droplets are well-controlled. Sufficiently monodisperse droplets can be created directly, without thorough sorting, by membrane emulsification [9], in which droplets are typically separated from the porous membrane using a synchronised actuator. Although many droplets can be created simultaneously, the major drawbacks of this approach are that the detachment threshold and pore size cannot be continuously adjusted *in situ*.

By contrast, serial microfluidics presents an efficient and rapid method for producing *specific* microdroplets. The fluids are confined to channels between 10-100 μm

diameter and pumped by automated syringes. In a well-designed system, the apparatus becomes portable, very small amounts of fluid are required and the products are highly reproducible. The channels are fabricated through photolithography (typically in polydimethylsiloxane resin, PDMS [10]) or by etching (glass [11]). Although the generation is serial, the supported bulk flow rates are several μL min^{-1}, yielding droplets at rates of 1 - 50 kHz. The droplet sizes are adjustable *in situ* with the flow-rate ratios.

3.3.2   Flow focusing junction (FFJ)

A flow-focusing junction is a cross-shaped intersection of channels used to shear droplets from a microfluidic flow [12].

In the design used here (Figure 3.1), two input channels for the continuous phase lie at right angles to the main flow axis, whilst the input channel for the discontinuous phase opposes the output channel. The combination of relative flow rates, capillary number and rheological properties dictate the fluid dynamics and the resulting emulsion. Finding the conditions associated with producing a desired emulsion is therefore another multi-parameter optimisation procedure, for which there is no general predictive theory. However, flow at these length scales is almost exclusively laminar [13] due to a low Reynolds number. The simplest metric for mapping the parameters to the flow regime is the capillary number; a rule of thumb is that formation of droplets occurs below a critical capillary number of unity.

For conventional IFT, the flow velocity, v, can be decreased to match this condition; at ULIFT, the critical capillary number is normally exceeded:

$$Ca = \frac{\eta_W v}{\sigma_{OW}} \approx 1 \tag{3.3.1j}$$

$$\Rightarrow \sigma_{OW}^C = \frac{Q\eta_W}{\pi R_A^2} \approx 0.1 \text{ mN m}^{-1} \tag{3.3.1k}$$

where R_A is the aperture size of the junction and $Q = Q_O + Q_W$ are the volumetric flow rates. Breakup into individual droplets is inhibited by Marangoni flow, which becomes stronger at ULIFT since the differences between dynamic and equilibrium

IFTs are greater. The presence of an IFT *higher* than σ^C is necessary for droplet detachment instead of tipstreaming [14] into a long cylinder.

Two-step procedures are available to sidestep these difficulties by producing droplets at high IFT and only then introducing the required conditions for ULIFT. This would normally require the addition of a component or change in environmental conditions. In these systems, the input surfactant concentration can be lowered and the total flow rate increased such that a higher dynamic IFT persists over the detachment timescale, as demonstrated in [15]. Under these conditions the surfactant cannot complete its adsorption to the newly-created interface - lowering its IFT- until after the surface has already pinched off under a combined effect of viscous shear and the Rayleigh-Plateau instability. The resulting droplets eventually relax to an equilibrium IFT that is ultralow.

In the high-shear end of the 'dripping' regime,[16] the droplets are marginally smaller than the aperture size R_A. For trappable droplets, an aperture size in the range 5-15 μm is required. The droplet size scales as [15, 17]:

$$\frac{R_D}{R_A} \propto \left(1 + \frac{Q_O}{Q_W}\right)\left(\frac{R_A^2 \sigma}{Q_W \eta_W}\right)^{1/3}, \tag{3.3.1l}$$

so decreases weakly with higher flow rate of the continuous phase.
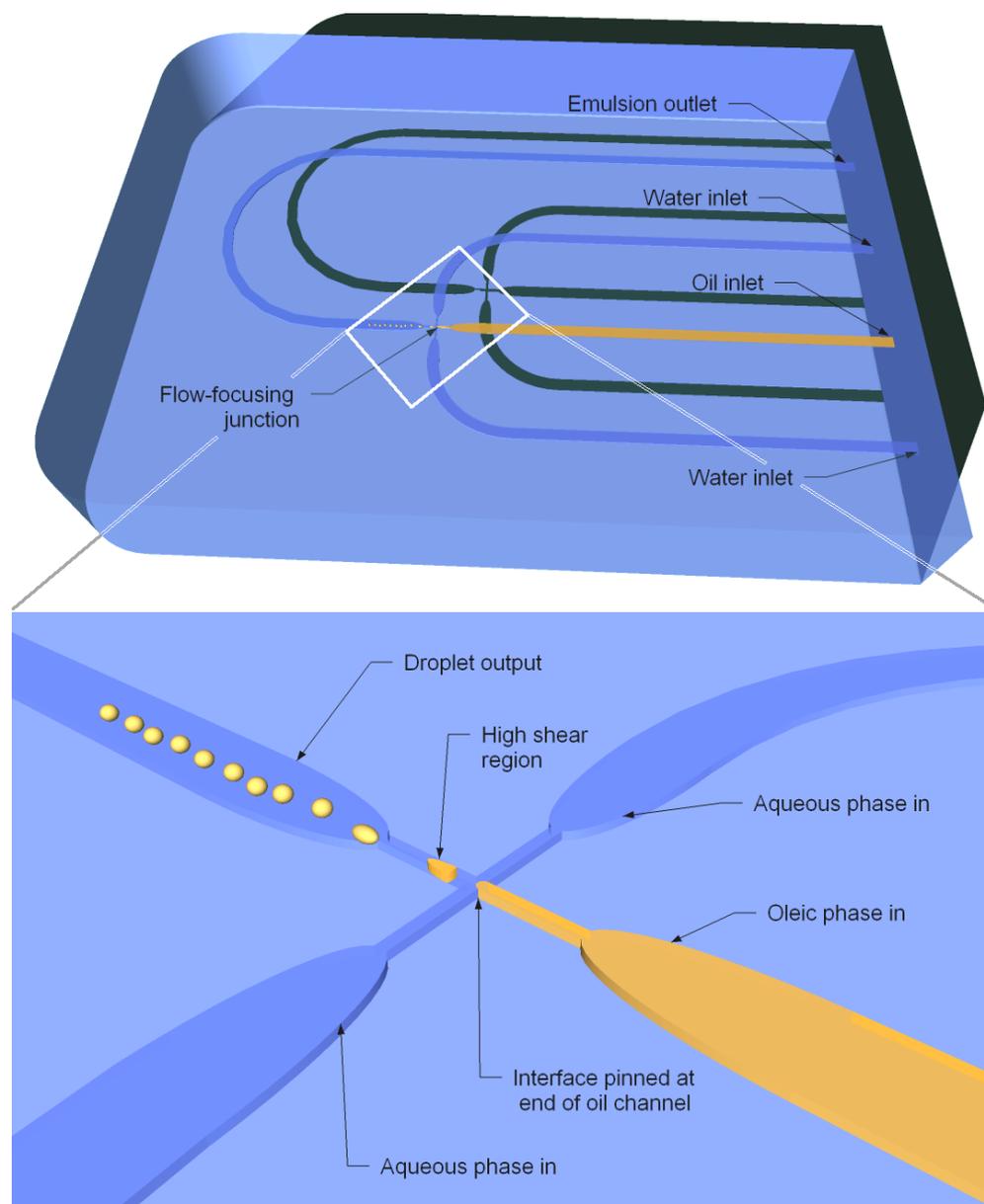
Figure 3.1: Schematic of the *Dolomite* chip (*top*) and the channels comprising the FFJ within (*top, inset; below*), of order 10 μm in diameter. The flow of the water-rich continuous phase is split evenly between the side channels. These act to shear droplets from the slower, oil-rich phase into a flowing emulsion.

3.4   Materials and methods

The glass FFJs used herein (*Dolomite Microfluidics*) are composed of four channels, each 135 μm in length. Each chip is supplied by 500 μm width inlet and outlet channels coupled to tubing. This fluorinated ethylene-propylene (FEP) tubing was used across all limbs of the microfluidic network, of 250 μm internal diameter unless otherwise stated.

In the standard chip size (`3200146`), the cross-junction is $R_A^2 = 14$ μm $\times$ 17 μm; in the smaller size (`3200152`) it is $R_A^2 = 5$ μm $\times$ 8 μm. Hereafter these are referred to as 14 μm and 5 μm FFJs respectively.

A resistance thermometer (`PT100A`) and a 10 W Peltier cell (*Ferrotec*, `9508/023/030 B`) were attached to the bottom and top external walls of the chip, respectively. The Peltier cell was driven by a proportional-integral-derivative (PID) control unit (*Omega*, `CN32PT-220`). The Peltier cell includes a through aperture of 5 mm diameter to enable optical access. The heated FFJ setup was mounted in a custom miniaturised microscope setup to follow the generation performance *in situ* in brightfield. This mini-microscope was constructed from: standard 1" *ThorLabs* components including pseudo-collimated LED (`M660L3`) illumination at 660 nm and a 150 mm Galilean telescope supported by 30 mm cage framework; a 20$\times$, NA 0.4 dry objective lens (*Leica*, `506076`); and a scientific CCD camera (*Imaging Source*, `DMK 23F618`, 640 $\times$ 480 px, 120 fps).
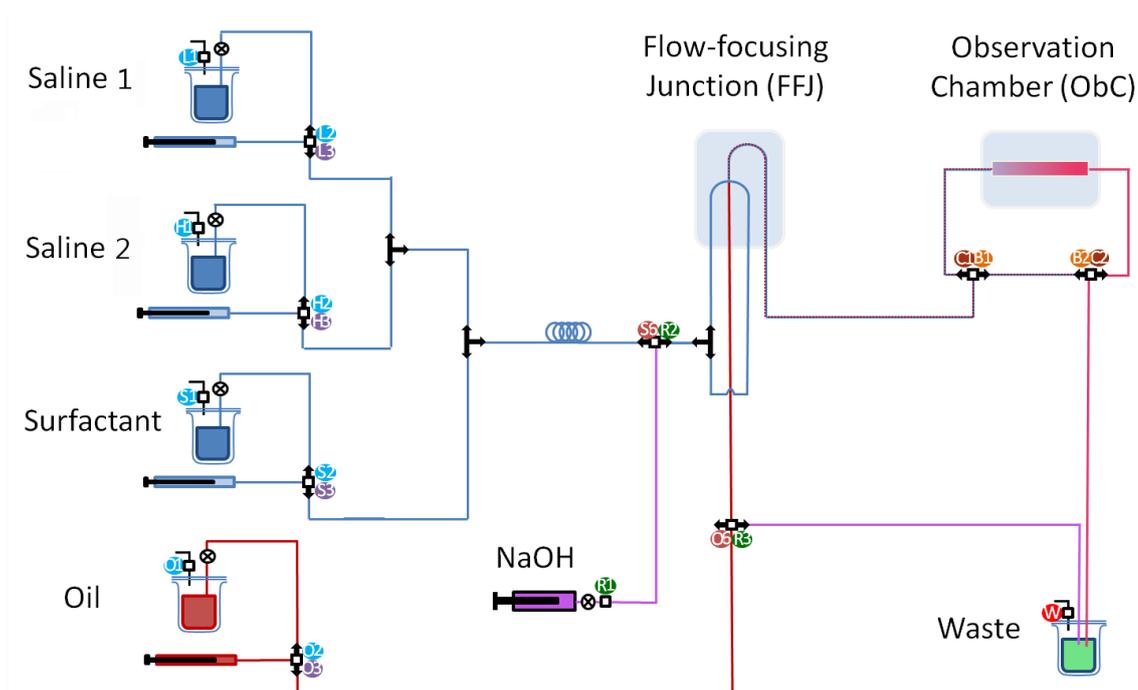
Figure 3.2: A simplified schematic of the four-syringe automated system is shown including the switch groups (coloured circles).

3.4.1 Observation Chamber (ObC)

An exploded view of the microfluidic ObC is shown in Figure 3.3. As these chips are thin, they are easily coupled to the brightfield illumination and imaging/trapping objective in an optical sense. Access to the upper side renders them responsive to Peltier heating with the same precision PID control as the FFJ, in spite of the thermal load of the objective on the underside. The PID response parameters are optimised using an in-built simplex algorithm to give stable working ObC and FFJ temperatures to $\pm$ 0.2 K within 10 min after selection.
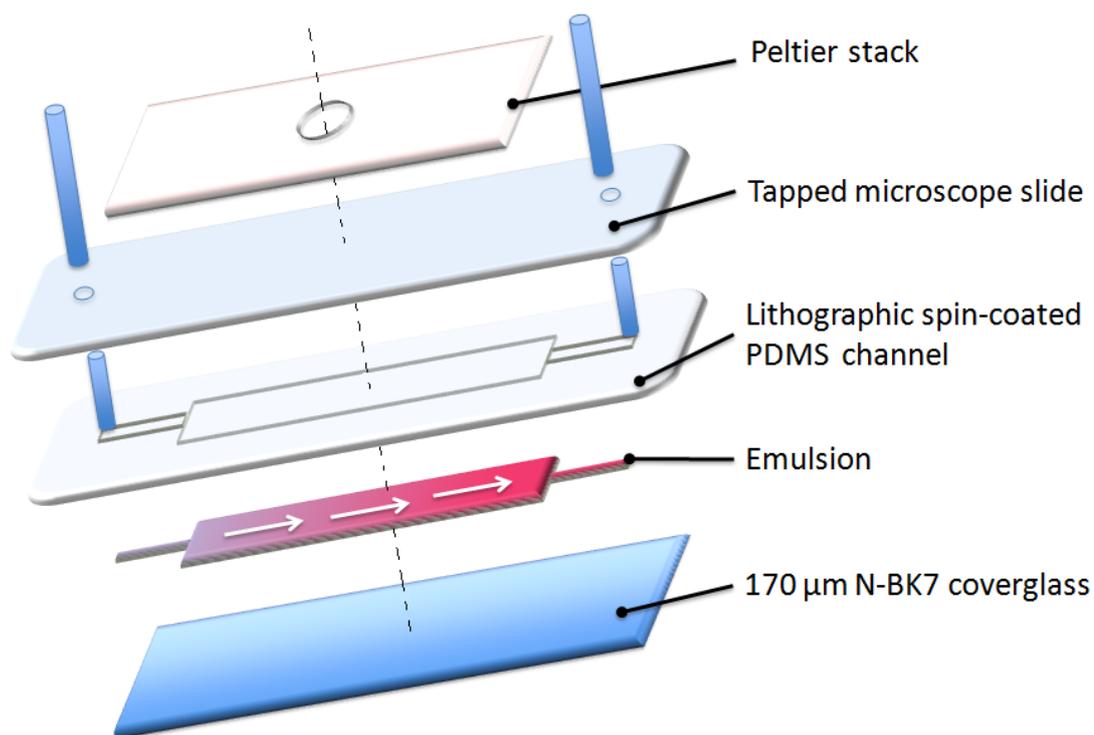
Figure 3.3: A layer-by-layer schematic view of the typical observation chamber used in the microfluidic platform. The design allows the droplets to be heated, and facilitates their optical manipulation and imaging.

The alkane oils used in this work, particularly heptane, cause significant swelling of PDMS and polyisoprene syringe plungers. Therefore, use of glass in syringes and chips is preferable. However, the ObC is rendered less fragile and more amenable to in-house manufacture by the use of PDMS for the channel template. The internal surfaces, particularly the nonpolar PDMS, must be hydrophilised to prevent oil wetting and disrupting the intended flow profile. Plasma exposure is used to bond the chip, but the hydrophilic surface is short-lived. Piranha solution (§ 1.5.1) is too risky to handle under pressure, given its highly corrosive nature and evolution of oxygen gas. Instead, the surface hydroxyl moities must be replenished by regular treatment with hydroxide bases. The concentration and duration is limited to 0.1 M NaOH for 30 min since glass is susceptible to caustic etching. This protocol ensures correct channel wetting for tens of hours of operation.

3.4.2   Pumps, syringes and flow rates

The aqueous side channels of the focusing junction must be supplied with an identical composition and flow rate to ensure the correct symmetric operation of the FFJ. For this purpose, the aqueous flows are combined and split using passive Y-junctions, with sufficient intervals of tubing to ensure diffusive mixing of salt. The minimum mandatory mixing length is $L = Q/4\pi D \approx 0.1$ m for a maximal flow rate $Q \approx 60$ μL min^{-1} and electrolyte diffusion coefficient $D \approx 10^{-9}$ m^{2}s^{-1} [3].

All solutions were passed through 2-μm-pore PTFE filters before loading into the syringes. Any adventitious dust particles carried by the solution risk blocking the FFJ chip, particularly the smaller size. Stainless steel frits (1 μm pore size) were introduced in the Y-junctions to prevent dust accumulating within the FFJ.

Four-syringe configuration

Use of four syringes affords full control of the aqueous composition and allows the AOT and saline solutions, $S1, S2$, to be stored in isolation. The location in concentration space is described in units of mM by:

$$\mathbf{C} = \Big[S1, S2, [AOT] \Big] \, ,$$

whereas the flow rate parameter space is described in units of μL min^{-1} by:

$$\mathbf{Q} = \Big[Q_{S1}, Q_{S2}, Q_{AOT}, Q_{Oil} \Big] \, .$$

Four stepper-motor pumps (*World Precision Instruments*, `Aladdin 2-220`) were loaded with glass syringes (*Hamilton, Gastight*). Volumes included 100 μL, 250 μL and 1 mL. The syringes were connected to the platform with *Luer-Lock* and 1/4" 28-UNF threads.

To avoid low (and therefore imprecise) individual pump flow rates, the total flow rate for continuous phase was divided as evenly as possible across the three relevant pumps. Thus, the concentrations of the loaded solutions were higher by a factor of roughly 3 corresponding to the subsequent dilution under mixing.

Two syringes were loaded with saline whose *output* concentrations bounded the optimal salinity (as defined in § 1.4) for ULIFT with a range of at least ±10%. As for the handshaken method, the salinity values were chosen to suit the working temperature in the ObC for best ULIFT at the point of deformation.

For heptane/H_2O/AOT/NaCl experiments at a working temperature of 30 °C, the optimal salinity would be $S^*(30\,^\circ\text{C}) \sim 60$ mM NaCl and so the *input* concentrations would be required to average to $S^*/(2/3) = 90$ mM. The saline syringes could therefore be filled with 80 mM and 100 mM respectively. For the same conditions using D_2O, the salinity range would be 50 mM and 70 mM for tuning around 40 mM output. The desired output AOT concentration is almost invariably 2 mM, so the input syringe concentration is $[AOT]/(1/3) = 6$ mM.

3.4.3 Valves and automation

In the final iteration of the microfluidic platform, the manual switches were replaced with solenoid isolation valves (*Kinesis*) of the kind commonly used in commercial chromatographs. The supporting electronics were designed to deliver the 5.5 V required for solenoid switching, yet hold at 2.6 V. Ohmic losses in the solenoid architecture cause a local increase in temperature of $\Delta T = 0.4$ K V$^{-2} \times (2.6$ V$)^2 \approx 3$ K above ambient. The heating of the emulsion in transit necessitates a further increase in the salinity to ensure the working PIT is not reached until the ObC.

The valves were activated from a power supply via a *mbed* microprocessor that controls a set of 8 relay switches. The *mbed* firmware was reconfigurable in a `C++` based proprietary development language. The eight relays required the switches to be arranged into groups (see logic table, Table 3.1). Within each, the switches were connected in parallel to supply a uniform control voltage. The microprocessor was sent `RS232`-type commands via USB serial port, whilst the graphical user interface (GUI) was written in `wxpython` module of the *Python* programming language (see Figure 3.7).

This interface permitted remote setting of flow rates and infusion/aspiration for the individual pumps, as well as the opening/closing of each group of valves.

The 26 switch valves in the system are connected logically in terms of which are active/inactive simultaneously, as shown in Table 3.1. The length of illumination and exposure of the FFJ were also synchronised using this script, allowing both internally-triggered and stroboscopic video images of the droplets to be acquired. The typical illumination time was 1-10 μs within a shutter speed of 50 ms.

The channel velocity v_{flow} is even lower through valves with excess internal volume. For intersections between upward- and horizonally-oriented paths, the residence time is sufficiently long to allow buoyant separation of the droplets according to their size, scaling as $v_{flow} \sim 1/R_T^3$, where R_T is the tube or channel radius. Larger droplets are retarded and build up at these locations, being released only periodically. The platform design avoids vertical features where possible.

3.5   Emulsion results

The flow rates were set to a standard of $\left[7.0, 7.0, 7.0, 0.0\right]$ and allowed to stabilise for a minimum of 10 min before measurements.

Tipstreaming occurred on applying a significant oil flow, $Q_O = 5.0$ μL min^{-1}. Reducing the oil flow rate caused the breakup point of the oil jet to retract closer to the focusing junction, approaching the *dripping* state at 3.5 μL min^{-1}. At this point the flow rate ratio was $Q_W/Q_O = 6$. At constant drop and channel sizes, the minimum flow rate ratio for breakup varies as $Q_W/Q_O \approx (\eta_W/\eta_O)^2 \approx 5$ [18].

Under brightfield, the droplets appeared qualitatively monodisperse around 15 μm in diameter. The downstream region was cluttered with droplets decelerating as the channel expanded. As the oil flow was further reduced, discrete transitions were observed between dynamic packing states of the droplets (see Figure 3.4). At $Q_O = 0.4$ μL min^{-1}, or a flow rate ratio of $Q_W/Q_O \approx 50$, droplets were generated in single-file. As expected from Equation (3.3.1l), the typical droplet size reduced slightly with greater flow rate ratio.
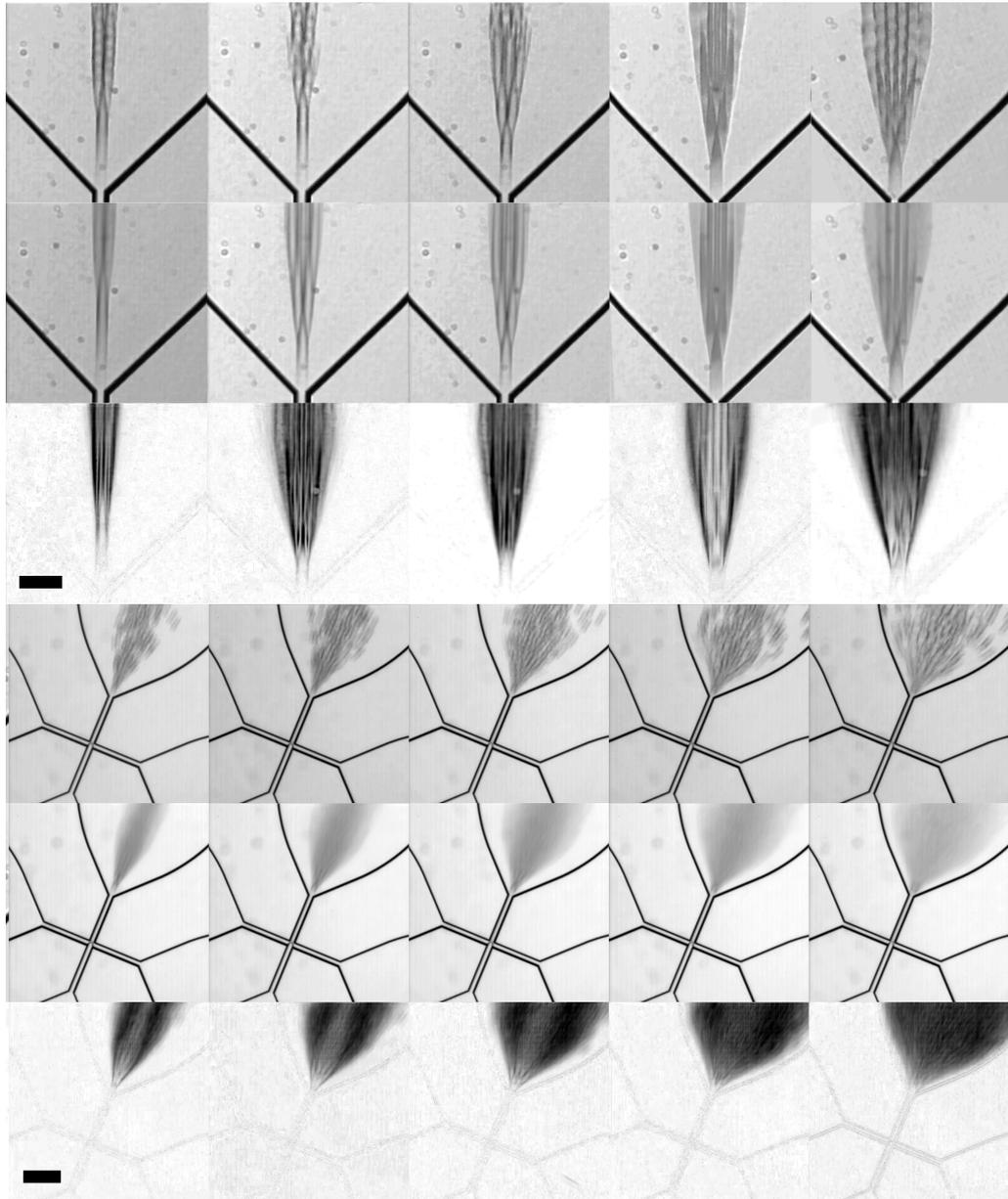
Figure 3.4: Stability of droplet generation in the 14 μm FFJ with standard [7.0, 7.0, 7.0, Q_O] μL min^{-1} aqueous flow rates and varying oil flow rates $Q_O = 0.4, 0.5, 0.6, 0.7, 0.8$ (*upper set*) and $1.0, 1.5, 2.0, 2.5, 3.5$ μL min^{-1} (*lower set*). *First row*: single raw frame of FFJ output channel showing motion-blurred droplet stream, *second row*: the pixel-wise median of frames over 5 s, and *third row*: the pixel-wise standard deviation of frames over 5 s, representing the temporal fluctuations. As the flow rate decreases, mean droplet size decreases. Discrete transitions occur from crowded droplets towards single file, strongly influenced by flow rate fluctuations. Upper set, scale bar 50 μm; lower set, scale bar 100 μm.

3.5.1   Flow rate fluctuations vs. hydraulic elasticity

The flow rate stability at these low values is limited by pump vibrations. The temporal Fourier spectrum of the density of generated droplets correlates well with the binary harmonics of the stepper motor frequency. As a result, there is a minimum acceptable bore speed. The bore speed depends strongly on the syringe volume; at first syringes of 5 mL volume were employed for the water channels and 1 mL for the oil. The glass syringes are each of 60 mm internal length. The bore speed at a given flow rate is therefore inversely proportional to the total syringe volume. Thus, smaller syringes of 100 μL volume were installed to avoid flow fluctuations.

However, the bore speed is related to the syringe refill frequency. By increasing the bore speed to combat jitter, a compromise was made on the length of time before the flow had to be interrupted to refill the syringes. The smaller 100 μL barrels require refilling at 15 min intervals at typical flow-rates of operation totalling $Q_W/3 = 7$ μL min^{-1}. Refilling from attached reservoirs is done at maximum bore speed, $\sim \times 10$ operation rates, such that an automated cycle takes around 2 min. Overall, this equates to 2 minutes' refilling for every 15 min of operation. Each valve encompasses 50 μL of dead volume, a considerable fraction of the syringe and chip capacities. Consequently, the flow is not simply arrested on switching, but impulsed (and even reversed) by the displacement of liquid. These events disturb the wetting of the FFJ channels and project emulsion droplets backwards into the input channels. The channels must then be cleared through (for 20 s at maximal flow rates, ~ 60 μL min^{-1}) to recover a controlled tipstreaming regime, from which the rate is again reduced incrementally to generate droplets.

Around $Q_O = 0.3$ μL min^{-1}, the interface retreated from the junction under fluctuations and water began to backflow into the oil channel. Yet, the oil path is closed; the backflow must be accommodated by elasticity of the tubing, which provides a hydrodynamic compliance, C, that depends on the Young's modulus Y and radius R_T of the tubing. The profile-averaged flow dynamics are governed by

the equations [19]:

$$Q(t) = \frac{\Delta p}{r} + C\frac{d\Delta p}{dt} \qquad (3.5.1\text{m})$$

$$r = \int \frac{8\eta}{\pi R_T^4} dL \qquad (3.5.1\text{n})$$

$$C = \int \frac{2\pi R_T^2}{Y} dL \qquad (3.5.1\text{o})$$

If backflow occurs, the oil path (r_O, C_O) does not necessarily have lower hydrodynamic resistance than the output emulsion path (r_E, C_E), but the maximum flow-rate ratio that is entirely stable against oscillatory backflow is dictated by the ratio of resistances:

$$\left(\frac{Q_W}{Q_O}\right)_{max} = \frac{r_O}{r_E} - 1 \approx \frac{\int_O R_T^{-4} dL}{\int_E R_T^{-4} dL} \qquad (3.5.1\text{p})$$

Though the stiffer glass syringes are preferred to plastic ones due to faster relaxation, the syringe, being of much larger radius than the tubing, makes only a small contribution to the stability expression. It is dominated by the stiffest, smallest apertures in the channel. By adding 1 μm-pore steel frits to the oil path, the resistance r_O of the channel to unwanted backflows was increased by two orders of magnitude. The generation was then stable beyond $Q_O = 0.03$ μL min^{-1} or $Q_W/Q_O \approx 700$. In the ObC, there was no evidence of sub-micron satellite droplets [2]. The invisibility results from a small population of poorly resolvable particles, with significant buoyant filtering in the tubing network. The monodisperse primary droplets thus produced were no smaller than $R_D = 5.7 \pm 0.3\mu$m.

---

[2]GB reported that these were typically generated around 2 μm diameter alongside the primary droplets.
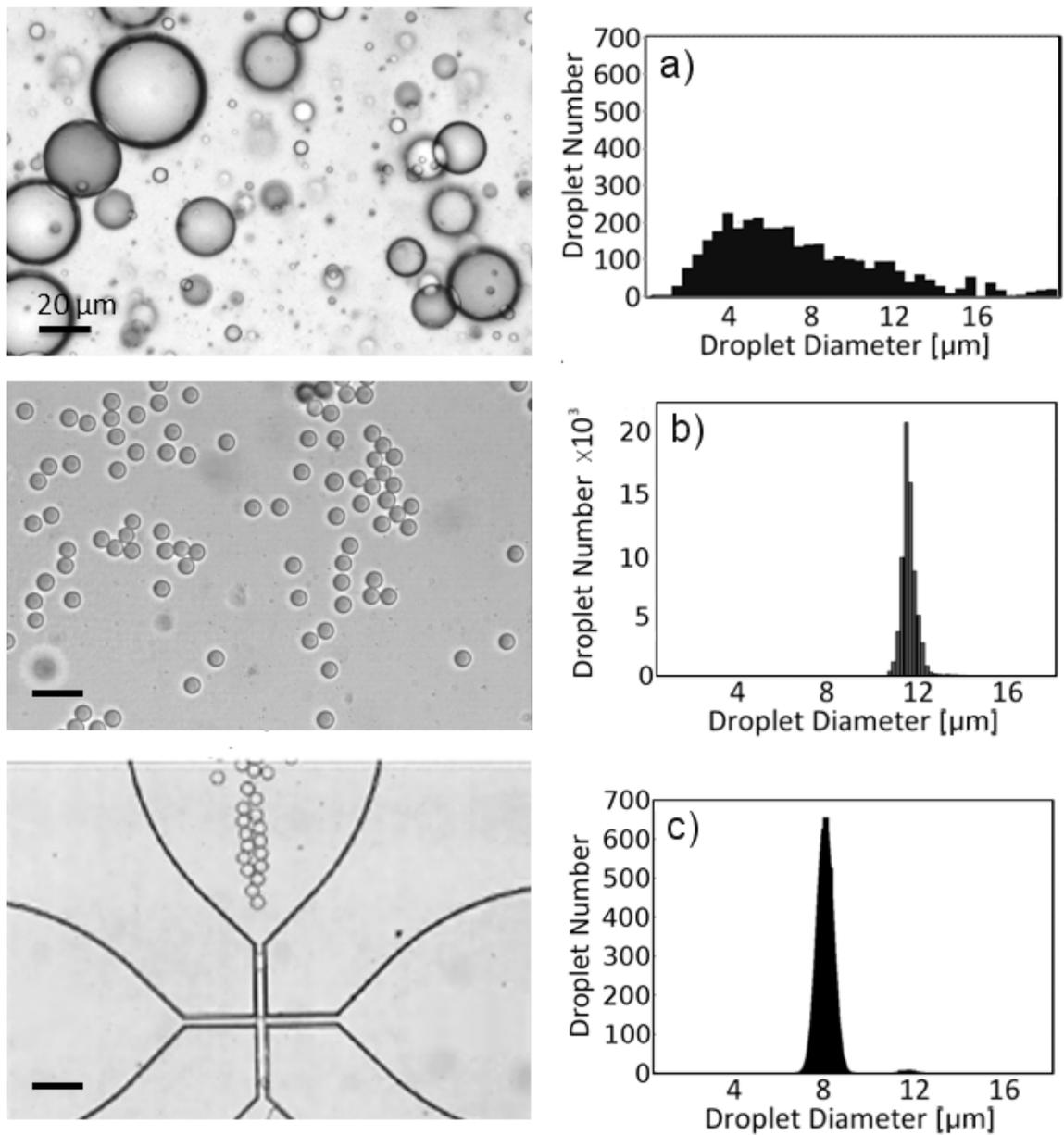
Figure 3.5: Examples of brightfield image and droplet size distribution of emulsions produced by a) manual agitation (imaged in ObC), or using the b) 14 μm FFJ chip (imaged in ObC) or c) 5 μm FFJ chip (imaged in FFJ). All scale bars 20 μm.

For the input channels carrying continuous phase, using tubing of wider internal radius $R_T = 600$ μm until the first mixing junction reduces the resistance that the pumps must cope with (or equivalently the pressure applied) for a given flow rate. The elasticity significantly increases as the tubing walls are thinner, so the characteristic settling time $\tau_{rC} = rC$ remains on the order of 5 min. The droplet

generation is not noticeably affected.

Although these emulsion droplets can be manipulated in the bulk using optical tweezers (see Chapter 2), they are unwieldy and prone to escape; at the size $R_D \sim 7$ μm, the buoyancy and viscous drag (at small speeds $\sim \mu$m s^{-1}) approach the typical escape force, ~ 10 pN, of the traps available to us.

As the minimum droplet size is dictated by the geometry, the FFJ channel size was reduced to 5×8 μm. The collaboration successfully generated $R_D \sim 4$ μm droplets in H$_2$O at a ratio $Q_W/Q_O \approx 100$ in a non-automated system, Figure 3.5. However, this was difficult to reproduce since the 5 μm chip was blocked by debris frequently, and irretrievably so. Frits combined with degassing membranes under vacuum (§ 3.5.3) could improve the performance, though at further expense of the responsiveness of the system.

3.5.2   PIT-induced polydispersity of generated emulsions

Hashimoto et al. showed that spatial confinement incites shear-driven instabilities on ULIFT droplets, jeopardising the dispersity of the emulsion [20]. Once droplets relax to an equilibrium ULIFT, they become similarly vulnerable to scission as they travel towards and within the ObC. The contents of the tubing become milky in appearance as the emulsion becomes increasingly polydisperse.

The net flow velocity $v_{flow} = Q/\pi R_T^2$ is sufficiently low as to be laminar at all points in the network, so the velocity profile across each channel will resemble the parabolic ideal. The maximum shear rate across a droplet is therefore $dv/dR = 2Q/\pi R_T^3$. This value can be compared to the critical shear rate $(dv/dR)^* = \sigma/\eta_O$, corresponding to a capillary number of η_W/η_O, at which viscous shear overcomes the interfacial forces maintaining the integrity of the droplet. Therefore a IFT limit exists, of order:

$$\sigma_{OW}^{shear} = \frac{2Q\eta_O}{\pi R_T^3} \approx 10 \ \mu\text{N m}^{-1}, \tag{3.5.1q}$$

below which droplets break up and recombine spontaneously in the tubing. The

IFT can fall below this threshold near the phase inversion temperature (PIT), which must therefore be set significantly higher than the temperature of the droplets in transit, i.e. the ambient temperature of $18 - 23$ ° C. The high specific area of the tubing renders heating in transit impractical. Instead, a high salinity was used and the Peltier voltage across the ObC was adjusted to obtain the desired deformability of droplets in view.

It was tempting to use the more capacious tubing after the FFJ to reduce the shear stresses on droplets (scaling as $\sim 1/R_T^3$), but droplets take an untenably long time to traverse between the FFJ and ObC; the responsiveness of the system is reduced.

3.5.3 Full platform design and switch logic

To describe a working design in sufficient detail that it can be reproduced, three sets of information are required. First, the flow network patterns or *modes* are defined corresponding to specific purposes, such as generating droplets and passing them into the ObC. Second, a picture is given of the fully integrated network of components and switches. Last, control logic that realises these different flow modes in the automated network is tabulated.

Let the flow modes be defined as follows:

1. *Shutdown*: for sealing all switches to secure the network against evaporation and contamination when not in use,

2. *Operate*: for supplying solvents to the FFJ such that monodisperse droplets are generated and passed into the ObC,

3. *Bypass*: as for *Operate* except that the ObC is isolated, such that droplets may be imaged and manipulated without external flow, yet leaving the generation undisturbed,

4. *Manual*: for the purposes of automation, this presents an override mode for

arbitrary control of individual switch groups,

5. *Vacuum*: for depressurising the fluoropolymer membranes, where used, so that inline degassing of solvents may resume,

6. *Refill*: for replenishing the syringes from reservoirs so that operation may resume,

7. *Purge*: for emptying the syringe and the network of stored liquid in case of spoilage or replacement,

8. *Rinse*: for cleaning and hydrophilising the network including the FFJ and/or ObC with dilute NaOH.

The integration of a vacuum system (untested) and purging pathways are detailed in the full circuit diagram, Figure 3.6.

	Mode						
Valve Group	*Shutdown*	*Operate*	*Bypass*	*Vacuum*	*Refill*	*Purge*	*Rinse*
L1/H1/S1/O1 ∧ L2/H2/S2/O2	0	0	0	-	1	0	0
L3/H3/S3/O3	0	1	1	-	0	1	1
L4/H4/S4/O4 ∧ R1/R2/R3	0	0	0	-	0	1	1
L5/H5/S5/O5 ∧ L6/H6/S6/O6	0	1	1	-	1	0	0
C1/C2 ¬ B1/B2	0	1	0	-	0	0	1
V1	0	1	1	0	1	1	1
V2	0	0	0	1	0	0	0
W	0	1	1	-	0	1	1

Table 3.1: A logic table for the full platform design, describing which groups of valves must be open (1), closed (0) or unconstrained (-) to obtain the desired mode, or set of network functions. Where the platform is automated, in *Manual* mode all the valves are unconstrained. Each valve group corresponds to one of the 8 relay switches controlled by the *mbed* microprocessor. The valves related by AND (/,∧) logic are connected in series to the NORMALLY OPEN terminal, whilst those related by NOT (¬) are connected in series to the NORMALLY CLOSED terminal.
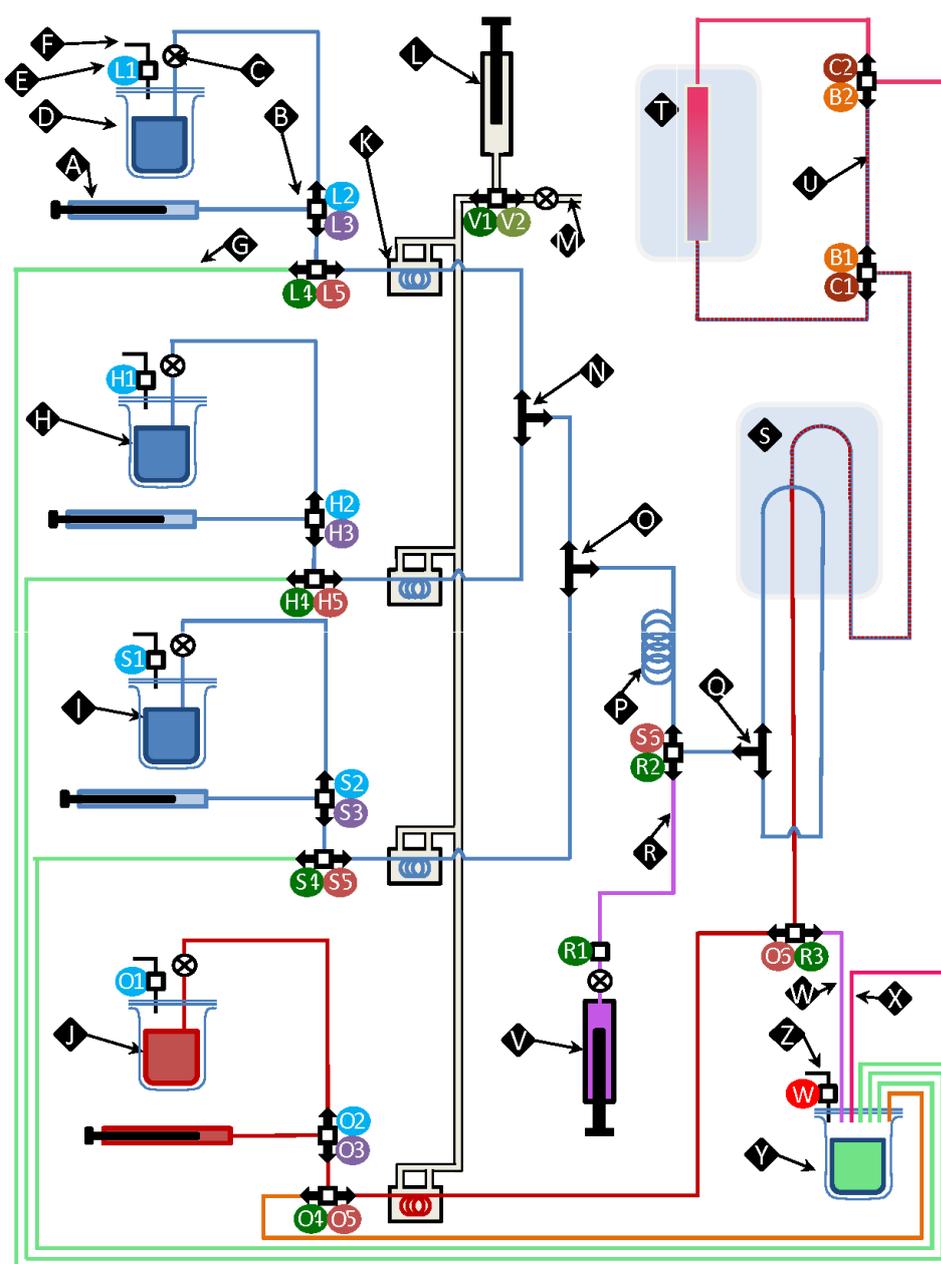
Figure 3.6: The unabridged microfluidic platform, capable of all defined flow modes. Each switching valve e.g. `R3` is encircled with the colour of its logic group. Other components **A-Z** are indexed in the Legend. The colours of each line reflect the fluid carried: aqueous (*blue*), oil (*red*), emulsion (*dashed purple*), waste aq. (*green*), waste oil (*orange*), waste emulsion (*pink*), alkaline rinse (*lilac*) and an evacuated atmosphere (*grey*).

Legend

A. Glass syringe for delivery of microfluidic solvent,

B. Three-way junction formed from two valves with a common input (in this case, valves `L2` and `L3` and the syringe port respectively),

C. Inline filter, PTFE 5 μm,

D. Saline reservoir, lower bound concentration; 50 mL airtight flask, to *Refill* syringe,

E. Two-way junction - a single valve to prevent evaporation/contamination of reservoir,

F. Air intake to equalise pressure in reservoir,

G. Purge line direct to waste,

H. Saline reservoir, upper bound concentration,

I. Aqueous surfactant solution reservoir,

J. Oil reservoir,

K. Inline de-gassing unit,

L. Vacuum syringe, 10 mL,

M. Gas purge outlet for *Vacuum* cycle,

N. Passive Y-junction for mixing of salines at a ratio equal to that of flow rates,

O. Passive Y-junction for mixing of surfactant solution and combined saline,

P. Length of tubing to ensure the continuous phase is completely mixed under diffusion,

Q. Passive Y-junction to split continuous phase equally into FFJ side channels,

R. Input channel for alkaline rinse,

S. Flow focusing junction (FFJ),

T. Observation chamber (ObC),

U. Channel to *Bypass* the ObC directly to waste,

V. NaOH syringe for *Rinse* cycle through operating lines,

W. Cleaning output for *Rinse* cycle, with flow reversed through oil channel in FFJ,

X. Waste emulsion line,

Y. Waste reservoir,

Z. Air pipe to equalise waste pressure to ambient.
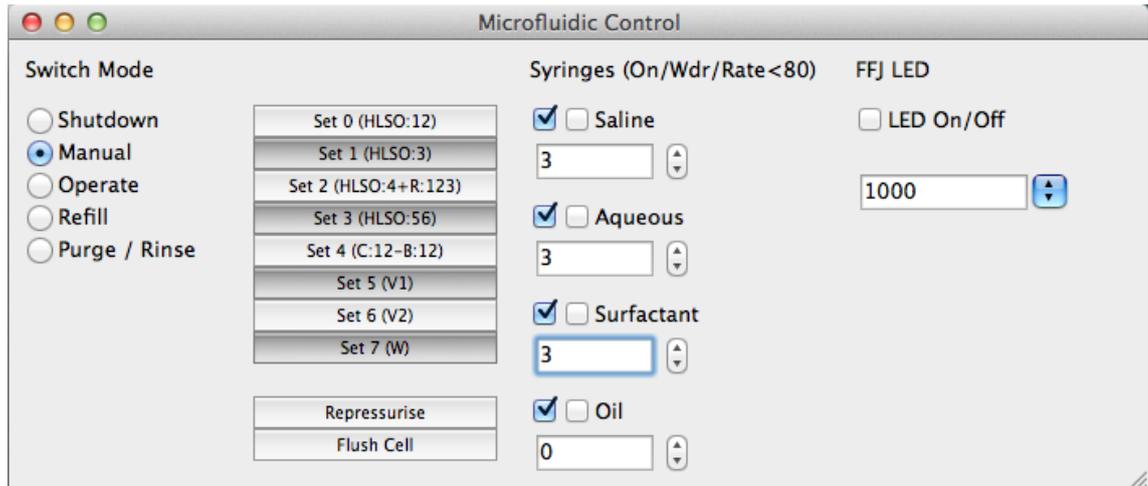
Figure 3.7: A user interface coded via serial microcontroller for activating logic groups of microfluidic switches, syringe pumps (flow rates in μL min^{-1}) and the FFJ mini-microscope (exposure in μs), see § 3.4.

3.6 Phenomenology without laser intervention

The initial work of Woods *et al.* was undertaken in the framework of oil and water being mutually exclusive, self-contained phases whose composition is time-invariant [21]. The assumption of oil droplet/water continuum mutual exclusivity is weak, as the phases are those of Winsor microemulsions. Invariance of composition is also violated significantly in the vicinity of the PIT. The results presented in this thesis, both below and in Chapter 4 attempt to tackle the transient phenomena of droplet shrinkage, bursting and degradation that do not occur in conventional emulsions. Moreover, these unusual behaviours appear not only on the initial mixing of the oil and aqueous solutions, but also on changes in temperature several hours afterwards.

Below the $c\mu c$, the oil and water behave as regular micellar solutions, with cmc levels of unimer surfactant. The portion of surfactant that exceeds the requirement for a concentration of $c\mu c$ in each phase will eventually draw oil and water into a surfactant-rich microemulsion phase. Which phase this is depends on the preferred Winsor equilibrium; that is to say, on the value of H_0. As a result, the equilibrium

compositions follow changes in H_0. The emergence of non-equilibrium processes associated with mass transport depends on the rate of these changes.

The emulsion behaviour is hysteretic and asymmetric with respect to the PIT, since water is in excess. On rapid heating across the PIT, droplets of heptane may *burst*. As the transition occurs, the droplet is destabilised in two ways. First, the affinity of AOT aggregates for water increases dramatically. This causes a spike in outwards osmotic pressure for reverse micelles present in the relatively surfactant-rich oil droplet, which is relieved by diffusion of the aggregated surfactant across the droplet interface. If the transition occurs faster than the diffusion can respond, the osmotic pressure can overcome the inwards Laplace pressure. The water-solubilising regions in the droplet will coalesce rapidly [22] and the droplet will fragment in a violent manner. This condition can be written explicitly:

$$\frac{2\sigma_{OW}}{R_D} < \frac{N_A k_B T}{D_\gamma} \frac{R_D^2 \Delta\gamma_W}{\Delta T_{WIII}} \frac{dT}{dt}. \tag{3.6.1r}$$

where D_γ is the diffusion coefficient of the aggregates, $\Delta\gamma_W$ is the difference in equilibrium aggregate concentrations in the aqueous phase either side of the transition, and ΔT_{WIII} is the temperature range in which the middle phase exists. Larger droplets burst preferentially, as expected from their lower Laplace pressure.

Second, the solubilisation capacity of water in oil decreases. Where water has been solubilised into the oil droplet as w/o, it will nucleate rapidly, precipitating a catastrophic phase inversion to o/w. The total droplet volume is difficult to estimate from brightfield images, but appears to decrease as a result of bursting. This indicates the loss of solubilised water and some oil to the continuous phase.

Bursting occurs more readily at low $\Omega < 20$ where droplets congregate. At this water-oil ratio, the initial uptake of AOT into oil reduces its concentration in water noticeably, thus exacerbating the change on heating. For a 5 μm droplet at 0.1 μN m^{-1}, a deficit of only 1% of the AOT content is predicted to cause bursting. A similar catastrophic bursting effect is caused by exposure to air, where the oil

evaporates rapidly until the w/o volume fraction exceeds a critical value for phase inversion. The global compositions favouring bursting of droplets far from equilibrium are also those which tend towards three-phases at equilibrium, where the surfactant-oil ratio is highest. (Figure 3.8).

In the opposite sequence of *cooling* towards the PIT, the droplets *shrink* by losing oil to o/w solubilisation in the continuous phase. The rate of this effect was measured with control for a similar, more spatially-dependent effect from absorption of alkanes into PDMS walls of the ObC. The rate of solubilisation-related shrinking, typically 0.1-1 μm min^{-1}, increases with proximity to the upper side of the PIT. In contrast to bursting, shrinking accelerates with increasing $\Omega > 100$, as the newly-introduced continuous phase can solubilise additional oil.

The microscopic results can be mapped onto the global formulation space with Ω and γ as working variables. This representation transforms the quasi-ternary basis (oil, brine, surfactant) of the compositional phase diagram to an experimentally meaningful format (Figure 3.8).

The margins of compositional change necessary for a observable difference in ULIFT behaviour are exceptionally small. Droplets in the same 100 μm field of view can exhibit PITs as widely spaced as 2 K, such that one population is rigid and the other severely deformed under thermal fluctuations. In the three-phase region, bimodal behaviour is expected, as ideally some droplets will be formed from middle phase and the remainder from excess oil. Much like droplet size, the local droplet composition is more broadly distributed with manual production than the microfluidic alternative. Although the droplet composition is coupled to the refractive contrast, it is also coupled to the interfacial tension. Thus, there are no high-contrast soft droplets and no low-contrast stiff droplets; the droplets reside on a single spectrum of deformability (Table 3.2).

Cat.	A	B	C	D
Appearance	Smooth, spherical	Smooth, spherical, slight shimmering	Amorphous, sphere-like. Visible capillary waves.	Other, often spherical or myeloid. Cloudy inclusions, poor fluorescence.
Contrast	High	Fair	Minimal	Fair/High
Trapping	Good (behaves like bead)	Good	Poor	Fair, often immobilised
Deformability	Inert, none detected: $\sigma > 50\ \mu\text{N m}^{-1}$	Fair, prolate shapes evident: $\sigma = 1 - 10\ \mu\text{N m}^{-1}$	Malleable, but local to trap site: $\sigma < 1\ \mu\text{N m}^{-1}$	Flexible, trappable appendages (constant surface area)
Threads	None	Rare	Occasional	None. Thin myeloids mimic threads without tension, see Chapter 4
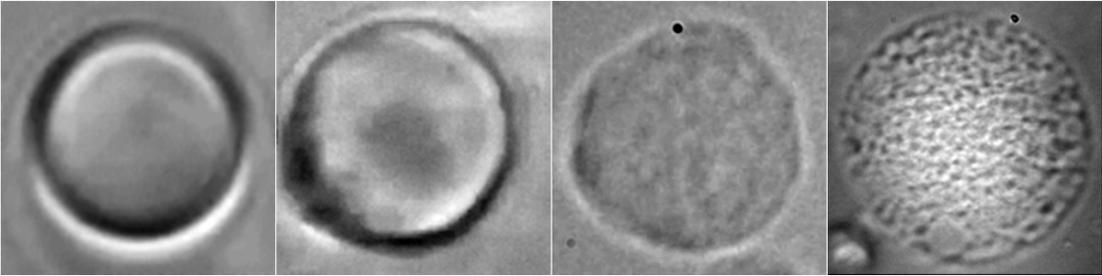
Table 3.2: Oily droplets in microemulsion-forming mixtures fall into four composition-related categories A-D by behaviour and appearance. Images are of droplets roughly 5 μm in diameter.

Figure 3.8: Phase diagram for $\chi = 1$ (in the proximity of the optimal salinity/temperature combination HLD ~ 0) mapped onto the experimental space; here the important parameters are the initial aqueous AOT concentration (scaling as $\sim \gamma/\Omega$) and the aqueous solution-oil volume ratio Ω. Logarithmic scales are used to highlight the low concentration used.

Oily droplets can be categorised qualitatively into four groups (Table 3.2), since properties such as deformability and reduced contrast are strongly correlated. The preferred candidate for the deformation experiment lies between categories B and C, where a droplet is highly deformable but still appears self-contained and homogenous. Droplets of different categories may coexist or interconvert both over time (non-equilibrium) and as a function of temperature and salinity (equilibrium). The conversion of a droplet between deformability categories is reversible except for the transition from C to D, in which bilayers are produced.

3.7 Droplet behaviour under IFT gradients

Since salinity is independent of environmental conditions, it makes an attractive choice for tuning interfacial tension in-situ. In the optical deformation experiments, the entire sample is replaced by serial inline generation (Chapter 3) of new droplets at the variable source salinity. Alternatively, adjustments in salinity can be made quickly by simple flushing of an *open*-channel observation chamber with the intended concentration, but this has the unwanted effect of diluting the oil droplets. Nonetheless, a *closed* channel is stagnant and droplets within will not be diluted, even in contact with a flow that introduces additional salt by diffusion. In this section a modified ObC is used with a closed channel (Figure 3.9) and the behaviour of static droplets is tracked in a time-dependent salinity gradient.

3.7.1 Materials and methods

NaCl and AOT concentrations of [39.0, 49.0, 8.0] (see § 3.4.2 for definition) are used together with the 14 μm Dolomite FFJ. Droplets are first generated at 11.3 μm diameter at the lowest salinity [10, 0, 6, 0.1] and allow to stabilise for 3 min. The channel is then closed and fluid is introduced at a higher salinity S_∞ with no further droplets. This salt concentration exceeds that required for deformable droplets, S^* (§ 1.4). Droplets are flushed away everywhere but a small area near the inlet from the FFJ. A salinity gradient develops, such that optimal conditions for ULIFT form in a narrow front (travelling from left to right in Figure 3.10).
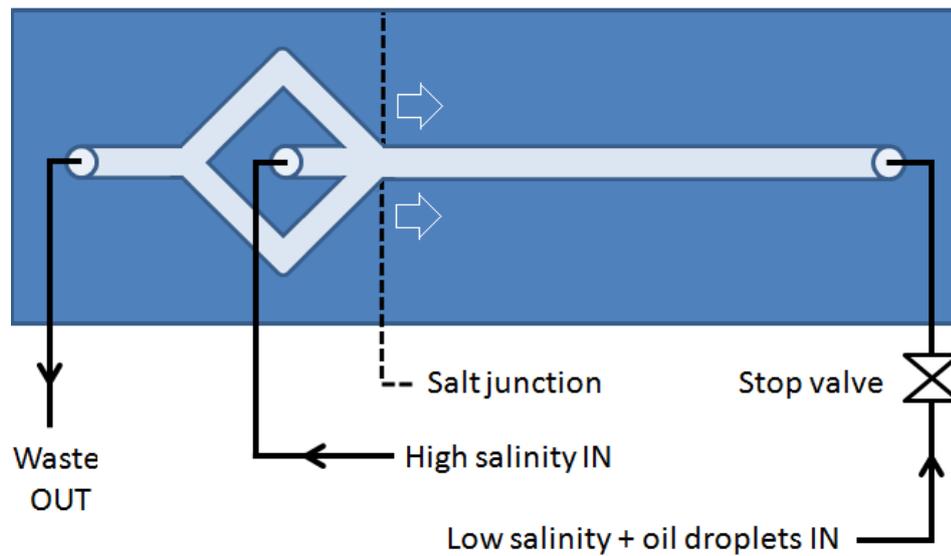
Figure 3.9: A schematic of the modified ObC used to expose droplets to a salinity gradient. Droplets are generated by FFJ in a low-salinity medium and the ObC is filled. The valve is then switched, with some droplets remaining in the stagnant long channel. The experiment begins at the moment a high-salinity medium is introduced as a continuous flow, such that the local salinity increases via diffusion from the salt junction.

As droplets in a salinity gradient are not equilibrated, there is no steady-state reference for their deformability. However, the IFT of the surfactant system (AOT in H_2O/NaCl) can be inferred from the ambient temperature of 21.6 °C, whose optimal salinity is $S^* = 43.7$ mM NaCl. At flow parameters [0.74, 1.26, 0.6, 0] the infused saline is $S_\infty = 45.3$ mM and the corresponding PIT is about 21.9 °C.

When the otherwise-invisible front passes through the first droplets at the junction, each droplet varies between rigid and deformable states (Table 3.2) on the order of tenths of Hz, subsiding over a few minutes. Neither salinity nor temperature can fluctuate locally under diffusion from a constant source of salt and heat. Instead, the oscillation could come from fluctuations in advective flow following the initial pressure spike (§ 3.5.1). After this time, the front settles into monotonic one-dimensional diffusion and decelerates accordingly as shown in Figure 3.10. When droplets first

meet the front and become deformable they also begin to microemulsify, losing oily material to the continuous phase. Spontaneous emulsification continues even behind the front where salinity is high and droplets become less deformable. This reflects the tendency for oil to be solubilised in normal micelles at salinity higher than optimal.

It is important to gauge whether there is a delay between the expected arrival time of diffusing salt and the onset of deformability. The frontier of salt concentration S^* is expected to reach the droplets at a displacement x from the junction after a time τ^*:

$$\tau^* = \frac{x^2}{2D_{NaCl}}\left(1 + \mathrm{erf}^{-1}\left(1 - \frac{S^* - S_0}{S_\infty - S_0}\right)\right)^{-2} \qquad \approx 3 \text{ ms } \times (x/\mu\mathrm{m})^2 \qquad (3.7.1\mathrm{s})$$

where the diffusion coefficient of NaCl in water is $D \approx 2 \times 10^{-9}$ m^{2}s^{-1}. For widely-spaced droplets, the wave of deformation took 150 s to traverse the 150 μm field of view, centred roughly 300 μm from the junction. The expected time is 230 ± 60 s which is of the correct order. However, the delay increases to tens of minutes when droplets are tightly packed in clusters of 10 deep even adjacent to the junction. Droplets leaving such a cluster become deformable within seconds.

Given the small length scales within the droplets and clusters, very low diffusion coefficients would be required to explain this slow response. It may be that here the kinetics are limited not by transfer of individual molecules, but of much larger oil or water domains associated with a microemulsion, which have the appropriate $D \sim 10^{-13}$ m^{2}s^{-1}.
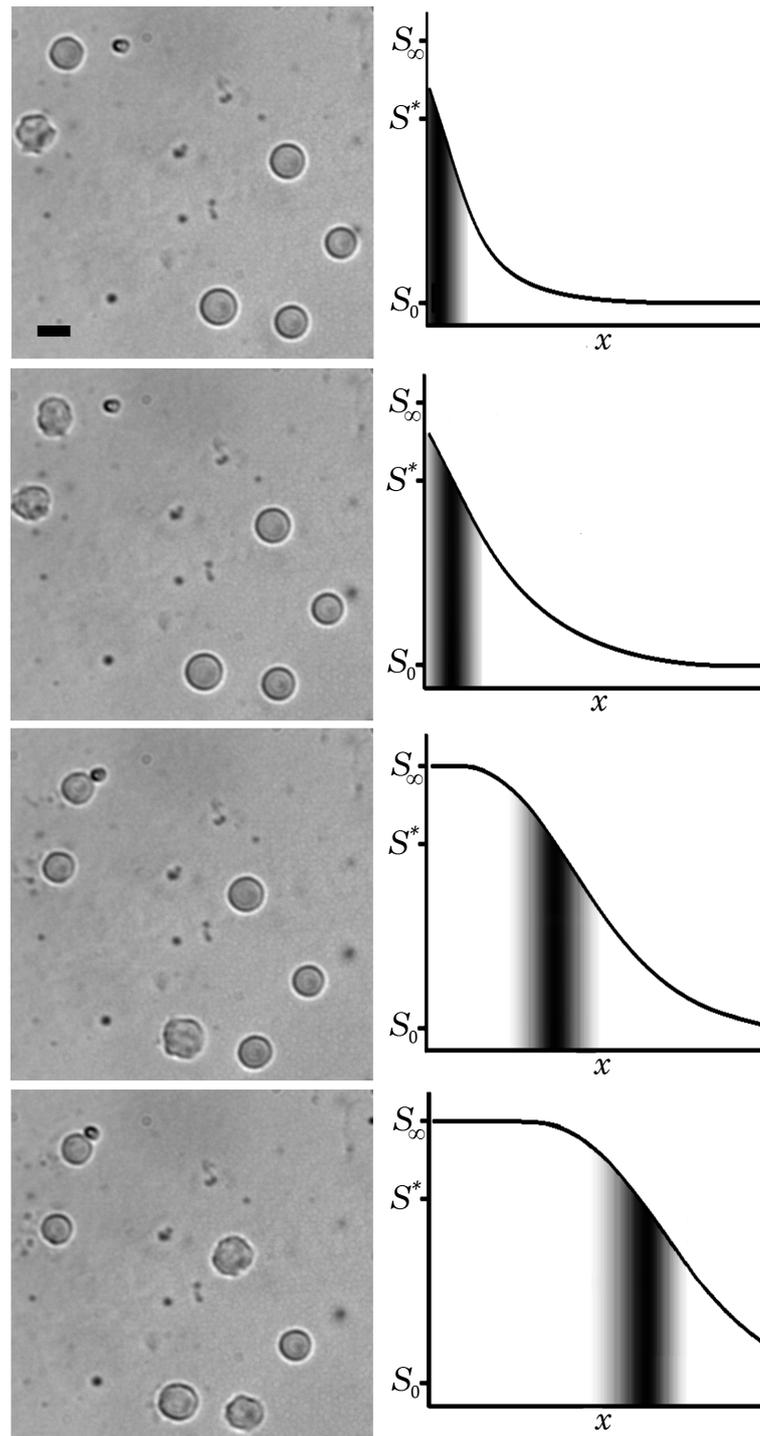
Figure 3.10: Emulsion droplets displaying transient ULIFT in a diffusive salinity gradient, with higher salinity introduced from left of field-of-view. Salinity and deformability are shown schematically as a function of position along the channel. Each descending row corresponds to a timestep circa 20 s. Scale bar is 20 μm.

Glossary

Symbol	Definition	Unit
β	Drag coefficient	N s m^{-1}
C	Hydrodynamic compliance to flow	N s^2 m^{-3}
Ca	Capillary number	-
cmc	Critical micellar concentration	M
$c\mu c$	Critical microemulsion concentration	M
$D_{O,\gamma}$	Diffusion coefficient, e.g. oil or surfactant	m^2 s^{-1}
FEP	Fluoro ethylene-propylene (tubing)	
FFJ	Flow-focusing junction	
f	Dispersion frequency	s^{-1}
H_0	Spontaneous curvature	m^{-1}
L	Dispersion amplitude	m
N_A	Avogadro's constant	mol^{-1}
NaOH	aqueous sodium hydroxide	
ObC	Observation chamber	
Δp	Pressure drop along channel	N m^{-2}
PDMS	poly-dimethylsiloxane resin	
PID	Proportional-integral-derivative controller	
PIT	Phase inversion temperature	°C
$Q_{O,W}$	Volumetric flow rate, of oil or water	m^3 s^{-1}
r	Hydrodynamic resistance to flow	N s m^{-4}
R_A	Effective aperture radius	m
R_D	Droplet radius	m
R_T	Tubing radius	m
Re	Reynolds number	
S, S^*, S_t	Aqueous salinity, optimal, at time t	M
S_{AOG}	Spreading coefficient, of oil on glass in air	-
$T, \Delta T$	Temperature, variability	°C, K
ΔT_{WIII}	Temperature range of Winsor III equilibrium	K
$V_{O,W}$	Molecular volume of oil, water	m^3
v	Velocity (flow, creaming)	m s^{-1}

x	Displacement in channel	m
x_∞	Mole fraction solubility of water in oil	-
η	Viscosity	N s m^{-2}
γ	Surfactant bulk concentration	M or % wt.
ρ	Density or specific gravity	kg m^{-3}
χ	Fraction of ionic surfactant in total surfactant	-
σ_{OW}	Interfacial tension, between oil and water	N m^{-1}
σ^C	Critical interfacial tension for breakup	N m^{-1}
θ_{AWG}	Contact angle, of water on glass under air	deg$^\circ$
τ_{rC}	Hydrodynamic settling time	s
Ω	Volumetric water-to-oil ratio	-

References

[1] I. Klink, R. Phillips, and S. Dungan, "Effect of emulsion drop-size distribution upon coalescence in simple shear flow: a population balance study", *J. Colloid Interface Sci.* Vol. 353, no. 2, pp. 467–475, 2011.

[2] J. A. Boxall, C. A. Koh, E. Sloan, A. K. Sum, and D. T. Wu, "Droplet size scaling of water-in-oil emulsions under turbulent flow", *Langmuir*, vol. 28, no. 1, pp. 104–110, 2012.

[3] W. M. Haynes, Ed., *CRC Handbook of Chemistry and Physics.* CRC Press, OH, 1977.

[4] M. Smoluchowski, "On the practical applicability of Stokes' law of resistance and its modifications required in certain cases", eng, *Pisma Mariana Smoluchowskiego*, vol. 2, no. 1, pp. 195–208, 1927.

[5] J. Weiss, N. Herrmann, and D. McClements, "Ostwald ripening of hydrocarbon emulsion droplets in surfactant solutions", *Langmuir*, vol. 15, no. 20, 6652–6657, 1999.

[6] B. Janczuk and A. Zdziennicka, "A study on the components of surface free energy of quartz from contact angle measurements", *J. Mater. Sci.* Vol. 29, no. 13, pp. 3559–3564, 1994, ISSN: 1573-4803.

[7] J. Harkot and B. Janczuk, "The role of adsorption of sodium bis(2-ethylhexyl) sulfosuccinate in wetting of glass and poly(methyl methacrylate) surface", *Appl. Surface Sci.* Vol. 254, no. 9, pp. 2825–2830, 2008, ISSN: 0169-4332.

[8] M. E. Schrader, "Young-Dupre revisited", *Langmuir*, vol. 11, no. 9, pp. 3585–3589, 1995.

[9] S. Joscelyne and G. Tragardh, "Membrane emulsification - a literature review", *J. Membrane Sci.* Vol. 169, no. 1, pp. 107–117, 2000, ISSN: 0376-7388.

[10]   J. McDonald and G. Whitesides, "Poly(dimethylsiloxane) as a material for fabricating microfluidic devices", *Acc. Chem. Res.* Vol. 35, no. 7, pp. 491–499, 2002.

[11]   C. Iliescu, H. Taylor, M. Avram, J. Miao, and S. Franssila, "A practical guide for the fabrication of microfluidic devices using glass and silicon", *Biomicrofluidics*, vol. 6, no. 1, 016505, p. 016 505, 2012.

[12]   P. Hassan, G. Verma, and R. Ganguly, *Soft Materials: Properties and Applications*. London: Elsevier, 2012, pp. 1–59, ISBN: 978-0-12-385142-0.

[13]   Y. Kimura, "Microrheology of soft matter", *J. Phys. Soc. Jpn.* Vol. 78, no. 4, p. 041 005, 2009.

[14]   S. L. Anna and H. C. Mayer, "Microscale tipstreaming in a microfluidic flow focusing device", *Phys. Fluids*, vol. 18, no. 12, p. 121 512, 2006.

[15]   G. Bolognesi, A. Hargreaves, A. D. Ward, A. K. Kirby, C. D. Bain, and O. Ces, "Microfluidic generation of monodisperse ultra-low interfacial tension oil droplets in water", *RSC Adv.* Vol. 5, pp. 8114–8121, 11 2015.

[16]   T. Fu, Y. Wu, Y. Ma, and H. Z. Li, "Droplet formation and breakup dynamics in microfluidic flow-focusing devices: From dripping to jetting", *Chem. Eng. Sci.* Vol. 84, 207–217, DEC 24 2012.

[17]   W. Lee, L. M. Walker, and S. L. Anna, "Role of geometry and fluid properties in droplet and thread formation processes in planar flow focusing", *Phys. Fluids*, vol. 21, no. 3, 032103, p. 032 103, 2009.

[18]   C.-X. Zhao and A. Middelberg, "Two-phase microfluidic flows", *Chem. Eng. Sci.* Vol. 66, no. 7, pp. 1394–1411, 2011, Microfluidic Engineering, ISSN: 0009-2509.

[19]   H. Bruus, *Microscale Acoustofluidics*. Royal Society of Chemistry, 2015, pp. 1–28, ISBN: 978-1-84973-671-8.

[20]   M. Hashimoto, P. Garstecki, H. A. Stone, and G. M. Whitesides, "Interfacial instabilities in a microfluidic Hele-Shaw cell", *Soft Matter*, vol. 4, pp. 1403–1413, 7 2008.

[21]   D. A. Woods, C. D. Mellor, J. M. Taylor, C. D. Bain, and A. D. Ward, "Nanofluidic networks created and controlled by light", *Soft Matter*, vol. 7, pp. 2517–2520, 6 2011.

[22]   A. Schuch, L. G. Leal, and H. P. Schuchmann, "Production of w/o/w double emulsions. part i: visual observation of deformation and breakup of double emulsion drops and coalescence of the inner droplets", *Colloids Surf. A*, vol. 461, pp. 336–343, 2014, ISSN: 0927-7757.

Chapter 4

Microemulsion transitions in optical tweezers

4.1 Introduction

During the deformation experiments on the microemulsion-forming mixture of brine, heptane and the anionic surfactant, AOT, it was observed that irradiated droplets exhibited unexpected dynamics; these included the nucleation of new phases, catastrophic phase inversion and spontaneous formation of vesicles. A more detailed study was carried out to determine the effect of focused lasers both on single microemulsion phases and on droplets of microemulsions in an excess phase, the results of which are reported here.

The quaternary system of water, salt, alkane and anionic surfactant has a phase diagram and interfacial tensions that are highly temperature-sensitive. Since optical tweezers heat water (owing to the weak absorption by water of the near-IR wavelengths typically used for trapping), this study was carried out with the so-called temperature-insensitive' microemulsion containing a mixture of an anionic and a non-ionic surfactant with oil and brine. It is the specific mixture of surfactants which suppresses the temperature dependence of the monolayer curvature [1] that governs observable microemulsion properties. Consequently, these quinary systems form a three-phase (Winsor III) microemulsion over a wide temperature range.

Despite the temperature insensitivity of the macroscopic phase diagram, such microemulsions still show rich dynamics when locally perturbed by focused IR lasers. The macroscopic phase behaviour of the temperature-insensitive emulsions is described, before discussing the effects of a focused laser beam on a continuous sample of the middle phase. Use of D_2O to mitigate laser heating allows the partial decoupling of thermal and optical effects. Finally, focused IR lasers are used to irradiate droplets of oleic or middle phase suspended in the excess aqueous phase.

4.1.1 Temperature-insensitive microemulsions

If the interface's spontaneous curvature H_0 is insensitive to changes in temperature, both the phase behaviour and IFT are also expected to be temperature-insensitive. In practice, this condition is achieved using a mixture of a nonionic and an ionic surfactant as the amphiphilic component. An electrolyte, NaCl, is added to control the ionic contribution to the preferred curvature.

The quinary composition is specified by four parameters - χ, γ, S, Ω - in terms of each component's weight fraction m, density ρ and molar mass M:

1. the volumetric water-oil ratio, $\Omega = m_{Aq}/m_{Oil} \cdot \rho_{Oil}/\rho_{Aq}$;

2. the total amphiphile concentration, $\gamma = (m_I + m_{NI})/(\Sigma m)$, expressed either as weight fraction in total (dimensionless percentage), or as a molar concentration in water prior to mixing (units of mM);

3. the amphiphilic ratio, or the weight fraction of ionic surfactant in the amphiphilic mixture, $\chi = m_I/(m_I + m_{NI})$;

4. the molar concentration of NaCl in water prior to mixing, assuming a saline density of 1 kg m^{-3}, or salinity, $S = (m_{NaCl}/m_{Aq}) \cdot (\rho_{Aq}/M_{NaCl})$.

At a unique value, denoted χ^*, the curvature of the mixed monolayer exhibits the desired low sensitivity to temperature, *i.e.* $\partial H_0/\partial T = 0$. As ionic surfactant is present, the ionic strength alters (decreases) H_0 almost independently of temperature. The particular salinity at which $H_0 = 0$ for a given χ is denoted $S^*(\chi)$. The ideal formulation for temperature-insensitive ULIFT is therefore an

amphiphilic ratio of χ^* and a salinity of $S^*(\chi^*)$, abbreviated S^{**}. The quinary systems $AOT/C_{12}E_5/n$-heptane/NaCl-brine, $AOT/Brij$-$L4/n$-decane/NaCl-brine and $AOT/C_{12}E_4/n$-decane/NaCl-brine are used in this work.

4.2 Experimental

4.2.1 Optical setup and laser heating

All tweezing experiments were performed on **Setup A** (§ 2.4.1) at 22 ± 2 °C ambient. At very high source powers > 0.5 W, air bubbles nucleated in the immersion fluid and were thermally trapped in the field of view. Bubbles form since the solubility of air in liquids decreases with increasing T. Bubble formation was eliminated by replacing the fluorocarbon coupling fluid with water, for which the thermal variation of gas solubility is less.

The tightly focused laser also causes localised heating of the sample. The increase in temperature, ΔT, is proportional to the optical power P. At fixed power, the temperature increase and distribution are determined by the optical intensity distribution, together with the optical absorption and thermal characteristics of the fluid sample and its enclosing substrates (§ 4.7). For a high numerical aperture at $\lambda = 1064$ nm, laser heating of the order 20 K W^{-1} is typical in water, while in D_2O there is an order of magnitude less heating. The maximum temperature rise predicted in the experiments reported here is 5 K in water. For middle-phase microemulsions, the water and oil solubilisations are roughly equal; the heating is expected to be close to the average of the bulk phases (see § 4.7).

4.2.2 Formulations

The AOT (sodium bis(2-ethylhexyl)sulfosuccinate, 96%, *Acros Organics*), Brij-L4 and $C_{12}E_{4/5}$ (dodecyl tetra/pentaethyleneglycol ethers, 98%, *Sigma-Aldrich*), NaCl (AR grade, *Fisher*) and D_2O (*Cambridge Isotope Labs.*) were all used as received.

UHP H_2O was obtained from a *MilliPore* unit (*MilliQ*). The oils *n*-decane and *n*-heptane (99% and 99.5%, *Fisher*) were purified through silica under N_2.
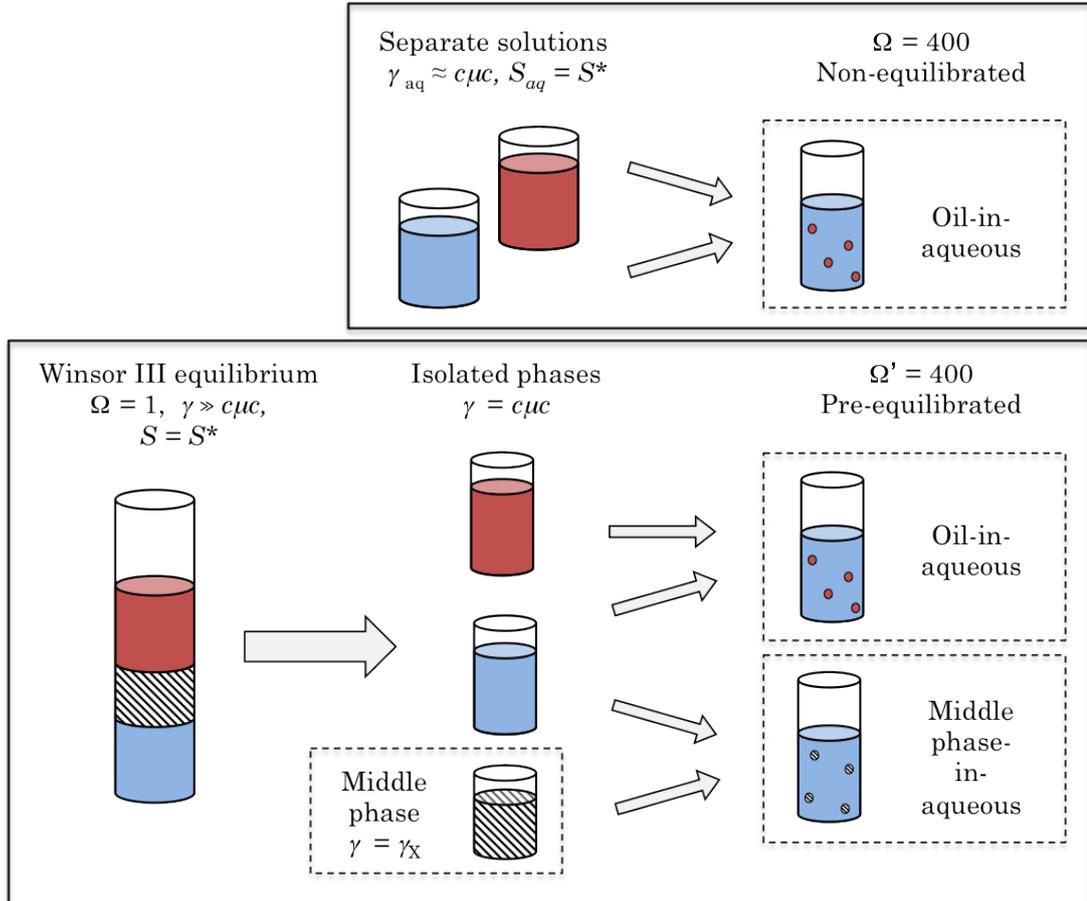
Figure 4.1: Sequences to prepare trappable emulsion droplets of either: non-equilibrated oil (as used in [2]), equilibrated oil or middle phase.

Non-equilibrated samples:

Aqueous stocks of NaCl, AOT and nonionic surfactant were mixed and heated to 60 °C for 30 min, to inhibit the production of vesicles. Acid/base ester hydrolysis was avoided by maintaining $5.5 < \text{pH} < 7.5$. AOT is known to form (oil-free) vesicles on dissolution [3], particularly in mutual conditions of moderate salinity > 100 mM and AOT > 10 mM. A minority of alkane or middle-phase was added to 5 mL aqueous solution of $\gamma_W = 2$ mM or <0.1 % in a volume ratio $\Omega = 400$. This mixture was agitated manually to form a polydisperse emulsion of oil/water. A gentle inversion of

the phial suffices to shear droplets to the 1–10 μm size needed for optical tweezing. The emulsion sample was introduced immediately to the microscope chamber to capture transient behaviour within 100 s of mixing (see Figure 4.1, upper).

Equilibrated samples:

Each composition forming three-phase equilibrium ($S \approx S^*$), $\gamma \gg c\mu c$, typically $\gamma = 1\%$) was allowed to resolve into layers after mixing. Separation took place in 15 mL centrifuge tubes (for formulation scans) or a 100 mL separation funnel (for microscopy samples) for 1 week at $18 \pm 2\,°C$, after which no change in phase volumes was detected. Isolation of each of the three phases in the funnel was confirmed by the persistence of optical clarity on agitation. Where desired, a minority of excess oil or middle-phase was then reintroduced to 5 mL of the excess water phase in a volume ratio $\Omega' = 400$. This mixture was agitated manually to form a polydisperse emulsion. A gentle inversion of the phial suffices to shear droplets to the 1 - 10 μm size needed for optical tweezing (see Figure 4.1, lower).

For temperature insensitivity studies, decane compositions at $\chi = 0.66$ across $120\,\mathrm{mm} < S < 220\,\mathrm{mM}$, varying from WI - WIII - WII were included. For samples at temperatures of 20 - 60 °C, incomplete creaming/sedimentation altered the measured phase volumes. These volumetric errors were independent of temperature, and were mitigated by centrifugation at 2 kG.

4.3 Macroscopic phase behaviour

For the heptane/$C_{12}E_5$ system, $\chi_H^* = 0.62 \pm 0.02$ [4] and for the decane/$C_{12}E_4$ system $\chi_D^* = 0.66 \pm 0.02$ [5] are reported. The substitution of Brij-L4 for $C_{12}E_4$ does not alter $\chi_D^* = 0.66$ (see below). The value of S^{**} was determined with simple observations associated with minimum IFT: either (i) a maximum in coalescence rate [6] (resolution of layers after agitation), or more quantitatively, (ii) equal solubilisation volumes independent of γ [7]. It was found that $S_H^{**} = 120 \pm 7$ mm and $S_D^{**} = 190 \pm 10$ mm respectively; the latter resembles the value of $S_D^{**} = 170 \pm 10$ mm determined similarly for pure $C_{12}E_4$. Even though the optimal salinity of the temperature-sensitive

AOT system, $\chi = 1, T = 25$ °C, decreases from 45 mm to 30 mm on water deuteration, the optimal conditions S^{**}, χ^* of the H_2O and D_2O T-insensitive systems are indistinguishable.

The apparent phase volume fractions of Winsor equilibria at $\chi = \chi^*, S = S^**, \Omega = 1$ remained constant within error ($<5\%$ variation) over the temperature range 20 °C – 90 °C after thermal equilibration within ± 1 °C for 1 h in a water bath. This volumetric temperature sensitivity $(\partial V/\partial T)$ is an order of magnitude lower than for the Winsor III range of 10 °C – 75 °C reported [8] for the decane/$C_{12}E_4$ system at $\chi = 0.60 \pm 0.01$. χ was reproducible to a precision of ± 0.02.

4.4   Microscopic behaviour of isolated phases under optical tweezing

4.4.1   Microdroplets of oleic in aqueous phase

In this section, phases that are separated manually from the three-phase equilibria (according to § 4.2.2) are referred to as 'isolated' phases. At all compositions χ, γ in both heptane and decane systems, isolated oil in isolated water appeared homogeneous and unresponsive to the focused laser. Excluding the middle phase has removed the reservoir of surfactant. The absence of ULIFT suggests that the surface is vulnerable to surfactant starvation at the $c\mu c$ levels in oil and water. Also, the $c\mu c$ of the nonionic surfactant in oil, $c\mu c_{ON}$, is far greater than that of the ionic surfactant in either phase (Table 1.3), so if oil and water phases isolated at some intermediate $\chi \approx \chi^*$ are recombined at $\Omega = 1$, the solution consists overwhelmingly of nonionic surfactant ($\chi_{c\mu c} < 0.05$). However, the amphiphilic ratio in the microemulsion monolayer within the recombined emulsion, χ_M, is *increased* relative to the fraction χ of all ionic surfactant in the initial three-phase equilibrium. For

efficient formulations in which the volume of the monolayer ϕ_S is negligible,

$$c\mu c_{I,N} = \frac{\Omega \; c\mu c_{IW,NW} + c\mu c_{IO,NO}}{\Omega + 1} \tag{4.4.1a}$$

$$c\mu c = \chi c\mu c_I + (1 - \chi)c\mu c_N \tag{4.4.1b}$$

$$\chi_{c\mu c} = \chi \frac{c\mu c_I}{c\mu c} \tag{4.4.1c}$$

$$\chi_M = \frac{\chi\gamma - c\mu c_I \chi_{c\mu c}}{\gamma - c\mu c} \tag{4.4.1d}$$

The rigidity of the oil in water emulsions produced from a three-phase mixture of low $\gamma \approx c\mu c$ implies that the temperature sensitivity is restored, which agrees with $\chi_M \gg \chi$. It is surprising that the IFT of an oil/water interface depends on the amphiphilic ratio *of the microemulsion interface* and not that of any of the constituent phases, even when the microemulsion is not explicitly present. It is known from the Chun-Huh relation that the properties of the microemulsion are determined by the IFT of the monolayer. The observation above provides evidence for the more profound reverse conjecture - that the monolayer and microemulsion are mutually determined.

The strong dependence of $c\mu c_{NO}$ on temperature [9] causes the nonionic surfactant to preferentially partition into the oil phase and the monolayer to become depleted in a way that increases χ_M at high T. However, the change *in situ* of $c\mu c_{NO}$ due to laser heating here is less than a factor of 1.3. The effect on χ_M is only significant at very low $\chi < 0.2$, very high T and low $\gamma/c\mu c$ and $\Omega_M \approx 1$, which are not conditions encountered here ($\chi > 0.6$, $T < 35$ °C, $\gamma/c\mu c > 3$, $\Omega > 100$).

The reported χ in the initial equilibrium becomes a more accurate estimate of χ_M as $\gamma_M \to \gamma_X$; a three-phase equilibrium amount $\gamma = 1\% \approx 23$ mM is used hereafter. In all experiments, χ_M reflects the bulk temperature sensitivity of the microemulsion droplets at the chosen χ.

4.4.2   Isolated microemulsion phase

In contrast, the isolated middle phase undergoes reproducible microscopic phase transitions under the action of a focused laser. The most immediate of these is a

binary phase separation above a threshold laser power (Figure 4.2, $0 - 40$ s). Subsequently, a third phase nucleates (Figure 4.2, $40 - 42$ s).
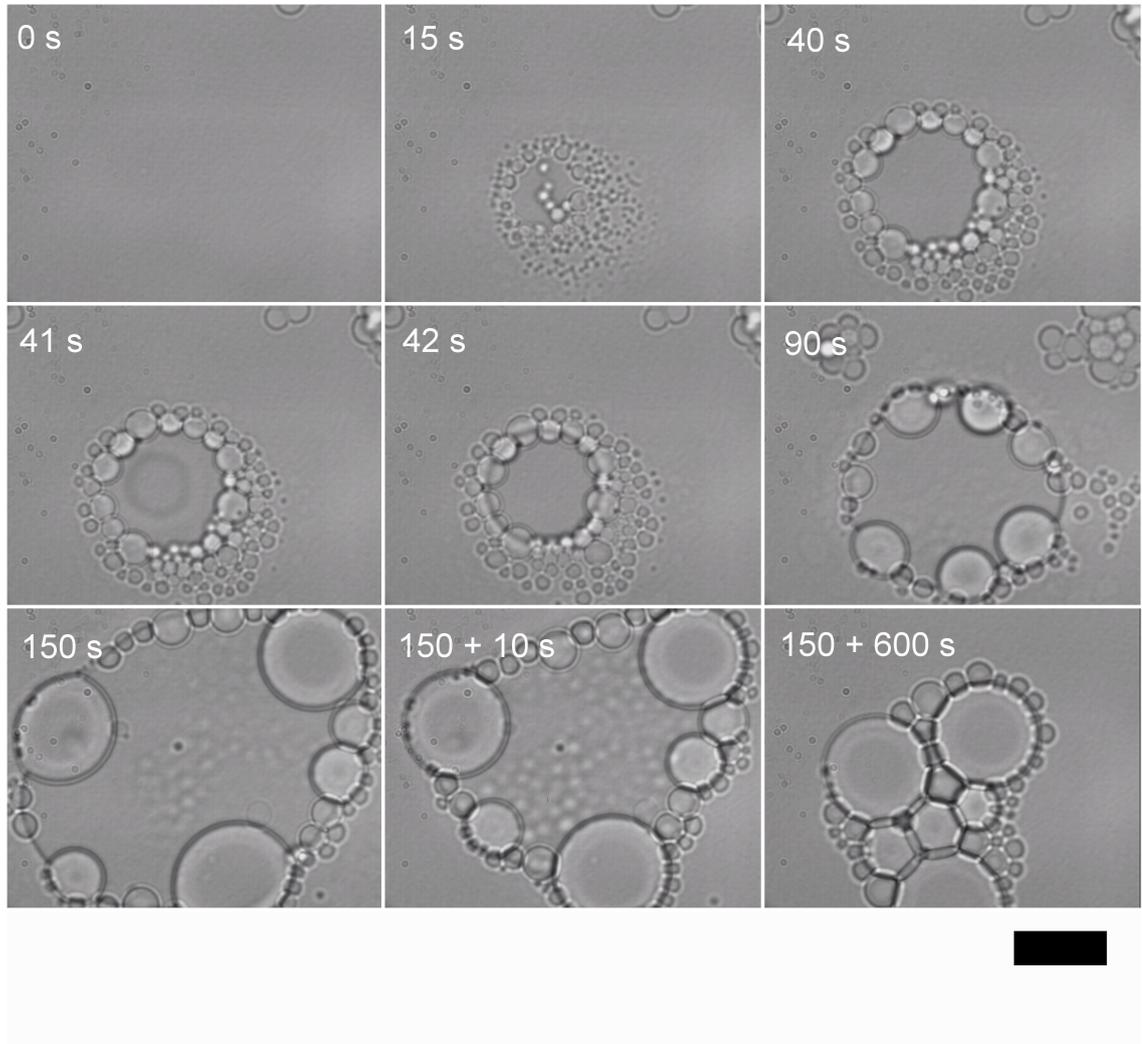
Figure 4.2: Nucleation and aggregation of a water-rich phase A′ expelled from bulk middle-phase (decane/Brij-L4, $\chi_D = 0.66$, $S = 190$ mM) under laser heating at a coverslip, followed by true nucleation of the water-depleted region M′ (at 40-42s; note the new interface expanding rapidly from laser focus). The central region M′ merges with the bulk when the laser heating is removed (at 150 s), but droplets of the expelled phase persist and coalesce. Laser power at sample is 250 mW ($\Delta T \approx 5$ K). Times given denote laser on duration + laser off duration. Scale bar 10 μm.

To understand the events in Figure 4.2, consider an idealised, pseudoternary

$\Omega - \gamma$ phase diagram at fixed χ and $S = S^*$ (Figure 4.3a). Note the point X near $\Omega = 1$, originating from a tricritical point and corresponding to the middle phase at the phase inversion condition. Initially the local composition of the isolated microemulsion phase matches the global composition X at all points. If the quinary mixture matches the ideal scenario $\chi = \chi^*$, then Figure 4.3a would be unchanged at other temperatures; thus laser heating would have no observable effects.

If instead the temperature insensitivity is thought to be imperfect, with $\chi < \chi^*$, then $\mathrm{d}H_0/\mathrm{d}T < 0$ and the stable microemulsion becomes hydrophobic under laser heating (Figure 4.3b). When the laser is turned on, the local temperature increases, and so the material near the focus disproportionates along the tie line A'-X-M' to form a small fraction of aqueous phase A' and a majority of M' (Figure 4.3c). For small changes in the X point, the compositions towards M' are usually indistinguishable from the parent phase X, since they have negligible interfacial tension and refractive contrast, whilst those approaching A' quickly become water-rich. Thus at first, only one type of droplet appears to nucleate (Figure 4.2, $0-40$ s). Since these droplets are water-rich, they have a lower refractive index than the parent middle phase and are expelled from the laser beam. The beam occupies an hourglass-shaped volume above and below the focal plane. The droplets therefore congregate in a ring about the focus in the focal plane. Nucleation of micron-sized aqueous droplets progresses until the focal region becomes adequately water-deficient and oil-rich, nearing the limit M', to create a visible interface with the parent X (Figure 4.2, $40-42$ s).

The first indication of this new interface is the partial wetting of the expelled droplets, which cease to be spherical and instead adopt lens-like shapes that satisfy Neumann's Triangle for the interfacial tensions between X, M' and A' (Figure 4.2, $42-150$ s).

If the laser is then turned off, the interface between the water-deficient phase M' and the parent X becomes diffuse and the large thermal fluctuations of the interface indicate vanishing interfacial tension. The region rapidly shrinks in volume, merging with the surrounding parent phase in a matter of seconds (Figure 4.2, ≥ 150 s).

The water-rich droplets do not appear to change in size, but become spherical when the M′-X boundary disappears. Over the space of several hours, the droplet volume fraction decays very slowly, until the uniform composition X is finally reattained.

The persistence of droplets is unexpected. If the phase behaviour is reverted to that at ambient temperature, both compositions M′ and A′ should be similarly unstable. Moreover, it is possible to identify these as metastable droplets with compositions A-E_A, in which they enrich even further in water (Figure 4.3d). To understand the compositional pathways taken between equilibrium points on the diagram, refer to the familiar expression for bulk Gibbs free energy, $g_j = \Sigma n_i \mu_i$ as applied to each phase j.

It is written in terms of the quinary components' chemical potentials μ_i, weighted by the molar amounts n_i in each. The (molar) lever rule enables comparison of the effective contributions of each phase to the total chemical free energy of a system, $G = \Sigma g_j$. This idealised energy surface can be mapped onto the (mass fraction) phase diagram, which admits non-equilibrium compositions.

Intermediate compositions are necessarily unstable along a tie line; thus a free energy maximum must occur along its length. Whilst the free energy gradient is steeply negative along all the paths A-E_A and M′/M_B-X, the difference in primary phase separation dynamics must be associated with the free energy barrier along the Winsor tie lines W-E_A-X. This barrier means that the droplets prefer not to change in composition, but instead to dissolve back into the parent phase. A steady refractive contrast is observed. The rate of dissolution is limited by the component that diffuses most slowly. The X and M_B/M′ phases are bicontinuous, encouraging mass transport between them, whilst the droplet is continuous only in the aqueous phase.
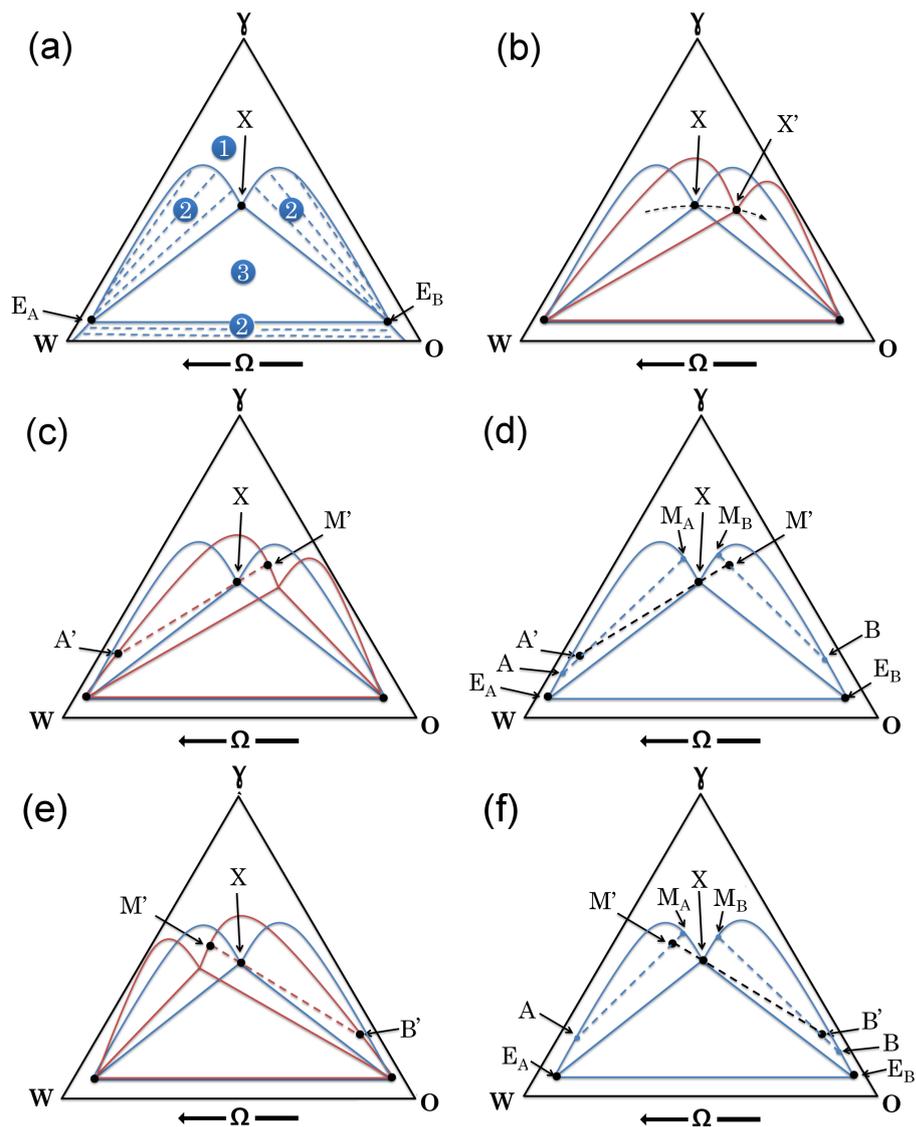
Figure 4.3: A schematic pseudoternary phase diagram describing the predicted sequence of microemulsion compositions during and after laser heating: (a) an idealised, optimal ($H_0 = 0$) system at ambient temperature, with symmetric Winsor III triangle (*blue*). Approximate tie lines are shown for the biphasic regions. (b) In the region of laser heating, the triangle (*red*) tilts towards the solvent preferred by the surfactant at high T, here oil (i.e. $\chi < \chi^*$). (c) At this higher T, stable phase separation occurs in which the microemulsion expels the dispreferred phase, here water-rich A'. (d) Returning to ambient T as the laser is turned off, further phase separation occurs, here of M' and A', whose products are unstable (or metastable) with respect to the initial composition. (e) and (f): As for (c,d), but in the case where oil is expelled from the microemulsion (i.e. $\chi > \chi^*$) such that the roles of oil and water are interchanged. Note that the vertical scale (surfactant concentration) is greatly exaggerated; typically $\gamma_X \approx 2\% wt$.

A 'secondary' phase separation ($M' \rightarrow M_B + B$) is predicted to occur from primary separation products if the temperature returns to the initial value, for example when the laser is turned off. It is difficult to make direct observations and assignments of all phases (see Figure 4.9e), since no more than three phases may form a mutual boundary. Even if the minor products of secondary phase separation are created spontaneously, they may be present in small amounts, and exist on a spectrum of non-equilibrium compositions which resemble one another closely.

If the stage is translated while the laser is on, the rate of A'/M' primary phase separation in the new location tends to exceed the rate of merging in the original location. The laser heating decays toward ambient T only over a distance of hundreds of microns, or several fields-of-view from the focus. As the separated phases build up, a three phase junction forms (Figure 4.4). The interaction of the laser with this junction is interesting, since the refractive indices follow the order $M' > X > A'$. As for the unrestricted A'/M' boundary (Figure 4.4e), the oily M' is deformed to occupy the focal volume and displaces both water and to a lesser extent, parent phase X. The parent phase is unable to displace water as a result. Further nucleation of A' occurs along the M'/X interface (Figure 4.4a-c), since the thermal conductivity of M' is poorest. The contact angles are initially about $120 \pm 10°$ suggesting very similar IFTs between the three phases. When the laser is turned off and M' starts to merge with X, the $X/A'/M'$ angle immediately collapses to $180°$, which corresponds to a vanishing $\sigma_{M'X}$ tension as the $\sigma_{A'M'}$ and $\sigma_{A'X}$ tensions become similar (Figure 4.4d).

The phase separation could in principle be driven by either optical or thermal effects. To distinguish the two, D_2O was substituted in place of H_2O, which has an absorption coefficient at 1064 nm that is far lower, whilst having an almost identical refractive index. In the D_2O-substituted microemulsion, the laser causes no phase transition at powers < 190 mW, unless the focus travels within about 20 μm of the coverslip. The soda lime glass heats more efficiently than the fluid, showing that the phase dynamics are thermally-driven.
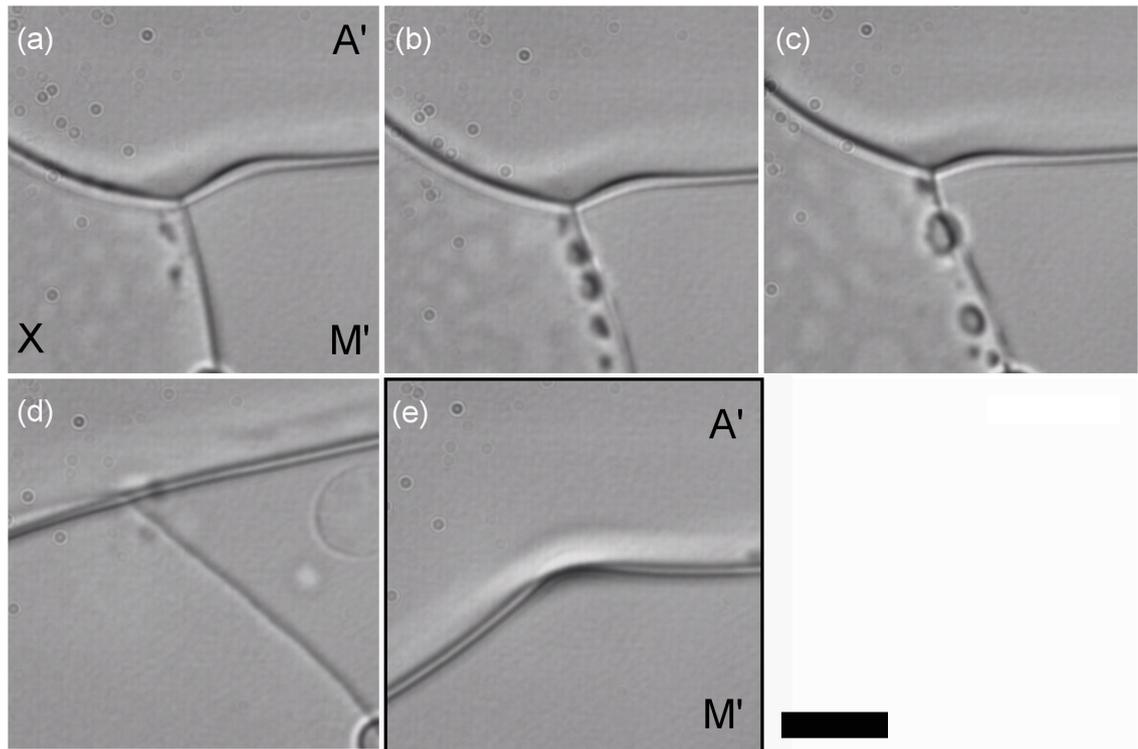
Figure 4.4: (a-c) Laser on: a three-phase boundary produced by primary phase separation of the bulk microemulsion (decane, $\chi_D = 0.66$), also deformed by the optical forces. Nucleation of water-rich material continues along the oil-rich surface between X and M′; (d) Laser off: at ambient temperature, the oil-rich daughter phase equilibrates with the microemulsion. The refractive contrast, wetting angles and IFT of the lower interface decrease. The water-rich phase is largely unaffected; (e) Comparison with the deformation between daughter phases A′ and M′. Laser power is 250 mW ($\Delta T \approx 5$ K). Scale bar 10 μm.

In the centre of the channel, homogeneous nucleation can occur only above the threshold >190 mW or an estimated $\Delta T = 2.4 \pm 0.4$ K. For comparison, the threshold power for H_2O-based microemulsion is 100 mW in the centre of the cell, where a similar $\Delta T = 2.0 \pm 0.3$ K is estimated. The optical stresses are not significantly different in H_2O and D_2O media, being of like refractive index, but D_2O heats far less. The higher power requirement for phase separation in D_2O, commensurate with an equivalent increase in temperature, indicates that thermal mechanisms are dominant. No nucleation of a separate D_2O-depleted phase (in the manner of

Figure 4.2) was observed, which reflects a slower rate of phase separation relative to mass transport.

In the central location, the absorptive flux is most efficiently concentrated near the droplet, which should experience a maximal temperature increase if the medium is uniform. The region depleted of heavy water does not form an interface with the parent. It seems that, despite the optical gradient, the low depletion rate is compensated for by inward diffusion of D_2O and outward diffusion of decane.
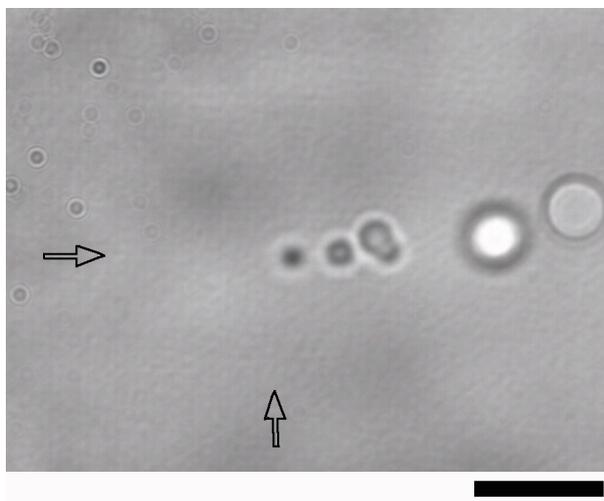

Figure 4.5: Nucleation of a heavy-water-rich phase expelled from bulk middle-phase (D_2O-decane $\chi = 0.66$ system) under laser heating. The arrows mark the location of the laser focus. Neither the laser or stage are moving; nuclei grow and drift out of the field of view under a convection current. Laser power at sample is 250 mW ($\Delta T \approx 5$ K). Scale bar 10 μm.
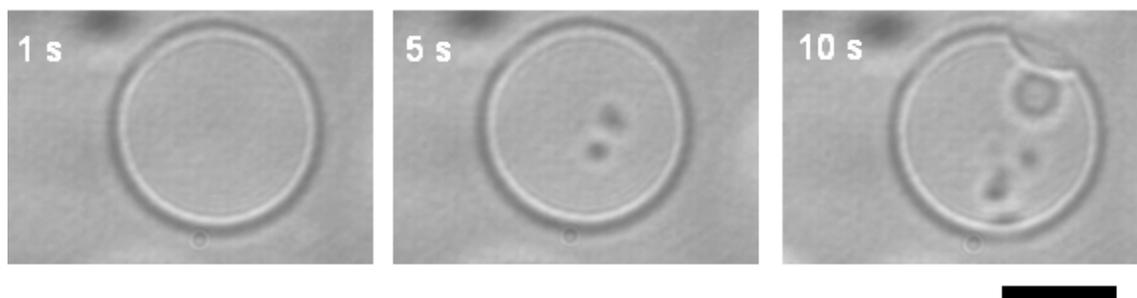
Figure 4.6: Nucleation and coalescence of a water-rich phase from a middle-phase droplet (heptane, $\chi_H = 0.66$) immersed in aqueous medium. Laser power is 200 mW ($\Delta T \approx 4$ K). Scale bar 3 μm.

4.4.3 Microdroplets of microemulsion in aqueous phase

A droplet of microemulsion was studied in the excess aqueous phase. Under ULIFT conditions, the droplet can be optically trapped and deformed. As before, the focused laser was able to nucleate aqueous droplets within the parent (Figure 4.6). However, laser powers >100 mW were sufficient to induce nucleation as the surrounding water contributed about the same amount to the laser heating as the microemulsion. At high powers >200 mW, thermal convection of the daughter droplets within the parent was observed. At low powers, these daughters coalesced with the aqueous continuum.

For $\chi < \chi^*$ (*e.g.* heptane/H$_2$O, $\chi = 0.62$), at higher powers, the internal aqueous drops did not merge with the external aqueous phase. Unlike similar observations of laser-induced material exchange in microemulsions[10], the total volume of the droplet did not appear to reduce from observations of the cross section. It appears that the monolayer around each nucleus forms the inner leaflet of a bilayer, and is matched with a section of the droplet interface that forms the outer leaflet. The water droplets remain within the parent droplet, separated from the external aqueous phase by an oil-swollen bilayer. This mechanism drives two irreversible phenomena:

1. *Myelins.* Following nucleation (Figure 4.7a-b), the water droplets inside the parent droplet become increasingly apparent. Through phase transfer, the parent droplet develops gradually into a cluster of <1 - 3 μm wide, tubular,

radially extending vesicles surrounding a rigid oily core of increased refractive contrast (Figure 4.7c). Superficially, this resembles the sequences of lyotropic phases formed at high surfactant concentration [11], or when pure surfactant dissolves in water. However, no birefringence was detected with crossed polarisers.

2. *Giant vesicles (GUVs).* The droplet interface fluctuates and buckles violently over < 1 s, thereafter becoming plastic, with little interfacial recoil when deformed and released by the laser. The phase separation occurs rapidly enough for only one giant vesicle to be produced instead of many separate nuclei, replacing the droplet in its entirety. The myelinic structure resulting from (i) may also become a giant vesicle, albeit more slowly, when irradiated again after several minutes (Figure 4.7d-f). Although multilamellae are clearly visible to begin with, the endpoint appears to be a giant *unilamellar* vesicle (GUV). The refractive contrast drops drastically, suggesting that the oil has solubilised in the continuous phase, or resides only within the bilayer.
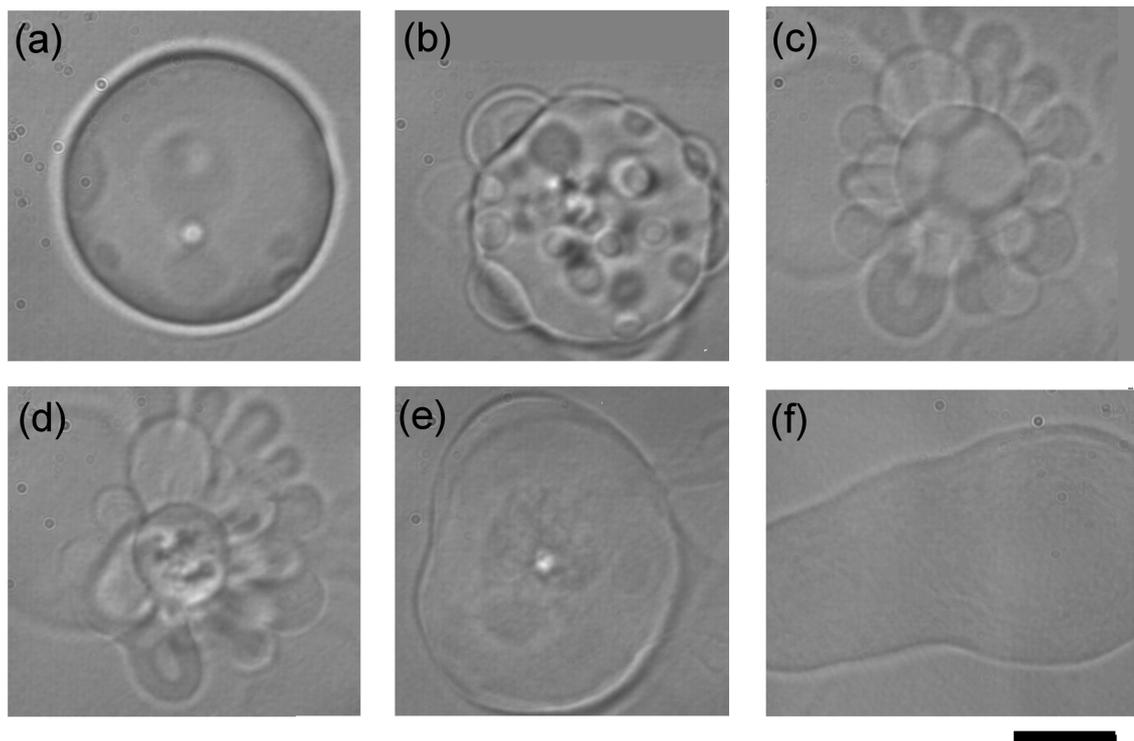
Figure 4.7: Myelinic transition followed by secondary GUV transition (heptane, $\chi_H = 0.62$): (a) water nucleation from a spherical microemulsion droplet; (b) phase transfer of water nuclei producing compact, surface-bound vesicles; (c) laser off: the vesicles unfurl and oil spreads into the bilayers; (d-e) laser on: the myelins collapse into a single giant vesicle, which remains trappable but (f) eventually becomes impervious to water nucleation. Scale bar 5 μm.

The low preferred curvature causes the myelins and GUVs to become more cylindrical over time, such that the average surface curvature also decreases. Under optical manipulation, tubular branches can be pulled out (see Figure 4.7, *(d)*), tens of μm long, which, until a yield strain is exceeded, retract slowly if released. If encapsulated within the bilayer, oil does not fully wet the bilayer's interior but tends to form a shallow lens on one side of the vesicle which allows strong trapping. The dewetting is consistent with a positive Hamaker constant for an alkane film in water. Rarely, the oil even forms a separate, trappable droplet enclosed by the vesicle. Solubilisation of oil inside vesicles to this extent is unusual even at low preferred curvature [3]. Unlike the systems studied in [12], the vesicles never undergo 'pearling'

when perturbed with the laser. There is no bilayer asymmetry which might give rise to vesicular distortions such as pearling. Both sides of the bilayer are equilibrated with oil, and have equally low spontaneous curvature. Vesicle formation was more common in the heptane system. The minimum IFT is lower in the heptane system than in the decane systems ($\sigma \lesssim 1$ μN m^{-1}) and the bending moduli are similar ($\kappa \approx 1.1$ $k_B T$, see § 1.6.1).

Notably, a mixture of surfactants of opposite preferred curvature is used. The *local* ratio of surfactants χ provides a degree of freedom by which the inner and outer monolayers may disproportionate in composition; in principle this could act to stabilise the opposite real curvatures present in a bilayer. However, the spontaneous curvature of the monolayer varies only on the order of μm^{-1}K^{-1}. The laser heating generates a small change in free energy of bending $\sim \kappa \Delta H_0^2$ relative to the excess free energy of demixing, which is far denser, of order $k_B T$ per adsorbed surfactant molecule. Simple bending will occur without resort to surfactant disproportionation into an asymmetric bilayer.

If $\chi > \chi^*$ (*e.g.* decane/H$_2$O, $\chi = 0.76$), the nucleation of droplets occurs as before (with an analogous sequence of phase diagrams, see Figure 4.3), except that the microemulsion expels excess oil (X $\rightarrow$ B' + M$'$ phase separation) under laser heating rather than aqueous phase. The nucleated oil droplets have a higher refractive index than the parent droplet, so are trapped at the laser focus. They are also optically deformable (Figure 4.8). Vesicles were never observed in this system. If the laser is removed, the oil merges with the oil-deficient phase over minutes rather than hours. As the continuous phase is aqueous, rather than microemulsion in this case, it cannot supply oil to the oil-depleted region. Without this competition, the oil droplets nucleated by the laser redissolve more quickly.
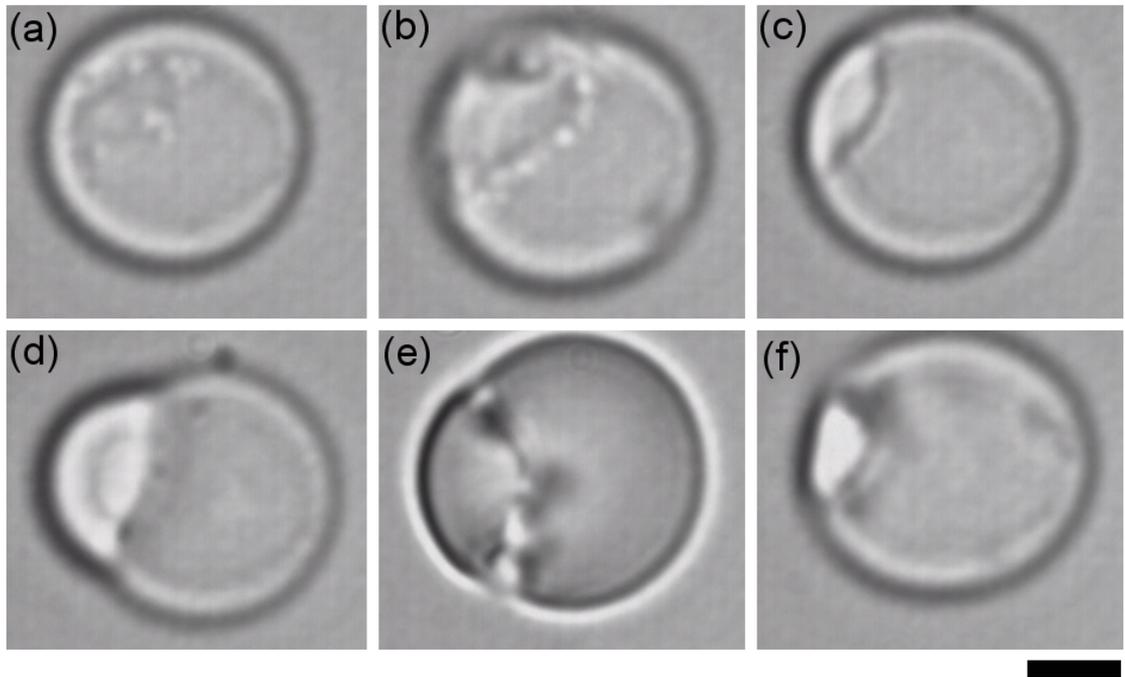
Figure 4.8: (a-b) Nucleation, (c) partial wetting and (d) trapping of oil B' expelled from a microemulsion droplet in aqueous medium (decane $\chi_D = 0.76$ system); (e) nucleation near the oil surface and convection of nuclei within the droplet. Laser power is 250 mW ($\Delta T \approx 4$ K); (f) laser off: vanishing tension and shrinking/merging of B' with the parent phase. Scale bar 4 μm.

Microemulsion-based nanothreads

For sufficiently low IFT two traps can be used to bifurcate the microemulsion droplet (Figure 4.9). Around the bifurcation point at high powers, the neck of the droplet and the trapped nodes differ noticeably in stiffness. If the IFT decreases with laser heating, the thread experiences compressive Marangoni forces which stabilise it. The thread can be seen to flex under viscous drag if the nodes are translated. Alternatively, if the IFT increases with T, the thread experiences tensile Marangoni forces which make it more likely to break when stressed.
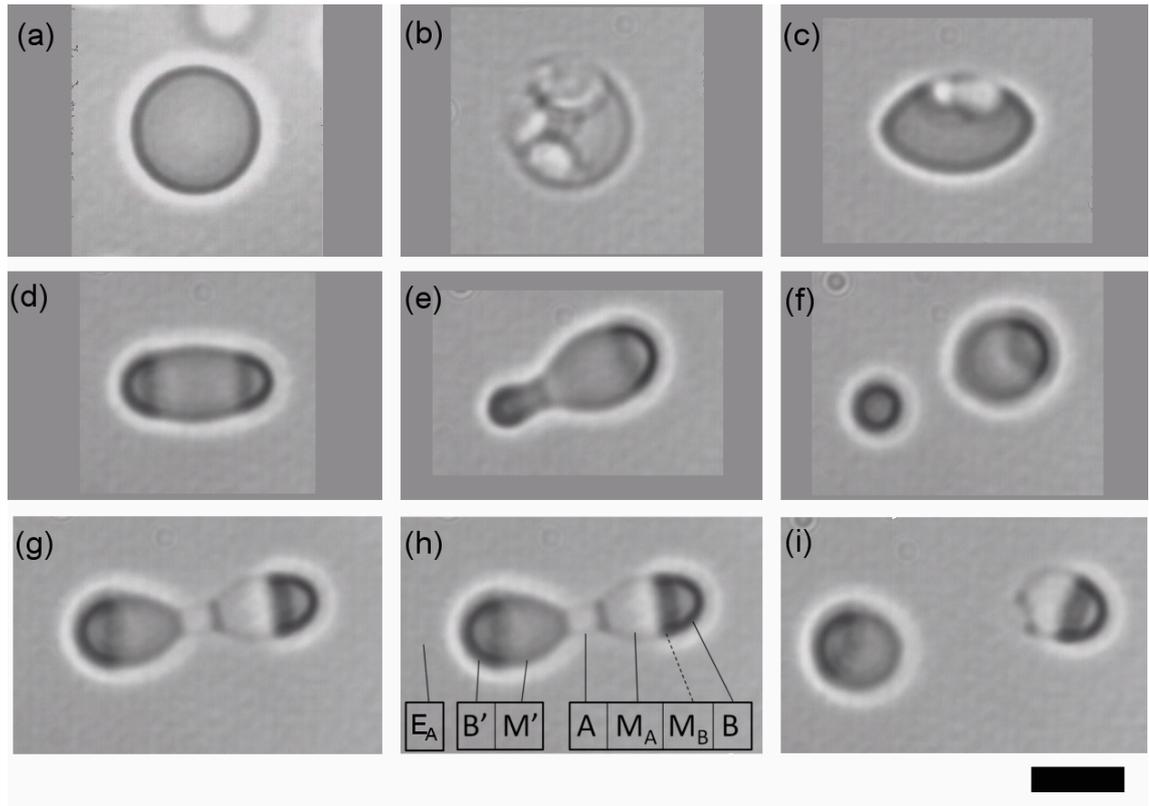
Figure 4.9: (a-b) Nucleation of oil B' from a middle-phase X droplet (decane system, $\chi_D = 0.76$) in excess water E_A under laser heating with two coincident traps; (c) traps are displaced by 6 μm: nucleation is arrested and the droplet deformed; (d) oil B' nuclei accumulate at the trap nodes, displacing the water-rich microemulsion; (e-f) further trap separation to 9 μm: the droplet undergoes asymmetric bifurcation with a thread (not resolved). Primary phase separation is still visible; (g-h) traps merged to 0 μm and split again to 9 μm: the left trap contains the primary separation products (Figure 4.3e) and the cooler right trap contains the secondary products (Figure 4.3f). The phases' proximity to the traps corresponds to the hierarchy of increasing refractive index; (i) the phases do not change further on bifurcation or at rest over the timescale of a few minutes, but the water-rich bridge does not support a thread connecting the two droplets. Laser power at sample is 150 mW (*left*) and 100 mW (*right*) ($\Delta T \approx 3$ K, 2 K). Scale bar 4 μm.

This explanation is consistent with the observations of beads of oil suspended along the thread being pulled away from the centre. Not only does the thread pro-

vide a gauge of the local interfacial tension, but also gives insight into the thermal distribution due to laser heating, and the thermal response of the interface. Rotating the half-waveplate halfway between the respective Malus maxima equalises the trap strengths for each node. For an equilibrium shape to be attained, the optical pressure across the thread must compensate the Laplace pressure by supporting flow. It does so until the nodes become equal in size and shape, reflecting that the optical trap strength greatly exceeds the IFT.

In separating the traps, the laser heating is also divided. Violent nucleation of the kind leading to vesicles is replaced by gradual phase separation, like the bulk case. At small separations and low powers, the oil-rich expelled phase is trapped at the foci, while the water-rich microemulsion is displaced from the traps to form a bridge between the two oil phases. In Figure 4.9e, the neck is formed by expelled oil B attached to microemulsion M′, while in Figure 4.9g-h the neck is an aqueous phase A. If the division of laser power is altered so that one trap is cooler and weaker than the other, a different kind of phase separation occurs (Figure 4.9g-i). The appearance of seven rather than three unique phases is surprising; the temperature variation across the length of the droplet enables both primary ($X \rightarrow B' + M'$) and secondary ($B' \rightarrow B + M_B$, $M' \rightarrow A + M_A$) phase separation to be observed simultaneously (Figure 4.3). Although the brightfield response partly depends on the local curvature and thickness of the droplet, a distinction between phases can be made by comparing the refractive quality of the interfaces. The seven-phase arrangement is independent of further trap displacement, but does not support a thread. It is possible, however, to connect two vesicles with a thread of middle phase (not shown).

It appears that the composition of a stable thread in aqueous continuum must be oily or middle phase, *i.e.* oil-continuous. Since the bending and thermal energy are comparable, the width of the thread (Chapter 5) is roughly the same size as the domains of the corresponding microemulsion phase! It is therefore intriguing that microemulsion phase and oily threads are able to coexist, and moreover that oil-rich microemulsion phases are able to *support* threads themselves. Is it possible that

the Gibbs surface no longer corresponds to the surface over which the interfacial tension acts? How a bicontinuous thread can support tension along its length is a open problem, one which is intimately related to the interfacial fluctuations between microemulsion and excess phases.

For D₂O-substituted microemulsion droplets dispersed in excess D₂O (lower phase of WIII), no transitions were observed. The droplets were still deformable at ULIFT. The lower absorbance of the deuterated medium provides ΔT lower than the threshold for phase separation at the powers investigated (<250 mW).

4.5 Microscopic behaviour of nonequilibrated phases under optical tweezing

4.5.1 Microdroplets of oil in aqueous solution

For practical applications the situation where a pure oil is dispersed in an aqueous surfactant solution without equilibration, is of interest. As ULIFT is desired, an input aqueous concentration of surfactant $\gamma_W = 2$ mM is chosen, roughly $5 \times cmc$ as recommended by Binks [13]. The resulting concentration is barely diluted, $\gamma \approx \gamma_W / (1 + \Omega^{-1})$. The $c\mu c$ itself is very difficult to measure volumetrically as, by definition, it presents an infinitesimal amount of middle phase. Any remaining surfactant above the $c\mu c$ will tend to create additional monolayer, thereby solubilising the oil into middle phase. Thus the behaviour of the emulsion droplets is predicted to fall on a spectrum between that of (i) excess oil droplets in excess water and (ii) middle phase droplets in excess water. One might expect equilibration to follow emulsification fairly rapidly, limited by diffusion, to arrive at a stable mixture of oily E_B and microemulsified X droplets. The reality is more dynamic; sporadic cases were observed at $\chi = 1$ where oil droplets spontaneously appeared

1. to change in composition towards microemulsion erratically,

2. to solubilise into the continuous phase (either shrinking or shedding small droplets), or

3. to form vesicles over the order of tens of minutes.

The variety of composition and latency of equilibration are likely related to the free energy barriers between pure oil O (or excess oil E_B) and middle phase X. This is analogous to the water expelled from the $\chi < \chi^*$ microemulsion (§ 4.4.2) which is metastable even at ambient temperature.

For pure AOT, $\chi = 1$, these processes accelerate markedly in the vicinity of the phase inversion condition, just as observed by [14] and [15], although observed here at much longer times after mixing. It is this heating towards the phase inversion which appears to drive the transitions when droplets interact with the laser beam. If the temperature is changed very quickly to just *through* the phase inversion temperature, the oil droplets may burst and disperse in ms (see Figure 3.8), in the vein of catastrophic phase inversion [16]. This implies that a high internal volume fraction of aqueous phase is nucleated quickly, much like a spinodal decomposition.

4.6 Thermal or optical effects?

How can the thermally-driven effects at microscopic level be reconciled with the temperature insensitivity on the macroscopic level? In the first case, a 60 μm field of view is studied at video rates of 60 Hz, and in the latter, 10 cm phase tubes are studied at 20 min intervals. Both situations represent thermal equilibrium, since the length and time scales of observation fulfil the diffusive relation $L^2/t < \psi/\rho c_P$, where ρ and c_P are the density and heat capacity of the sample. Thus, the disparity remains unless the volume fraction of any nucleated phases at complete separation (e.g. in Figure 4.3c and Figure 4.4, if all possible A$'$ is extracted from X) is undetectably small, $\phi(A') < 5\%$. This is very difficult to verify using only 2D imaging, but appears unsatisfactory (see § 6.3.5). This question can be resolved by looking at the nature of the microscopic driving forces and the convective motion they promote.

A similar discrepancy between macroscopic and microscopic behaviour has been made, and water nucleated under laser heating, for a different bicontinuous microemulsion [10] of higher optical absorbance, albeit with a more diffuse laser, which

emphasised the effect of thermodiffusion over optical gradient forces. As in the present work, fluctuations of ± 2 K in the ambient temperature never give rise to phase separation even on the microscale. Therefore $\chi \approx \chi^*$ must hold here such that the equivalent laser power (200 mW in water medium) would be insufficient to cause phase separation simply by *uniform* photothermal heating. This work provides counterexamples of oil and water nucleation at the focus at much lower powers (~ 190 mW water, 150 mW oil from M drop in water), which implies that there must be an additional mechanism.

In cases of very high power absorbance $\Delta T > 3$ K, advection occurs visibly over the longest scales of $L \sim 10$ - 100 μm. This is most prominent in large oil reservoirs at the coverslip, whose water nuclei recirculate in the thermal flow. Advection does not appear to alter the shape of the parent oil droplet (§ 4.7) Including any minor influence of advection constitutes an involved hydrodynamic problem that lies outside the scope of this thesis. However, the diffusive timescale for thermal equilibration of the chamber is on the order of $t = 10$ ms, which allows changes in laser heating to be considered instantaneous with laser power. The emergence of subdroplets is thought to be limited instead by homogeneous nucleation and growth processes, as determined by the quasi-steady state optical and thermal distributions. The behaviour of these nuclei at the laser focus will depend strongly on their size, R_N. The competition between optical stabilisation (for subwavelength, high-index objects the potential scales as $-R_N^4$) and the surface energy penalty (that scales as R_N^2) determines a critical nuclear size. For ULIFT of 1 μN m^{-1}, the critical radius of an oil droplet is about $R_N = 0.1$ μm and the nucleation barrier is of a feasible order, 15 k$_B T$.

Phase transfer and recirculation of nuclei are stimulated by a combination of advective forces: either optical (electrostrictive) or thermophoretic gradients. The latter consists of Marangoni and thermodiffusive components. Buoyancy or density effects are thought to be negligible for such small nuclei ($F = 4\pi \Delta \rho g R_N^3 / 3 \sim 1$ fN).

For oil-rich phases, optical forces are 'attractive', i.e. directed towards the focus (high refractive index), whilst thermodiffusive (due to low thermal conductivity) and Marangoni (assuming ambient temperature corresponds to minimum IFT) forces are repulsive. For water-rich nuclei, optical and Marangoni forces are repulsive, whilst thermodiffusive forces are attractive. The optical forces ($F \approx \Delta n P/c \sim 1$ pN) dominate on the scale of the focal spot size i.e. with a micron of the trap focus, whilst Marangoni forces ($F = 4\pi R_N^2 \nabla T \cdot \partial\sigma/\partial T \sim 0.1$ pN) extend further, over the thermal decay length of $L = 1/4\pi\alpha \sim 1$ mm. The Marangoni effect is strong for phase-inverting systems, but again relies on some pre-existing temperature sensitivity, or $\chi - \chi^* \neq 0$. This is exaggerated in cases of strong optothermal absorption such as the phase separation and advection at the coverslip.

Oil nucleation is predicted to occur only at ULIFT~ 1 μN m^{-1}, a condition that is largely guaranteed by the existence of the bicontinuous microemulsion. However, classical nucleation theory fails to account for the production of water (low-index phase) under thermal steady state, since in its description, water nuclei are never stabilised by introduction of the optical field. The observed water nucleation is likely to be driven in part by proximity to the thermal phase boundaries as described in Figure 4.3, though detailed knowledge of the temperature dependence of the phase diagram is lacking. Given that small, free oil droplets within about 10 μm are cleared quickly by thermophoresis, the water must be relatively thermophilic. Nucleation of water could be incited instead by the thermal gradient around the laser axis. Thermodiffusion is one mechanism known to cause phase separation very near the critical temperature of binary liquid systems that are related to microemulsions [17]. However, the Soret effect is highly formulation-dependent in a manner that is not easily predicted. These forces are also typically weak compared to others considered here ($F \approx k_B T \cdot S_T \nabla T \sim$ fN) given the typically low values of the Soret coefficient $S_T \sim 0.01$ K^{-1} [18].

If only the dominant photothermal mechanism is considered as χ increases through the balanced amphiphile ratio, χ^*, water nucleation on laser heating (a nonionic-like,

more hydrophobic microemulsion with higher T) is expected to cease in favour of oil nucleation (an ionic-like, more hydrophilic microemulsion with higher T). Laser-induced nucleation of water occurs at the macroscopically balanced value $\chi_D^* = 0.66$. Also, while oil nucleates at $\chi_D = 0.76$ as expected, it does so at a similar rate to the water in the $\chi_D = 0.66$ case. The similar rates could indicate that χ^* lies roughly equidistant from the two values. In effect, χ^* appears to shift upwards (away from $\chi_D^* = 0.66$) in the presence of the laser, even though it is unaffected by bulk heating. It is tempting to attribute this shift to a purely optical effect. However, the optical gradient attracts the high-index phase, oil; therefore, the laser would again be expected to promote the nucleation of oil rather than water droplets at the focus (instead reducing the effective χ^*). A possible scenario is that χ^* in the absence of the laser is slightly underestimated and the dependence of the nucleation rates on $\chi - \chi^*$ is weak except anomalously at the balance point. A more consistent conclusion is that Soret-type thermophoresis of water towards the focus occurs at an unprecedented magnitude in this system, such that it overcomes both Marangoni and optical forces. These hypotheses could be tested by scanning χ more thoroughly, at different laser powers, to find the point at which neither oil nor water are nucleated at the focus.

4.7 Appendix: Laser heating

4.7.1 Premise

The optical absorption of a focused laser produces inhomogeneous heating even within a uniform volume. Given the thermal sensitivity of properties such as interfacial tension and density that are significant to the shape and dynamic stability of the examined droplets, the 3D thermal distribution is of interest. It is possible to refer to a qualitative extent of the heated region, or otherwise resort to semi-analytical treatment (or a fully discrete numerical model, see § 4.7.2).

Description of a localised heat source on the local temperature change ΔT requires the thermal conductivity, ψ and Beer absorption coefficient at 1064 nm wave-

length, α_{1064} (Table 4.1). By dimensional arguments, the peak temperature rise in a homogeneous medium necessarily has order $\Delta T/P \propto \alpha/\psi = 24$ KW^{-1}. These ratios act as 'photothermal resistances' for each medium.

	H$_2$O	D$_2$O	n-heptane	n-decane	soda-lime glass
n_{1064}	1.324[a]	1.323[a]	1.387[b]	1.404[b]	1.513[c]
ψ (W m^{-1}K^{-1})	0.598[d]	0.589[d]	0.123[d]	0.132[d]	0.94[d]
α_{1064} (m^{-1})	14.6 ± 0.5	1.3 ± 0.1	4.0 ± 0.3	5.0 ± 0.1	58[c]
α_{1064}/ψ (K W^{-1})	24 ± 1	2.2 ± 0.1	33 ± 3	38 ± 2	62

Table 4.1: Refractive indices and photothermal properties of the emulsions' constituent liquids and substrates at 25 °C. Absorption coefficients α are natural (corresponding to 1/e optical intensity) rather than decimal. [a][19]; [b][20]; [c][21]; [d][22].

4.7.2 Detailed analysis for bulk heating

The coupled optics-heat problem in the bulk is asserted compatible with an axisymmetric cylindrical coordinate system (Figure 4.10).

Neglect of advection

Most physical effects which break axisymmetry, such as optical polarisation, are insignificant to energy flow. However, convection cells cannot be described within this model symmetry. They are expected to appear when the characteristic length scale l or advective flow velocity v exceed some critical threshold. The Péclet number [23] estimates the ratio between advective and diffusive heat transfer J_{adv}, J_{diff}, and so describes a critical relation $v^*(l)$ dependent on the thermal diffusivity of the medium ζ:

$$Pe_L = \frac{J_{\mathrm{adv}}}{J_{\mathrm{diff}}} = \frac{vl}{\zeta} \tag{4.7.1e}$$

For water at room temperature, $\zeta = 1.43 \times 10^{-7}$ m^{2}s^{-1}. To demonstrate that diffusion dominates at all relevant scales $l < 100$ μm in the problem, consider the
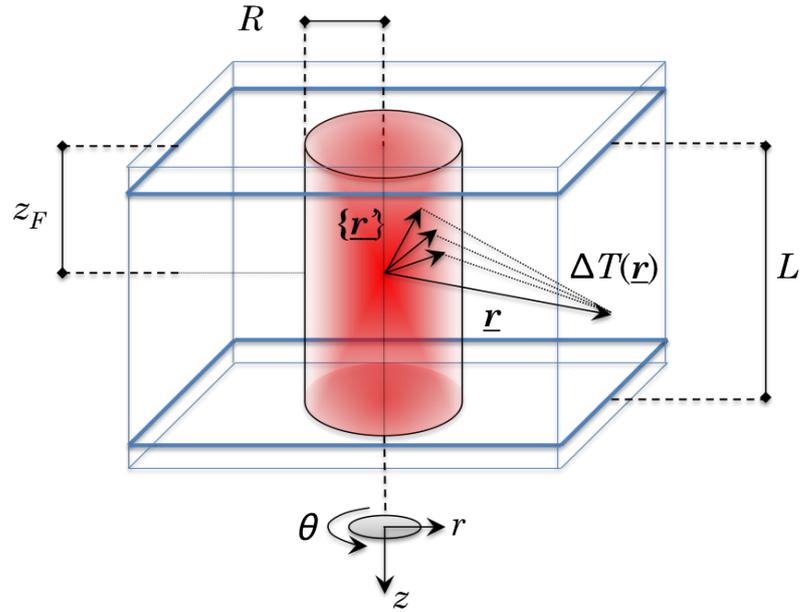
Figure 4.10: A schematic view of the coordinate system and relevant parameters used to determine the 3D temperature profile under laser heating.

desired condition $Pe_L < 1\%$:

$$
\begin{aligned}
v^* &> 0.01 \times \frac{\zeta}{l} \\
&> \frac{0.01 \times 10^{-7} \text{ m}^2\text{s}^{-1}}{10^{-4} \text{ m}} \\
&> 10^{-4} \text{ m s}^{-1}
\end{aligned}
\tag{4.7.1f}
$$

The argument arrives at a contradiction since the convection velocity must be disruptively high $> 10\ \mu\text{m s}^{-1}$ in order for advection to influence the temperature gradients by even 1%. Even without the generality of including advection, it is important to establish a baseline behaviour of a microscopic, isotropic medium subject to the familiar diffusive heat equation.

The heat equation and Green's function

Assuming diffusive heat flow only, the governing equation is Fick's first law of diffusion (also known as Fourier's law of conduction [23]):

$$
\mathbf{J}(\mathbf{r}) = -\psi \nabla T(\mathbf{r})
\tag{4.7.1g}
$$

This describes a relationship between the temperature T and heat flux J as a function of position $\mathbf{r}$ and defines the thermal conductivity ψ. Next, consider a set of parallel surfaces enclosing a point heat source. In the steady state, the heat dissipated is the same as the heat generated. As the flux J through each surface is necessarily conserved, the flux divergence is constant and equal to Q, the power generated per unit volume at the source. This yields the heat equation:

$$\nabla \cdot \mathbf{J}(\mathbf{r}) = Q \tag{4.7.1h}$$

$$\nabla^2 T(\mathbf{r}) = -\frac{Q}{\psi} \tag{4.7.1i}$$

This is an ordinary differential equation whose solutions are additive; as such, the point sources within an arbitrary distribution can be treated individually. For a single point source located at the origin, the temperature response follows the Green's function, $G(\mathbf{r})$, for the 3D Laplacian operator, ∇^2:

$$G(\mathbf{r}) \equiv \frac{1}{4\pi|\mathbf{r}|\psi} \quad \text{which satisfies} \quad \nabla^2 G(\mathbf{r}) = \delta^3(\mathbf{r}) \tag{4.7.1j}$$

where $\delta(x)$ is the Dirac δ-distribution.

The general distributed solution

The convolution properties of a Green's function allow expression of the solution for a real, finite distribution of heat sources using calculus:

$$\Delta T(\mathbf{r}) = Q(\mathbf{r}) \otimes G(\mathbf{r}) \tag{4.7.1k}$$

Options exist for i) integrating over real space or ii) Fourier frequency space, where it is possible to make use of the convolution theorem. Here a real-space approach is used, as it is more intuitive at each step, whereupon subtlety in more approximations might be necessary.

$$\Delta T(\mathbf{r}) = \iiint_{V'} Q(\mathbf{r}') \times G(\mathbf{r} - \mathbf{r}') \, d\mathbf{r}' \tag{4.7.1l}$$

$$\Delta T(\mathbf{r}) = \iiint_{V'} Q(\mathbf{r}') \times \frac{1}{4\pi\psi|\mathbf{r} - \mathbf{r}'|}\, \mathrm{d}\mathbf{r}' \tag{4.7.1m}$$

The thermal flux $J(\mathbf{r})$ is assumed equal to the rate at which optical energy is absorbed. For this, the optical intensity distribution $I(\mathbf{r})$ and the linearised Beer's law definition of the absorption coefficient (per unit length) are given as follows:

$$Q(\mathbf{r}) \approx \alpha I(\mathbf{r}) \quad \text{where } \alpha \equiv \frac{\mathrm{d}\ln I(\mathbf{r})}{\mathrm{d}z} \tag{4.7.1n}$$

Attenuation of the beam intensity across the sample depth L is neglected; this is equivalent to taking the limit $L \ll \alpha^{-1}$, such that the beam focused at z_F is unaffected by the medium.

$$\Delta T(\mathbf{r}) = \frac{\alpha}{4\pi\psi} \iiint \frac{I(\mathbf{r}')}{|\mathbf{r} - \mathbf{r}'|} r'\mathrm{d}\theta'\, \mathrm{d}r'\, \mathrm{d}z' \tag{4.7.1o}$$

A partial solution for the Gaussian beam

The range of integration covers a volume between the parallel plates of the chamber and radially outwards to a cutoff distance R. A realistic choice is determined by the working distance of the objective as $R \approx \pi w_0 \mathrm{WD}/\lambda$.

$$\Delta T(\mathbf{r}) = \frac{\alpha}{4\pi\psi} \int_{-z_F}^{L-z_F} \int_0^R \int_{-\pi}^{+\pi} \frac{I(\mathbf{r}')}{|\mathbf{r} - \mathbf{r}'|} r'\mathrm{d}\theta'\, \mathrm{d}r'\, \mathrm{d}z' \tag{4.7.1p}$$

The intensity $I(\mathbf{r}')$ of a `TEM`$_{00}$ laser beam is described, at least in the scalar paraxial approximation, by the Gaussian beam profile given in Equation (2.1.1e). The relevant integral for the thermal distribution becomes:

$$\Delta T(\mathbf{r}) = \frac{P_0\alpha}{2\pi^2\psi w_0^2} \int_{-z_F}^{L-z_F} \int_0^R \int_{-\pi}^{+\pi} \frac{r'}{|\mathbf{r} - \mathbf{r}'|} \frac{1}{1 + (z'/z_R)^2} \exp\left\{ \frac{-2r'^2}{w_0^2(1 + (z'/z_R)^2)} \right\} \mathrm{d}\theta'\, \mathrm{d}r'\, \mathrm{d}z' \tag{4.7.1q}$$

Axisymmetric reduction

Only the position vector introduces any angular dependence:

$$|\mathbf{r} - \mathbf{r}'| = \sqrt{r^2 - 2rr' \cos\{\theta - \theta'\} + r'^2 + (z - z')^2} \tag{4.7.1r}$$

Thus, the integral is factorised to solve part of it analytically (with the use of elliptic integral functions):

$$\mathscr{I}_\theta = \int_{-\pi}^{+\pi} \frac{\mathrm{d}\theta'}{|\mathbf{r} - \mathbf{r}'|} \tag{4.7.1s}$$

$$\mathscr{I}_\theta = \frac{4}{\sqrt{(r - r')^2 + (z - z')^2}} \mathscr{K}\left\{ \frac{4rr'}{(r - r')^2 + (z - z')^2} \right\} \tag{4.7.1t}$$

where $\mathscr{K}(x)$ is the complete elliptical integral of the 1st kind.

The diffusive thermal distribution is reduced to a 2D numerical integral, which is the general result of this analysis. A full Runge-Kutta numerical integration of Equation (4.7.1t) was performed to yield the 3D temperature distribution, whose axial cut is shown in Figure 4.11.

$$\Delta T(\mathbf{r}) = \frac{2P_0\alpha}{\pi^2\psi w_0^2} \int_{-z_F}^{L-z_F} \frac{1}{1 + (z'/z_R)^2} \int_0^R \frac{r'}{\sqrt{(r - r')^2 + (z - z')^2}} \mathscr{K}\left\{ \frac{4rr'}{(r - r')^2 + (z - z')^2} \right\}$$
$$\exp\left\{ \frac{-2r'^2}{w_0^2(1 + (z'/z_R)^2)} \right\} \mathrm{d}r' \, \mathrm{d}z' \tag{4.7.1u}$$

Special case at the focal point

The highest temperature gain is at the focus $r, z = 0$. Here the elliptical function reduces to the special value $\pi/2$ and expressing the radial part becomes analytically possible in terms of error functions. The subsequent axial integration is over a Voigt-like function which remains intractable. This is also true for the Fourier transform approach suggested above.

$$\Delta T(\mathbf{0}) \approx \frac{P_0\alpha}{\sqrt{8\pi}\psi w_0} \int_{-z_F}^{L-z_F} \frac{1}{\sqrt{1 + (z'/z_R)^2}} \exp\left\{ \frac{2z'^2}{w_0^2(1 + (z'/z_R)^2)} \right\}$$
$$\times \left(\mathrm{erf}\left\{ \sqrt{\frac{2(R^2 + z'^2)}{w_0^2(1 + (z'/z_R)^2)}} \right\} - \mathrm{erf}\left\{ \sqrt{\frac{2z'^2}{w_0^2(1 + (z'/z_R)^2)}} \right\} \right) \mathrm{d}z' \tag{4.7.1v}$$

For an ideal Gaussian beam shape with diffraction-limited focus, the relations $2w_0 \geq n\lambda/\pi NA$ and $z_R = \pi w_0^2/\lambda$ hold. Thus for an numerical aperture $NA = 1.2$

in an aqueous medium of refractive index $n = 1.33$, the dimensions are $w_0 = 188$ nm and $z_R = 80$ nm.

The chosen chamber thickness is $L = 200$ μm, the typical focus at a depth $z_F = 40$ μm, and $R = 150$ μm is taken from the objective working distance of WD ≤ 280 μm. Performing the partial axial integration step on Equation 4.7.1u over 256 intervals with the above parameters for water:

$$\Delta T(\mathbf{0}) \approx \frac{P_0 \alpha}{\sqrt{8\pi}\psi w_0} \times 0.77 \ \mu\mathrm{m} \tag{4.7.1w}$$

$$\Delta T(\mathbf{0})/P_0 = 16 \pm 2 \ \mathrm{KW}^{-1} \tag{4.7.1x}$$

which is of the correct order.

4.7.3 Discussion

The thermal distribution derived here matches that of a finite element model in COMSOL written by GB with the same parameters (Figure 4.11). In each, the peak temperature change drops by half within a typical 2 μm in the radial direction and 8 μm in the axial direction. However, there is a small discrepancy at the peak value within the beam waist; the FEM gave 17.2 K W^{-1}, and the full integration 14.7 K W^{-1}, both of which agree roughly with the semi-analytic result of 16 ± 2 K W^{-1}. The dimensions of the laser focus used in each are slightly different.

The Gaussian beam description $I(\mathbf{r})$ is of limited physical accuracy at the focus, since the paraxial approximation (by which it is derived as a solution to the wave Helmholtz equation) breaks down within $r < \omega_0, z < z_R$ for NA > 0.5. The true profile is somewhat broader. In the semi-analytic and full integration methods this is compensated for by the use of a modified form for the beam waist, but not in the FEM. The beam waist in the FEM is 160 nm, while the modified waist is 188 nm; correcting the FEM peak result down by this factor gives a peak heating of 14.6 K W^{-1} which agrees well. The redistribution of power between the paraxial and true beams lies within a wavelength of the focus. As such, the uncorrected FEM
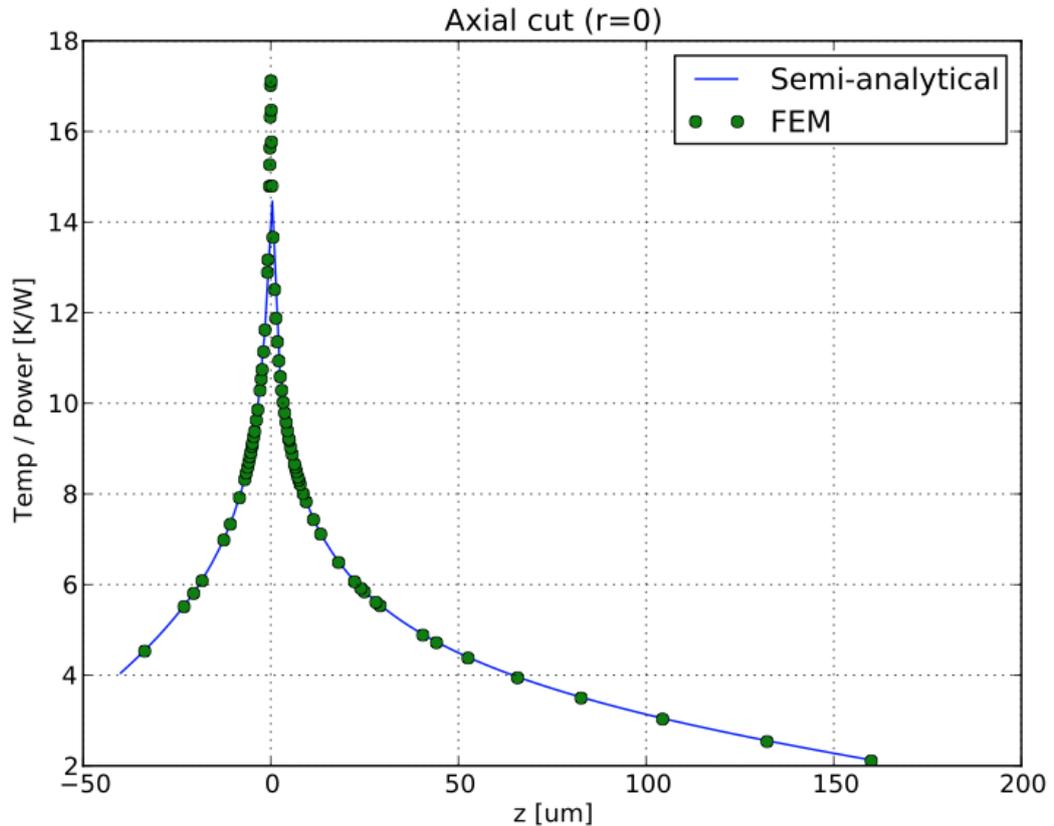
Figure 4.11: Validation of Equation 4.7.1t for the derived laser-heating distribution along the beam axis (blue line) against a finite-element COMSOL model (green circles, written by GB), using the same parameters as described in the section prose (except the beam waist, whose difference accounts for the deviation in the FEM model at the focus).

curve as shown in Figure 4.11 still validates the semi-analytic method for calculating the temperature distribution.

A previous calculation in water yielded an upper estimate of 19 K W^{-1} [24]. The experimental range of peak heating reported in literature is vast for water; 8 K W^{-1}, [25], 14.5 K W^{-1} [26], 16 K W^{-1} [27] and 22 K W^{-1} [28]. The experimental authors report very similar photoabsorption and thermal conductivity measurements for the fluids, as well as using similar laser foci at 1064 nm and $NA > 1$. A variety of systems were used, from polymer beads trapped in water, to aqueous solutions of temperature-sensitive fluorophore with no trapped particles; thus some studies

failed to measure the temperature directly at the focus.

Otherwise, the position and type of chamber walls appear to be the main reasons for the data scatter. The temperature distribution can be described adequately by the maximum heating at the focus (ΔT) and a characteristic decay length; however, the latter is difficult to define since the Green's function for the heat equation is a power-law decay. Moreover, the corresponding solution in free space is divergent in 2D, so the actual value for a quasi-steady state temperature must depend strongly on the boundary conditions of the chamber. The analysis here shows, in agreement with other authors [25] that the peak temperature is sensitive to L and z_F, but insensitive to R. The presence of the laser at extreme z has a large impact on the steady state temperature even in the centre of the channel. The total heat flux is expected to be roughly proportional to L, since (within the assumption that $L \ll 1/\alpha \approx$ cm) the total laser power is almost constant along this axis.

In literature cases reported towards the lower end of the heating range, the focus lay much closer to the coverslip (smaller L within 10 μm [25]). The thermal conductivity and absorption of the coverglass materials (e.g. Table 4.1) differed widely from those of the liquids, thereby suppressing or exacerbating the rise in temperature. The presented model could be refined to reflect the ability of the chamber walls to conduct heat away faster than the infinite aqueous volume assumed here.

When compared with the dimensional analysis result, α/ψ, the analysis implies a proportionality constant of 0.7 ± 0.1, in agreement with results in non-aqueous fluids [28]. In that study, the heating in deuterated water was reduced by a factor 9 relative to water. Similarly, the photothermal resistance of D_2O measured here is lower by a factor of 11. When using D_2O in this thesis the peak heating is therefore considered to be 1.4 K W^{-1}.

For a given power, the presence of an oil droplet at the focus increases the peak temperature in a way which rises logarithmically with droplet size, due to the greater

ratio α/ψ in oil. However, the steady-state *surface* temperature, which determines interfacial tension, is necessarily independent of the thermal conductivity of the interior, ψ_O. Since the absorption coefficient of oil is lower than that of water, and the surface recedes from the focus, the *surface* temperature is expected to decrease weakly with droplet size. The first effect is very small since the most of the beam path is outside the droplet ($L \gg R_D$). The second implies thermal inhomogeneity for large or deformed droplets in H_2O, which contributes to the surface dynamics observed at very high power in Chapter 4. At the low optical powers used in Chapter 5 onwards, the resulting interfacial tension gradients are at most a few percent of the Laplace pressure and cannot alter the equilibrium droplet shapes significantly.

The average interfacial tension of the deformed droplets can therefore be estimated adequately as a function of trap power; this is done by calculating the temperature distribution (Equation 4.7.1t) for bulk H_2O or D_2O, reading the temperature increase at the undeformed drop radius, adding to the measured ambient temperature and converting with the PIT-tension curve.

Glossary

Symbol	Definition	Unit
A	Majority aqueous phase, secondary nucleation of A$'$	
B	Majority aqueous phase, secondary nucleation of B$'$	
A$'$	Minority aqueous phase, primary $\chi < \chi^*$ nucleation	
B$'$	Minority oil phase, primary $\chi > \chi^*$ nucleation	
E$_{A,B}$	$c\mu c$-like compositions, possible decay products of A,B	
M$_A$	Minority m.e. phase, secondary nucleation of A$'$	
M$_B$	Minority m.e. phase, secondary nucleation of B$'$	
M$'$	Majority m.e. phase, primary nucleations	
X	Initial middle phase composition	
AOT	Aerosol OT, ionic surfactant	
Brij-L4	Commercial line of C$_{12}$E$_4$, nonionic surfactant	
C$_{12}$E$_{4,5}$	polyoxyethylene glycol ethers, nonionic surfactants	-
cmc	Critical micellar concentration	M
$c\mu c$	Critical microemulsion concentration	M
G	Gibbs free energy	J
GUV	Giant unilamellar vesicle	
H_0	Spontaneous curvature	m^{-1}
R_N	Nuclear radius	m
S, S^*	Initial aqueous salinity, optimal	M
S^{**}	Initial aqueous salinity that is optimal at χ^*	M
S_T	Soret coefficient	K^{-1}
V	Volume	m^3
χ	Fraction of ionic surfactant in total surfactant	-
$\chi_{H,D}$	Values for heptane, decane system	-
χ^*	Value of χ, minimum monolayer T-sensitivity	-
$\chi_{c\mu c}$	Fraction of ionic surfactant in cμ c	-
γ	Total surfactant weight fraction in total mixture	-
γ_W	Total initial surfactant concentration in water	-
κ	Bending modulus	J
ϕ_A	Volume fraction of phase A	-

Ω	Volumetric water-to-oil ratio	-
G	Green's function	K W^{-1}m^{-1}
I	Optical intensity	W m^{-2}
J	Heat flux	W m^{-2}
L	Chamber depth	m
NA	Numerical aperture	-
NIR	Near-infrared	
$n, \Delta n$	Refractive index, contrast	-
P	Optical power	W
r	Coordinate perpendicular to beam axis	m
R	Integration radius	m
R_D	Droplet radius (spherical)	m
z	Coordinate along beam axis	m
z_R	Rayleigh range of Gaussian beam	m
$T, \Delta T$	Temperature, Laser heating	K
t	Time	s
α	Natural absorption cross section, $\lambda = 1064$ nm	m^{-1}
ψ	Thermal conductivity	W m^{-1} K^{-1}
ζ	Thermal diffusivity	m^{2}s^{-1}
λ	Optical wavelength	m
ω_0	Beam waist	m

References

[1]   M. Kahlweit and R. Strey, "Phase behavior of quinary systems: tracing the three-phase body", *J. Phys. Chem.* Vol. 91, no. 6, pp. 1553–1557, 1987.

[2]   D. A. Woods, C. D. Mellor, J. M. Taylor, C. D. Bain, and A. D. Ward, "Nanofluidic networks created and controlled by light", *Soft Matter*, vol. 7, pp. 2517–2520, 6 2011.

[3]   E. A. Kubatta and H. Rehage, "AOT-vesicles produced at the oil-water interface", *Tenside Surfactants Deterg.* Vol. 48, no. 3, pp. 221–227, 2011.

[4]   B. P. Binks, P. D. I. Fletcher, and D. J. F. Taylor, "Temperature insensitive microemulsions", *Langmuir*, vol. 13, no. 26, pp. 7030–7038, 1997.

[5]   M. Kahlweit and R. Strey, "Phase behavior of quinary mixtures of the type water-oil-nonionic amphiphile-ionic amphiphile-salt", *J. Phys. Chem.* Vol. 92, no. 6, pp. 1557–1563, 1988.

[6] B. P. Binks, W.-G. Cho, P. D. I. Fletcher, and D. N. Petsev, "Stability of oil-in-water emulsions in a low interfacial tension system", *Langmuir*, vol. 16, no. 3, pp. 1025–1034, 2000.

[7] C. Huh, "Interfacial tensions and solubilizing ability of a microemulsion phase that coexists with oil and brine", *J. Colloid Interface Sci.* Vol. 71, no. 2, pp. 408–426, 1979.

[8] T. Sottmann and C. Stubenrauch, "Phase behaviour, interfacial tension and microstructure of microemulsions", *Microemulsions: Background, New Concepts, Applications, Perspectives, ed. C. Stubenrauch, John Wiley & Sons, Oxford*, 2009.

[9] B. Binks, P. D. I. Fletcher, and T. D. J. F., "Microemulsions stabilized by ionic/nonionic surfactant mixtures. effect of partitioning of the nonionic surfactant into the oil", *Langmuir*, vol. 14, no. 18, pp. 5324–5326, 1998.

[10] M. Tanaka, H. Monjushiro, and H. Watarai, "Laser photophoretic migration with periodic expansion-contraction motion of photo-absorbing microemulsion droplets in water", *Langmuir*, vol. 20, no. 25, 10791–10797, 2004.

[11] O. Ghosh and C. A. Miller, "Liquid-crystalline and microemulsion phase behavior in alcohol-free Aerosol-OT/oil/brine systems", *J. Phys. Chem.* Vol. 91, no. 17, pp. 4528–4535, 1987.

[12] S. Chaïeb and S. Rica, "Spontaneous curvature-induced pearling instability", *Phys. Rev. E*, vol. 58, pp. 7733–7737, 6 1998.

[13] B. P. Binks, "Emulsion type below and above the CMC in AOT microemulsion systems", *Colloids Surf., A*, vol. 71, no. 2, pp. 167–172, 1993, ISSN: 0927-7757.

[14] N. Shahidzadeh, D. Bonn, O. Aguerre-Chariol, and J. Meunier, "Spontaneous emulsification: relation to microemulsion phase behaviour", *Colloids Surf. A*, vol. 147, no. 3, pp. 375–380, 1999, ISSN: 0927-7757.

[15] T. Nishimi and C. A. Miller, "Spontaneous emulsification of oil in Aerosol-OT/water/hydrocarbon systems", *Langmuir*, vol. 16, no. 24, pp. 9233–9241, 2000.

[16] J. Salager, L. Marquez, A. A. Pena, M. Rondon, F. Silva, and E. Tyrode, "Current phenomenological know-how and modeling of emulsion inversion", *Ind. Eng. Chem. Res.* Vol. 39, no. 8, pp. 2665–2676, 2000.

[17] J. P. Delville, C. Lalaude, E. Freysz, and A. Ducasse, "Phase separation and droplet nucleation induced by an optical piston", *Phys. Rev. E*, vol. 49, pp. 4145–4148, 5 1994.

[18] R. Piazza, "Thermophoresis: moving particles with thermal gradients", *Soft Matter*, vol. 4, pp. 1740–1744, 9 2008.

[19] J. E. Bertie and Z. Lan, "The refractive index of colourless liquids in the visible and infrared: contributions from the absorption of infrared and ultraviolet radiation and the electronic molar polarisability below 20500 cm^{-1}", *J. Chem. Phys.* Vol. 103, no. 23, pp. 10 152–10 161, 1995.

[20] J. H. W. G. den Boer, G. M. W. Kroesen, and F. J. de Hoog, "Measurement of the complex refractive index of liquids in the infrared using spectroscopic attenuated total reflection ellipsometry: correction for depolarization by scattering", *Appl. Opt.* Vol. 34, no. 25, pp. 5708–5714, 1995.

[21] M. Rubin, "Optical properties of soda lime silica glasses", *Solar Energy Materials*, vol. 12, no. 4, pp. 275–288, 1985, ISSN: 0165-1633.

[22] W. M. Haynes, Ed., *CRC Handbook of Chemistry and Physics.* CRC Press, OH, 1977.

[23] G. Sawhney, *Heat And Mass Transfer, 2nd. ed.* I K International Publishing House, 2010, ISBN: 9789380578392.

[24] A. Schönle and H. S. W., "Heating by absorption in the focus of an objective lens", *Opt. Lett.* Vol. 23, no. 5, pp. 325–327, 1998.

[25] E. Peterman, F. Gittes, and C. Schmidt, "Laser-induced heating in optical traps", *Biophys J.* Vol. 84, no. 2, pp. 1308–1316, 2003, ISSN: 0006-3495.

[26] Y. Liu, D. Cheng, G. Sonek, M. Berns, C. Chapman, and B. Tromberg, "Evidence for localized cell heating induced by infrared optical tweezers", *Biophys J.* Vol. 68, no. 5, pp. 2137–2144, 1995, ISSN: 0006-3495.

[27] U. Delabre, K. Feld, E. Crespo, G. Whyte, C. Sykes, U. Seifert, and J. Guck, "Deformation of phospholipid vesicles in an optical stretcher", *Soft Matter*, vol. 11, no. 30, 6075–6088, 2015.

[28] S. Ito, T. Sugiyama, N. Toitani, G. Katayama, and H. Miyasaka, "Application of fluorescence correlation spectroscopy to the measurement of local temperature in solutions under optical trapping condition", *J. Phys. Chem. B*, vol. 111, no. 9, 2365–2371, 2007.

Chapter 5

Linearity, Bifurcation and Nanothreads

The previous sections have addressed the introduction of surfactant-stabilised oil droplets to an aqueous continuum and the complexity of their phase behaviour when exposed to focused lasers. Any assumption that the composition of a given droplet is invariant holds only within fairly limited conditions of low laser heating and a sufficient margin away from phase-inversion.

Whilst compositional stability is not guaranteed within the range of ultralow interfacial tensions of interest to deformation, the internal composition does not necessarily affect the presence or response of the interface itself. As long as the volume, refractive index and deformability of a given droplet do not change excessively during measurement, the *equilibrium shapes of droplets and networks* may be defined under optical deformation. The remainder of this thesis is largely dedicated to investigating what these shapes are, and which forces determine them.

5.1   A parametrisation for deforming droplets

Table 5.1 gives a review of the parameters that govern the existence and evolution of stable droplet shapes.

Independent parameters		Dimensionless parameters	
Variables		Independent	
IFT	σ	Optocapillary ratio	ϵ
Drop size	R_D	Number of traps	M
Optical power	P	Trap separation†	$L'_A \equiv L_A/R_D$
Number of traps	M	Capillary length†	$L'_C \equiv \sqrt{\sigma/\Delta\rho g R_D^2}$
Trap separation	L_A		
Constants		Dependent/Constant	
Laser geometry	NA, λ	Laser dimensions†	$w_0/R_D, z_R/R_D$
Refractive contrast	Δn	Refractive contrast	Δn
Bending modulus	κ	Helfrich length†	$L'_\kappa \equiv \sqrt{\kappa/\sigma R_D^2}$
Buoyancy	$\Delta\rho g$		

Table 5.1: The factors thought to influence steady-state droplet deformation (*left*) can be represented in a non-dimensional basis using composite length scales (*right*). The optocapillary number is defined by Equation (5.1.1a) below.

Buckingham dimensional analysis allows definition of the optocapillary number ϵ, as

$$\epsilon = \frac{Pf(NA, \Delta n)}{R_D \sigma c},$$

(5.1.1a)

which quantifies the relative strength of the optical and capillary forces. It is approximately equivalent to the ratio:

$$\frac{|F_{grad}|}{|F_{surf}|} = \frac{\Delta n PQ/c}{2\pi R_D \sigma}.$$

(5.1.1b)

where Q is the efficiency factor defined in § 2.2.2. The cofactor $f(NA, n)$ is fixed by defining a critical value $\epsilon = 1$ at a transition to *nonlinear* deformation, such

as a minimum in the projected droplet radius from numerical simulations [1]. It depends on the refractive geometry in the similar way to the efficiency factor Q, though accounting for the deformation of the droplet. [1]

Given a number of traps of equal power and set of governing length scales (Table 5.1, *right*), an approximate one-to-one correspondence is expected between ϵ and droplet shape. However, neither the true shape nor the optocapillary number can be measured by 2D imaging without first assuming some symmetry of the shape.

5.2 Linear deformations

For a single trap (or equivalently, multiple overlaid traps in phase), the extension is largely axial along the beam [2]. Elongation will induce thinning in order to conserve volume. Therefore, the projected radius along the beam axis decreases with beam power. For a droplet contained within the focal volume, this will be the same as the imaged radius [3]. Droplets vary reversibly in apparent diameter across the dynamic range of the laser power, without hysteresis (Figure 5.1) in a way that is consistent with prolate-spheroidal symmetry.

---

[1]The approximate relation is $f \sim \Delta n Q / 2\pi$. For a droplet in a single trap, Tapp estimates $f(NA, \Delta n) \approx \Delta n \exp\left(-NA\right)/\pi$, a *decreasing* function of NA at fixed power. This result is counterintuitive and does not relate to the true trap-stiffness Q factor that increases with NA in all cases. In the unique case of an isolated trap, the equilibrated droplet surface is located far from the focus and so the momentum flux is spread more evenly over the surface, decreasing f at higher NA. This is not the case for multiple traps separated on the order of the droplet radius; the intensity gradient near a focal point increases as NA^4. Results presented in this thesis largely use constant $NA = 1.2$ and $\Delta n \approx 0.05$, such that knowledge of the precise form of $f(NA, \Delta n)$ is unnecessary for comparison of droplet shapes on arrays of similar geometry.
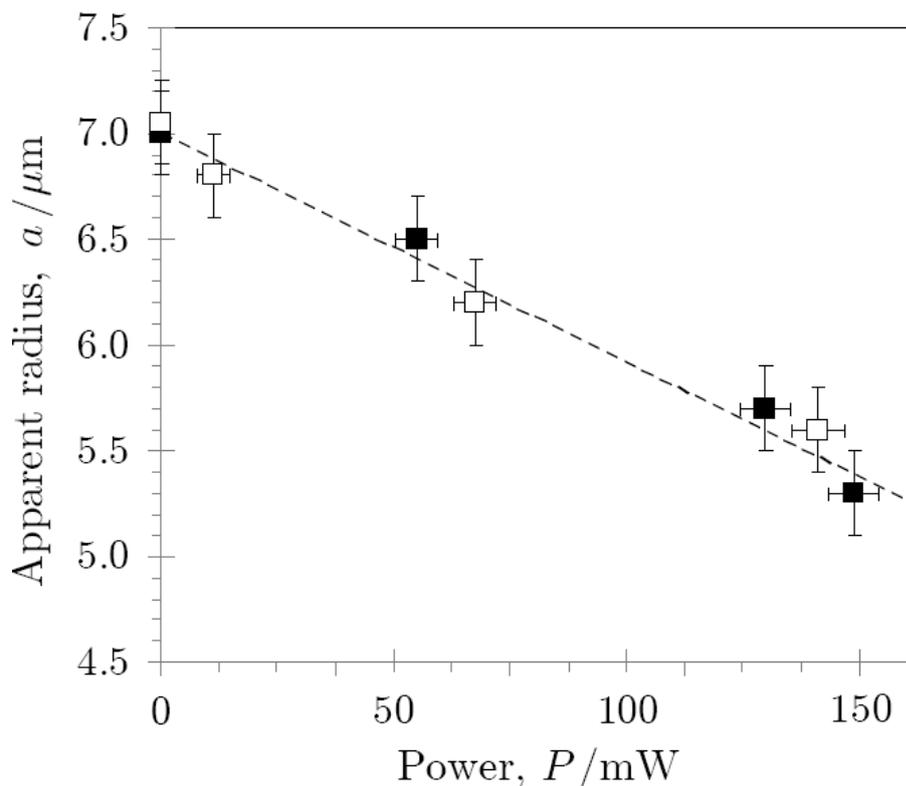
Figure 5.1: Under brightfield microscopy, the apparent radius of a heptane droplet ($\chi = 1$) in a single trap changes monotonically with increasing ($\square$) and decreasing ($\blacksquare$) trap power. The dashed line is a fit ($R^2 = 0.94$) to the theoretical spheroid given by Equation (5.3.1c) at the estimated $\sigma = 2.5$ μN m^{-1}.

5.3   Nonlinear deformations

5.3.1   Nonlinear deformations in a single trap

As the surface tension weakens, a droplet in a single trap can be considered to approach a limit in which its shape is determined only by the trap. In the absence of all forces other than the gradient force, a fluid particle should conform to the shape of the iso-intensity contour that matches its volume. Noting that a Gaussian focus has a hyperbolic profile along the beam axis, the intensity contours are only ellipsoidal up to half the beam waist ($I = I_0/e$) and become catenoidal further away from the focus [4]. These figure-of-eight shaped intensity contours imply that

the optical pressure encourages the equilibrium drop shape to pinch at the equator for all but the smallest visible drops ($R_D > w$) as calculated by Tapp *et al.*[1] For axial elongation in a single trap, the radiation pressure at the equatorial surface of the drop is significant at it lies near the focus. The negative axial curvature is stabilised so that the droplet does not split when filling the illuminated volume. However, 2D imaging techniques cannot provide experimental verification of the shape distribution in the axial direction. The topic of 3D imaging is covered in Chapter 6, with specific reference to the axial deformation in § 6.2.1.

5.3.2   Oscillations across two closely-separated traps

When dual beams (§ 2.4.1) are overlaid, a given stiff oil drop can be trapped as if it were spherical bead. As the beams are separated slowly by about a drop radius, the drop jumps into the stronger trap. Repeating with careful adjustment to equalise the trap powers, the drop's behaviour changes drastically with decreasing (but not ultralow) interfacial tension. The drop is no longer confined to one trap, but bounces between the trap locations indefinitely (Figure 5.2, *left*). The frequency increases with optical power until, on the slightest of stage movements, the drop is tangentially ejected at great speed. Viscous damping dominates over inertial effects such that an escaping droplet decelerates exponentially, its motion becoming isotropic at a distance $x_{rest} = m_D v_0 / \beta$, where m_D, v_0 and β are the mass, ejection velocity and friction coefficient of the droplet respectively. While the ejection can appear violent at several 100 μms^{-1}, the particle's momentum corresponds to that transferred by only $m_D v_0 \lambda / 2\pi\hbar Q \sim 10^8$ photons, which the beams deliver in less than a microsecond.

The drop's oscillation in position cannot be simple diffusion between trap sites in a fixed potential, since the drop would be increasingly localised at higher powers. Instead the movement implies some feedback mechanism for the position. For a larger refractive contrast this could be accounted for by variations in the way the droplet scatters the optical field. The dependence on interfacial tension implicates deformation, which could cause asymmetric scattering and a restoring lateral force.

As such, the oscillation of solid spheres has not been observed. On decreasing IFT further, to ultralow values, the oscillation frequency decreases, reflecting the periodic storage of energy in the transient surface deformations. In this limit, the deformation approaches the trap separation and the droplet relaxes into a static equilibrium (Figure 5.2,*right*).
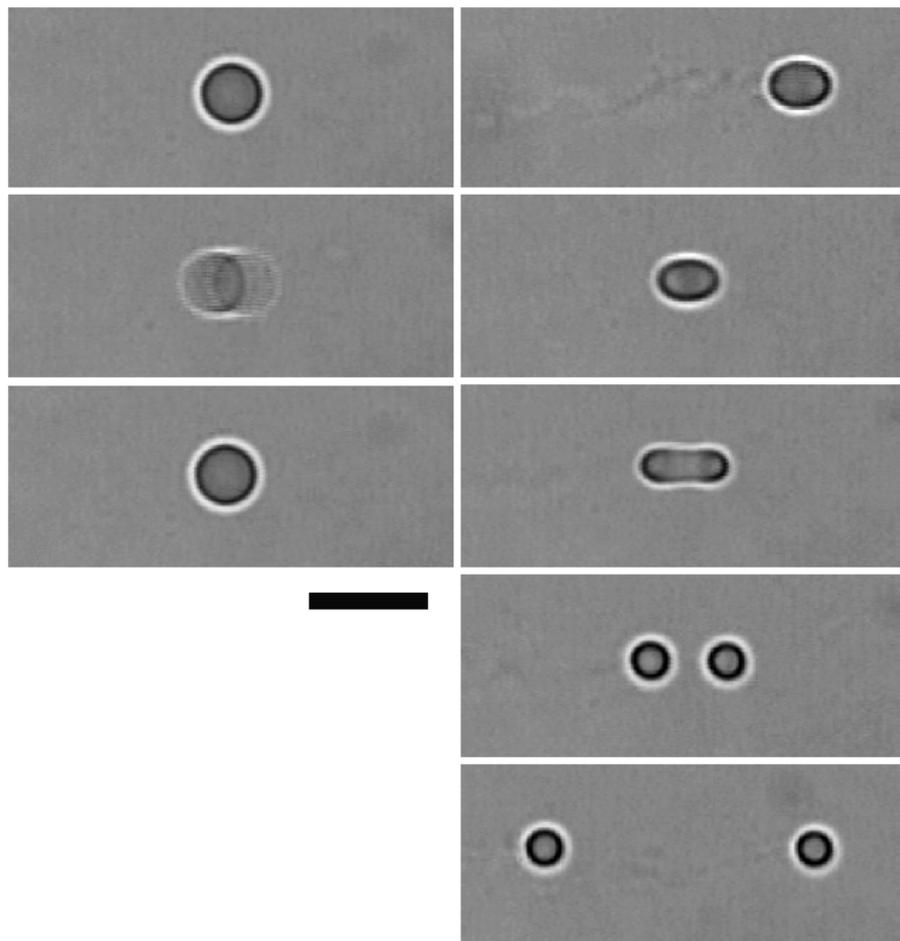

Figure 5.2: A droplet is trapped in two traps of equal power with increasing separations (0 (2.8 *top right*), 3.0, 4.8, 6.8, 22.8) μm; (*left*) at low IFT, the droplet still appears as a rigid sphere, but oscillates in position; (*right*) at ULIFT, the same droplet conforms to both traps simultaneously at small separations and does not oscillate. Some microemulsification is visible (*top right*). Separating the traps further forms a nanothread. Scale bar 10 μm.

5.3.3 Nonlinear deformations in multiple traps

For a droplet in *two* coplanar traps, the linear deformation again manifests as a prolate elongation, albeit along the intertrap axis. In combination with the weaker axial deformation, this generates an approximately ellipsoidal shape. As Tapp's ϵ predicts only the axial deformation, a practical deformability metric is needed for the lateral elongation. The maximum achievable aspect ratio, Λ, was measured in the focal plane, at a fixed refractive index and laser power. Since the optical and surface forces are equal at equilibrium, it is interesting that a second form of the optocapillary number $\bar{\epsilon}$ can be defined, based on the increase in Laplace pressure p_L integrated over the surface A. As the mean curvature of a spheroid is known [5], $\bar{\epsilon}$ can be expressed in terms of Λ in a spheroidal approximation,

$$\int p_L dA = \int p_L dA_{sphere}(1 + \beta \bar{\epsilon}^2 + \ldots) \tag{5.3.1c}$$

$$\bar{\epsilon} = \frac{1}{\sqrt{\beta}} \left[\frac{\int p_L dA}{\int p_L dA_{sphere}} - 1 \right]^{1/2} \tag{5.3.1d}$$

$$= \frac{1}{\sqrt{\beta}} \left[\frac{\int H(\Lambda) dA_{spheroid}(\Lambda)}{4\pi R_D} - 1 \right]^{1/2} \tag{5.3.1e}$$

$$= \frac{1}{\sqrt{\beta}} \left[\frac{1}{2\Lambda^{1/3}} \left(\Lambda + \frac{\cosh^{-1}(\Lambda)}{\sqrt{\Lambda^2 - 1}} \right) - 1 \right]^{1/2} \tag{5.3.1f}$$

which is necessarily parabolic (the first order term is zero since the integrand is even). As it properly accounts for volume conservation, the integrated curvature model is more accurate at moderate deformations than linear models [3, 6] based on the droplet semiaxes,

$$R_{\text{minor}} = R_D \left(1 - \frac{\bar{\epsilon}}{2} + \ldots \right) \tag{5.3.1g}$$

$$\bar{\epsilon} = 2 \left(1 - \frac{R_{\text{minor}}}{R_D} \right) = \frac{2}{3}(\Lambda - 1) \tag{5.3.1h}$$

to which it reduces at small deformations with the factor $\beta = 2/5$. It indicates that a spheroid has lower apex curvature than estimated in the linear model and so a droplet can initially be stretched further at the same power and surface tension. A practical outcome of these models is that small changes in shape with varying power can be used to estimate the interfacial tension, if $\bar{\epsilon}(\Lambda) = \epsilon(\sigma, P)$ is assumed. The linear and spheroidal models do not distinguish between two-trap lateral and

single-trap axial elongations; for the small single-trap deformation in Figure 5.1 they give respective estimates of 2.0 ± 0.2 μN m^{-1} and 2.5 ± 0.3 μN m^{-1}, which resemble the spinning-drop tensiometry due to Aveyard [7].

Experimentally, when stretching a droplet with two parallel, coplanar traps, a splitting instability (Figure 5.4) occurs when Λ increases to a threshold value Λ_∞. If this instability cannot be reached, maximum Λ with respect to trap separation corresponds to a minimum in ULIFT. For droplets of 3-10 μm diameter, the transition is observed in brightfield at $\Lambda_\infty = 2.2 \pm 0.2$. At this point the deformation must become nonlinear, such that by definition $\bar{\epsilon}(\Lambda_\infty) \equiv 1$. However, the spheroidal approximation also breaks down, predicting $\bar{\epsilon}(\Lambda_\infty) = 0.6$ and a more distant transition. The model does not account for the distribution of the optical pressure higher than a quadrupolar term. At the transition, the droplet shape is clearly no longer spheroidal.
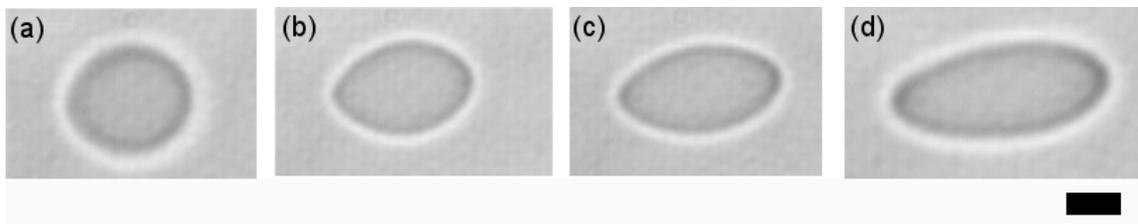
Figure 5.3: Laterally-stretched droplets of excess oil in excess water (heptane, $\chi = 0.62$, $\gamma = c\mu c$) with increasing displacement of two traps from (a-d). Although decane droplets show higher refractive contrast (Table 4.1), heptane droplets have lower minimum IFT and deform further. The largest aspect ratio shown is $\Lambda = 2.23 \pm 0.09$. Scale bar 4 μm.

5.4 Necking and nanothreads

What shape can be expected as nonlinearities appear? As the traps are separated more widely, their influence on the central part of the droplet decreases. The local shape will approach a minimal surface subtending the trapped regions. As fluid

flows towards the nodes and the neck thins, this minimal surface is first a spheroidal section, then a catenoid and finally two separate spheres. An instability is expected at some $\Lambda > 2$, since splitting the droplet into two no longer results in a larger surface area than the catenoid. Thus, at Λ_∞, two daughter droplets develop. However, the monolayer fails to split under the influence of surface tension (Figure 5.4). Instead a cylindrical thread remains between the two nodes. This is a *nanothread*, so called as the typical diameter is less than can be resolved by optical microscopy, i.e. $R_N \ll \lambda/2$.

The conjoined daughters - or *nodes* of the network - rejoin at a trap separation of the sum of the radii of the spheres, indicating that no minimum thread length applies. Unlike separate droplets, they always coalesce with no kinetic barrier. On extension of the thread, no maximum length is encountered; if limited only by a volume constraint, a thread formed from a micron-sized droplet could be as long as several millimetres - an aspect ratio of up to 10^5.
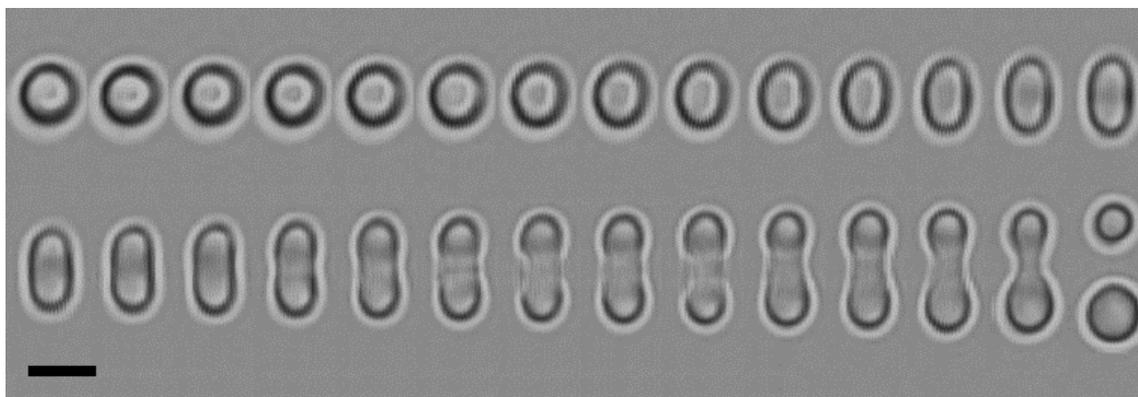
Figure 5.4: Systematic necking of droplet (heptane, $\chi = 0.62$, 4.6 μm dia.) in brightfield over small symmetric separation increments (0.02 μm/s at 0.75 fps). Scale bar 4 μm.

How such an enormous volume-to-area ratio is maintained with finite IFT is not immediately obvious. Reduction in the interfacial area implies either shortening or thinning the thread; shortening is prevented by optical pressure when both ends are trapped reservoirs. On the other hand, thinning the tube increases the local

curvature and the bending contribution to the free energy. This small bending energy of the interface is thought to stabilise the tube against the ultralow surface energy [8]. The characteristic scale is the Helfrich length $L_\kappa = \sqrt{\kappa/\sigma}$. However, the dependence of the surface free energy on the spontaneous curvature H_0 is remarkably strong, such that the nanothread behaviour differs qualitatively as the temperature changes.

5.4.1 Thread force and recoil

The optical force required to produce a nanothread in this configuration is simply the tension along the droplet's circumference,

$$F_{surf} \approx 2\pi R_D \sigma. \tag{5.4.1i}$$

However, the thread tension, F_N, is far smaller. If $H_0 = 0$, F_N scales according to its radius R_N,

$$F_N = 4\pi R_N \sigma, \tag{5.4.1j}$$

so the drops will *always* remain trapped on extending the thread. The equilibrium thread radius calculated from the free energy functional (see § 5.6 for derivation) is comparable to the Helfrich length,

$$R_N = \sqrt{\kappa/2\sigma} \quad = L_\kappa/\sqrt{2} \tag{5.4.1k}$$

and the corresponding tensile force is, more precisely (see § 5.6),

$$F_N = 2\pi\sqrt{2\kappa\sigma} - 4\pi\kappa H_0 \cdot \mathrm{sgn}\,(H), \tag{5.4.1l}$$

which is of order 0.1-10 pN at ULIFT. Nanothreads cannot exist without such a tensile force, here provided by a pair of optical tweezers. The experiments of Woods *et al.* [9] show that when one end is released, the free droplet recoils towards the trapped droplet. At a sufficient distance from the coverslip ($\sim 20\ R_D$), they do so at a terminal velocity consistent with the prediction from Stokes' Law balanced against this thread tension.

Simultaneous measurement of the drop's size and recoil velocity provides an experimental estimate of the product $\kappa\sigma$ for the thread. The combination of SAXS and droplet recoil yields the bending moduli in the Winsor III regime (Table 1.4), assuming the two interfacial tensions are equivalent. These moduli are in very good agreement with the literature [10, 11] at the WII-WIII boundary in the quaternary systems ($\chi = 0, 1$) in both heptane (1.0, 1.1 k_BT respectively) and decane (1.25, 0.9 k_BT).

At first glance, one might assume the nanothread properties follow the symmetry of the IFT with respect to the PIT. However, this was not the case for the emulsion, whose inversion behaviour was influenced by the water-biased volumetric ratio Ω. For a nanothread, behavioural asymmetry stems from its mean curvature remaining positive (towards oil) as the spontaneous curvature changes sign. Consistent with the newly-derived second term in § 5.4.1, the tensile force depends strongly on the sign of the spontaneous curvature (Figure 5.10), unlike the radius and radial stiffness. The tensile force vanishes and the thread thins as the spontaneous and real curvatures become similar. For the anionic formulations considered in this study, this occurs as the temperature increases far above the PIT. This insight helps to explain why no minimum in tensile force with temperature has been observed (Figure 5.5, [9]).
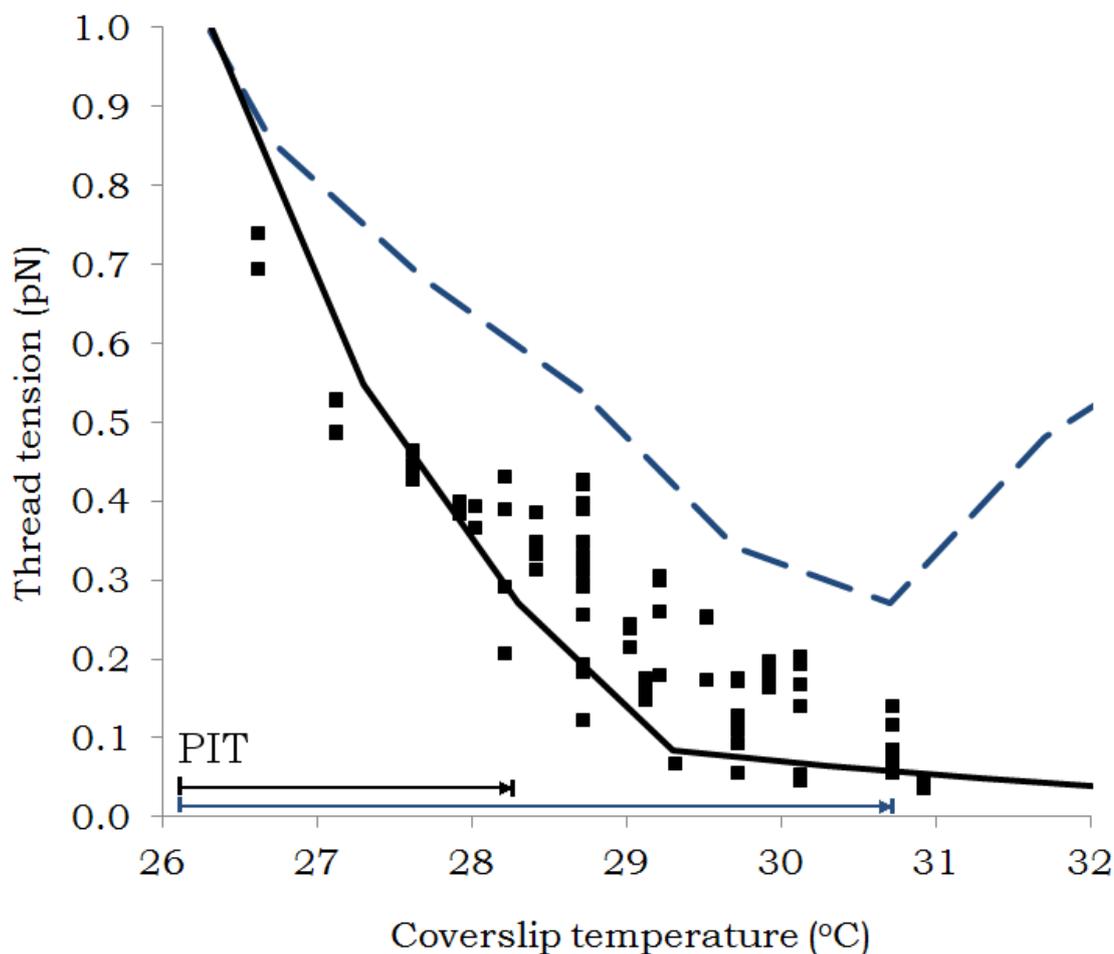
Figure 5.5: Nanothread tension as a function of temperature, obtained by Woods using the recoil method (black data redrawn from [9]). The data are fitted using Woods' first order model with a temperature shift of +4.8 K (dashed blue line) and the current model accounting for spontaneous curvature, with a shift of +2.2 K (solid black line). Laser heating is estimated as +0.9 K.

At extreme ULIFT, threads become soft and diaphanous, with sufficiently low tension that the diameter of the thread and its transverse thermal excitations can be resolved. One implication of Figure 5.10 (see Appendix) is that nanothreads become unstable under thermal fluctuations above the PIT and break into small o/w droplets. However, most such observations have been associated with the simultaneous bursting or shrinking of the supporting nodal droplets (§ 3.6). Where this can be avoided, some evidence exists for low-tension nanothreads connecting well-behaved

rigid droplets above the PIT (§ 4.7). It is unclear as to whether this arises from the spontaneous curvature effect proposed above, or merely from laser-induced temperature differences between the warmer, trapped droplets and the cooler nanothread. This ambiguity could be resolved in future by using D_2O to reduce temperature gradients in nanothread experiments.

5.4.2 Handles

As the interfacial tension decreases yet further, the interface loses its ability to transmit optically-induced stresses across the droplet. The response time to a perturbing deformation increases as $\eta R_D/\sigma$, whilst each trap acts more locally. This renders the droplet's centre-of-mass less sensitive to attempts at manipulation, even with multiple traps around its periphery. Instead the traps fill with oil up to a characteristic radius of $3F_{esc}/8\pi\sigma \sim 1~\mu m$, at which the surface and gradient forces balance. These *handles* may be detached from the body with ease to form nanothreads.

5.4.3 Dumbbell symmetry

In the crossover regime $\epsilon \approx 1$, the optical forces can prevent the two nodes from escaping under the thread tension, $F_{esc} > 4\pi\sigma R_D$, but cannot otherwise overcome Laplace pressure in each individual node. Apart from the tether points, the nodes are always circular in 2D profile, but in this regime their radii agree with those of prolate spheroids under volume conservation. At this ϵ, the volumetric split between the nodes is never precisely equal. The symmetric shape represents an unstable equilibrium; it has up to $\sim 20\%$ greater surface area than an asymmetric dumbbell. Thus, when splitting the droplet at lower speeds, the initial equilibrium is unperturbed and the incidence of symmetric shapes is increased.

For a constant separation speed, dumbbells are increasingly symmetric when the interfacial tension is lower, corresponding to the limit $\epsilon \gg 1$ (Figure 5.6). Near the critical IFT (top row), the collapse is swift, highly asymmetric and occurs at relatively small separations. As the ULIFT decreases further, the necking is slowed such that liquid is entrapped as a freely-diffusing bolus on the thread. At the lowest

ULIFT, the bifurcation becomes symmetric according to the ratio of (equal) trap strengths.
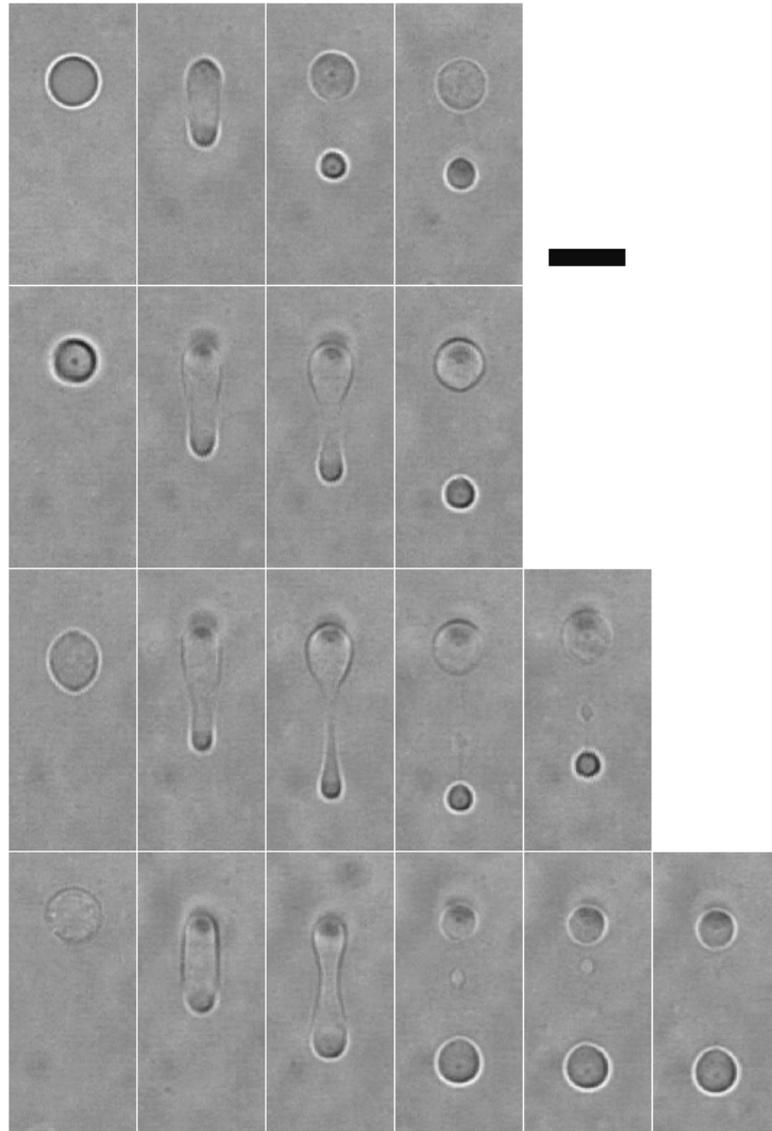

Figure 5.6: Four examples of nanothread formation at decreasing ULIFT, captured at ~ 0.5 s intervals with increasing dual trap separation (left to right). Scale bar 10 μm.

The scenarios above describe the preferred dumbbell geometry in equilibrium for different $\epsilon > 1$. However, following a change in conditions and thus ϵ, flow between reservoirs is necessary for the geometry to equilibrate. Woods showed that nanoth-

reads do support flow over timescales of minutes to hours.

There are parallels between the surfactant-based nanothreads investigated here and of surface-immobilised lipid vesicles [12, 13]. Similarly-thin tubes can be drawn mechanically from one vesicle and capped with another vesicle. The stable tubes allow the flow of liquid between the vesicles by three mechanisms [14]: constrained diffusion, Marangoni transport and electrophoresis (analogous to the optical gradient force here). The main differences are that the surfactant nanothreads are formed from two-solvent microemulsions, with much lower ULIFT and bending rigidity $\kappa \approx k_B T$. Thus, their properties are determined largely by the phase-inversion phenomenon that does not occur in lipid-in-water systems.

5.5 Thread networks in brightfield

When more than two traps are manipulated (§ 2.4.2), multiple threads can be drawn from the same droplet to create a nanofluidic network. The capability for interactive tweezers opens up a rich experimental space for probing the stability and dynamics of networks in different trap arrangements.

Woods measured the acute angle at which a V-network of three nodes collapses to a Y-junction as 17 °. Our results for the same surfactant system verified this at 20 ± 3 °. Assuming a catenoidal neck for surfactant nanothreads, the theoretical minimum angle of stability is:

$$\theta_{V \rightarrow Y} = 2 \tan^{-1}(\sqrt{R_N/R_D}) \approx 20° \tag{5.5.1m}$$

which does not depend on the spontaneous curvature and is therefore identical to the result derived for lipid tubules [15]. Our prediction ($R_D = 2 \ \mu$m, $R_N = 50$ nm) corresponds very well with the experimentally measured values. Nonetheless, collapse can occur at node-to-node angles up to at least 90° if the threads' tension is low enough that they fluctuate and collide with one another (Figure 5.9).

The connectivity of the network becomes a richer problem when four equal traps are used to extend the droplet. A softer and larger droplet has a slower viscous response in its untrapped regions. As a result, its stability is increasingly influenced by dynamic considerations, such as the energy of thermal fluctuations and the viscosities of the fluids. The characteristic relaxation speed is $\sigma/\eta_W \sim 100\ \mu\text{m s}^{-1}$ at ULIFT.

At relatively low separation rates, the centre of the droplet thins as the array expands. This sheet collapses to the edge of the array that initally supports the largest volume of oil. This fluid then drains into the vertices to form a linear U-shaped network of four nodes, thereby conserving the topology of the initial body. The network shown in Figure 5.7 is equilibrated since the interval between steps is > 1 s - many times slower than the viscous response time. Until the neck drains fully, the minimum angle of stability is much larger than the equilibrium angle. If thermal fluctuations are significant, the network can instead decay to a double-Y junction.
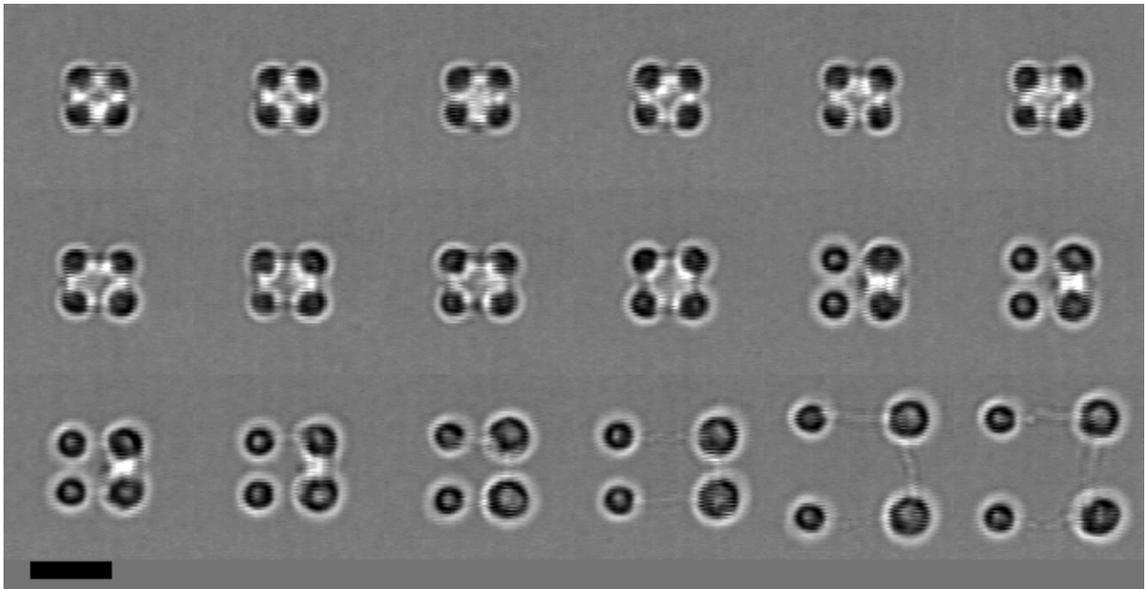
Figure 5.7: A 6.4 μm droplet is suspended by a rectangular 4-trap array at increasing separations up to 12 μm. Conditions are 4.5 mW/trap, 20.6 °C, 43.0 mM NaCl in H_2O, $\chi = 1$. Scale bar 10 μm.

If the rate of trap separation is comparable to the speed of the viscous relaxation, no sheet appears. Instead four nodes are pulled out independently with a thread connecting each to the remainder of the droplet. This untrapped central mass drains until an unstable X-junction is formed [9]; at this point either the threads snap or the junction disproportionates into a double Y-junction.
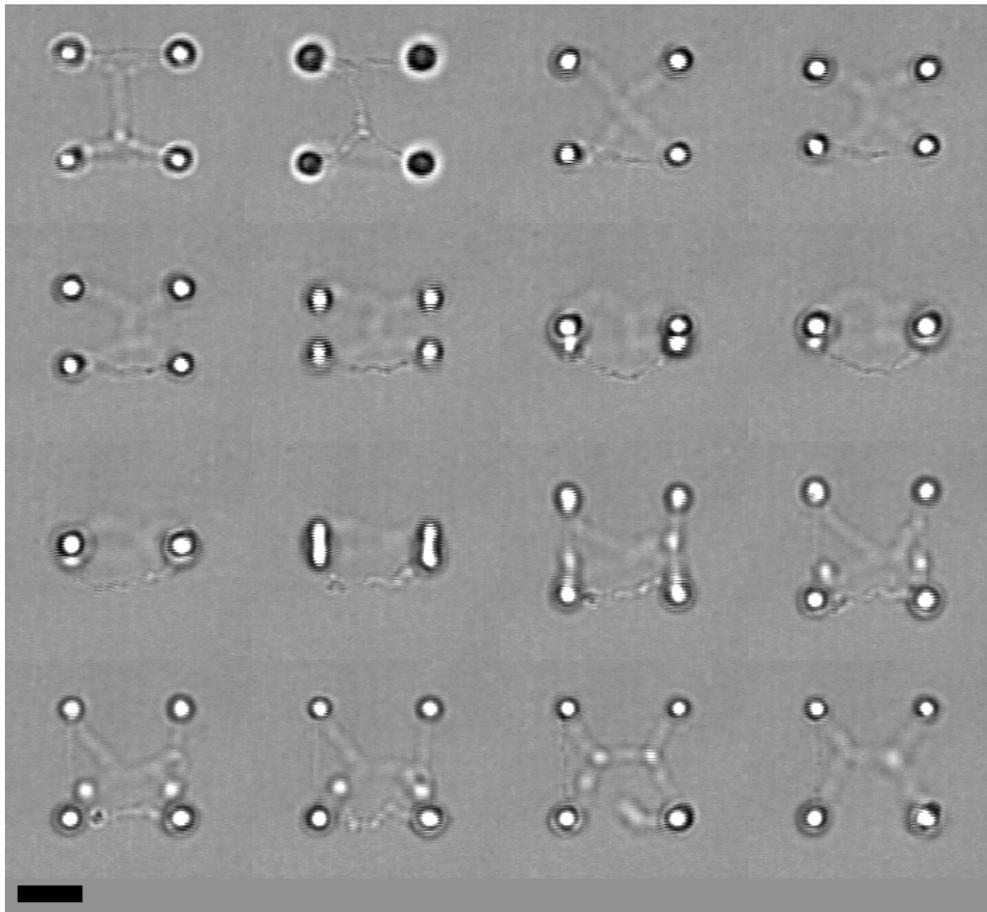

Figure 5.8: Interconversion of double Y-network orientation by collapsing the rectangular 4-array through a line. Chronological order is left-right descending with intervals of $\sim$0.1 s. Conditions as for Figure 5.7. Scale bar 10 μm.

The most stable fully-connected network on a rectangular array is one of two equilateral junctions (a *double-Y*-network). However, for arrays with aspect ratio less than $\sqrt{3}$, the network is doubly-degenerate in perpendicular directions. One orientation may be converted to the other in two ways. The array can be stretched

perpendicularly to the central thread, shortening it until the junctions meet and the thread reappears in the other orientation. Alternatively, by collapsing the rectangular array through a line of two traps, as shown in Figure 5.8, the resulting central thread becomes parallel to that line.
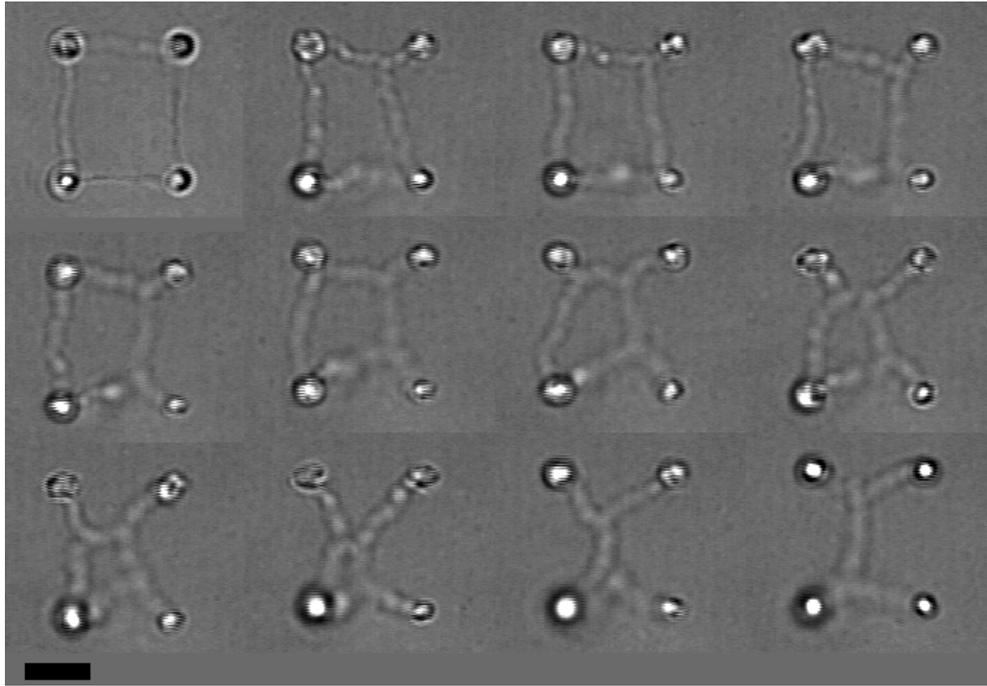

Figure 5.9: Recovery of a double-Y junction from a rectangular closed-loop network created by coalescence of node pairs. Chronological order is left-right descending with intervals of ~ 10 s. Conditions as for Figure 5.7. Scale bar 10 μm.

The topological constant of a network can be increased by holding the ends against each other until they coalesce. However, this process is stochastic and unreliable even at ULIFT where coalescence is most likely. Where closed loops are formed, they decay to double-Y networks either through thread breakage, detachment and recoil (Figure 5.8) or by gradual V-to-Y collapse at the nodes (Figure 5.9).

5.6 Appendix: Theory of nanothread stability under phase inversion

The effect of nonzero spontaneous curvature around the inversion point is considered for a steady state nanothread. If entropic and fluctuation effects can be assumed negligible, the Helfrich equation determines the curvature and IFT contributions to free energy,

$$G = \int \left[\sigma_0 + 2\kappa(H - H_0)^2 + \bar{\kappa}K + ... \right] dA \qquad (5.6.1\text{n})$$

where terms are as defined in Chapter 1. Cylindrical constraints apply for a steady-state thread, such that local curvatures are identical everywhere; curvature is zero in the longitudinal axis and finite in the other:

$$|c_1| = 0 \quad |c_2| = 1/R \qquad (5.6.1\text{o})$$

$$K = 0 \qquad H = \frac{\text{sgn}\,(H)}{2R} \qquad A = 2\pi RL \qquad (5.6.1\text{p})$$

$$G = 2\pi RL \left(\sigma_0 + 2\kappa(H - H_0)^2 \right) \qquad (5.6.1\text{q})$$

$$G = 2\pi L \left[\left(\sigma_0 + 2\kappa H_0^2 \right) R + \frac{\kappa}{2R} - 2\kappa H_0 \cdot \text{sgn}\,(H) \right] \qquad (5.6.1\text{r})$$

where thread subscripts *e.g.* $R_N, L_N \to R, L$ are dropped for clarity. The quantity $\text{sgn}\,(H)$ refers to the geometry with a specified monolayer orientation, as defined with the same convention as the spontaneous curvature, i.e. positive for (convex) w/o and negative for (convex) o/w. As the thread is in equilibrium with larger droplet reservoirs, its volume is not constrained. Minimising the free energy to find the equilibrium radius,

$$\frac{dG}{dR} = 0 \quad \rightarrow \quad R = \sqrt{\frac{\kappa}{2\sigma}} \quad \text{where } \sigma = \sigma_0 + 2\kappa H_0^2. \qquad (5.6.1\text{s})$$

The free energy per unit length is identified with a tensile force, and the equilibrium radius is substituted. Then H and R are eliminated in terms of H_0,

$$\frac{G}{L} = F_N = 2\pi\sqrt{2\kappa\sigma} - 4\pi\kappa H_0 \cdot \text{sgn}\,(H) \qquad (5.6.1\text{t})$$

As the spontaneous curvature increases from zero, the ideal IFT - identified with that of a planar geometry - increases and so the thread thins; thus the mean

curvature also increases. The radial stability of the thread at equilibrium is dictated by the curvature of free energy with respect to changes in radius,

$$\frac{d^2G}{dR^2} = +\frac{\kappa}{R^3} \tag{5.6.1u}$$

The equilibrium radius is stable regardless of the signs of H or H_0, with thinner threads becoming exceptionally rigid against changes in thickness. The spontaneous curvature is proportional to the change in temperature from the phase inversion point by a factor $dH_0/dT = 8.5 \times 10^6$ m^{-1}K^{-1} for heptane/AOT/NaCl/H$_2$O [16], so a similar force-temperature curve can be calculated.
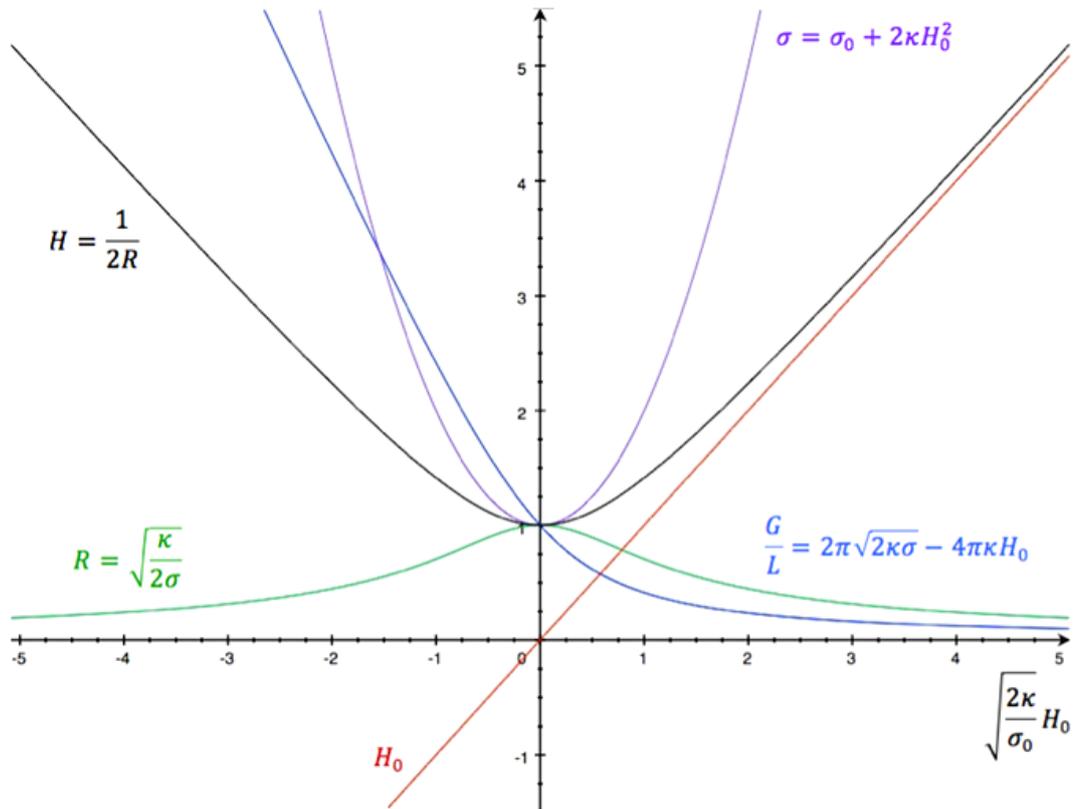
Figure 5.10: Idealised properties of an oil-in-water thread varying with spontaneous curvature (non-dimensionalised), following from the Helfrich expansion without thermal fluctuations. Each function is normalised by its value at the inversion point, where $H_0 = 0, \sigma = \sigma_0$.

An extra term appears in the expression for the thread tension, which sensibly states that the threads free energy is lower under conditions favouring a microemul-

sion of the same sense. For a o/w thread, $sgnH > 0$ and the tension decreases with T. For a thread in equilibrium, the condition $|H| > |H_0|$ is always fulfilled, so there is always some curvature term stabilising the thread radius against thinning due to IFT. However, this weakens as H_0 increases with the same sign as H, and the thread's tensile force vanishes even faster than the IFT rises. Although the thread is radially more stable in a free energy sense, a lower tension would make the thread more vulnerable to other influences along its length, such as thermal fluctuations.

Glossary

A	Interfacial area	m^2
AOT	Aerosol OT, ionic surfactant	
Brij-L4	Commercial line of C$_{12}$E$_4$, nonionic surfactant	
C$_{12}$E$_{4,5}$	polyoxyethylene glycol ethers, nonionic surfactants	-
cmc	Critical micellar concentration	M
$c\mu c$	Critical microemulsion concentration	M
F_N	Tension force along thread	-
G	Gibbs free energy	J
H	Mean curvature	m^{-1}
H_0	Spontaneous curvature	m^{-1}
K	Gaussian curvature	m^{-1}
L	Thread length	m
L_A	Trap separation, normalised to drop radius	m, -
L_κ	Helfrich length	m
L_C	Capillary length	m
M	Number of traps	-
NA	Numerical aperture	-
$n, \Delta n$	Refractive index, contrast	-
P	Optical power	W
p_L	Laplace pressure	N m^{-2}
Q	Trapping efficiency factor	-
R, R_N	Thread radius	m
R_D	Droplet radius, undeformed	m
R_{minor}	Droplet semiminor axis, spheroid	m
$T, \Delta T$	Temperature, Laser heating	K
t	Time	s
V	Volume	m^3
z	Coordinate along beam axis	m
z_R	Rayleigh range of Gaussian beam	m
$\Delta\rho$	Buoyant density difference	kg m^{-3}
ϵ	Optocapillary number, first order perturbation parameter	-

$\bar{\epsilon}$	Quasi-second order parameter $\approx \epsilon$	-
γ	Total surfactant weight fraction in total mixture	-
γ_W	Total initial surfactant concentration in water	-
κ	Bending modulus	J
ϕ_A	Volume fraction of phase A	-
Ω	Volumetric water-to-oil ratio	-
θ	Angle between threads	deg
Λ	Aspect ratio for small to moderate deformations $\epsilon < 1$	-
Λ_∞	Value at which lateral splitting occurs in two traps	
β	Spheroidal model, constant to be determined	-
λ	Optical wavelength	m
ω_0	Beam waist	m

References

[1] D. Tapp, J. M. Taylor, A. S. Lubansky, C. D. Bain, and B. Chakrabarti, "Theoretical analysis for the optical deformation of emulsion droplets", *Opt. Express*, vol. 22, no. 4, p. 4523, 2014.

[2] S. Ellingsen, "Theory of microdroplet and microbubble deformation by gaussian laser beam", *J. Opt. Soc. Am. B*, vol. 30, no. 6, pp. 1694–1710, 2013.

[3] P. C. Moller and L. B. Oddershede, "Quantification of droplet deformation by electromagnetic trapping", *Europhys. Lett.* Vol. 88, no. 4, p. 48005, 2009.

[4] D. Bonessi, K. Bonin, and T. Walker, "Optical forces on particles of arbitrary shape and size", *J. Opt. A: Pure and Applied Optics*, vol. 9, no. 8, S228, 2007.

[5] K. M. Jansons and C. G. Phillips, "On the application of geometric probability theory to polymer networks and suspensions, i", *J. Colloid Interface Sci.* Vol. 137, no. 1, pp. 75–91, 1990, ISSN: 0021-9797.

[6] U. Delabre, K. Feld, E. Crespo, G. Whyte, C. Sykes, U. Seifert, and J. Guck, "Deformation of phospholipid vesicles in an optical stretcher", *Soft Matter*, vol. 11, no. 30, 6075–6088, 2015.

[7] R. Aveyard, B. P. Binks, S. Clark, and J. Mead, "Interfacial tension minima in oil-water-surfactant systems: behaviour of alkane-aqueous NaCl systems containing Aerosol-OT", *J. Chem. Soc., Faraday Trans. 1*, vol. 82, pp. 125–142, 1 1986.

[8] L. Bo and R. Waugh, "Determination of bilayer membrane bending stiffness by tether formation from giant, thin-walled vesicles", *Biophys J.* Vol. 55, no. 3, pp. 509–517, 1989.

[9] D. A. Woods, C. D. Mellor, J. M. Taylor, C. D. Bain, and A. D. Ward, "Nanofluidic networks created and controlled by light", *Soft Matter*, vol. 7, pp. 2517–2520, 6 2011.

[10] T. Sottmann and R. Strey, "Ultralow interfacial tensions in water-n-alkane-surfactant systems", *J. Chem. Phys.* Vol. 106, no. 20, pp. 8606–8615, 1997.

[11] B. Binks, H. Kellay, and J. Meunier, "Bending elastic modulus of monolayers at oil-water interfaces", *Thin Solid Films*, vol. 210-211, Part 1, pp. 118–120, 1992, ISSN: 0040-6090.

[12] R. Karlsson, A. Karlsson, and O. O, "A nanofluidic switching device", *J. Am. Chem. Soc.* Vol. 125, no. 28, pp. 8442–8443, 2003.

[13] L. Dagdug, A. M. Berezhkovskii, S. Y. Shvartsman, and G. H. Weiss, "Equilibration in two chambers connected by a capillary", *J. Chem. Phys.* Vol. 119, no. 23, pp. 12 473–12 478, 2003.

[14] R. Karlsson, A. Karlsson, A. Ewing, P. Dommersnes, J.-F. Joanny, A. Jesorka, and O. Orwar, "Chemical analysis in nanoscale surfactant networks", *Anal. Chem.* Vol. 78, no. 17, pp. 5960–5968, 2006.

[15] T. Lobovkina, P. Dommersnes, J.-F. Joanny, J. Hurtig, and O. Orwar, "Zipper dynamics of surfactant nanotube Y junctions", *Phys. Rev. Lett.* Vol. 97, p. 188 105, 18 Nov. 2006.

[16] B. P. Binks, P. D. I. Fletcher, and D. J. F. Taylor, "Temperature insensitive microemulsions", *Langmuir*, vol. 13, no. 26, pp. 7030–7038, 1997.

Chapter 6

3D imaging of deformed droplets

6.1   Fundamentals of 3D imaging techniques

A droplet is commonly described as a single, extended object of constant volume. If it is optically homogeneous, only the boundary location needs to be identified to determine the distribution of volume and *vice versa*. Equilibrated shapes are not expected to be hollow, as vacancies of a detectable size are unlikely to be stable. Many 3D imaging techniques are capable of reconstructing the shape of such a system satisfactorily. However, fluorescent confocal and structured illumination microscopy (SIM) do not require these assumptions *a priori*. Each can resolve arbitrary volumetric distributions, as each z-section is independent. Their 3D reconstruction is superior to stereoscopic imaging, particularly with feature-poor or occluded shapes.

The bulk of the 3D imaging results were obtained using confocal fluorescence microscopy, with examples of droplets[1] in 2-, 3- and 4-trap arrays from structured illumination sectioning.

---

[1]As for Chapter 5, the surfactant was AOT only ($\chi = 1$) and did not include the nonionics required for reduced temperature sensitivity. For the AOT/heptane/NaCl/H_2O and -D_2O quaternary systems, the surface tension varies strongly with salinity and temperature in a well-characterised manner (Chapter 1).

6.1.1 Confocal laser scanning microscopy

In confocal laser scanning microscopy, the field of view is illuminated by a focused laser such that a region of fluorescent oil is excited, but only light emitted from a volume matching the point-spread function (PSF) is passed through a pinhole to the camera at any instant [1]. The PSF z-dimension represents the axial resolution of the confocal microscope, which is many times smaller than the equivalent widefield fluorescence microscope. The laser focus and pinhole are rastered in xy to produce each z-section exposure. Increased resolution comes at the expense of signal; the low light levels require a low-noise scientific camera and long rastered exposures of 100 ms or more despite high-intensity excitation [2]. Typically, a stage-fixed sample is scanned in z by stepping the objective-to-stage distance, but for trapped objects, the trapping focus or detection plane must be moved instead. Here, this trap refocusing is achieved by displacing a telescope lens, although this introduces spherical aberration.[2] Experimental details including a rigorous calibration are given in § 6.6.

6.1.2 Structured illumination microscopy

Loss of image contrast with distance from the focus is a familiar effect which SIM exploits as a sectioning tool. It does so by imposing a known spatial modulation on the excitation light, for example with a periodic transmittance mask [4]. By shifting the periodic mask in xy and taking further frames, a set of three or more images per z slice is obtained, whose sum recovers the full widefield image. However, the *variance* between these images contains only information from the focal region carried by the input modulation. As higher frequency signals are transferred with less contrast at a given amount of defocus, finer modulation leads to a thinner z-section until the diffraction limit is reached.

    The primary advantages of SIM over confocal microscopy are that photobleaching

---

[2]Aberration-free refocusing is a developing area of non-adaptive optics, though constrained to unity magnification by Abbe's sine condition [3].

and exposure times are reduced. No emitted light needs to be rejected, since all of its structure corresponds to useful signal from the focal region. To build a z-stack of a trapped object, again either the trap or the SIM illumination plane must be refocused. For an optimal number of images per slice, SIM is expected to yield better signal-to-noise performance and sectioning response than confocal scanning microscopy [5]. For experimental details refer to § 2.4.3.

6.2   Single trap deformations

6.2.1   Elongation

3D imaging shows that droplets in a single trap are elongated along the z-axis as was inferred from the brightfield contraction in the lateral directions (§ 5.2). Although the droplets shown in Figure 6.1 are relatively stiff (of several μN m^{-1}), the axial aspect ratio is $\Lambda \leq 1.12$, significantly less than the value of 1.25 predicted from the spheroidal approximation described in § 5.2.

For single-trap deformations in the weak, spheroidal regime, the 3D aspect ratio scales linearly with the applied trap power for samples in D_2O. As the surface tension decreases, the droplet becomes more elongated and the trapping potential it experiences becomes less sensitive to its axial position. However, the buoyant force on the droplet's centre of mass is constant. As a result, the droplet's centre-of-mass is displaced further above the laser focus with increasing optocapillary number, ϵ (Figure 6.3) and decreasing capillary length L'_C.

As ϵ approaches unity, an hourglass shape develops in which the surface aligns with the iso-intensity contours of the beam § 5.3.1, with saddle curvature at the beam waist. The aspect ratio of the contours approaches $\Lambda \leq \sqrt{2e}/NA \approx 1.9$ a few z_R away from the focus. As for the two-trap dumbbells, the shapes are first asymmetric at the transition and become more symmetric as ϵ increases further. The illuminated face becomes increasingly flattened and its edge becomes more sharply curved.
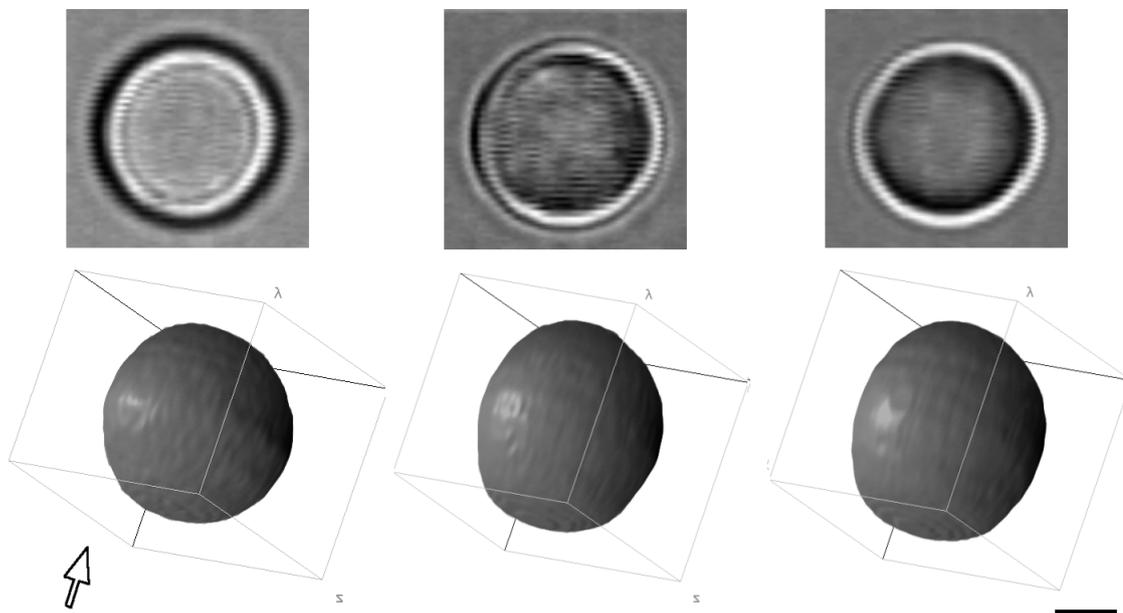
Figure 6.1: A single drop in a trap *(left to right)* deforming linearly along its axis with increasing optocapillary number below the PIT; *(top)* brightfield; *(bottom)* 3D volumes of each, rotated to emphasise variations. The arrow indicates the laser's direction of propagation (vertically upward in the laboratory). All to scale bar 2 μm. Conditions are $R_D = 3.2$ μm, $T_A = 20.9$ °C, $S = 44.0$ mM in H_2O, $\sigma = (9, 7, 6)$ μN m^{-1}, $P = (12, 19, 24)$ mW, $\epsilon = (0.1, 0.3, 0.4)$.

Unlike the two-trap case, the transition from barrel to hourglass shape is abrupt, occurring over a small range of ϵ close to 1 (Figure 6.2). The sequence of deformations is similar to that predicted in collaborative simulations [6]. The power required to induce saddle curvature in a $R_D = 2.4$ μm drop at $\sigma = 1.8$ μN m^{-1} is 24 mW, about half the 55 mW predicted from simulation for an smaller, softer $R_D = 2$ μm drop at $\sigma = 1$ μN m^{-1}. It is possible to avoid the constant empirical prefactors involved in the choice of $\epsilon = 1$ by instead comparing the ratio $P/\sigma R_D$ directly; the discrepancy is almost a factor of 5. While the uncertainty in the experimental ratio is large because of the sensitive surface tension, it is no greater than a factor of 2. That is to say, the experimental conditions for the transition give a Tapp-Lubansky-Taylor optocapillary number of just $0.2 - 0.4$. A force not accounted for

by the simulation is encouraging the droplet to recurve at a lower ratio of optical to surface forces; buoyancy is such a candidate. At the linear side of the transition, the upward, shadowed side of the droplet is more pointed and the illuminated side is flattened relative to the sphere. Although the optical forces on the two sides are not precisely equal due to the centre-of-mass displacement under scattering force, it is known that scattering-related asymmetry is small in the simulations, in which buoyancy is not included. The presence of significant asymmetry in experiment indicates that buoyancy can influence the shape subtly even when the capillary length is still large, $L'_C > 8$. It appears that buoyancy on the scale of the 'handle' could be facilitating the curvature transition associated with $\epsilon = 1$, by stretching the droplet vertically and flattening its longitudinal curvature.

Figure 6.4 [3] captures the transition point for a droplet of similar size, $2R_D \sim 5 \ \mu$m. Although the brightfield views are ambiguous in themselves, they give useful information as they are especially sensitive to the curvature of slightly defocused transparent objects [7]. Comparing the brightfield with the 3D volumes, the development of the waist is recognisable as the dark central spot.

For a smaller droplet of $2R_D \sim 3 \ \mu$m, at extreme $\epsilon > 10$, (see Figure 6.5), the shape no longer changes significantly, reflecting its adherence to the optical contours. The shapes are more symmetric across the waist than the larger droplets above, as a result of lesser buoyancy. However, the upper and lower faces show ridges and cusps which would not be expected from a diffraction-limited focus.

---

[3]Experiments in Figure 6.4 and a few others are performed above the PIT; laser heating increases the interfacial tension faster than the optical trap strength. Counter-intuitively, ϵ increases as the trap power decreases.
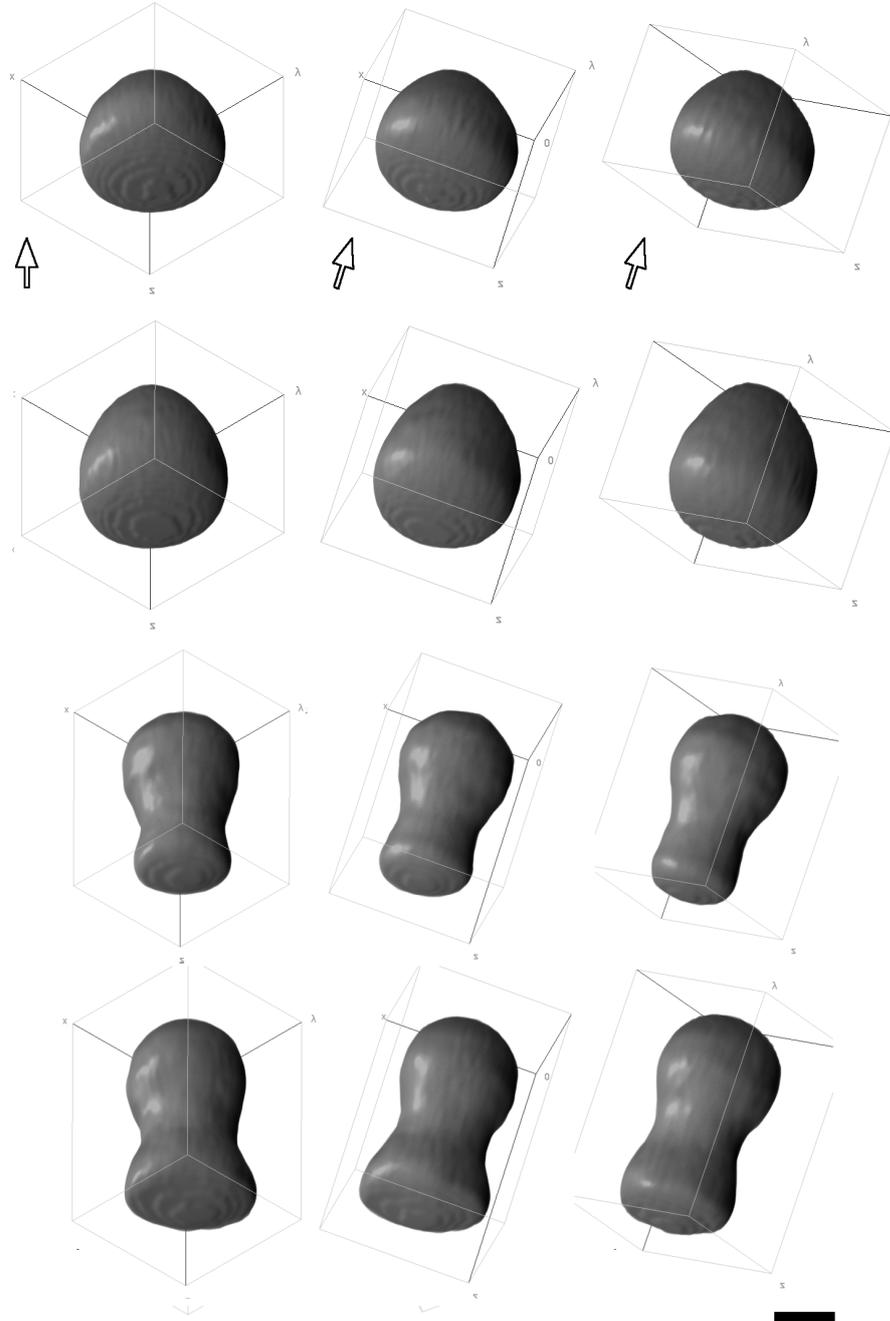
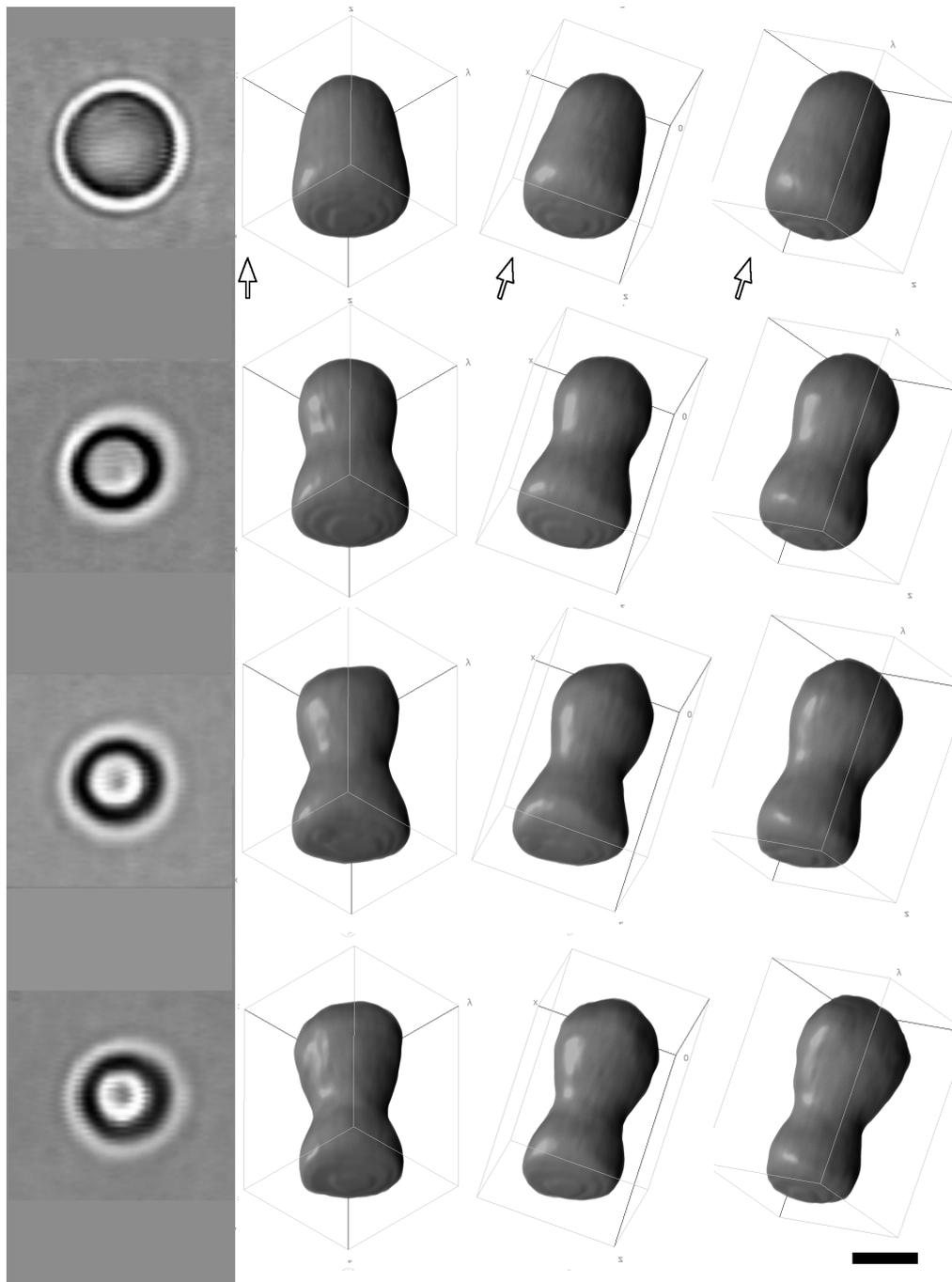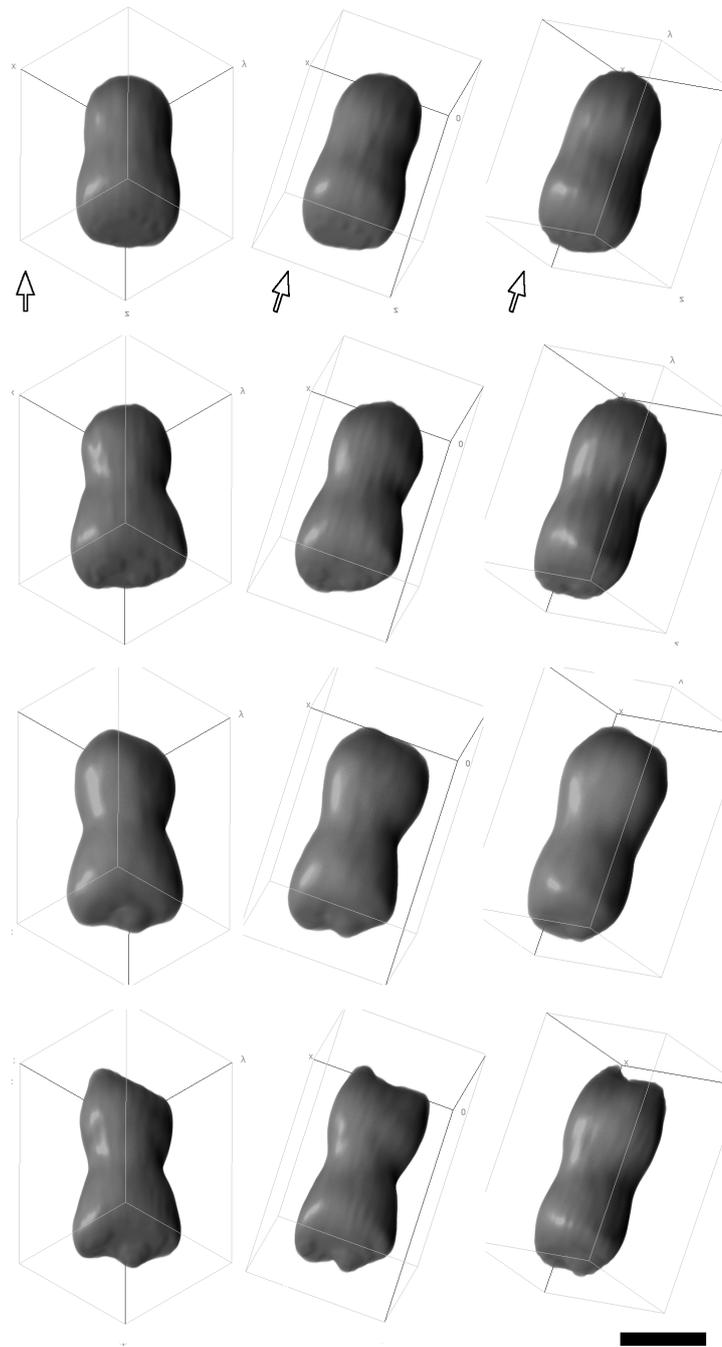Figure 6.2: 3D confocal volumes of a single drop in a trap; *(top to bottom)* development of the shape with increasing optocapillary number below the PIT; *(left to right)* identical volumes shown in three orientations. The arrow indicates the laser's direction of propagation (vertically upward in the laboratory). All to scale bar 2 μm. Conditions are $R_D = 2.4$ μm, $T_A = 20.2$ °C, $S = 43.0$ mM in H_2O, $\sigma = (2.8, 1.8, 1.8, 0.9)$ μN m^{-1}, $P = (12, 19, 24, 29)$ mW, $\epsilon = (0.3, 0.8, 1.2, 1.3)$.
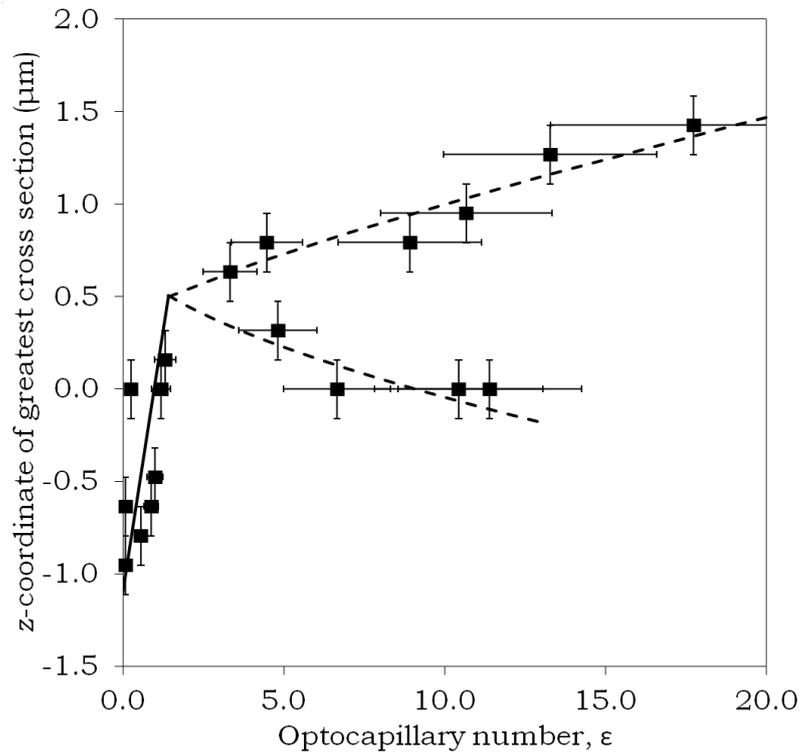
Figure 6.3: The widest part of the droplet moves upwards relative to the focus as the droplet becomes more deformed by a single trap. For small deformations ($\epsilon < 1$) this displacement is linear (solid line). For nonlinear deformations ($\epsilon > 1$), the widest cross section corresponds to the approximate midplane of either the upper or lower halves of the hourglass shaped droplet, which continue to separate (dashed lines).

The exceptionally high deformability of this droplet even allows the identification of aberrations in the beam used to trap it. In this case, the *bowtie*-like elliptical faces imply the presence of astigmatism and the concentric ridges and points on the faces imply spherical aberration.[4]

---

[4]As the instantaneous effect of spherical aberration on the optical intensity distribution cannot be symmetric around the focus, its equal presence on both sides shows that the aberration inverts in sign in the middle of the axial scan. The measured droplet shape is affected only at the extremes of z. See § 6.6.10.

Figure 6.4: A single drop in a trap; *(top to bottom)* development of the shape with increasing optocapillary number above the PIT; *(left to right)* brightfield views; identical 3D volumes shown in three orientations. The arrow indicates the laser's direction of propagation (vertically upward in the laboratory). All to scale bar 2 μm. Conditions are $R_D = 2.1$ μm, $T_A = 20.9$ °C, $S = 43.0$ mM in H_2O, $\sigma = (3.1, 1.8, 1.4, 0.7)$ μN m^{-1}, $P = (29, 24, 19, 12)$ mW, $\epsilon = (1.0, 1.6, 1.8, 1.8)$.

Figure 6.5: A single drop in a trap; *(top to bottom)* development of the shape with increasing optocapillary number and decreasing power above the PIT; *(left to right)* identical 3D volumes shown in three orientations. The arrow indicates the laser's direction of propagation (vertically upward in the laboratory). All to scale bar 2 μm. Conditions are $R_D = 1.5$ μm, $T_A = 21.0$ °C, $S = 43.0$ mM in H_2O, $\sigma = (1.1, 0.4, 0.3, 0.3)$ μN m^{-1}, $P = (29, 24, 19, 12)$ mW, $\epsilon = (1.5, 8.3, 14, 17)$.
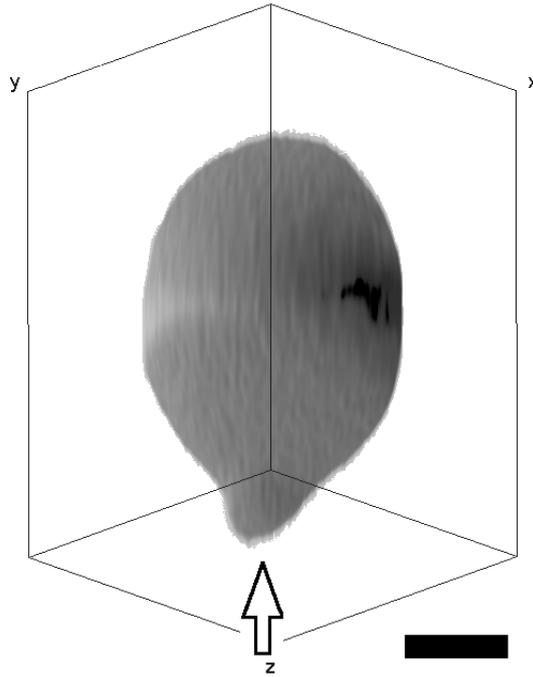
Figure 6.6: A single large drop in a trap; 3D volumetric reconstruction. The arrow indicates the laser's direction of propagation (vertically upward in the laboratory). Scale bar 2 μm. Conditions are $R_D = 3.2$ μm, $T_A = 20.9$ °C, $S = 29.5$ mM in D_2O, $\sigma = 1.2$ μN m^{-1}, $P = 17$ mW, $\epsilon = 1.2$.

For larger drops such as that shown in Figure 6.6, the hourglass transition does not occur since the buoyancy force is great enough to pull the majority of the fluid into the upper region far from the trap. The lower region is a *handle* (see § 5.4.2) with which the droplet is retained in the trap. Drops can only remain intact under buoyancy when the capillary length is greater than $L = \sqrt{R_D^2/3R_H}$, where R_H is the radius of the drop waist. For the droplet shown in Figure 6.6 this condition corresponds to an IFT of 0.4 μN m^{-1}, not very far below the experimental IFT.

6.3   Multiple trap deformations

6.3.1   Linear arrays

The separation of two or more overlaid traps breaks the rotational symmetry of the droplet in a novel way, generating many interesting shapes. However, ϵ, as used to catalogue and interpret them, must be redefined for a droplet subtending several traps. The values quoted here are divided by the number of traps, ϵ/M.

A representative example of the two-trap confocal stack is given in Figure 6.7. Rather than the prolate cigar-shape expected from the 2D view, the droplet is extended in z about the same distance as between the traps, giving a oblate pebble-shape. The illuminated face shows nothing of the protrusions seen in other samples, but is markedly flattened, and the oval points sharpened, relative to the rear face. At an IFT of 6 μN m^{-1} only convex structures are accessible, but elongation and flattening are easily identified. The increasing x, y curvature towards the laser axis-droplet intersections is a feature consistent with a local balance between Laplace and optical pressures.

The morphology changes with trap separation very differently in cases of transitional and very high ϵ/M. For moderately deformable droplets (Figure 6.9), the trapped reservoirs retain an elongated, convex, acorn-like shape as the droplet is stretched apart. A neck begins to appear at a separation of $L_A \sim R_D$, in that the surface becomes saddle-curved simultaneously in all directions perpendicular to the separation axis.
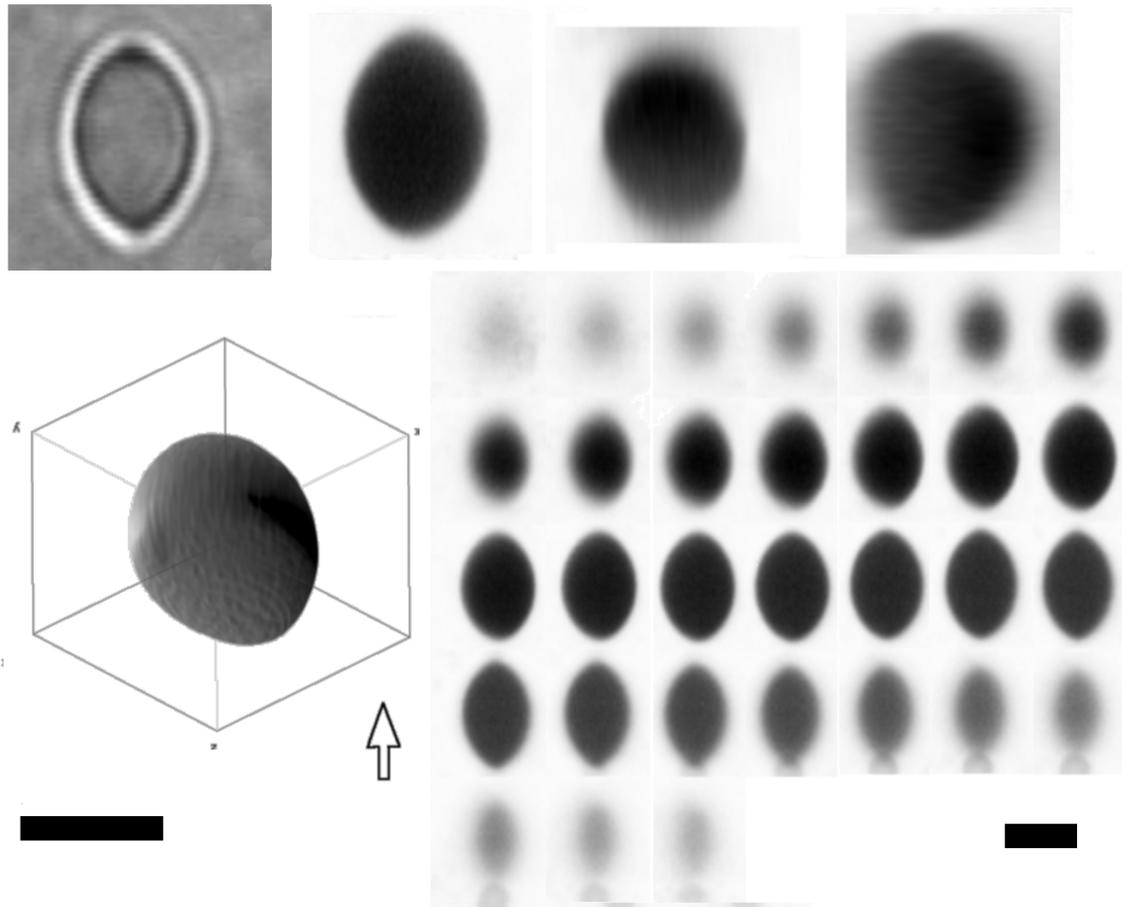
Figure 6.7: Two traps; *(top left)* brightfield view; *(top right)* confocal cross-sections in xy, xz and yz planes through the approximate centre-of-mass; *(bottom left)* 3D volumetric reconstruction. The arrow indicates the laser's direction of propagation (vertically upward in the laboratory); *(bottom right)* confocal xy frames as a function of z from top (shadowed) to bottom (illuminated), at half scale. All to scale bar 5 μm, except inset scale bar 2 μm. Conditions are $R_D = 3.3$ μm, $T_A = 20.5$ °C, $S = 45.0$ mM in H_2O, $\sigma = 7$ μN m^{-1}, $P = 39$ mW, $\epsilon/M = 0.7$, $L_A = 4.3$ μm.

At larger separations $L_A/R_D > 1$ but less than that required for collapse to a thread, the neck develops an interesting asymmetry. A perfect circular-catenoidal neck would require perfect circles as bounding contours. However, the end reservoirs show an axial elongation similar to that of droplets in single traps. The vertical cross-sections are shown in Figure 6.8. At the extrema of the droplet along the axis of separation, this ratio is as great as $\Lambda_{xz} = 1.7$, approaching that of the iso-intensity

contours. The cross sections at the trap locations are extended along the axis by $\Lambda_{xz} = 1.2$ on both sides. Moreover, the central cross section is also elliptical, but instead with an axial *contraction* of $\Lambda_{xz} = 0.85$. Elliptical catenoids are minimal surfaces with the property that where the bounding contours broaden in the z direction, the neck narrows in z more steeply along its length. The overall result is that the volume of the neck region is conserved; the axial deformation of the trapped reservoirs does not require material to be removed from regions of higher optical intensity to be added to the neck. The capillary ratio is very high, $L'_C > 20$, so asymmetry in z due to buoyancy is very weak. The neck does not appear to bend upwards, nor does it attach to the upper part of the reservoirs.
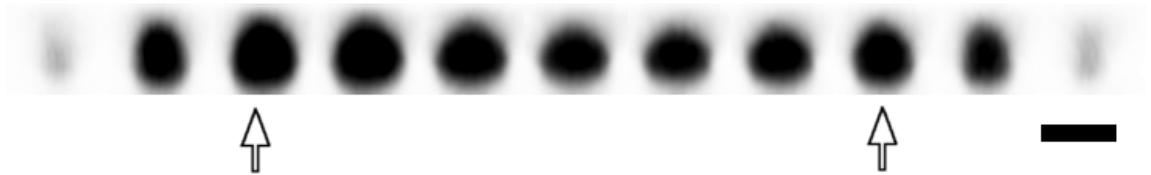
Figure 6.8: A droplet extended across two traps as shown in Figure 6.9, lowest figure; *(left to right)* vertical yz cross sections at 0.64 μm intervals along the separation axis x. The arrows indicates the two lasers' x positions and direction of propagation (vertically upward in the laboratory along $+z$). All to scale bar 3 μm.

For droplets of exceptionally high deformability, as in Figure 6.10 above the PIT, the shapes obtained resemble overlapping single-trap shapes of high ϵ. Around $L_A/R_D \sim 1$, the droplets first become concave in the lateral direction between the foci. Where the flattened illuminated faces meet, there is a slight downward bulge. There is no counterpart on the shadowed side.
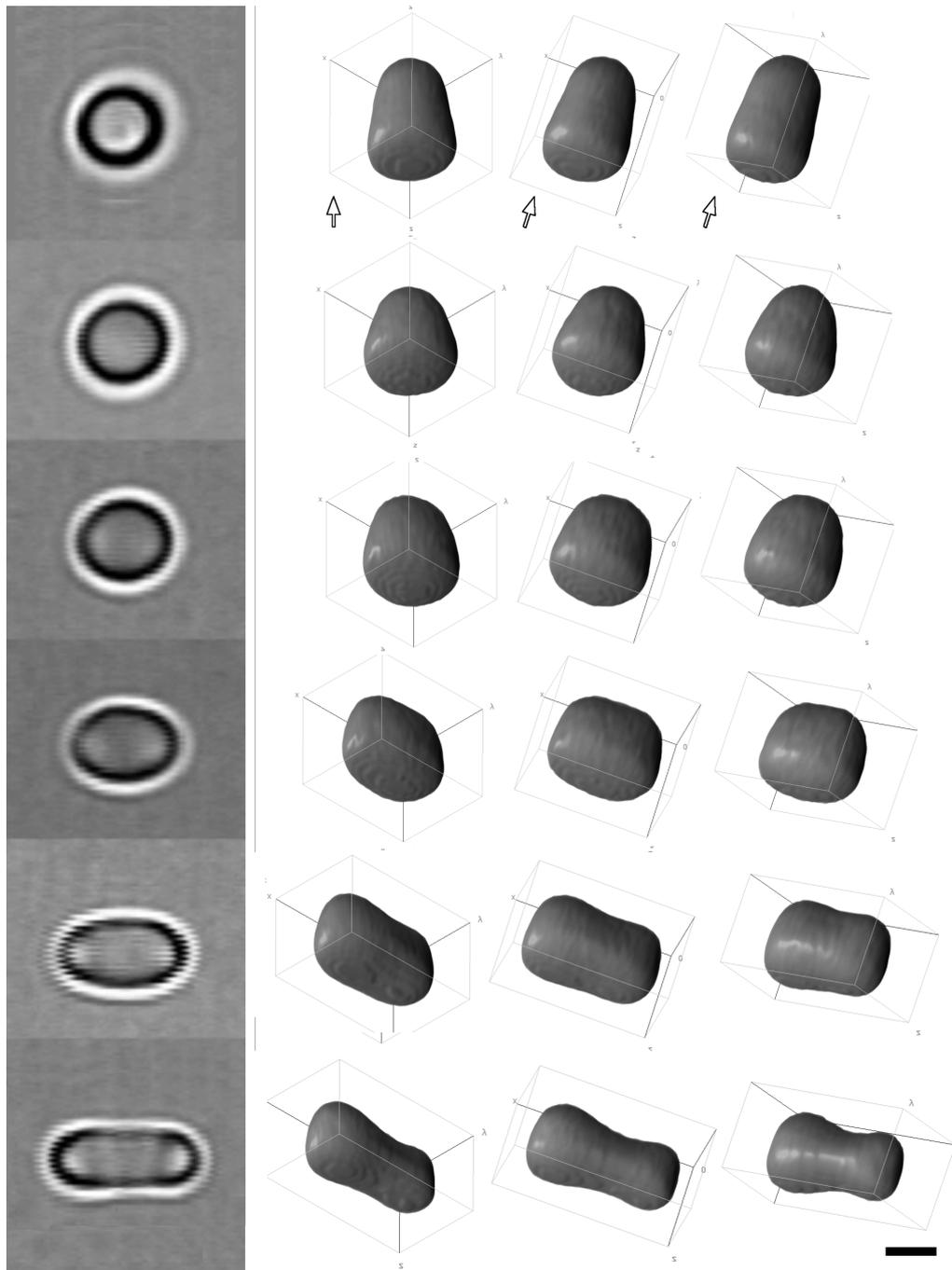
Figure 6.9: Two traps at moderate optocapillary number; *(top to bottom)* development of the shape with increasing trap separation; *(left to right)* brightfield views; identical 3D volumes shown in three orientations. The arrow indicates the laser's direction of propagation (vertically upward in the laboratory). All to scale bar 2 μm. Conditions are $R_D = 2.0$ μm, $T_A = (20.5, 20.6, 20.7, 20.8, 20.8)$ °C, $S = 29.5$ mM in D$_2$O, $\sigma = (4, 8, 7, 6, 5, 5)$ μN m^{-1}, $P/M = 15$ mW, $\epsilon/M = (1.0, 0.8, 0.9, 1.1, 1.4, 1.4)$, $L_A = (0, 0.7, 1.4, 2.2, 2.9, 3.4)$ μm.

This difference probably stems from the mild astigmatism evident in the traps, whereby the elliptical beams extend along the separation axis - and therefore overlap - on one side of the focus but not the other. At larger separations, the neck rises well above the z-plane of the foci to conjoin the shadowed halves of the reservoirs. Relative to Figure 6.9, ϵ/M is made larger at constant power by decreasing IFT by an order of magnitude. Consequently, the effect of buoyancy on the shapes in Figure 6.10, as quantified by the capillary length $L'_C > 4$, is far greater.

Thread measurements

Separating the traps further results in an asymmetric bifurcation consistent with the brightfield dimensions (Figure 6.10, lowest). Although the nanothread itself cannot be resolved in a confocal reconstruction whose threshold is set by the droplet volume, its presence can be inferred from the 120°-angled cusps where it attaches to the reservoirs. The thread itself is discernible in the cross-sections of the upper half of the split droplet, albeit only at high contrast (Figure 6.11). The peak emission intensity is about $50\times$ less for the thread than the larger reservoir. The reservoir extends over the confocal depth of field, $DoF = 3n_W\lambda/2NA^2 = 0.8\ \mu$m, where n_W is the refractive index of water, whilst the thread appears over a width of $W = 0.4\ \mu$m due to its fluctuation during exposure.

The true thread dimensions obey $\pi R_T^2 = DoF \cdot W/50$ assuming uniform oil luminosity, such that $R_T = 50 \pm 6$ nm. The corresponding estimate of the IFT is $\sigma = \kappa/2R_T^2 = 0.8\pm0.1\ \mu$N m^{-1}, which matches that calculated from the laser-heated temperature and salinity within error. A similar thread calculation is used in § 6.3.3.

A summary of the morphologies observed when varying the optocapillary number and trap separation for a smaller droplet in two traps is given in Figure 6.12.
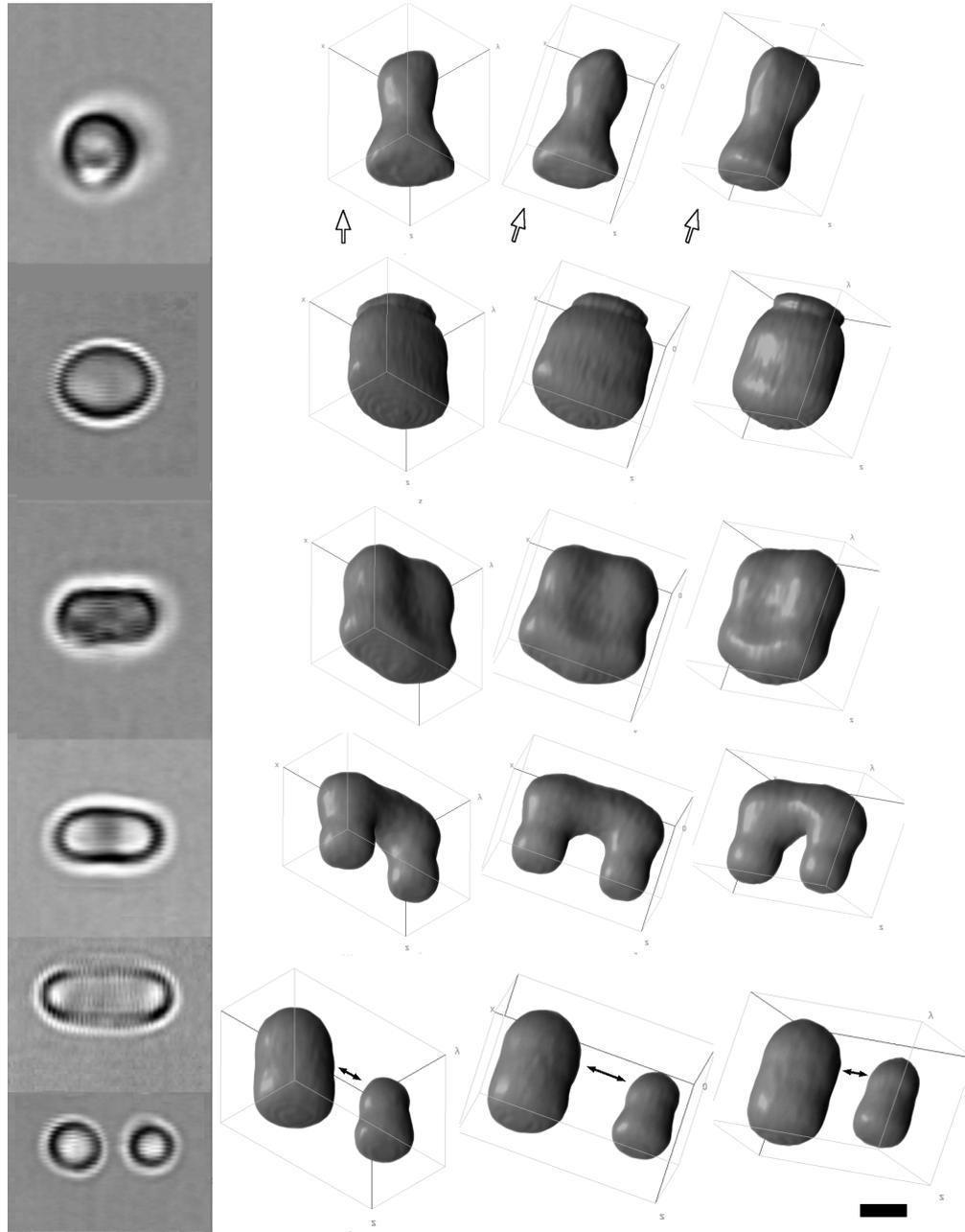
Figure 6.10: Two traps at very high optocapillary number; *(top to bottom)* development of the shape with increasing trap separation; *(left to right)* bright-field views; identical 3D volumes shown in three orientations. The unfilled arrows indicates the laser's direction of propagation (vertically upward in the laboratory); in the final row, the smaller double arrows indicate the position of the nanothread as shown in Figure 6.11. All to scale bar 2 μm. Conditions are $R_D = 2.4$ μm, $T_A = (20.2, 20.5, 20.3, 20.6, 20.4)$ °C, $S = 43.0$ mM in H_2O, $\sigma = (0.3, 0.4, 0.3, 0.9, 0.6)$ μN m^{-1}, $P/M = 15$ mW, $\epsilon/M = (12, 14, 17, 7, 10)$, $L_A = (0, 0.7, 1.4, 2.2, 2.9, 3.4)$ μm.
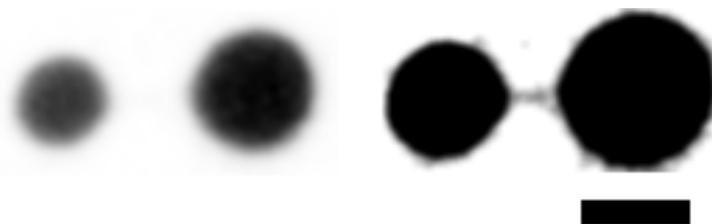
Figure 6.11: An xy cross-section of the bifurcated droplet shown in Figure 6.10, in the midplane of the upper part; (*left*) with contrast normalised to the droplet centre as used for reconstruction, with thread not visible; (*right*) the same frame at $20\times$ digital saturation, revealing the nanothread averaged over the 1s confocal exposure. Scale bar 3 μm.

The lateral asymmetry between the trap positions probably arises from a slight mismatch in trap powers [5] The weaker and less-developed side follows a similar trend to the stronger trap, albeit delayed to lower IFT, in that the underside of the droplet moves upwards across the focus and curves around it. The droplet's upper surface also moves upwards uniformly, eventually extending beyond the endpoint of the scan. At high ϵ/M, the stronger trap pinches the respective half of the droplet into an hourglass at its focal point. At the lowest IFTs, the droplet appears rougher as its fluctuations increase and it begins to shed oily, microemulsifying debris, primarily at the illuminated side of the hourglass.

---

[5]In timesharing (Setup B) and the random mixing algorithm (Setup C), the trap powers are not equalised manually but are equal by definition and are indistinguishable in practice. Most likely, the difference in power stems from the decrease in the holographic diffraction efficiency with different displacements from the zeroth-order beam (§ 2.4.3). The quoted power P/M is half the known calibrated transmission for a single trap at the centre of the field of view.
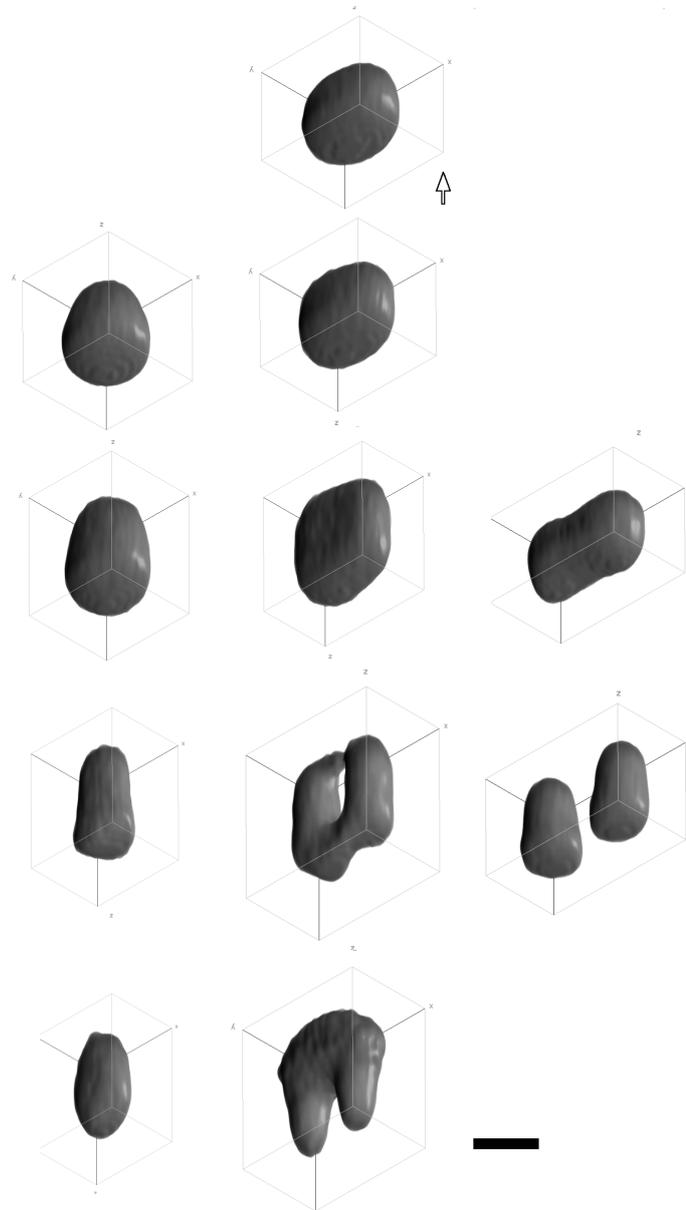
Figure 6.12: Shapes produced *above* the PIT at different optical powers (*i.e.* optocapillary numbers) and separation of two traps; *(top to bottom)* decreasing optical powers $P/M = (29, 24, 19, 14, 9)$ mW; *(left to right)* increasing trap separations, $L_A = (0.7, 1.4, 2.2)$ μm. The arrow indicates the laser's direction of propagation. All to scale bar 2 μm. Conditions are (reading L→R then T→B) $R_D = 1.5$ μm, $S = 43.0$ mM in H$_2$O, $T_A = (21.1; 21.0, 20.9; 21.0, 20.9, 20.9; 20.9, 20.9, 20.8; 20.9, 21.0)$ °C, $\sigma = (3.8; 3.0, 1.8; 2.4, 1.8; 1.4, 1.8, 1.4; 0.7, 1.1, 1.3)$ μN m^{-1}, $\epsilon/M = (1.2; 1.5, 2.0, 2.0; 1.6, 1.9, 3.6; 2.7, 2.5; 2.6, 4.8)$.
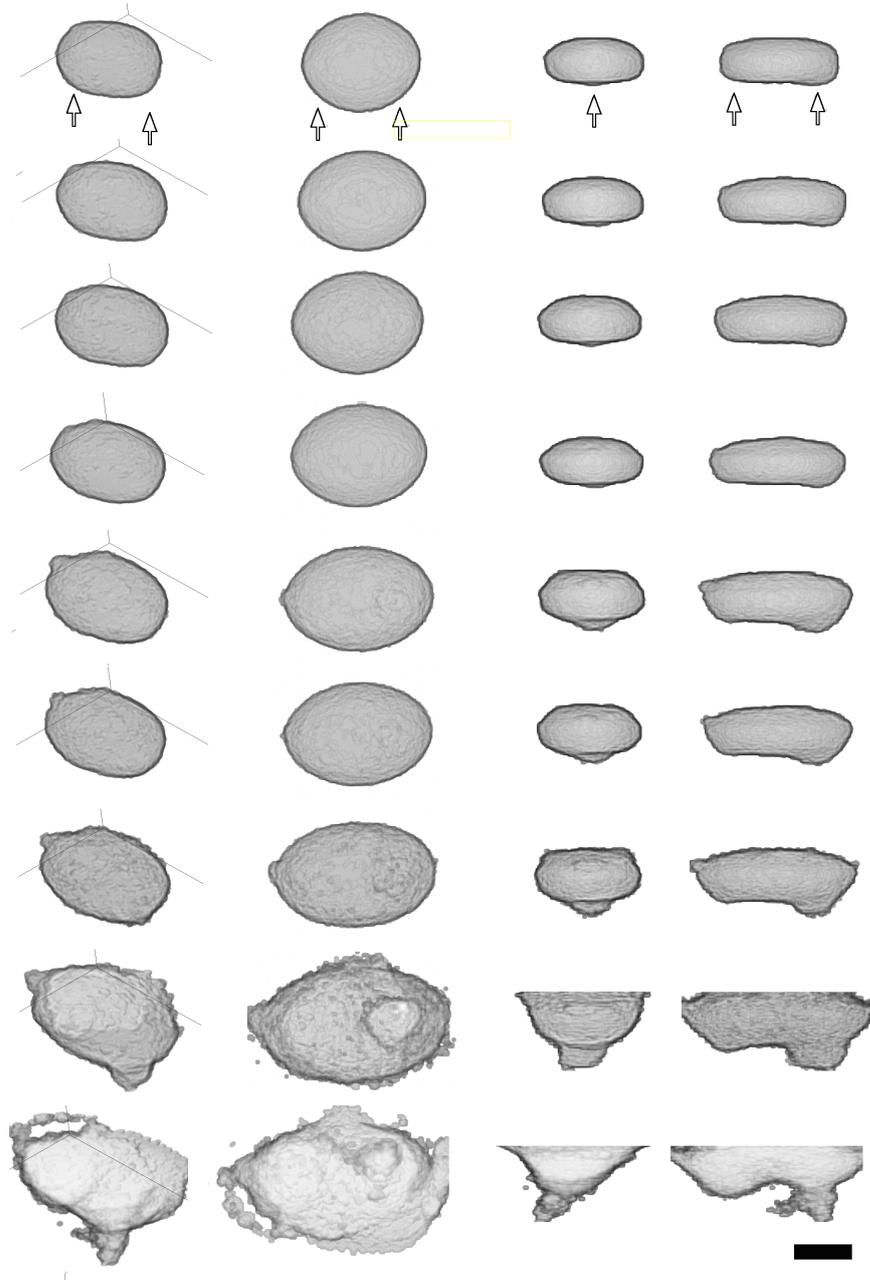
Figure 6.13: Large droplet in two traps at moderate optocapillary number, stacks obtained by SIM; *(top to bottom)* shape with increasing trap power; *(left to right)* identical volumes, median-intensity projections in four orientations: *oblique, xy, yz, xz.* All to scale bar 4 μm. Conditions are $R_D = 3.8$ μm, $L_A = 6.0$ μm, $S = 30.0$ mM in D$_2$O, $T_A = 20.6$ °C, $\sigma = (20, 16, 13, 10, 7, 5, 3, 2, 0.8)$ μN m^{-1}, $P/M = (69, 75, 81, 87, 93, 99, 105, 111, 117)$ mW, $\epsilon/M = (0.8, 1.1, 1.5, 2, 3, 5, 8, 14, 30)$,

As ϵ/M decreases, the IFT becomes significant, but it can only act on the centre of mass if it varies strongly across the surface. In most of the results in this chapter, the traps are close to the surface and laser-heating in H_2O is strong. However as discussed in § 4.6, the typical thermal gradients are insufficient to generate appreciable thermocapillary stresses in any direction. The thermal forces on the interface are attractive towards the regions of high intensity below the PIT and repulsive above the PIT. Since thermal forces vary with optical power, their effect on the shape cannot be easily distinguished from the effect of trapping forces.

For Figure 6.13, the highest power (117 mW) is around the minimum used in § 4.6, but the IFT is far more temperature-sensitive in these experiments. It is feasible that the difference in attractive thermocapillary forces could contribute to the asymmetry across the two trap positions, particularly since the hourglass surface lies within 1.4 μm of the stronger trap's focus. This set of conditions corresponds to upper limits of $\Delta T = 1.8$ K and $\nabla T = 0.08$ K μm^{-1} from § 4.7, whilst $T - T^* = 0.3$ K, such that $\delta\sigma/\delta T = 3$ μN m^{-1}K^{-1} and so $\nabla\sigma \leq 0.24$ N m^{-2}. This capillary stress is significant compared to the Laplace pressure at this necking point, $p_L \leq \sigma/1.4$ μm $= 0.6$ N m^{-2}. By this calculation the thermocapillary stress has forced the neck diameter to decrease by as much as 40%, compared to the case of uniform interfacial tension at the same average value. The difference in trap powers across the droplet would appear larger than the true value. The estimated difference from a rough correlation of the droplet shapes is $\pm 8\%$ of the mean P/M, which is greater than the calibrated upper limit of $\pm 3\%$ due to variations in holographic diffraction efficiency over the separation distance of 10 μm.

By comparison across the PIT, where Marangoni forces should reverse direction, the significance of thermal forces in the rest of the results - whose power and therefore thermal variation across the surface is less by almost an order of magnitude - can be neglected (see § 6.3.3).

For large droplets (Figure 6.14), a significant departure from a sphere can be achieved without pulling out handles from the lower surface. By keeping the separation around one drop radius, $L_A/R_D \sim 1$, and maintaining a moderate optocapillary number, $\epsilon/M \sim 1$, the droplet extends in both x and z almost equally. Here, the oblate shape is oriented edge-on to the beam axis, whereas for larger separations $L_A/R_D \gg 1$, as in Figure 6.13, it is oriented facing the beams.
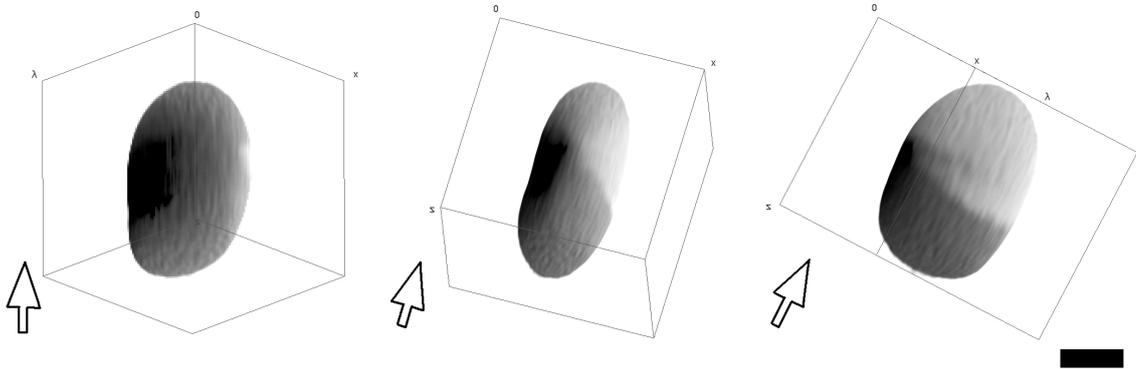

Figure 6.14: Two traps; *(left to right)* identical 3D volumes shown in three orientations. The arrow indicates the laser's direction of propagation (vertically upward in the laboratory). All to scale bar 4 μm. Conditions are $R_D = 3.4$ μm, $T_A = 21.2$ °C, $S = 29.5$ mM in D$_2$O, $\sigma = 6$ μN m^{-1}, $P/M = 20$ mW, $\epsilon/M = 0.9$, $L_A = 3.2$ μm.

Adding a third trap in the centre (Figure 6.15) roughly doubles the end-to-end separation required to split the droplet. Notwithstanding the tendency for a droplet to split asymmetrically by volume, the bifurcation behaviour of each side can be treated as approximately independent of the other. The invisible nanothread created by the first split does not affect the shape of the larger reservoir, which is the same as that produced by two traps in the absence of a third (compare with Figure 6.12, centre).
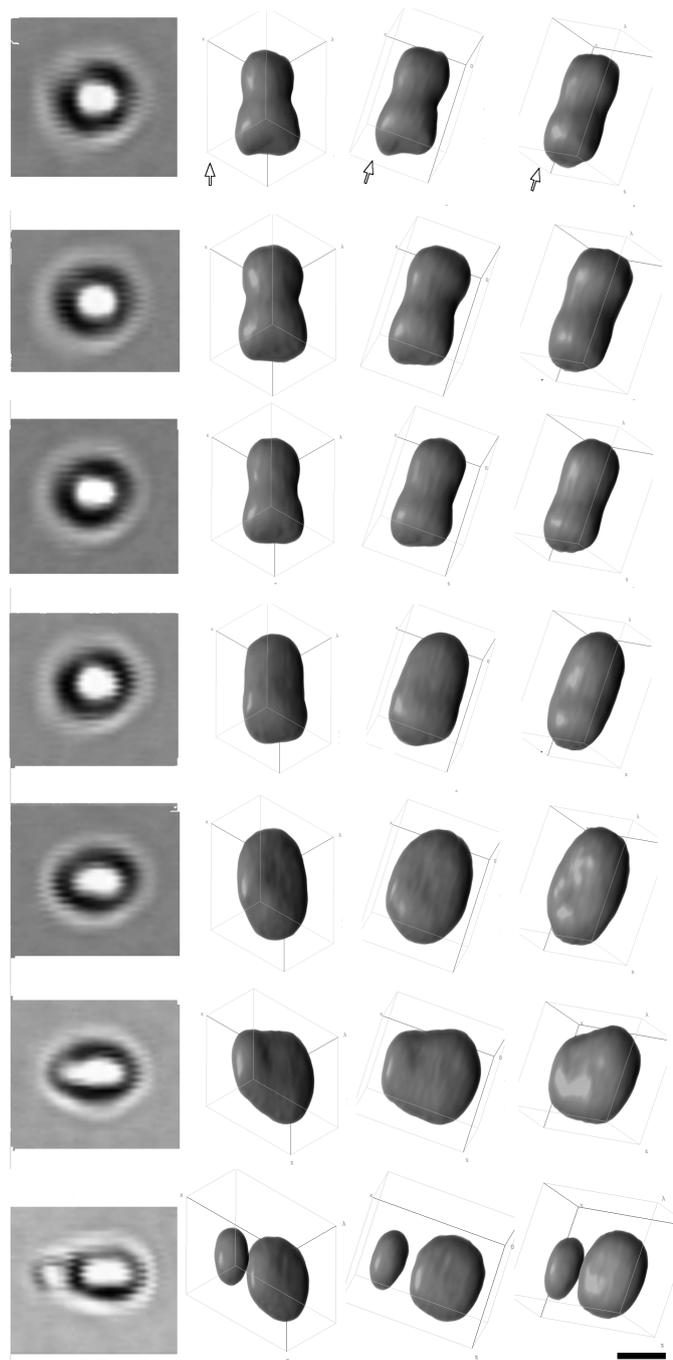
Figure 6.15: A droplet suspended in three colinear traps; *(top to bottom)* increasing end-to-end separation L_A = $(0, 0.4, 0.7, 1.4, 2.2, 2.9, 3.6)$; *(left to right)* brightfield views; identical 3D volumes shown in three orientations. The nanothread implicit in the bifurcation not resolved. All to scale bar 2 μm. Conditions are $R_D = 1.6$ μm, $S = 43.0$ mM in H$_2$O, $P/M = 6.4$ mW, $T_A = (20.6, 20.4, 20.3, 20.7, 20.7, 20.7, 20.7)$ °C, $\sigma = (0.9, 0.9, 1.9, 2.6, 2.5, 2.5, 2.5)$ μN m^{-1}, $\epsilon/M = (3.7, 3.7, 2.0, 1.3, 1.4, 1.4, 1.7)$.

6.3.2   Triangular arrays

For regular, coplanar arrays of three traps, a pleasingly regular threefold symmetry is preserved in the droplet surfaces.[6] In Figures 6.16 and 6.17, the separations are larger than the examples obtained with two traps. The dimensions of the illuminated base, marked by slight shoulders or cusps, match the known trapping positions.
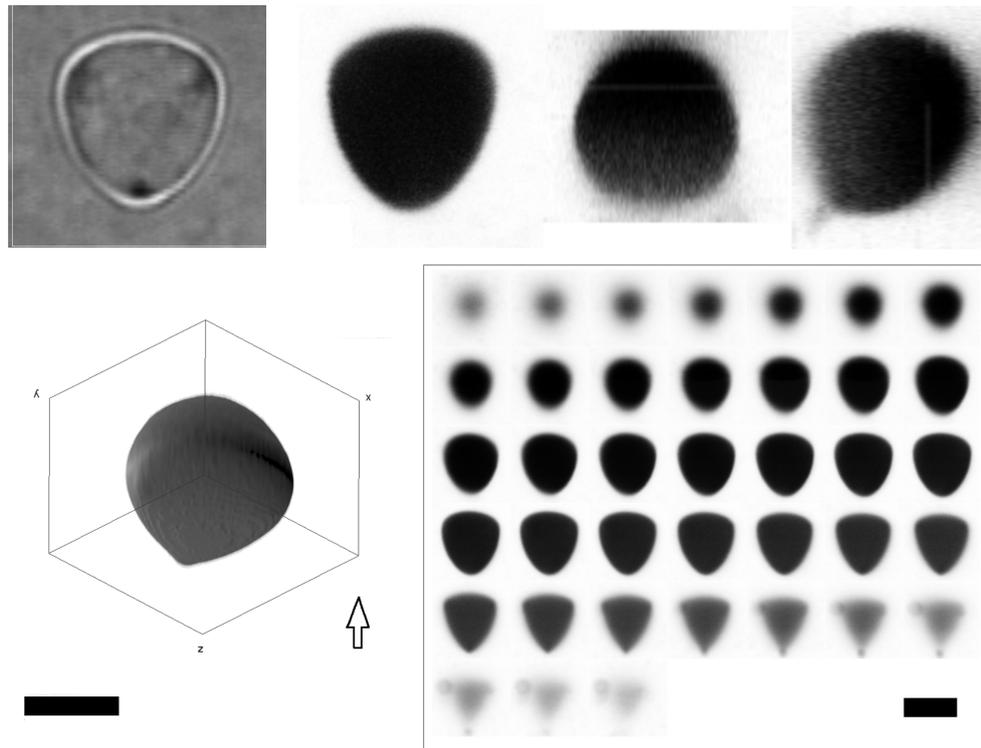

Figure 6.16: Three traps; *(top left)* brightfield view; *(top right)* confocal cross-sections in xy, xz and yz planes through the approximate centre-of-mass; *(bottom left)* 3D volumetric reconstruction. The arrow indicates the laser's direction of propagation (vertically upward in the laboratory); *(bottom right)* Confocal xy frames as a function of z from top (shadowed) to bottom (illuminated), at half scale. Both scale bars 5 μm. Conditions are $R_D = 4.4$ μm, $T_A = 20.5$ °C, $S = 45.0$ mM in H_2O, $\sigma = 4$ μN m^{-1}, $P/M = 13$ mW, $\epsilon/M = 0.6$, $L_A = 9.0 \times 7.2$ μm.

---

[6]Equal separations in x, y do not relate precisely to an equilateral triangle, but an isoceles subtending a square.
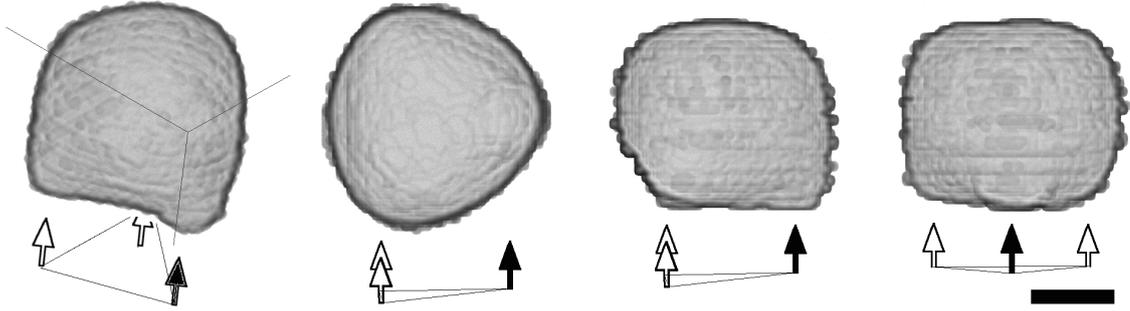
Figure 6.17: Three traps. Stacks obtained by structured illumination microscopy; identical volumes shown as median-intensity projections in four orientations: *oblique*, *xy*, *yz*, *xz*. Arrows indicate lateral position and direction of trapping beams. Scale bar 3 μm. Conditions are $R_D = 3.8$ μm, $S = 30.0$ mM in D_2O, $T_A = 20.7$ °C, $\sigma = 8$ μN m^{-1}, $P/M = 74$ mW, $\epsilon/M = 0.7$, $L_A = 5.7 \times 5.0$ μm.

In the first case the markedly triangular lower face is also flattened due to its larger trap separation, while the upper side remains rounded. In the latter, the xy cross-section of Figure 6.17 very closely resembles a Reuleaux triangle - a curve of constant width in every orientation. As for the ovals of greatest separation relative to the initial radius (Figures 6.7, 6.9 and 6.13), neither shows notable elongation along the vertical axis.

Interpretation of the sequence in Figure 6.18 is particularly clear since the ϵ/M is almost constant over the dynamic range of the laser power. Decreased laser powers makes the droplet soften since the temperature is above the PIT. As the separation of the traps is also constant, the principal variable is the capillary length, which decreases from $L'_C \approx 12$ to ≈ 6. This property indicates strongly that the differences in shape result solely from the buoyant stress across the droplet. While the droplet is distorted only mildly from a sphere in terms of aspect ratio, this has much to do with the particular separation of the traps at $L_A/R_D = 0.7$ so that lateral stretching compensates for axial elongation. The main development is the inversion in curvature of the illuminated surface; it changes from a convex, rounded triangle to an acute, concave one, whose points begin to protrude. The equatorial

surfaces (or the oblong faces of the triangular prism), at first coplanar with the beam axis, become more rounded as the optical forces decrease.
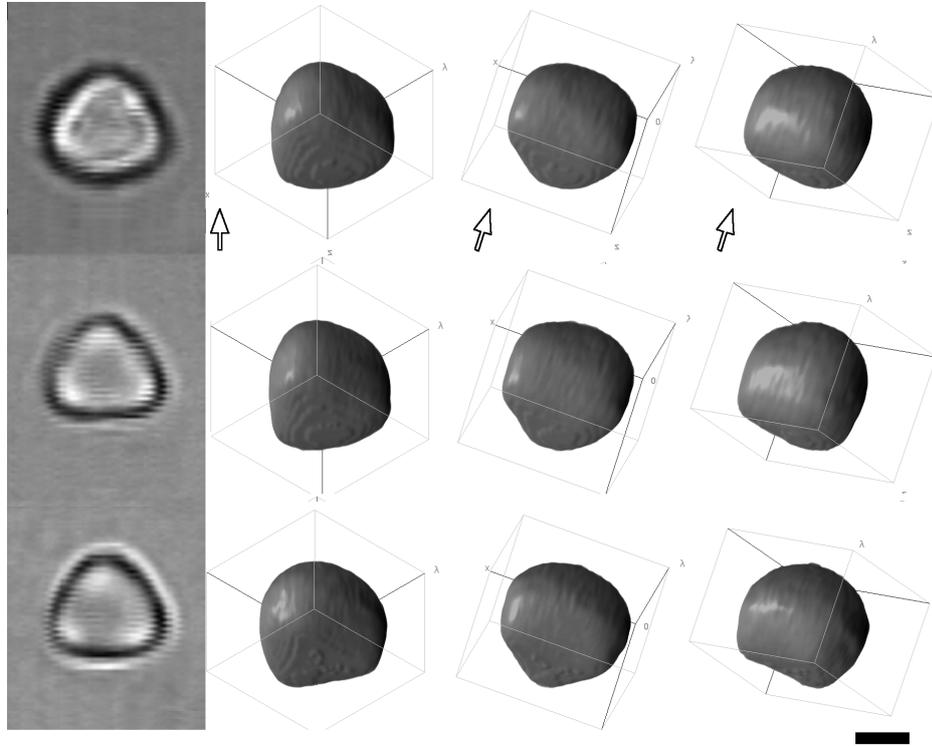

Figure 6.18: A droplet is stretched in three traps. One stack is shown per row; *(left to right)* identical 3D volumes shown in three orientations; *(top to bottom)* decreasing interfacial tension and optical power *above* the PIT. The arrow indicates the laser's direction of propagation (vertically upward in the laboratory). All to scale bar 2 μm. Conditions are $R_D = 2.4$ μm, $S = 43.0$ mM in H_2O, $T_A = 20.5$ °C, $\sigma = \mu$N m^{-1}, $P/M = (10, 8, 6, 3)$ mW, $\epsilon/M = (1.5, 1.7, 1.7, 1.7)$, $L_A = 3.6 \times 3.6$ μm.

The same trends are visible in Figure 6.19, in which the capillary length also decreases, from $L'_C \approx 8$ to ≈ 3. The larger, more buoyant shapes are flattened to a greater extent on the upward, shadowed side and are thinned along z. However, the temperatures lie below the PIT and ϵ/M increases with higher P due to laser heating. The strongest effect of higher ϵ/M is that the handles dominate the lower half of the object, with a distinctive trefoil xy cross-section and saddle curvature along the lines between trap positions. For the highest ϵ/M, a very weak concavity

(negative mean curvature) is observed in the centre of the trap array.

The trends in droplet elongation and edge definition of the illuminated half continue with triangular prism-like droplets (Figure 6.20). The illuminated faces are flattened with a smooth but well-defined edge. The trap intersections protrude with increased ϵ/M in a way that resembles the handles in Figures 6.6 and 6.13. Yet for a small coplanar array of three or more distinct traps, each pair of traps can also support flattened vertical faces extending upwards to the equator of the droplet.
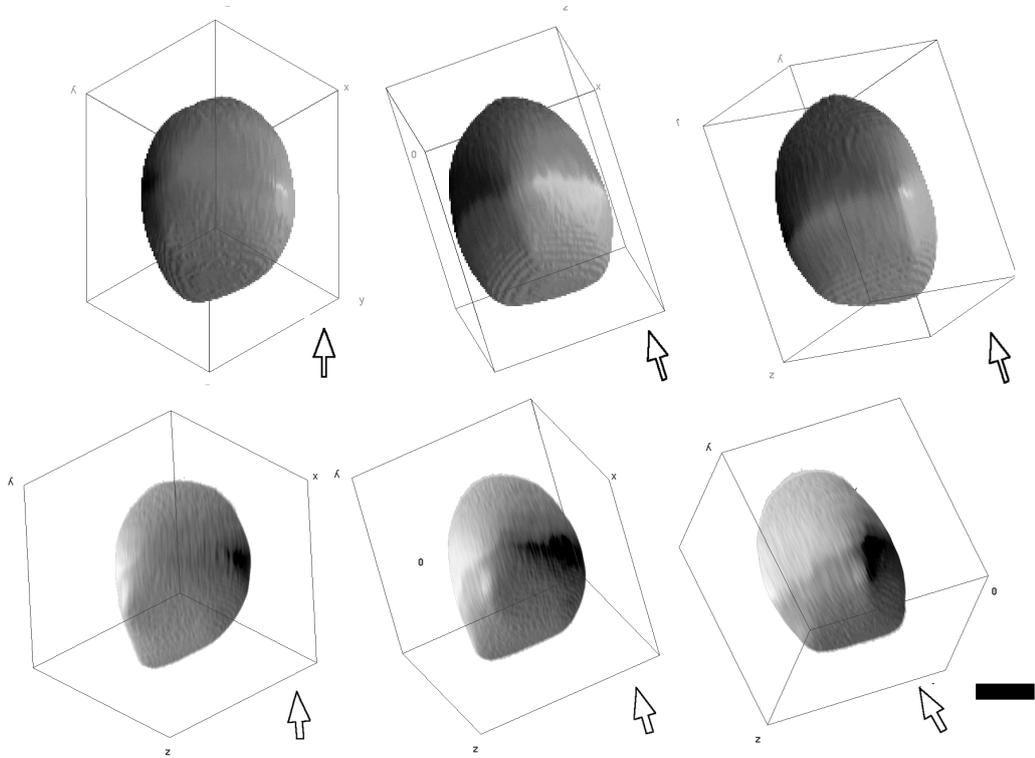

Figure 6.20: A droplet is stretched in three traps. One stack is shown per row; *(left to right)* identical 3D volumes shown in three orientations. The arrow indicates the laser's direction of propagation (vertically upward in the laboratory). All to scale bar 3 μm. Conditions are $R_D = (4.1, 4.0)$ μm, $S = (29.5, 31.5)$ mM in D$_2$O, $T_A = (21.2, 21.5)$ °C, $\sigma = (1.9, 1.2)$ μN m^{-1}, $P/M = 13$ mW, $\epsilon/M = (1.5, 2.4)$, $L_A = 5.0 \times 5.0$ μm.
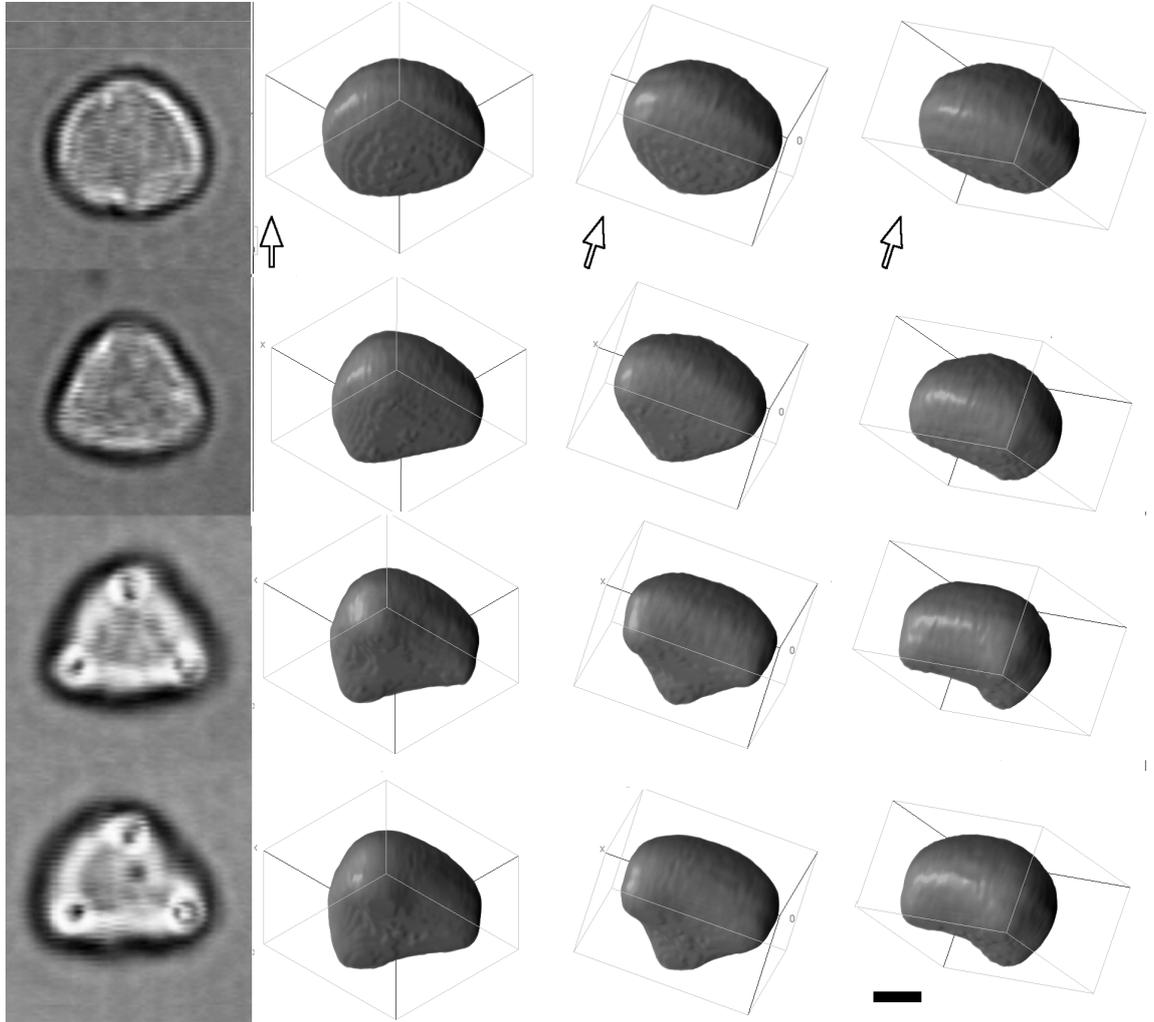
Figure 6.19: A droplet is stretched in three traps. One stack is shown per row; *(left to right)* identical 3D volumes shown in three orientations; *(top to bottom)* increasing optocapillary number and power below the PIT. The arrow indicates the laser's direction of propagation (vertically upward in the laboratory). All to scale bar 2 μm. Conditions are $R_D = 2.9$ μm, $S = 46.0$ mM in H_2O, $T_A = 21.9$ °C, $\sigma = (1.8, 0.7, 0.4, 0.3)$ μN m^{-1}, $P/M = (3, 6, 8, 10)$ mW, $\epsilon/M = (0.5, 2.9, 7.9, 8.8)$, $L_A = 5.4 \times 5.4$ μm.

Each shape becomes increasingly triangular, though remaining convex, in cross-section toward the illuminated underside, whose surface lies within half a micron from the focal plane. For large drops at small separations $L_A/R_D = 0.7$ or less, the extension in z is roughly maximal, around 0.2-0.3 R_D (Figure 6.21); while the upper surface is almost spherical, on the lower face there are three protrusions of relatively high curvature, each marking the intersection with a trap axis.
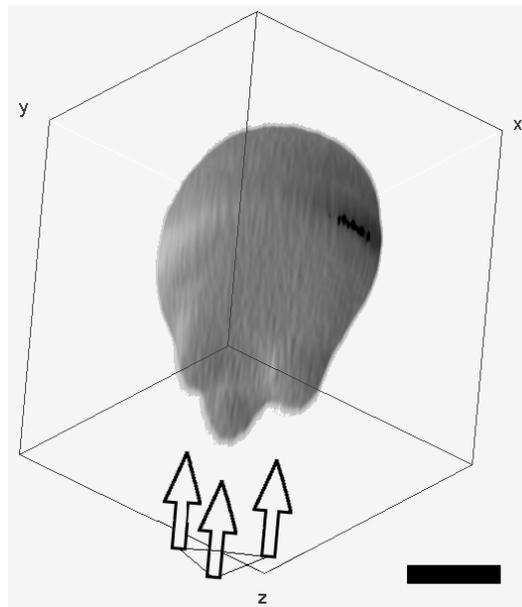

Figure 6.21: A large droplet is stretched in three closely spaced traps. The arrow indicates the laser's direction of propagation (vertically upward in the laboratory). Scale bar 3 μm. Conditions are R_D =4.6 μm, $S = 30.0$ mM in D_2O, $T_A = 20.8$ °C, $\sigma = 0.4$ μN m^{-1}, $P/M = 13$ mW, $\epsilon/M = 5.8$, $L_A = 3.6 \times 3.6$ μm.

These handles strongly resemble the feature in the single trap scan (Figure 6.6). The shape instils confidence as the simultaneous capture of three equally sized foreign bodies is unlikely and the handles cannot be thresholded out. The face between the protrusions includes concave regions ($H < 0$); it is therefore not a minimal surface as would be imposed by interfacial tension in isolation. For droplets with intermediate trap spacing of $L_A/R_D = 1.6$ Figure 6.22 and high deformability $\epsilon/M > 1$, the surface furthest from the traps is still influenced by overlapping handle structures.
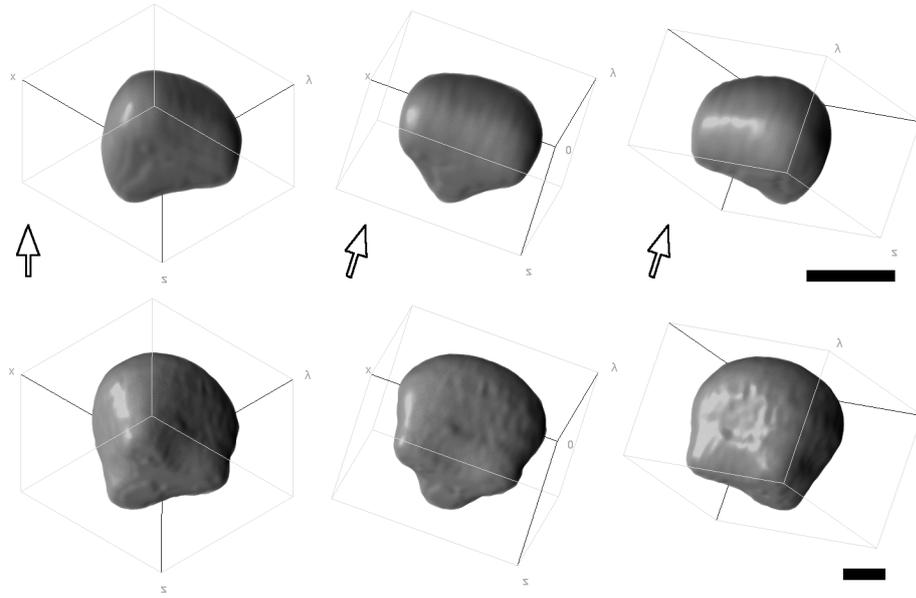
Figure 6.22: Two different droplets in three traps at constant $L_A/R_D = 1.6$ with only the larger droplet (lower) showing the dimpled faces of negative mean curvature near its horizontal midplane. The arrow indicates the laser's direction. Both scale bars 2 μm. Conditions are $R_D =$(1.5,3.4) μm, $S = (43.0, 44.0)$ mM in H$_2$O, $T_A = (20.3, 20.5)$ °C, $\sigma = (0.6, 0.3)$ μN m^{-1}, $P/M = (9, 12)$ mW, $\epsilon/M = (1.8, 3.2)$, $L_A = (2.5 \times 2.5, 5.4 \times 5.4)$ μm.

Within a small range of array sizes relative to the handle size, the lack of overlap between the hourglass necks leaves a vacancy on each of the lateral faces (Figure 6.22, lower). These faces have negative mean curvature in accordance with Tapp *et. al.* ([6], Figure 7c.), though again accessible at lower powers and optocapillary numbers in experiment ($P/M = 12$ mW, $\epsilon/M \approx 3.2$) compared to those in the simulation ($P/M = 40$ mW, $\epsilon/M \approx 7.0$, $L_A/R_D = 1.7$). The predicted sharpening of the vertices in optical *Taylor cones* ([6], Figure 9b.) is not observed here, even at similar powers to the simulation ($P/M = 8$ mW, $\epsilon/M \approx 1.1$, $L_A/R_D = 2.1$). Comparing these parameters, the Taylor cone effect may exist only for oblate polygonal droplets, typical of larger relative array sizes $L_A/R_D > 1.8$ and *lower* optocapillary numbers where the surface does not recurve near the traps. The more general classification of droplet shapes by these parameters into oblate, prolate and recurving aligns well with their simulations in cases where buoyancy is less dominant.

6.3.3 Rectangular arrays

Four-trap arrays make a step towards more subtle sculpturing of the droplet including the creation of right angles in the surface, as in Figure 6.23. This square is very similar to the triangle in Figure 6.16, in that the separation and elongation match to approximate a regular prism or cube. [7] As for binary and triangular arrays, separations of $L_A \approx R_D$ generate oblate shapes (Figure 6.24) with polygonal lateral cross-section.[8] Even so, a greater area is spanned by the traps at typical separations, leading to departures from spheroidal shapes at $L_A > R_D$. In Figure 6.25, the sequence shown in Figure 6.19 continues in that the handles emerge from the body at the trap locations and the remaining material billows upwards under its own buoyancy. The shape resembles a table. At greater optocapillary number, each handle increasingly acts as an independently trapped droplet, with flattened illuminated sides and hourglass pinching at the focal plane (Figure 6.26).

At yet greater separations or at lower IFT, the volume of material is insufficient to cover the trap array in a way that is stable against collapse to a network Figure 6.27. The particular network is in a U-shape (as explained in § 5.5) and can be resolved in the confocal frames as shown in Figure 6.28. The average radius calculated using the same method in § 6.3.1 is $R_T = 80 \pm 11~\mu$m, corresponding to an interfacial tension of $\sigma = 0.3~\mu$N m^{-1}, again in agreement with the temperature-based IFT calculation. Surprisingly, the two threads connecting the smaller nodes attach below the focus whilst the other sits at the very top of the larger nodes. It would be unfavourable for the highly-curved pinch points to pass through the oppositely-curved centre of the hourglass part of each node, so the statistics of whether the thread was created above or below the focus should be preserved.

---

[7]The asymmetry in the last three frames indicates that the shape is collapsing to just one or two anchoring points (see § 6.6.10).

[8]The shapes presented at $\epsilon/M \approx 1$ in Figures 6.24 and 6.25 strongly resemble each other above and below the PIT. This observation provides further evidence that Marangoni forces are not considerable for the experiments in this chapter.
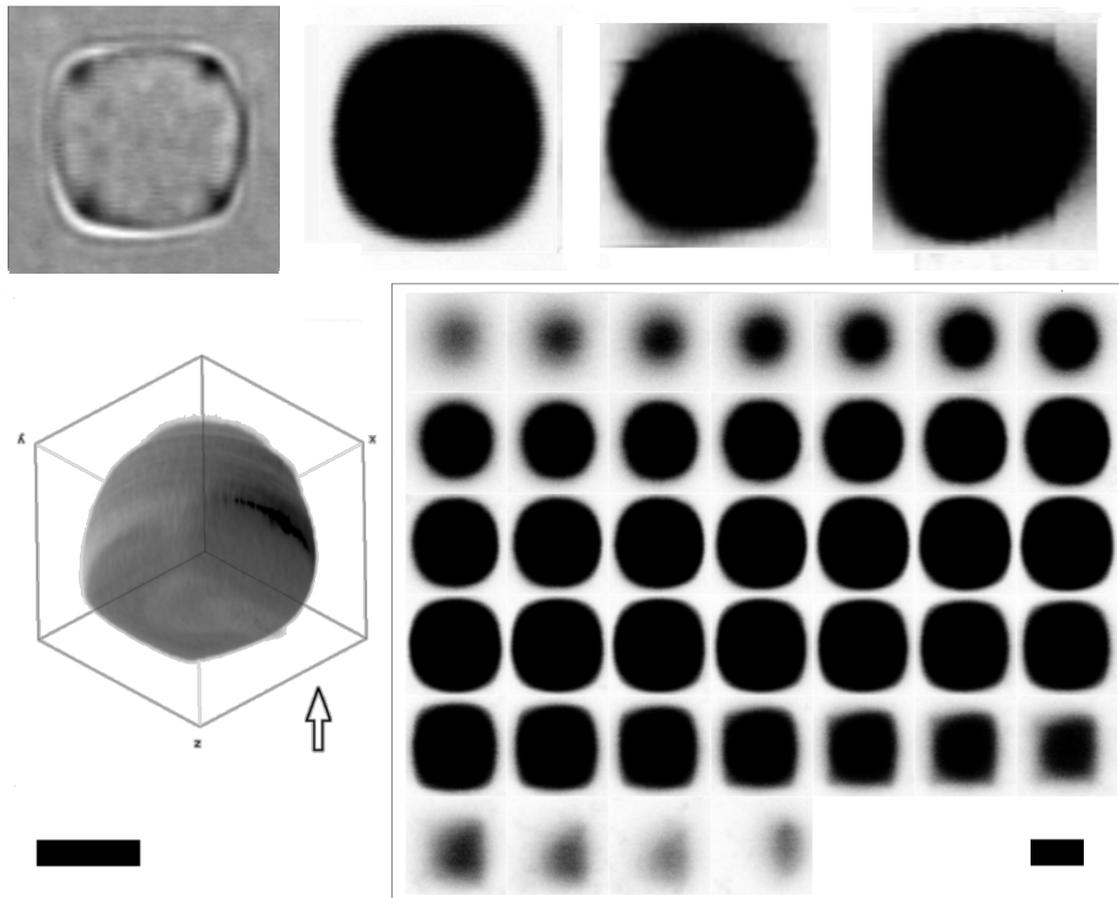
Figure 6.23: Four traps in a square coplanar arrangement; *(top left)* brightfield view; *(top right)* confocal cross-sections in xy, xz and yz planes through the approximate centre-of-mass; *(bottom left)* 3D volumetric reconstruction. The arrow indicates the laser's direction of propagation (vertically upward in the laboratory); *(bottom right)* confocal xy frames as a function of z from top (shadowed) to bottom (illuminated), at half scale. Both scale bars 5 μm. Conditions are $R_D = 4.6$ μm, $T_A = 20.9$ °C, —mbox$S = 45.0$ mM in H_2O, $\sigma = 5$ μN m^{-1}, $P/M = 9.3$ mW, $\epsilon/M = 0.4$, $L_A = 4.0 \times 4.0$ μm.

Figure 6.24: Four traps *above* the PIT. One stack is shown per row; *(top to bottom)* increasing moderate optocapillary number with decreasing power. *(left to right)* identical 3D volumes shown in three orientations. The arrow indicates the laser's direction of propagation (vertically upward in the laboratory). All to scale bar 4 μm. Conditions are $R_D = 3.1$ μm, $S = 44.0$ mM in H_2O, $T_A = (21.1, 20.9, 20.6)$ °C, $\sigma = (3.1, 1.7, 1.1)$ μN m^{-1}, $P/M = (7.3, 6.1, 4.7)$ mW, $\epsilon/M = (0.7, 1.0, 1.2)$, $L_A = 3.2 \times 3.2$ μm.
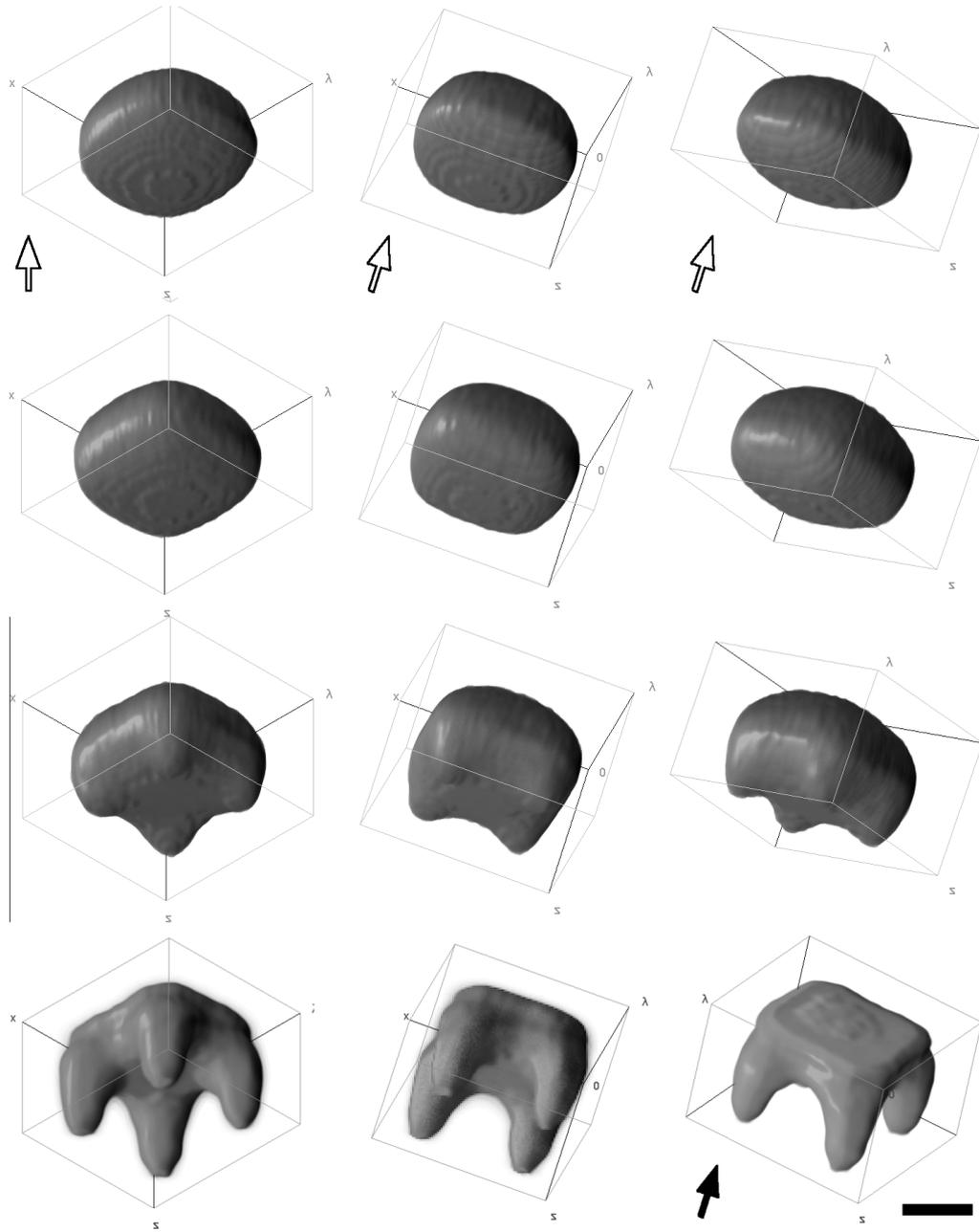
Figure 6.25: A droplet in four traps below the PIT. One stack per row; *(top to bottom)* increasing optical power and optocapillary number. *(left to right)* identical 3D volumes shown in three orientations. The arrow indicates the laser direction (vertically upward in the laboratory). All to scale bar 4 μm. Conditions are $R_D = 2.3$ μm, $S = 43.0$ mM in H$_2$O, $T_A = (20.5, 20.6, 20.6, 20.6)$ °C, $\sigma = (1.3, 0.9, 0.6, 0.3)$ μN m^{-1}, $P/M = (4.7, 5.0, 6.1, 7.3)$ mW, $\epsilon/M = (1.0, 1.4, 3.8, 6.6)$, $L_A = 2.2 \times 2.2$ μm.
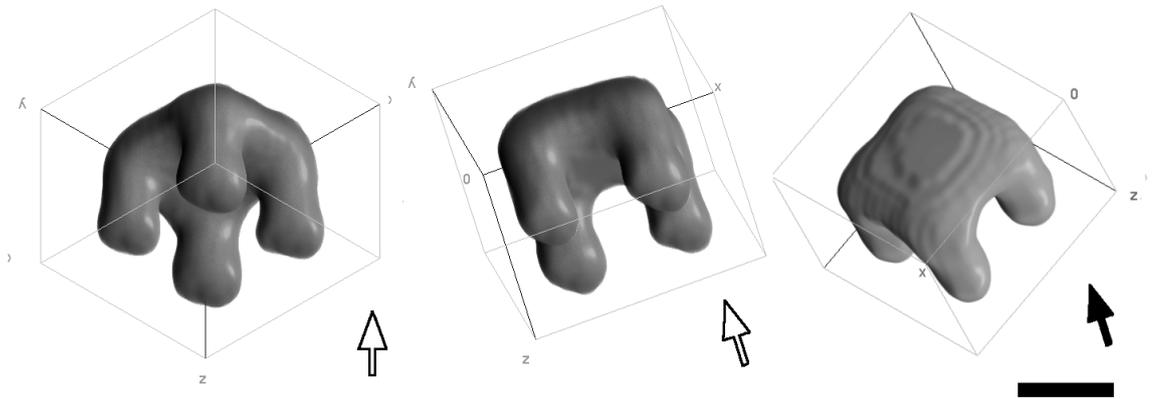
Figure 6.26: A droplet in four traps at extreme deformability; *(left to right)* identical 3D volumes shown in three orientations. The arrow indicates the laser's direction of propagation (vertically upward in the laboratory), filled if pointing out of the page. Scale bar 2 μm. Conditions are $R_D = 1.7$ μm, $S = 45.0$ mM in H$_2$O, $T_A = 21.4$ °C, $\sigma = 0.4$ μN m^{-1}, $P/M = 7.3$ mW, $\epsilon/M = 9$, $L_A = 3.2 \times 3.2$ μm.
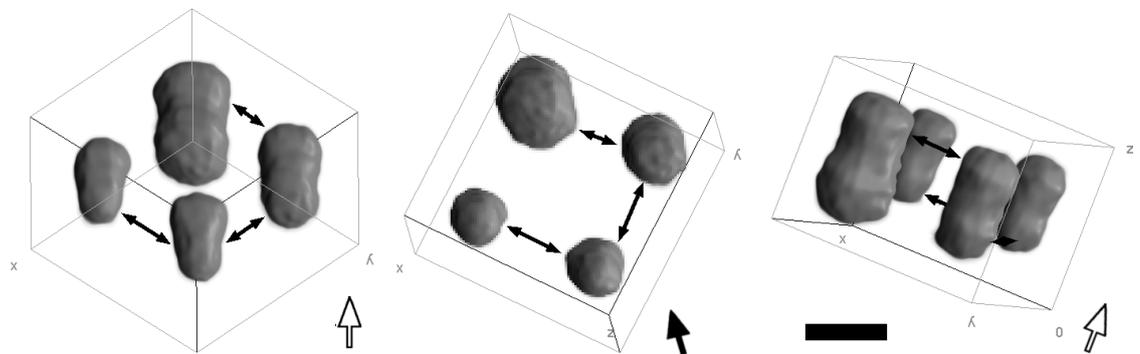
Figure 6.27: A droplet split into a U-network in four traps; *(left to right)* identical 3D volumes shown in three orientations. The arrow indicates the laser's direction of propagation (vertically upward in the laboratory), filled if pointing out of the page. The smaller arrows indicate the positions of the three nanothreads. Scale bar 3 μm. Conditions are $R_D = 1.7$ μm, $S = 43.0$ mM in H$_2$O, $T_A = 20.6$ °C, $\sigma = 0.5$ μN m^{-1}, $P/M = 7.3$ mW, $\epsilon/M = 6$, $L_A = 3.4 \times 3.4$ μm.
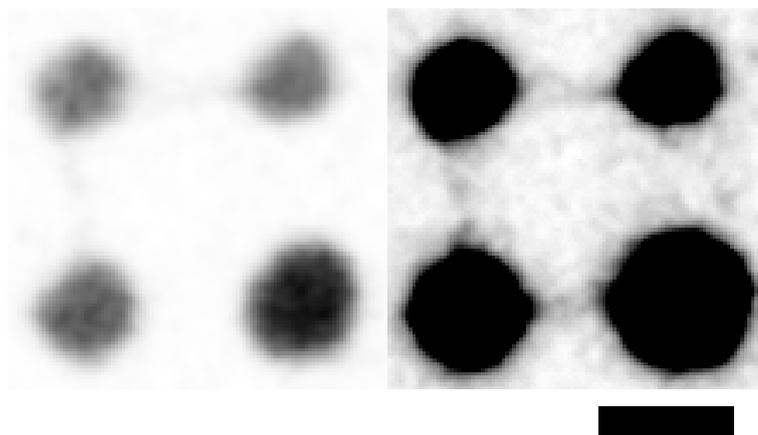
Figure 6.28: The average of the two xy cross-sections of the bifurcated droplet shown in Figure 6.27 containing the three threads; (*left*) with contrast normalised to the droplet centre as used for reconstruction, with thread not visible; (*right*) the same frame at $20\times$ digital saturation, revealing the nanothreads averaged over a 1 s confocal exposure. Scale bar 3 μm.

6.3.4   Networks and emulsification

Deformable droplets around $R_D = 3$ μm appear stable in a single trap at full power. However, on occasion the trap failed to hold the object for the duration of the scan. Confocal stacks are truncated with no indication of movement or change in deformation, implying that escape occurred within an interval step in z.

Vulnerability to loss increases for larger, more deformable droplets at greater trap separation. The central mass between the traps becomes so soft that it detaches and is lost (see Figure 6.29). However there is still material of the same deformability left in each of the traps, resembling the handles in other samples. Amazingly, very soft threads are visible between the trapped droplets forming a network, even in the volumetric reconstruction. The Y-junction itself is not trapped and requires radial tension to persist, so these must be nanothreads rather than microemulsifying debris. In individual exposures (not shown due to low SNR) the threads are jagged and branching with prominent Brownian fluctuations. The traps are identical, so if there is a means of mass transport, the nodes should become

equal in volume. Instead, one of the nodes is many times larger than the others - a condition which persists throughout the scan. Poiseuille flow would scale as the 4th power of the thread width (square of the IFT); the IFT must be exceptionally low to allow threads of detectable width. Such a flow would be driven by the Laplace pressure difference across the thread (which scales linearly with IFT). If there is flow along the threads, it could be offset by spontaneous emulsification, which should be proportionally greater for the smaller reservoirs.

Figure 6.29 shows the impressive elongation of the reservoirs along the trap axes. The migration of the thread pinch point during the scan causes multiple peaks to appear on the inner side of the large droplet. After a stable period of about 10 min, the threads disintegrate as the temperature passed through the PIT under a change in ambient temperature.

The process of tearing and loss itself can be followed with short exposures (not shown). The drop becomes spherical as it escapes and rises to the cell surface under buoyancy within a single frame, consistent with the expected terminal velocity. It is still attached by threads via a Y-junction to the remaining trapped reservoirs. The threads appear especially thick, partly because of their diffusive blur. The majority of features are dynamic (change with t and z) rather than just static (change with z). For this reason 3D representation is no longer meaningful. The reservoirs taper towards the end of the scan, which likely reflects their shrinkage over time caused by spontaneous emulsification. At higher trap strength and smaller trap separations, bodily escape does not occur even at very low IFT. Most of the attempted dumbbell shapes with two traps are initially successful but 'unzip' into two bodies connected by a thread.
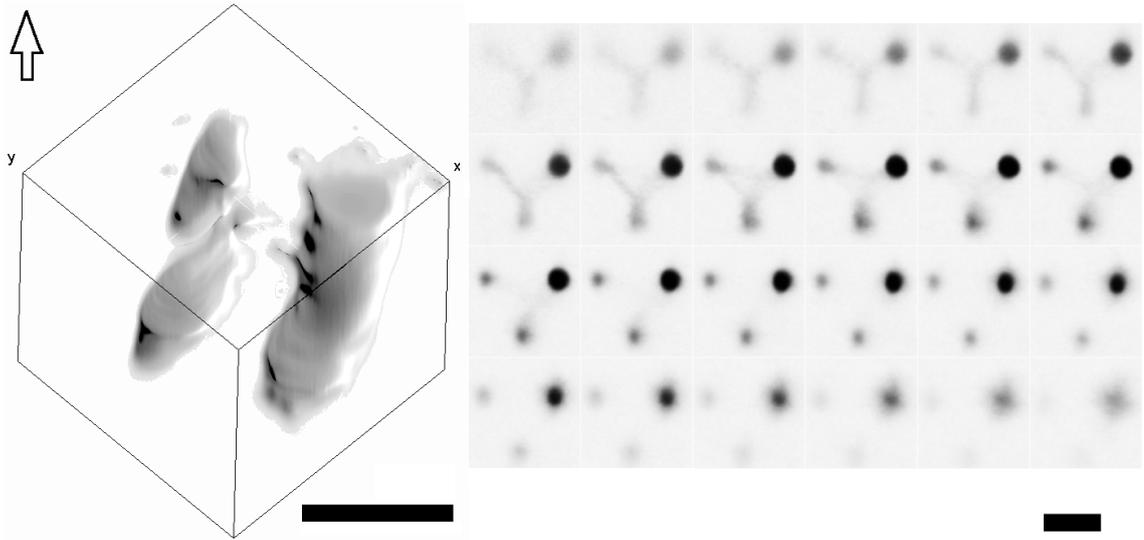
Figure 6.29: A network formed in three traps by loss of the central mass; (*left*) 3D volumetric reconstruction. The arrow indicates the laser's direction of propagation (vertically upward in the laboratory); (*right*) confocal xy frames as a function of z from top (shadowed side) to bottom (illuminated side) at half scale; both scale bars 4 μm. Conditions are $R_D = 1.7$ μm, $T_A = 20.6$ °C, $S = 43.0$ mM in H_2O, $\sigma = 0.9$ μN m^{-1}, $P = 9.3$ mW, $\epsilon/M = 5.5$, $L_A = 3.5 \times 3.5$ μm.

Within 0.1 K of the PIT, the interfacial tension becomes so low that the droplets are deformed easily, even at laser powers $P < 3$ mW barely considered viable for trapping at all. Unfortunately, the oil emulsifies rapidly, often before a 3D shape can be identified. Islands of material remain around the traps, but eventually shrink away. Figure 6.30 shows a triangular array in the early stages of emulsification while the nodes are still connected. Although the scan starts from the midplane of the object, each reservoir elongates with a bullet-like shape.
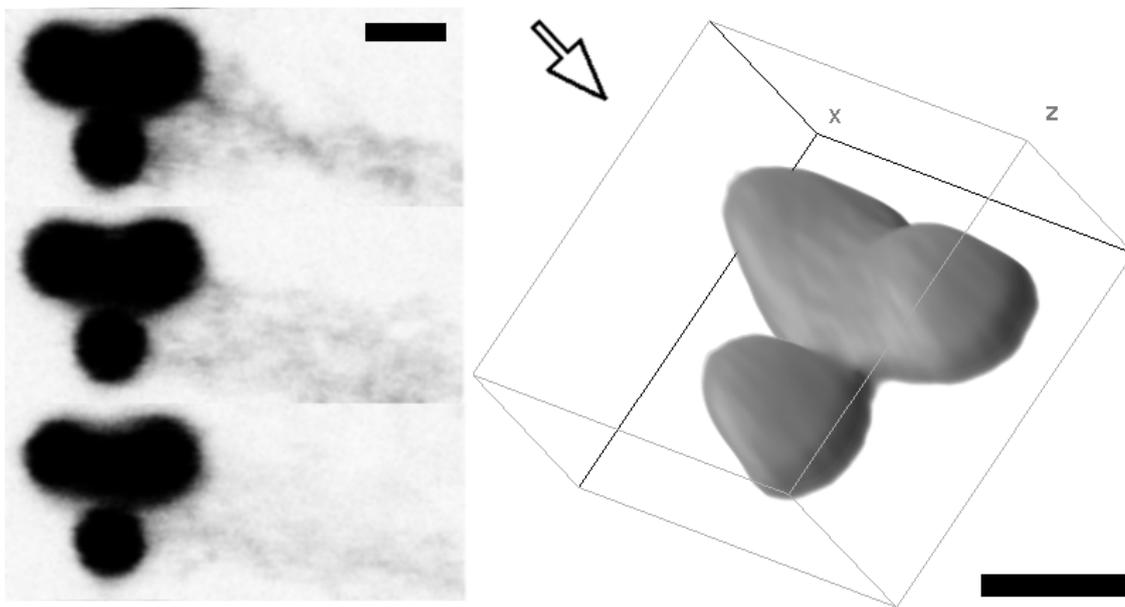
Figure 6.30: A droplet formed in three traps at the lowest ULIFT; (*left*) confocal xy frames at the same equatorial z at time intervals of 20 s, at half scale; (*right*) an incomplete 3D volumetric reconstruction prior to shrinkage. The arrow indicates the laser's direction of propagation (vertically upward in the laboratory); both scale bars 3 μm. Conditions are $R_D = 2.6$ μm, $T_A = 20.9$ °C, $S = 30.0$ mM in D$_2$O, $\sigma = 0.3$ μN m^{-1}, $P = 9.3$ mW, $\epsilon/M = 3.5$, $L_A = 2.5 \times 2.1$ μm.

6.3.5   Phase transition

The formulation $\chi = 1$ used here is capable of phase inversion as described in Chapter 4. Figure 6.31 shows a droplet that has been held in to a single trap at high power (40 mW) initially above the PIT (in the shrinking regime). When the power was set to a low value (10 mW) the droplet passed downwards through the PIT, but back again as a result of the rising ambient temperature, causing the preferred emulsion type to invert to w/o briefly. The nucleation of a phase with low fluorophore concentration (water-rich) shows that the droplet was able to solubilise water quickly while below the PIT and release it as the temperature rebounded, without bursting. The necessary rate of solubilisation and oily character suggests the droplet consists of middle phase or similar microemulsion, which is rare in the temperature-sensitive system.

The water-rich vacancies congregate at the interface, whose surface energy they can lower by partial wetting, and where the trap intensity is minimal. The behaviour closely resembles the stronger laser heating of a microemulsion drop in the temperature insensitive system (Figure 4.6).
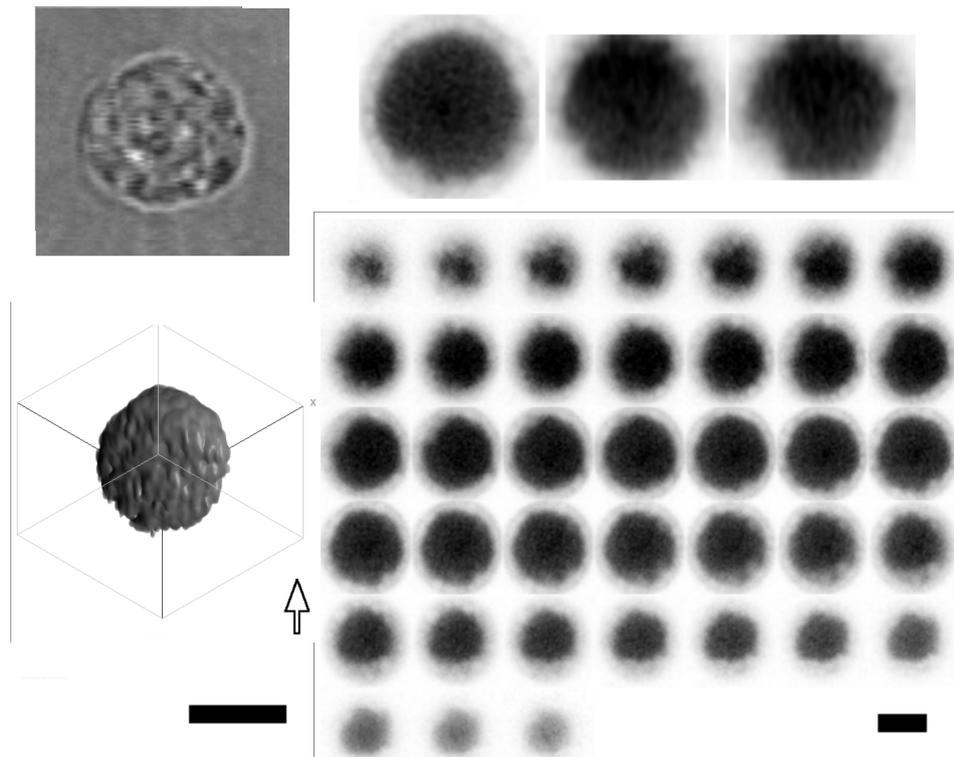
Figure 6.31: A drop in a single trap undergoing nucleation and phase inversion following a sharp decrease and rebound in temperature across the PIT; *(top left)* bright-field view; *(top right)* confocal cross-sections in xy, xz and yz planes through the approximate centre-of-mass; *(bottom left)* 3D volumetric reconstruction. The arrow indicates the laser's direction of propagation (vertically upward in the laboratory); *(bottom right)* confocal xy frames as a function of z from top (shadowed) to bottom (illuminated), at half scale. Both scale bars 4 μm. Conditions are $R_D = 2.6$ μm, $T_A = 21.7$ °C, $S = 46.0$ mM in H_2O, $\sigma = 27$ μN m^{-1}, $P/M = 10$ mW, $\epsilon/M = 0.1$.

6.3.6 Tetrahedral arrays

To take advantage of the rich potential for different optically-supported shapes, the trap arrays were extended into 3D arbitrary positions using holography (§ 2.4.3). A tetrahedron is the simplest regular shape that is not a trivial rotation of the arrays already considered.

The first example (Figure 6.32, top) is an irregular tetrahedron, in which two pairs of coplanar traps at the diagonals of a xy square are displaced from one another along z, (a 2:2 arrangement). The axial separation is half of that in the lateral directions. The droplet is by far the largest studied, which is possible from Setup C's greater trapping strength. The surface is pinned out by the four traps and subtle vertices are visible, though perhaps the deformability is too low for handles to emerge. The overall shape appears somewhere between an oblate oval and an oblate square, which are the shapes known to be generated in the respective limits of infinite axial separation (i.e. a binary array) and zero axial separation (i.e. a square array).

The second example (Figure 6.32, bottom) is a regular tetrahedron with three coplanar traps and one displaced along the axis (a 3:1 arrangement); the traps are 4.3 μm apart. The trapped droplet also has a higher deformability than for the 2:2 results. The preliminary results suggest that at moderate ϵ/M, handles can be displaced along the z axis in a continuous manner without affecting the surface pinned to the others. The remaining material is suspended between points as boundary conditions for the four faces of the tetrahedron. To a first approximation, the faces are minimal surfaces as shown by their saddle-ruling. Yet, the striking negative curvature of the lower face and rounded shoulders of the upper faces indicate an upward bulging under buoyancy. Although the capillary length is the lowest of all presented results, $L'_C = 3.5$, the presence of the displaced trap prevents this upper region from becoming a spheroidal section.
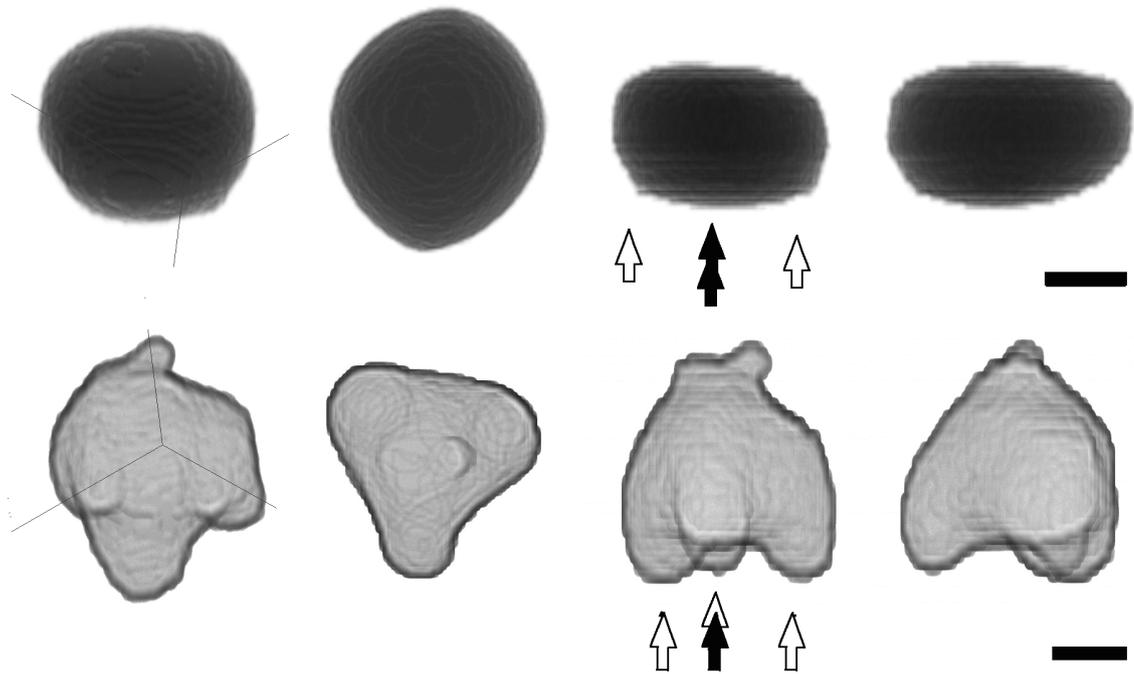
Figure 6.32: Four traps in tetrahedral arrays. Stacks obtained by structured illumination microscopy; (*left to right*) identical volumes shown as median-intensity projections in four orientations: *oblique, xy, yz, xz*. (*top*) A droplet in an irregular 2:2 tetrahedral trap array. Scale bar 5 μm. (*bottom*) A droplet in a regular 3:1 tetrahedral trap array. Scale bar 2 μm. Conditions are $R_D = (5.9, 3.8)$ μm, $S = 32.0$ mM in D$_2$O, $T_A = (22.1, 22.0)$ °C, $\sigma = (4.7, 0.6)$ μN m^{-1}, $P/M = (56, 44)$ mW, $\epsilon/M = (1.1, 13.6)$, $L_A(x, y, z) = (15 \times 13 \times 7, 4.3 \times 3.7 \times 3.5)$ μm.

6.4   Influences on steady-state deformations

The effects of buoyancy, flow, thermal changes and optical aberration are not only relevant to the successful recording of confocal stacks, but also our ability to interpret the shapes that they present. If any forces are large enough to risk pushing the object bodily from the trap or shift its centre of mass if it remains trapped, then it must be considered if they affect the steady-state deformations as well. Force gradients (or curvatures in potential) can be defined when a deformable object is trapped.

For an external flow rate of $v_F = 10\ \mu\text{m s}^{-1}$, the shear stress integrated across the circumference of the droplet is of order $5\pi\eta v_F \approx 0.1\ \mu\text{N m}^{-1}$, which elongates the droplet in the direction of flow.

The spherical aberration affects the local trap stiffness for the confocal apparatus in Setup B (§ 2.4.2. By contrast, the droplets characterised using structured illumination microscopy in Setup C (§ 6.1.2) do not suffer variable spherical aberration as the imaging arm is scanned instead of the trap. Yet, the results are comparable as shown in Figures 6.16 and 6.17.

It is straightforward to imagine droplets extending along the trap as they do, but why especially along the shadowed side? One may consider the limit of overwhelming trap strength $\epsilon/M \gg 1$ and high NA where the droplet conforms to the iso-intensity contours; ideally these are symmetric around each focus. The buoyancy and scattering forces break the axial symmetry in z, such that asymmetric arrays in xy (such as a scalene triangle) support chiral droplet shapes. Given the orientation of the microscope, they both act to push the material upwards in a way that depends on the lateral cross-sectional area. However, the scattering force relates to the overlap of the interface with the intensity distribution, whereas buoyant force relates to the hydrostatic pressure, which is independent of lateral position. The effect of buoyancy is isolated at regions far from the traps where there is no scattering force, but the converse is not generally true since buoyant force is position-invariant. The buoyancy effect is $dF_{buoy}/dz = \Delta\rho g A \approx 0.1\ \mu\text{N m}^{-1}$, where A is the xy droplet

cross-section, representing the tendency for the droplet to widen at the top. If the power is increased arbitrarily[9], a larger proportion of the droplet around the trap foci will be exposed to intensities where scattering forces overwhelm those of buoyancy. However, the global effect of scattering on shape asymmetry can only be observed by reversing the direction of the trapping beam, e.g. comparing identical droplets in upright and inverted microscopes.

In the regions spanning widely-spaced traps, where optical forces are negligible, a balance occurs between buoyancy and surface tension. Buoyancy generates a pressure difference on the upper and lower sections of the drop surface, which differ in shape so that the Laplace pressure may compensate. Thus, the local curvature asymmetry is related to the *local vertical thickness*, h_z, with the strongest curvature difference at the apex. In the limit of high buoyancy (larger/denser drop), the lower face flattens and the upper face stretches into a hyperboloidal, nose-cone shape.

$$2\sigma\Delta H = \Delta\rho g h_z \tag{6.4.1a}$$

$$\Delta H = \frac{h_z}{2L_C^2} \tag{6.4.1b}$$

where ΔH is the difference in mean curvature between vertically opposite points on the upper and lower surfaces.

Quantitative prediction of the shape is given by Tapp's numerical model [6] and lies outside the scope of this thesis. In this experimental geometry however, the vertical thickness is almost constant at the apex. Thus, the surface at the top and bottom midpoints should resemble spherical caps of near-uniform mean curvature. As these curvatures can be measured from the 3D stacks, the capillary length extracted by Equation (6.4.1a) gives an estimate of the interfacial tension. Although this analysis specifies only the difference in upper/lower mean curvatures ΔH, the average of the upper/lower mean curvatures $\langle H \rangle$ and the vertical thickness h are

---

[9]Formulation- and generation-based alternatives would be to decrease the droplet size, increase the droplet's refractive index or change its density to match that of the continuous phase more closely.

also determined by the extent to which the optical traps have stretched the object laterally. For regions outside the trap, such as for multiple trap arrays, these values cannot be greater than that of the undeformed droplet.

In general the traps must lower the local pressure, which in a steady state must also be equal to the internal pressure throughout the droplet. Since the Laplace pressure must balance this at all points outside the traps, the mean curvature in these regions and thus $\langle H \rangle$ must also decrease. In turn, the mean curvature in the trapped region must increase, since the integrated mean curvature over the entire drop cannot be less than the undeformed sphere. Unless the traps are separated vertically by more than $2R_D$, the fixed volume of the droplet also constrains the vertical thickness h to decrease. As such, conditions exist, $L_C \leq \sqrt{h_z/\langle H \rangle}/2$ for the lower surface to become flat or inverted. For trap arrays no taller than $2R_D$ as used here, a sufficient condition is that the capillary length approaches the undeformed droplet radius, $L_C' \leq 1/\sqrt{2}$. It is therefore possible to gain some control over this region of the shape - even without direct optical manipulation - by varying the interfacial tension.

6.5   Summary

The findings in this chapter can be summarised as follows:

- when the IFT is ultralow, characteristic hourglass 'handles' develop at the trap locations,

- when the IFT is ultralow, the broader surface spanning the traps becomes a near-minimal surface stretched by buoyancy,

- for drops much larger than the handle volumes, successively larger separations result in oblate shapes and networks respectively,

- polygonal vertices of >1 $\mu\mathrm{m}^{-1}$ curvature are achievable with specific combinations of trap separation and drop volume, at an optocapillary ratio around unity.

6.6 Appendix: Calibration of confocal imaging

6.6.1 Spatial calibrations

Under confocal imaging, rigid droplets yielded an aspect ratio of $y/x = 1.05 \pm 0.02$, in agreement with estimates obtained with a graticule across three different fields of view. Brightfield imaging of the graticule returned a pixellation of $7.47 \pm 0.03 \, \text{px}/\mu\text{m}$, square to within a factor 1.01 ± 0.04. Measuring the thickness of a coverslip by laser reflection gave a z-stage correction factor of 1.12 ± 0.02.

The effect of the lens position along the *Zaber* translation stage, z_L on the true motion of the trap, z_T, was determined by correlating it with the translation of the microscope objective. A mirror was fixed to the stage under water immersion and the trapping laser was focused onto it at low power, such that the reflected high-NA interference pattern was detected on the CCD. For each displacement step of the trap, the objective was required to move half a step in the opposite direction to compensate (the objective moves both trap and reflected imaging plane). Thus in the focal condition, $\Delta z_T = -2\Delta z_O$, where z_O refers to the displacement of the objective. The stepper interval was reduced to $z_L = 250 \, \mu\text{m}$ for greater detail in smaller objects. The step size was calibrated graphically (Figure 6.33) as $\Delta z_T = 0.159 \pm 0.006 \, \mu\text{m}$, in very close agreement with this prediction.

6.6.2 Intensity-based stack registration

Whilst the beam direction remained normal to the imaging plane along the *Zaber* travel, the focus moved unintentionally in the lateral plane, as seen in a similar graphical calibration (Figure 6.34). The lateral shift was relatively large compared to the precise axial shift, giving the illusion of a highly oblique propagation direction on reconstructing the stacks. Because the pointing of the beam is good at all times, and the slice thickness is small relative to the spacing, the slices are truly decoupled and can be translated independently to coincide with a common centre-of-mass.
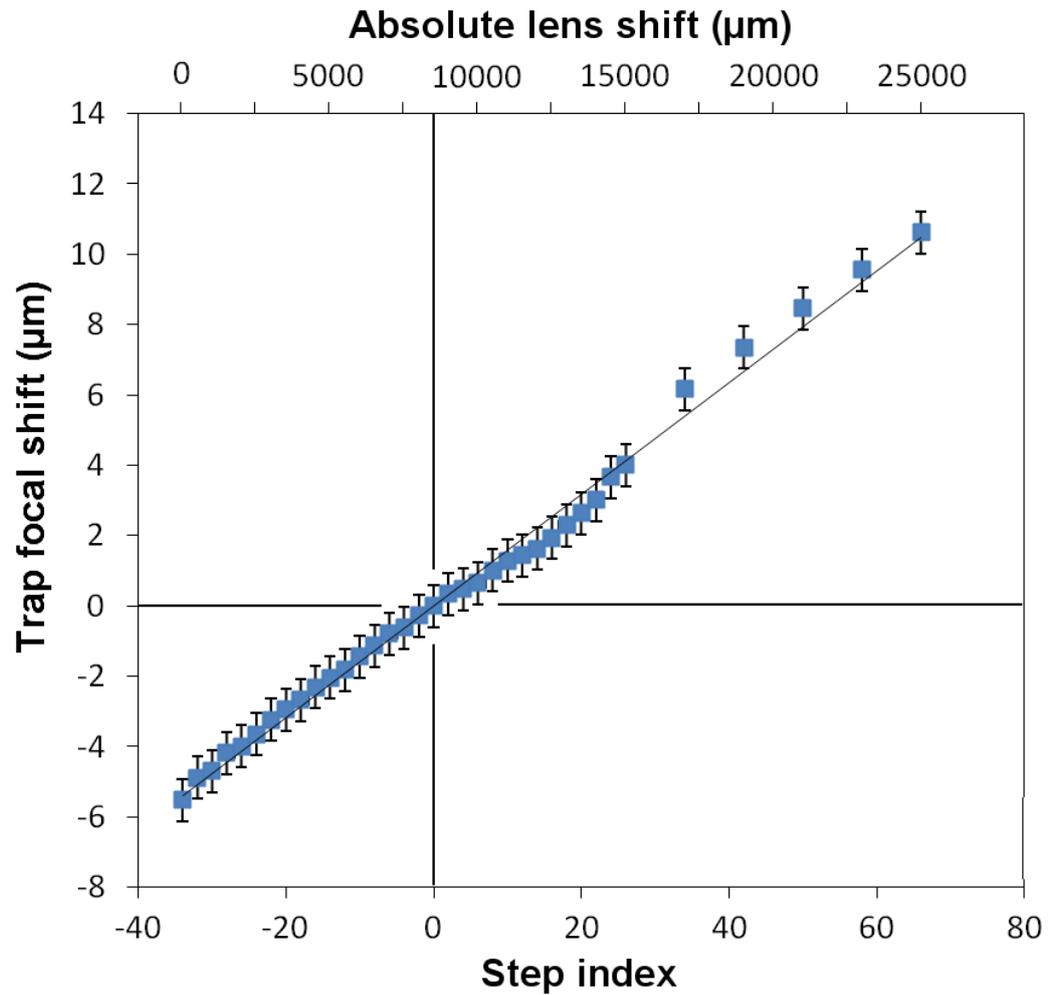
Figure 6.33: Calibration of trap motion in z under lens translation; the stepper interval is $\Delta z_L = 250$ μm (lens), equivalent to $\Delta z_T = 0.159$ μm (trap). The solid line is a linear fit ($R^2 = 0.993$).
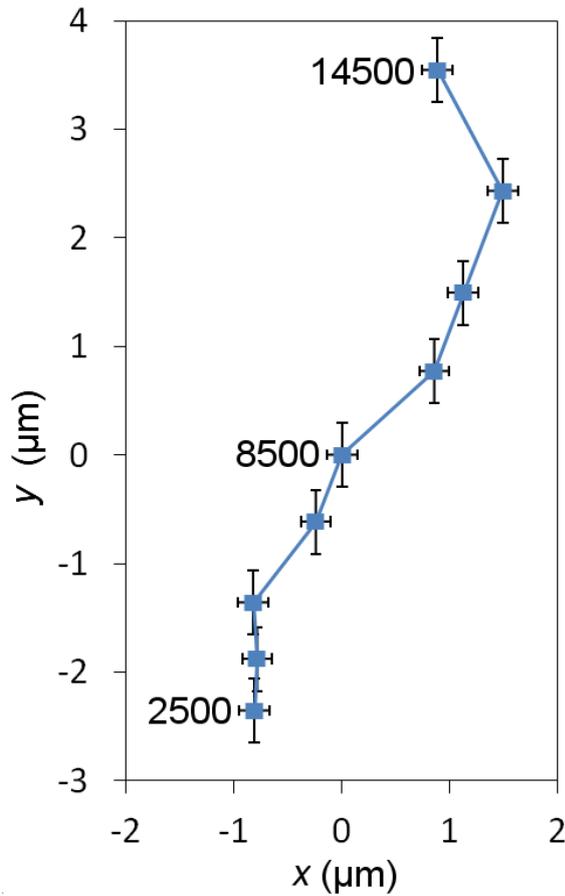
Figure 6.34: Calibration of trap motion in xy under lens translation as for Figure 6.33. The labels refer to z_L; a line is drawn to indicate the trap path (see § 6.6.2).

6.6.3 z_T: Absolute reference of trap focus in 3D

It is difficult to interpret the 3D stacks if the location of the trapping focal plane is unknown. It was estimated by measuring the absolute lens positions where the confocal imaging plane coincides with the equilibrium trapping points (or equators of trapped spheres). In the limit that the trapped object was small, the equilibrium z displacement past the laser focus lay within a Rayleigh range, around 80-100 nm. Therefore, the condition $z_T = 0$ was defined at the brightfield imaging focus for small objects, $z_L = 8500 \ \mu$m.
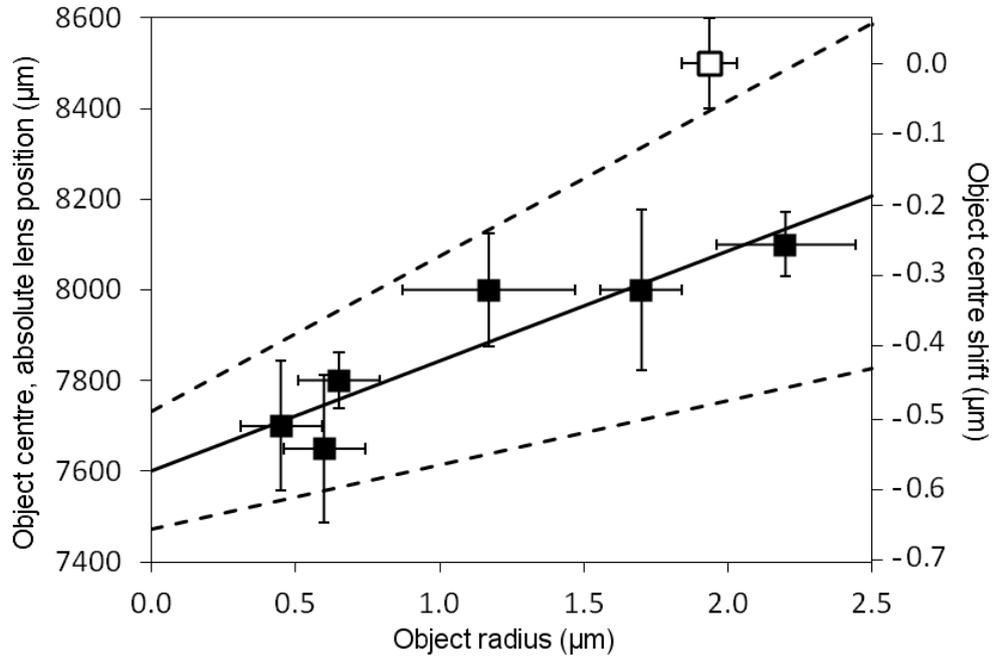
Figure 6.35: Absolute z coordinate of centre of mass of trapped spheres as a function of their size: rigid heptane droplets (*solid*); PS bead (*open*). The solid line is a linear fit ($R^2 = 0.85$) to the heptane data, whose intercept indicates the focus of the trapping laser beam. The dotted lines show the approximate amplitude of oscillations in the equilibrium z-position as a function of object size, as predicted by Mie scattering calculations [8]. Uncertainties in radii and position vary widely due to uncontrolled photobleaching history.

Where buoyancy may be neglected, the equilibrium position is dependent only on (increases with) the ratio of the surface-averaged scattering and gradient forces. In the Mie and geometric optics regimes, this ratio is expected to increase weakly with object size, as observed in Figure 6.35. A polystyrene bead's position - further behind the focus compared to a similar heptane droplet - is a consequence of its greater refractive index contrast in water and thus its greater scattering force.
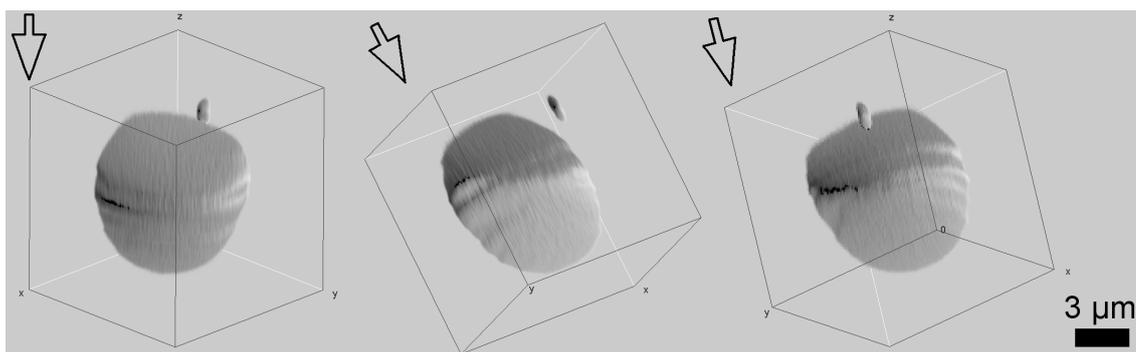
Figure 6.36: Rotations of a 3D confocal stack portraying a deformable heptane droplet stretched across two traps in a triangular array. A small amount of oil is trapped in the third location, revealing the location of the focal plane far below the droplet's centre of mass. Scale bar 3 μm. Conditions are $R_D = 2.4\,\mu$m, $S = 29.5$ mM in D_2O, $T_A = 21.0$ °C, $\sigma = 2.8\,\mu$N m^{-1}, $P/M = 13$ mW, $\epsilon/M = 1.0$, $L_A = 6.8 \times 6.5\,\mu$m.

In Figure 6.36, a droplet spans a triangular array, but has collapsed from one of the traps during the *Zaber* stepping prior to the scan. In effect an 'empty' third trap has been added. Although the droplet is significantly larger than the others, the shape is similar, albeit with a slight distorting influence towards the extra trap.

The equilibrium position of the material in the 'empty' trap also marks the approximate z-plane of focus for all three traps; it is clear that the droplet's centre of mass is far behind the trap foci. The difference is about $2.3 \pm 0.4\,\mu$m in z, which is enormous compared to the sub-micron Rayleigh range (the maximum shift possible for a sphere under the classical scattering force). This has important implications for the other results here and how the deformable droplets respond to high-NA optical trapping in general.

6.6.4 Processing

Due to the Gb-scale volumes of data in [`.ids, .ics`] form, a macro in *ImageJ (Fiji)* was constructed to register, filter, binarise, crop and analyse the stacks consistently. The output was the set of montage figures shown in Chapter 6, namely bandpass-

filtered slices, orthogonal cross-sections and 3D rotated representations.

6.6.5 Ambiguity in thresholding

Unfortunately, the thresholding process gives a range of shapes that cannot be rationalised without precise knowledge of the object volume.

For a single trap at very low ϵ, deformable droplets range from small, slightly oblate spheroids to large lemon-shaped objects of greater aspect ratio around 1.4 (Figure 6.6). If even more aggressive thresholding is used, internal voids appear and the reconstruction is no longer physical. This ambiguity is resolved by estimating the droplet size, either from volumetric imaging of the undeformed (spherical) droplet, or from its apparent diameter in brightfield images.

6.6.6 Photobleaching

Initially, the oil returned fluorescent signal at a satisfactory 9/12 significant bits. However, the signal dropped with exposure to the excitation laser; this was attributed to photobleaching. From the maximum decrease in contrast between frames, 7.5×10^{-2} step^{-1}, an upper limit of the natural decay time constant was estimated as 360 ± 20 s. Thus, each droplet became indistinguishable from background within about 10 minutes' exposure. This duration was about the longest acquisition possible at 10 averages over a full 20 μm depth. Yet, the darkening affected thresholding for the 3D representation. The fluorophore concentration could not be increased further as this would risk self-quenching and loss of ULIFT.

The sampling was instead reduced to 160 px across the field-of-view, and the number of averaged frames per slice to 4, the minimum indistinguishable from further averaging. At 6 mW excitation power (estimated 2 mW at sample), the PM597 bleaching time constant was 81 ± 19 s, or of the order of 50 slices over 7 μm. Decaying signal was more noticeable in a minority of stacks, leading to inconsistent, truncated shapes under thresholding. The time constant appeared to be scattered

widely, even at a specific excitation intensity. This variation between droplets could have been due to differences in surfactant aggregates with H_0 and therefore the environment in which fluorophore was solubilised. Nonetheless, correction for the exponential decay by simple multiplication is possible on a case-by-case basis.

6.6.7 Registration of fixed objects

Before the addition of optical traps was tackled, the performance of the confocal laser scanning microscope was tested for fixed objects using 4.2 μm-diameter, uniformly-fluorescent beads (*Bangs Labs*, FS05F/10536) dispersed in water.

Beads with strong adhesion to the underlying glass were identified by their lack of Brownian motion. A stationary, fixed sample appeared to move relative to the focal plane of the objective during the automated scan. The cross-sections showed unrealistic 'flare' - diffuse signal outside the volume -mostly above, and partly below, the object in z, giving the impression of an ovoid volume for a spherical body (Figure 6.37). While some layer structure was still visible despite linear interpolation between adjacent slices, there is no artificial flattening of the poles, which would otherwise have indicated undersampling. The slice spacing did not exceed the smallest feature size.

As the flare's biconic shape (particularly at weak threshold) mimicked that of the focused laser beam, it appeared to originate directly from fluorescence in the water phase; however this could not have been the case, as there was very little background signal in the absence of the bead. The point-spread function (PSF) of the imaging system resembled an apple core and contributed to strong axial blurring from imperfect confocal selectivity. The central spot resembled the diffraction-limited PSF for 580 nm at a numerical aperture of 1.2, which is roughly 0.3 μm $\times$ 1.1 μm. Yet, diffraction and imperfect confocality cannot account for the asymmetry across z which was probably a result of the high-index Mie scattering. This effect was less problematic in the lower-index oil droplets.
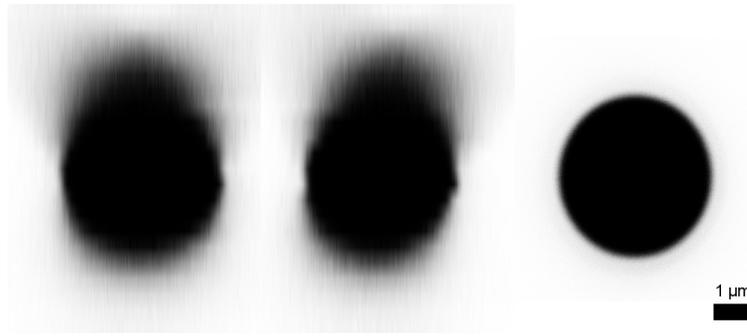
Figure 6.37: A solid bead fixed to the coverglass; interpolated orthogonal cross sections in the zx, zy, xy planes. Scale bar 1 μm.

An ideal confocal stack of an axially-symmetric object has perfect registration of all the layers. However, Figure 6.38 showed notable displacements of the xy centre-of-mass (weighted by pixel brightness). There are several possible explanations for a linear correlation of displacement $\Delta x, \Delta y$ with layer index m, only some of which reflect the true shape of the object:

i) ellipticity of the bead, particularly if directed along the semiaxes in the slices (true deviation with z)

ii) misalignment of a narrow excitation beam, if constant between samples (false deviation with z)

iii) stage drift (false deviation over time).

On the other hand, a random or oscillatory correlation would be

associated with:

iv) vibrations (false deviation over time).

v) flow shocks (false deviation over time)

In the case in point, the $\Delta x(m)$ correlation was roughly linear, equivalent to a feasible $d\Delta x/dt = -0.05$ μm min^{-1} stage drift; the $\Delta y(m)$ correlation was parabolic
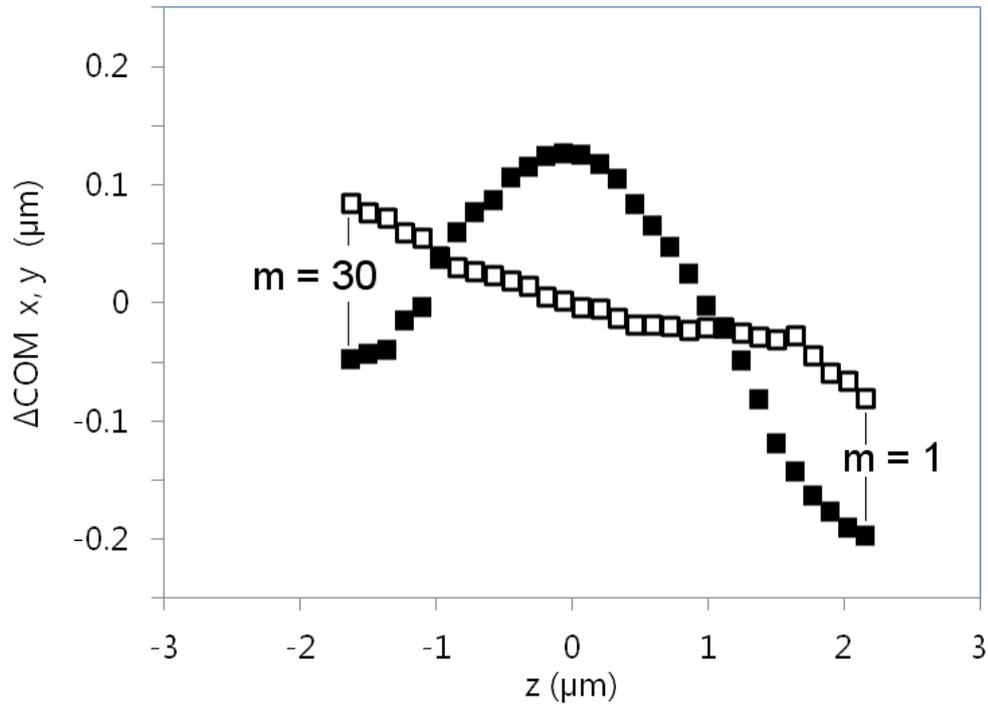
Figure 6.38: Apparent frame-by-frame variation of the x (*open*), y (*filled*) coordinates of the centre of mass of a solid, fixed bead with translation of the objective ($m\Delta z_O$). Here $z_O = 0$ is defined at the true centre of the bead as determined by its largest cross-section.

with a deviation of $d^2\Delta y/dz^2 = -0.08\mu\mathrm{m}^{-1}$.

In each case, the turning point coincided neatly with the mid-plane of the bead. This optical artifact derived from flare asymmetry, dependent on subtleties of bead curvature. Otherwise, there are good reasons to attribute the motion to stage drift: The excitation appeared uniform across the field of view. All oscillations of the fixed objects must be associated with the support, and vibrations > 0.1 Hz will have contributed only to symmetric blurring over each exposure.
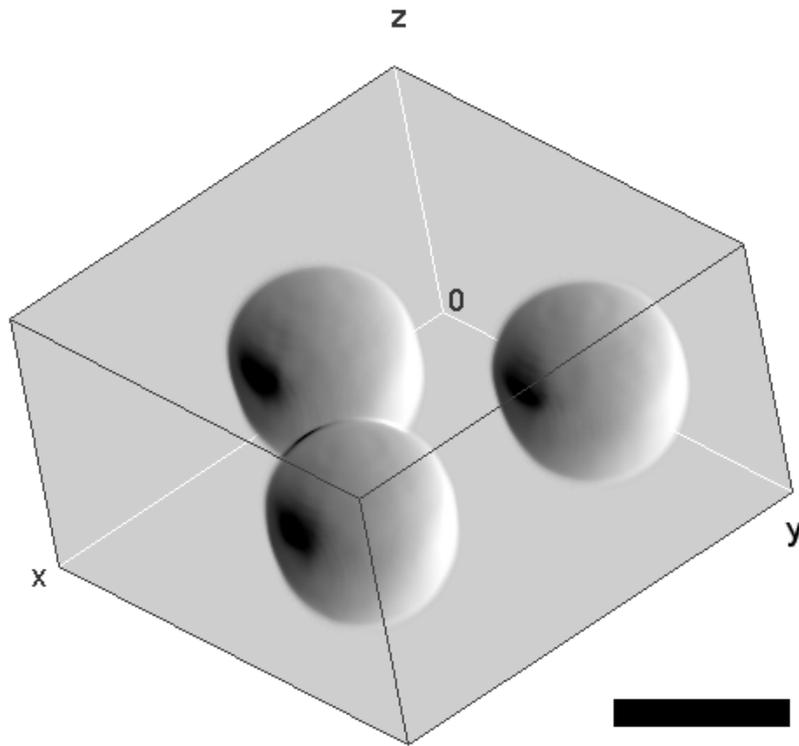
Figure 6.39: Three trapped beads in a triangular array of point traps, reconstructed from 3D confocal imaging. Scale bar 4 μm. Array properties are as follows: $P/M = 10$ mW, $L_A = 10.0 \times 8.6$ μm.

6.6.8   Registration of trapped objects

Trapped beads

The automated z-stepping procedure alone is ineffective for objects trapped in bulk fluid. Since both the fluorescence imaging and the trapping laser share an optical path through the objective, no motion of this objective is able to produce the required relative motion between the trapping position and the interrogated imaging plane. The trapped object merely follows the lens so that the same slice is imaged.

To counteract this, the trap's position was restored on each step by displacing a telescope lens in the optical train of the trapping laser (following Fällman & Axner, [9]), using a motorised *Zaber* micrometer. Each *Zaber* increment of 0.4 mm resulted in the trap moving $\Delta z_T = 0.257 \pm 0.009$ μm/step along the optic axis. The

travel constituted a range of roughly $\pm$ 10 μm around coincidence with the bright-field imaging plane in the objective's rest position. With a trap strength of order 10 μN m^{-1}, the time constant for the object to recoil into position was of order 10 ms, much less than the 1 s frame period. Thus, the object recovered a stable position before each exposure. The restoring force was sufficiently strong that blurring was minimal (as shown in Figure 6.39 even over 60 s of averaged 1 Hz exposures, suggesting that the distortion came from a scattering effect.

The essence of the procedure was

1. to shift the empty trap to the zero position (imaging focal plane),

2. to find, trap and manipulate an object using brightfield mode,

3. to assess the size of the object and shift it almost out entirely out of focus,

4. to change to confocal fluorescence mode and open the excitation laser shutter,

5. to check the measured cross-section matches the end of the object and adjust acquisition parameters,

6. to shift the object away fully (thus the minimum z-range is used),

7. to perform the automated stack interjected with manual z-steps,

8. to arrest the procedure once the object is traversed,

9. to shutter the excitation laser, and

10. to return to brightfield mode to re-assess the object.

Trapped rigid droplets

The sufficiency of the fluorescence signal from an effectively perfect sphere was tested by using stiff heptane droplets with salinity/temperature conditions far from the transition line. The droplet reconstruction (Figure 6.40) was more spherical than that of the beads; the scattering effect associated with the beads was absent.

This was attributed to the much lower refractive contrast and the smoothness of the interface. As suspected, thresholding to reflect this was quite difficult with photo-bleaching varying from one side to the other, and with noise. Nonetheless, the 3D volumes were almost spherical, yielding an aspect ratio y/x of 1.055 ± 0.007 that was consistent across 5 rigid heptane droplets varying from $R_D = 2.1$ to 4.8 ± 0.1 μm. This lateral correction factor matched the asymmetry in the CCD. Furthermore, foreign bodies could be picked out that were trapped alongside the droplets at higher resolution than the bead array.
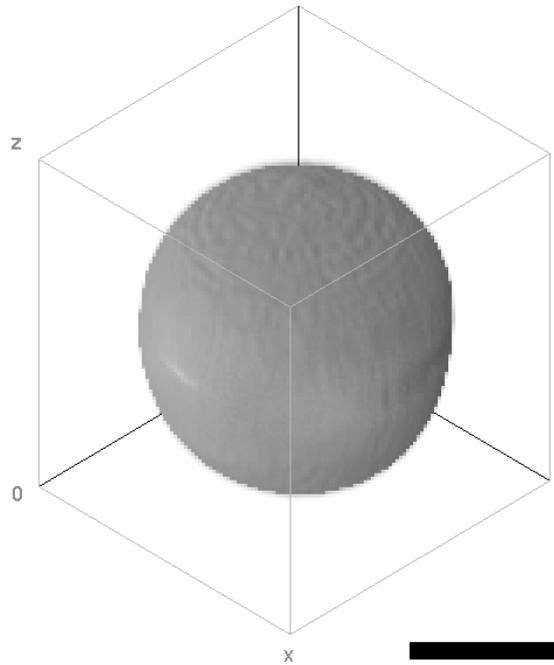
Figure 6.40: A single poorly-deformable drop in a trap; 3D volumetric reconstruction. Scale bar 4 μm. Conditions are $R_D = 3.8$ μm, $T_A = 19.9$ °C, $S = 38.3$ mM in H_2O, $\sigma = 32$ μN m^{-1}, $P = 11$ mW, $\epsilon = 0.08$.

The registration of slices may have been affected differently for a trapped particle (with a common-path objective) than for a fixed one:

i) non-axisymmetric deformation of the droplet (true deviation with z)

ii) misalignment of a narrow excitation beam, if constant between samples (false deviation with z)

iii) misalignment of the trapping beam, if constant between samples (false deviation with z)

iv) long ramps in external flow (false deviation over time).

A random or oscillatory correlation would be associated with:

v) vibrations of bench optics or laser pointing (false deviation over time).

vi) flow shocks (false deviation over time)

vii) confined Brownian motion in the trap (false deviation over time)

The particle tracks (Figure 6.41) were combinations of drift with time-invariant noise. Unlike the fixed objects, the drift was largely linear along the $+x, -y$ directions, equivalent to gradients of about $dy/dz \approx 1/10$ and $dx/dz \approx 1/30$. This indicated possible *iii*) angular trap misalignment. However, these gradients were inconsistent between samples; the gradients in y were unrealistically large to settle on trap misalignment as the sole cause. Given that the channel was aligned along y, the additional shift along y with m was due to steady changes in the flow rate between over the acquisition time, $\Delta v \approx \pm 10 \ \mu \mathrm{m \ s^{-1}}$ at $\dot{v} = 0.1 \ \mu \mathrm{m \ s^{-2}}$. As before, the long integration time discounts vibration and flow shocks. Instead, the noise probably originated from the localised Brownian motion in the trap. The rms displacement from this linear motion was around 20 ± 3 nm.

Representative rms displacements of beads and droplets from their drift paths, 21 ± 5 nm, and 22 ± 8 nm, respectively, were in excellent agreement. The coincidence for a variety of sizes and refractive index contrasts, $(R_D, \Delta n) = (2 \ \mu \mathrm{m}, 0.05)$ and $(4 \ \mu \mathrm{m}, 0.25)$, is somewhat surprising.
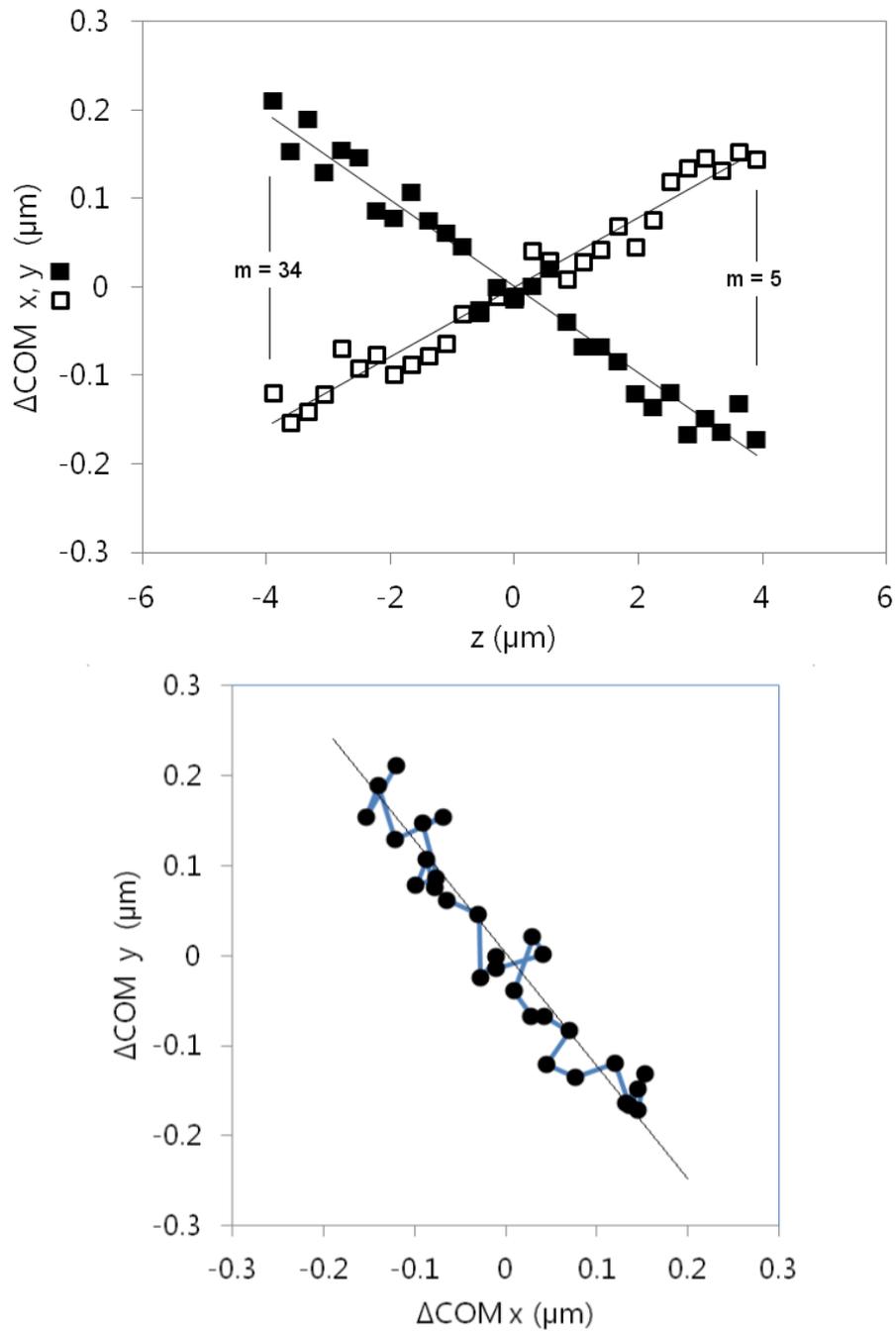
Figure 6.41: Apparent motion of the centre of mass of a trapped rigid droplet with axial displacement of the trap $(m\Delta z_T)$ using the telescope lens; (*top*) coordinates in x (*open,* linear $R^2 = 0.960$) and y (*filled,* linear $R^2 = 0.962$) as a function of calibrated axial trap position; (*bottom*) their projection onto the xy plane (linear $R^2 = 0.905$).

By assuming that these samples are representative of the trapping potential,

the equipartition theorem can be used Equation (2.2.1l), to show that the corresponding estimates of the trap strengths are of the expected order, $9 \pm 4 \ \mu$N m^{-1} at $P = 40$ mW. This gives an estimated 17 pN of escape force to distribute between the traps. The corresponding efficiency of the traps is $F/P = 0.4$ pN/mW or $Q \approx 0.1$, which is in agreement with the Fresnel prediction.

6.6.9   Tuning of laser-heating and salinity

The surface tensions quoted in this chapter are average values for each droplet. They are interpolated from Aveyard's data [10] using measurements of the ambient temperature, the bulk laser heating calculated from the laser power § 4.7, and the calibrated PIT corresponding to the sample salinity §§ 1.5.4 and 1.6.3. The accuracy in estimates of σ and therefore ϵ are limited to a factor of about 30% by the temperature sensitivity of the surface tensions.

Given the extreme IFT sensitivity to temperature for the pure AOT systems, the limiting factor for determining each shape quantitatively was just as likely to be drift in IFT as any systematic change in trap strength. In order for nonlinear shaping, typically it was necessary to lower the IFT of the droplets to 0.5 μN m^{-1}. For the heptane systems, this required an experimental temperature very close to the PIT, within $\pm$ 0.4 K. The stage temperature was measured with a digital thermometer, whose accuracy was $\pm$ 0.2 K. The droplet temperature fluctuated less than the probe reading, since the sample was largely coupled to the thermal load of the microscope rather than the surrounding air. The variation in trapping behaviour between droplets increases with lower IFT. At constant power, the behaviour of a given droplet is determined by long-term variations of the ambient temperature $\pm$ 0.5 K. Without any temperature control, the typical IFT was slightly too high for steady-state deformation - the difference in behaviour was only visible in realtime video whilst manipulating the elastic surfaces dynamically.

Adjustment of the salinity to follow the ambient temperature allows production of sustainably deformable droplets without spontaneous emulsification. The IFT

was usually too high to produce nanothreads or dumbbells, but IFT was not so high that droplet oscillation was observed between two closely spaced traps. A significant polygon-type deformation was still achieved if the maximum laser power was used.

The controlled laser-heating in H_2O is usually necessary to achieve the most extreme stable deformations. However, this strategy couples the trap strengths with the IFT, such that above the PIT, heating away from the transition inhibits deformation. Thus, it is preferable to work very close to the upper side of the PIT, where heating stabilises overly soft droplets, or on the low temperature side of the PIT, where maximum available trap strength coincides with minimum available IFT. For example, the (H_2O, 45.0 mM, 21.1 °C) samples are laser-softening so must be below the PIT, but are reasonably stiff and stable in the absence of the laser. Measuring the heating effect (§ 4.7) allows the estimation of an upper limit for the temperature increase as 0.6 K in Setup B. For a trapped object, the dynamic range of powers was constrained such that only the top ± 0.2 K of this could be varied. In the structured illumination Setup C, the temperature of the droplet environment was finely controlled to ± 0.2 K with a Peltier chip and thermocouple as designed in § 3.5.2, driven by closed-loop PID electronics.

Evaporative cooling

A pipette drop (50 μL) of water or ethanol was allowed to evaporate on the upper surface of the observation chip. The droplet deformability changed following the decrease in temperature. Droplets turned from rigid, or slightly elastic, to highly deformable over about 10 s, whereupon the sample temperature dropped to a plateau several tenths of a K lower than ambient. The limiting temperature change depended only on the thermal characteristics of the cell and the surrounding relative humidity. A detectable effect lasted for about 1 min for ethanol and 2 min for water, corresponding to the residence time of the finite solvent pool. As the temperature was restored to its original value, the original droplet deformability was recovered.

6.6.10 Escaping objects and competing forces

There is a far higher incidence of object loss from the trap towards the end of the scan. Particularly, larger droplets are less stable with respect to the *Zaber* stepping at the end of travel. In some cases, the droplet leaves material behind in the traps, whereas in most cases the entire body is ejected. Several contributing factors can be suggested.

Photothermal changes to IFT

First, a change in the IFT itself is explored. If IFT drops significantly such that the capillary length approaches the droplet dimensions, buoyancy is likely to tear away part of a large droplet suspended between traps, leaving small amounts of material as observed. By the same token, if IFT rises rapidly such that the optocapillary number becomes less than unity, a stretched drop snaps out of one or more traps cleanly. If ULIFT is lost rapidly and the trap separation exceeds the droplet diameter, simultaneous escape from all traps is possible.

As IFT is highly sensitive to temperature changes, heating from laser absorption or photobleaching could be at fault. The thermal diffusivity is $k_{aq}/c_P\rho > (300\ \mu\mathrm{m})^2\mathrm{s}^{-1}$, so any heat is dissipated across the field of view in a few ms. This inability to support strong temperature gradients means that IFT is reasonably constant across the droplet surface. The dissipation is about five orders faster than the photobleaching timescale, so any heat generated directly from the photobleaching reaction can be disregarded.

However, steady-state laser heating will remain. Under brightfield inspection of droplets just below the PIT in H_2O, accelerated emulsification (even bursting, see § 3.6) occured when the excitation shutter was opened. For the large part, experiments took place above the PIT - no radical change on initial exposure is apparent

for the majority of droplets. Still this proves that the excitation laser initially heated the droplets on the order of 0.1 K. This is about the same amount expected from the aqueous absorption cross section at 514 nm. The 1064 nm laser will have contributed significantly more heat, as its power and absorption cross sections were greater, with peak temperature increases of 0.6 K (*i.e.* 15 K W^{-1}) in water but only 0.05 K (*i.e.* 1.4 K W^{-1}) in D$_2$O. As expected from these numbers, the trapping laser heating has no apparent effect on droplet deformability for the D$_2$O solution. Unlike in H$_2$O, no cases were encountered where droplet deformability in D$_2$O decreased with trapping laser power.

Of course, being steady-state heating, none of the above offers an explanation as to why the events should occur primarily towards the end of the scan, during which laser power is constant. If laser heating is affecting stability or trap loss, it must have an underlying dependence on either time (t) or z-step (z, m), and account for the similarity between trap loss events in D$_2$O and H$_2$O.

It is interesting to ask if photobleaching can account for the loss events. Much like the changes in surface tension, changes in the properties of the cumulatively photobleached PM597 are independent of the aqueous phase; the underlying dependence is on exposure time, t. Namely, these are the quantum yield $\phi \approx 0.94$ and excitation cross-section, $\Sigma \approx 5 \times 10^4$ cm^{-1}M^{-1}. If the droplet fails to re-radiate the excitation light, its steady-state temperature will increase in a manner that can be estimated using Beer's and Fourier's Laws along the lines of $\Delta T \propto (1 - \phi)\Sigma$. In theory, ΔT could have changed by an order of magnitude in either direction due to photobleaching. Most likely, a fall in the excitation peak would have nullified Σ (i.e. the intensity absorbed drops faster than the intensity radiated). The contribution to the initial heating would disappear over the bleaching period. However, its expected value of 0.03 K min^{-1} is only of the same order as the ambient fluctuations. The slow onset cannot motivate any catastrophic, clean loss events for firmer droplets. On the occasions that the droplet was shifted successfully back to the starting position after the scan, the shape did not appear to change obviously from the first

pass. The loss events are not contingent on photobleaching.

Aberrations to trapping strength

Second, that the optical forces are themselves weakened, leading to droplet loss under surface and buoyancy forces. Neither objective nor *Zaber* stepping motions actually interrupt the presence of the traps, which dominate the object's motion as long as the z steps are well within the trapping range, i.e. the radius of the object. Throughout this work a constant trapping strength across the *Zaber* stepping range has been assumed. However, the variation of aberrations in the beamshape affects the trapping efficiency factor and therefore the optical forces for a given power. To collect information about the beam profile and aberrations, the reflected light calibration as used in § 6.6.2 was extended to out-of-focus locations. Figure 6.42 shows the spherical aberration introduced by the shift of the Zaber telescope lens. Though water-coupled to the mirror, the objective is designed for use with an $n = 1.518$ #1 coverslip. Position zero (corresponding roughly to optimal trapping) still showed some spherical aberration due to the omission of this coverslip.
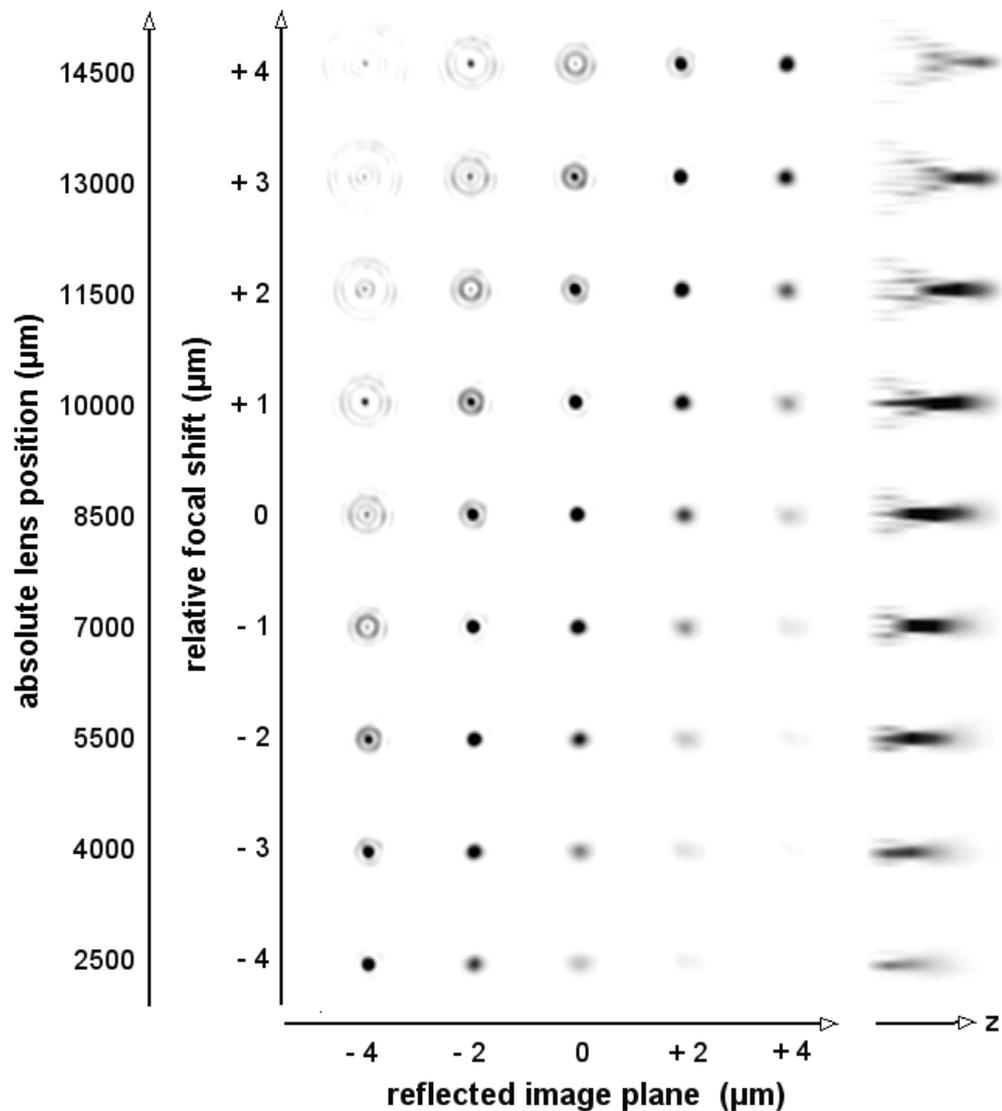
Figure 6.42: Reflected cross-sections of the trapping beam intensity, showing linear defocus with displacement of the lens and characteristic patterns of spherical aberration at the extremes of travel; (*right*) intensity profiles along the beam axis indicating negative spherical aberration.

By translating the telescope lens, the tube length of the trapping beam at the back aperture of the ∞-corrected objective was varied. Alongside the intended focal shift in z, this introduced spherical aberration which distributes the focus along z according to the angle of incidence. The marginal rays that give rise to the trap are displaced further than the paraxial rays. This effect degrades the axial intensity

gradients and thus weakens the traps along the optic axis. The lateral stiffness does not deteriorate as severely [11]. Aberration was estimated [12] as $\leq 0.6\lambda$ between the centre and end of travel, for which the axial gradient dropped as much as -30% towards the focal shift and -10% away from it. That said, the traps used in the experiment will have been weakened much less as all the interrogated volumes were no greater than 10 μm across, and spherical aberration scales quadratically with the focal shift. A parabolic variation of ≤ 10 % of the nominal trapping strength across the largest droplets is expected.

Figure 6.43: Escape force of polymer beads in water (solid boxes, solid parabolic fit to 5 pts, $R^2 = 0.991$) and deformable droplets (open boxes, dashed linear fit to 3 pts, $R^2 = 0.994$) at 23 mW in Setup B. The dotted curve is the solid curve scaled down to the maximum escape force for the deformable droplets.

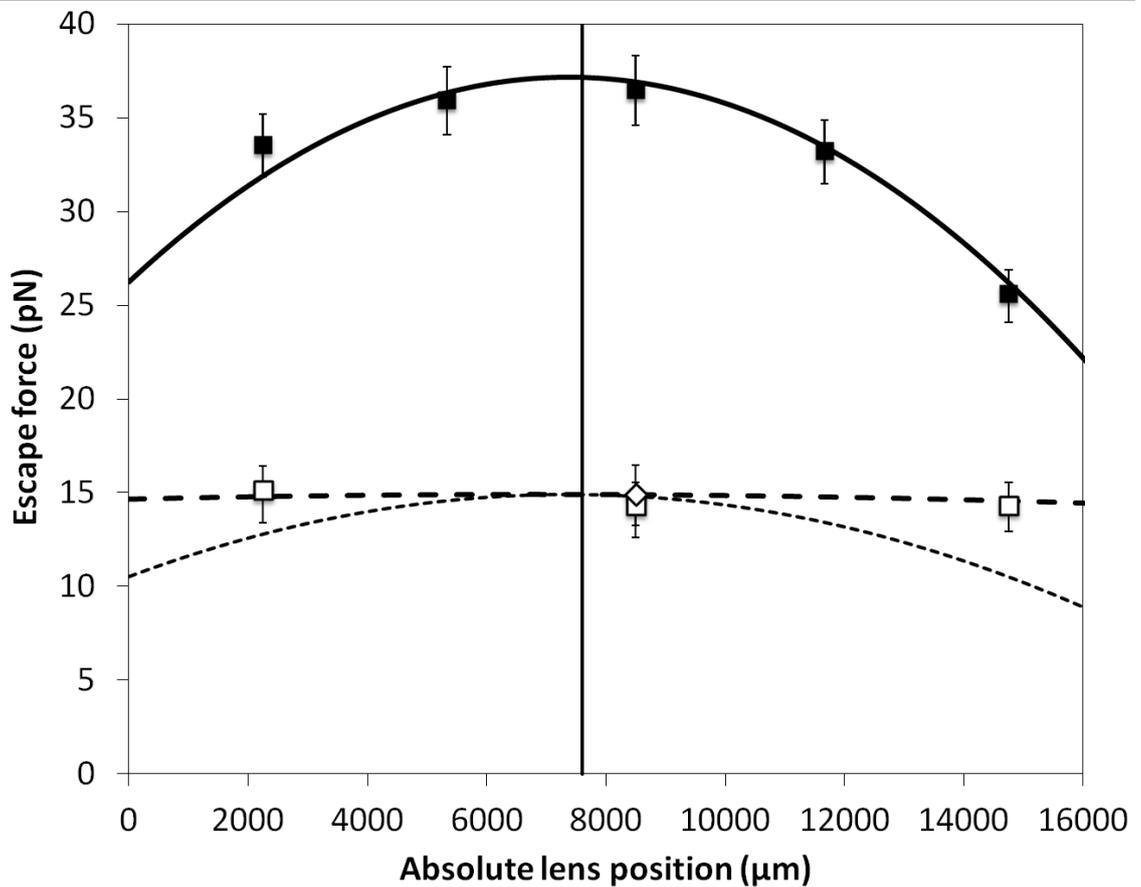What is more, *negative* spherical aberration occurs at the end of each run, when

the trap is at the top of the travel, furthest from the objective lens and the illuminated underside of the object is imaged. Here, the aberration weakens the trap mostly in the upward direction, in which the scattering force and buoyancy act already. However, buoyancy seems an unlikely candidate since the bulk forces amount to only $4\pi\Delta\rho g R^3/3 \leq 0.2$ pN, whilst the trap escape forces were thought to be $\Delta n P/c \geq 2$ pN, even at the minimum power used and distributed over 4 timeshared point traps. Notably, the occurrences of escape from the trap do not correlate well even with the z-calibrated trapping strength, (Figure 6.43). Escape should be stochastic only for much smaller droplets and weaker trap strengths, $kR^2 \sim k_B T$. There exists another fluctuating force, drag due to external flow, which underlies these anomalous loss events.

Flow disturbances and force gradients

Third, the open channel allowed evaporation of heptane droplets, which generated shock waves as droplets burst. These pressure waves were responsible for an oscillating flow along the channel axis, initially of perhaps $v_F \approx 50$ μm s^{-1}, which led to droplet escape. For this to happen during a scan, the required flow rate was $v_F \geq 20$ μm s^{-1} for even the weakest traps and largest droplets. At first, flow does not seem to explain selective expulsion from the trap at one end of the scan. However, the majority of the scans traversed the range 30-50 μm away from the bottom wall. The viscous drag increased by up to 20% during the scan as the droplet moved towards the faster-flowing centre of the channel.

Glossary

DoF	Depth of field, confocal detection	m
F_N	Tension force along thread	-
H	Mean curvature	m^{-1}
H_0	Spontaneous curvature	m^{-1}
K	Gaussian curvature	m^{-1}
L_A, L_A'	Trap separation, normalised to drop radius	m, -
L_κ	Helfrich length	m
L_C, L_C'	Capillary length, normalised to drop radius	m, -
M	Number of traps	-
NA	Numerical aperture	-
$n, \Delta n$	Refractive index, contrast	-
P	Optical power	W
PSF	Point spread function	-
p_L	Laplace pressure	N m^{-2}
R_N	Thread radius	m
R_D	Droplet radius, undeformed	m
SIM	Structured illumination microscopy	
S	Aqueous salinity	M
$T_A, \Delta T$	Ambient temperature, Laser heating	K
T^*	PIT, phase inversion temperature, optimal T	°C
x, y	Lateral image coordinates	m
z	Coordinate along beam axis	m
z_R	Rayleigh range of Gaussian beam	m
$\Delta\rho$	Buoyant density difference	kg m^{-3}
ϵ	Optocapillary number	-
κ	Bending modulus	J
ϕ_A	Volume fraction of phase A	-
Λ	Aspect ratio for small to moderate deformations $\epsilon < 1$	-
Λ_∞	Value at which lateral splitting occurs in two traps	
λ	Optical wavelength	m
ω_0	Beam waist	m

References

[1] J. Jonkman and C. M. Brown, "Any Way You Slice It-A comparison of confocal microscopy techniques", *J. Biomol. Tech.* Vol. 26, no. 2, pp. 54–65, Jul. 2015.

[2] K. Carlsson, P. E. Danielsson, A. Liljeborg, L. Majlöf, R. Lenz, and N. Åslund, "Three-dimensional microscopy using a confocal laser scanning microscope", *Opt. Lett.* Vol. 10, no. 2, pp. 53–55, Feb. 1985.

[3] E. Botcherby, R. Juskaitis, M. Booth, and T. Wilson, "An optical technique for remote focusing in microscopy", *Opt. Comm.* Vol. 281, no. 4, pp. 880–887, 2008, ISSN: 0030-4018.

[4] M. A. A. Neil, R. Juškaitis, and T. Wilson, "Method of obtaining optical sectioning by using structured light in a conventional microscope", *Opt. Lett.* Vol. 22, no. 24, pp. 1905–1907, Dec. 1997.

[5] N. Hagen, L. Gao, and T. S. Tkaczyk, "Quantitative sectioning and noise analysis for structured illumination microscopy", *Opt. Express*, vol. 20, no. 1, pp. 403–413, Jan. 2012.

[6] D. Tapp, J. M. Taylor, A. S. Lubansky, C. D. Bain, and B. Chakrabarti, "Theoretical analysis for the optical deformation of emulsion droplets", *Opt. Express*, vol. 22, no. 4, p. 4523, 2014.

[7] U. Agero, L. Mesquita, B. Neves, R. Gazzinelli, and O. Mesquita, "Defocusing microscopy", *Microscopy Research and Technique*, vol. 65, no. 3, pp. 159–165, 2004, ISSN: 1097-0029.

[8] Maia-Neto, P. A. and Nussenzveig, H. M., "Theory of optical tweezers", *Europhys. Lett.* Vol. 50, no. 5, pp. 702–708, 2000.

[9] E. Fällman and O. Axner, "Design for fully steerable dual-trap optical tweezers", *Appl. Opt.* Vol. 36, no. 10, pp. 2107–2113, 1997.

[10] R. Aveyard, B. P. Binks, S. Clark, and J. Mead, "Interfacial tension minima in oil-water-surfactant systems: behaviour of alkane-aqueous NaCl systems containing Aerosol-OT", *J. Chem. Soc., Faraday Trans. 1*, vol. 82, pp. 125–142, 1 1986.

[11] Y. Roichman, A. Waldron, E. Gardel, and D. Grier, "Optical traps with geometric aberrations", *Appl. Opt.* Vol. 45, no. 15, pp. 3425–3429, May 2006.

[12] C. J. R. Sheppard and M. Gu, "Aberration compensation in confocal microscopy", *Appl. Opt.* Vol. 30, no. 25, pp. 3563–3568, 1991.

[13] G. Bolognesi, A. Hargreaves, A. D. Ward, A. K. Kirby, C. D. Bain, and O. Ces, "Microfluidic generation of monodisperse ultra-low interfacial tension oil droplets in water", *RSC Adv.* Vol. 5, pp. 8114–8121, 11 2015.

[14] G. Bolognesi, Y. Saito, A. I. I. Tyler, A. D. Ward, C. D. Bain, and O. Ces, "Mechanical characterization of ultralow interfacial tension oil-in-water droplets by thermal capillary wave analysis in a microfluidic device", *Langmuir*, vol. 32, no. 15, pp. 3580–3586, 2016.

Conclusions

Summary

This thesis is the culmination of several interdisciplinary streams of work. As such the line between experimental and results chapters was indistinct, so that preparatory work for the optical deformation of droplets spanned novel developments in microfluidics, optics and holography, and microemulsion formulation.

In Chapter 1, the theory and practice of emulsion chemistry was presented for formulating at ultralow interfacial tension. Recipes for Winsor equilibria were adapted to produce emulsions of hydrocarbon oils in aqueous or deuterated continuum, which displayed ULIFT suitable for optical deformation when introduced to the platforms described above. A variety of techniques such as small-angle X-ray scattering, tensiometry and emulsion stability studies were employed to determine the interfacial properties under phase inversion and thus optimise them for optical deformability.

In Chapter 2, the techniques and calibrations were described which were required first, to generate and control arrays of optical point traps in a microscope, and second, to capture 3D images of fluorescent droplets. These techniques included realtime interactive holographic optical tweezing, brightfield microscopy and structured illumination microscopy. Whilst constructing a mechanical optical tweezing microscope in Setup A, a novel concept was put forward in the physical integration of these capabilities together with the microfluidic setup into a single platform in Setup C, with accommodations for photopolymerisation and Raman spectroscopy in Setup C+. Setup C was constructed and its performance validated with 2D bright-

field and 3D structured illumination microscopy results in the last two chapters.

In Chapter 3, methods for generating oil-in-water emulsion droplets for the purpose of optical deformation at ultralow interfacial tension (ULIFT) were described and compared. By considering constraints including wettability, shear, hydraulic impedance and temperature control for ultralow interfacial tension, a novel automated microfluidic platform was demonstrated, including four syringes to control the total flow rate, inline salinity, surfactant concentration and oil-water ratio. While the physical system needs refinements in filtering and flow stability to be used reliably, the smallest droplets thus produced showed properties suitable for optical deformation experiments. The non-equilibrium phase behaviour of these fomulations on the microscale was shown to be more complicated than first imagined, even in the absence of laser intervention. For the AOT quaternary systems, where the amphiphile is hydrophilic at high temperatures, the droplets shrink above the PIT. Below the PIT, the droplets absorb continuous phase, which when released on heating through the PIT causes them to burst (rapid heating) and to form vesicles (gradual heating). The deformability of the droplets was categorised and observed to vary between droplets and change rapidly even in the controlled environment of a microfluidic salinity gradient.

In Chapter 4, the investigation was extended with novel observations of rich phase behaviour induced by focused lasers in bulk microemulsion and microemulsion droplets in water. These behaviours were exacerbated at high optical power in the range of 100-250 mW and near the phase inversion condition, where interfacial tension is lowest and varies strongly with temperature. By choosing a system with tunable temperature sensitivity, the processes of phase separation and transfer, which underlie many of the non-equilibrium phenomena observed, could be decelerated. A broad array of vesicles, multiple emulsions and metastable phases emerged at graduated forms and rates, depending on the extent of laser heating, which was calculated as 14.7 KW^{-1} for $\lambda = 1064$ nm in bulk water. At different amphiphilic ratios, oil- and water-rich phases were each nucleated from microemulsion by the

laser. The vast majority of these changes were consistent with thermal variation of the phase diagram, which is dependent on the precise amphiphilic ratio. The behaviour of compositions with different laser heating responses after deuteration or emulsification, imply that laser absorption is the major, but not the sole driving force for phase separation. Given the localisation of the nucleation to the laser focus, the main candidate for the motivation of a non-thermal mechanism is the optical gradient force. However, low-index particles nucleate at certain monolayer compositions; therefore cases exist where thermophoresis also determines the phase behaviour. The findings in Chapters 1 and 4 clearly demonstrate that the droplets used for the deformation experiments are in fact oil-rich phases related to those of three-phase microemulsions. These investigations informed the procedures used in Chapters 5 and 6 so that phase transitions were avoided and the majority of droplets were made stable for deformation purposes.

In Chapter 5, an experimental framework for parametrising the deformation of ULIFT droplets with point traps was discussed. Deformations in each trap could then be identifed as linear or nonlinear through the use of a single parameter, the reduced optocapillary number ϵ/M. Brightfield imaging was used to document the response of the static shape to arrays of optical point traps, including the bifurcation from a spheroidal shape to two spheres connected by a nanothread. A theoretical model was developed for the stability, tension and dimensions of nanothreads near the phase inversion condition, and was validated against prior measurements of the thread recoil velocity. I also showed that nanothread networks have a hierarchy of stability and decay pathways including topological change.

In Chapter 6, I generated a diverse family of optically supported fluid shapes and measured the 3D morphology using both structured illumination microscopy (SIM) amd confocal laser scanning microscopy with 3D calibration of the trap and droplet positions. Despite a modest variation of spherical aberration in the trapping beams with displacement from the confocal plane, the shapes were consistent with those in SIM and brightfield, and across different droplet sizes. The shapes were

discriminated according to the input parameters, primarily the number of traps M, deformability ϵ/M and ratio of trap separation to droplet radius L'_A.

At moderate deformability $\epsilon/M \approx 1$, droplets evolved from prolate- to prism-like, to oblate shapes as L'_A increased from below unity to values above. At values greater than $L'_A = 1$ for two traps, stable dumbbells were found. For high deformability, $\epsilon/M \approx 10$, hourglass-like shapes - with grooved saddle curvature in the focal plane - were produced at small trap separations. At large trap separations, table-like shapes were observed, with buoyant membranes stretched across the optical handles.

Lateral asymmetry was rare and observed only at high powers (> 100 mW). It was ascribed to the enhancement of mismatched trap powers (and therefore gradient forces) by thermocapillary forces pushing the interface towards the focus at temperatures below phase inversion. This effect was significant only at high-power foci and when the IFT was highly temperature-dependent. Much akin to the gradient forces acting towards an isointensity surface, the thermocapillary forces act towards an isothermal contour matching the droplet volume. The feature size of shapes supported by point traps are restricted to the dimensions of the characteristic handle rather than those of the beam itself. I associated this phenomenon with the filling of the handle outwards to a surface where the interfacial and optical pressures become equal. It is noticeable that handles become larger with higher deformability ratio P/σ.

By contrast, axial asymmetry was widespread among ULIFT droplets. The buoyancy and scattering forces caused the lower face of the droplets to flatten against the focal plane, and the upper side to bulge. As these forces acted in the same direction, the effect of scattering force could not be distinguished except for smaller droplets at higher power. Under these conditions, the droplet asymmetry disappeared, proving the scattering force is dominated by the gradient force at the high NA used. Thus buoyancy was responsible for the observed asymmetry; in all droplet regions distant from the traps, hydrostatic and Laplace pressures balanced to produce greater positive mean curvatures on the upper side of the droplet than the lower side. Sev-

eral examples were presented of negative mean curvature on the underside of the droplet. There are also rare examples where the coupled effects of axial asymmetry, hourglass pinching and separation of the traps produced zero or even negative local mean curvatures at the equator of the droplet.

Implications for future work

The main difficulty in this project was that the control demonstrated over the droplet size and interfacial tension sufficed to give only a scattered set of shape data. The morphologies on the parameter space defined at the beginning of Chapter 5 have yet to be fully characterised. Further efforts are needed to sustain microfluidic control over the droplet size and temperature as envisioned in Chapter 3. Measurement of the IFT of individual microdroplets *in situ* would help to alleviate this issue. One such method is the nanothread recoil (§ 5.4.1), but this requires trapping and is limited to very soft droplets from which threads can be drawn. This method is also dependent on the laser power and associated local heating effects. An imaging technique would be preferable; at very low ULIFT, the overdamped capillary waves are visible under brightfield microscopy. The average amplitude of each excitation mode depends only on the properties of the interface, so the ULIFT of an untrapped droplet [13] can be extracted directly from the power spectrum of the fluctuations. Local estimates of bending modulus and dynamic IFT can also be obtained [14].

As a novel publication of 3D images of optically deformed droplets, this thesis has laid groundwork for the comparison of real and predicted shapes. For polygonal shapes, this comparison included the axial or lateral extension, sharpness of vertices and edges, and the flatness of faces. Predictions made by Tapp et al., such as the existence of negative mean and Gaussian curvatures have been verified experimentally, albeit in a qualitative manner. Alongside the development of these theoretical models, it would be valuable to define and measure quantitative experimental metrics, such as these local curvatures, or a basis representation in spherical harmonic

functions. This information could then be used for feedback in shape optimisation routines with control of parameters such as ambient temperature, trap power and position.

The next step in shape optimisation would be to move beyond 3D arrays of Gaussian point traps to a 3D 'optical landscaping' approach, as offered by holographic algorithms. Although in its infancy, in principle this capability would allow arbitrary shapes to be produced with feature sizes as small as the optical diffraction limit. The question can be posed: what hologram and droplet conditions are required to make a given complex shape? This is a difficult inverse problem in theory, but one that could be solved empirically using the platform presented here.

A major unexpected result of this work has been to highlight the extent to which buoyancy determines optically-deformed droplet shapes. The asymmetry it imposes on the droplet diversifies the range of shapes that can be generated with point traps. As buoyancy acts in one fixed direction and cannot be tuned easily in situ, it presents the droplet sculptor with difficulties when producing a regular shape. For simple point arrays, neutrally buoyant oils could be used to facilitate the production of symmetric shapes that resemble handles conjoined by minimal surfaces, where ΔH between upper and lower surfaces is zero. However, practical issues would have to be overcome, such as ensuring resolution of emulsion layers and measuring interfacial tensions by means other than centrifugation or spinning/sessile drop tensiometry. The microfluidic and deformation experiments described here have, in part, inspired novel techniques to measure IFT non-gravimetrically for individual microdroplets, based on thread recoil and capillary fluctuations.

A chief vision of the collaboration is to apply droplets connected by threads as nanofluidic networks, in which flow is driven with differential laser powers. Although this work contributes to our understanding of the stability and topology of these networks, their dynamics and flow properties have yet to be investigated in detail. While analogies exist for lipid vesicles, the attolitre scale of the nanothread junctions

is sufficiently small that reactions between individual molecules could be localised and probed in liquid media on an accessible timescale. As biological molecules are largely water-soluble, reverse emulsions with water droplets and networks would be of immense interest to applied fields such as molecular biology. The familiar formulations derived in this work could be used if supported by more sophisticated optical traps, or with the same techniques, new formulations could be developed for oils with lower refractive index than water, such as fluoroalkanes.

This work on formulation suggests that ULIFT with an aqueous phase is possible for a large class of oils, even with a limited range of common surfactants and additives. In chemists' terms, the 'rate-determining step' is to negotiate the considerable number of iterative experiments to find the optimal points, besides the variation of the minima themselves. As for many optimisation problems, the most productive strategy for entirely new oils was to start from the most similar optimal system and constrain the search to one or two degrees of freedom. In such a scenario, the formulator may consider either ternary systems, where the surfactant HLB itself can be varied, or quaternary systems with a mid-HLB surfactant, where the concentration of a single additive such as an electrolyte can be varied. Where IFT minima are not low enough for nanothread formation, as found here for toluene and styrene formulations, then substitution with extended surfactants and amphiphilic polymers might offer a way to diminish the IFT. The complications of phase behaviour addressed in this work may yet prove a barrier to how far the IFT can be lowered, or how closely the PIT can be approached, before the droplet or network is no longer useful for deformation. However, I imagine that this leaves a great range of accessible shapes and polymerisable materials to fulfil future scientific applications.

To summarise this thesis: the work confirms that microdroplets are amenable to optical deformation at ultralow interfacial tension, and that the chosen strategy poses a number of problems of fundamental interest to fluid mechanics, holography, industrial emulsion chemistry, and even thermodynamics. Yet it is not only microdroplets that can be manipulated, but nanothread networks; I believe this path of research is the most promising to arise from this collaboration and yet it remains untrodden. It is my hope that my work on sculpting droplets helps *optonanofluidic networks* to become a standard technique in molecular biology and chemistry, much like optical tweezing has in biophysics. Along the way, I have learned to design, construct and refine microfluidic and optical platforms which have opened a new window to the microscopic world.